

**POROSITY STUDIES OF A CERAMIC,
A GLASS AND CLAY**

**A Thesis submitted to Goa University for the Award of the Degree of
DOCTOR OF PHILOSOPHY**

in

PHYSICS

BY

Ms. RESHMA S. RAUT DESSAI

Research Guide

J.A.E. DESA

GOA UNIVERSITY

TALEIGAO GOA

2013



Dedicated to my

Parents

Mrs. Sargja S. Raut Dessai

&

Mr. Sada S. Raut Dessai

&

My Teacher

Prof. J. A. E. Desai

CERTIFICATE

This is to certify that the work incorporated in this thesis entitled, “**Porosity Studies of a Ceramic, a Glass and Clay** ” submitted by Ms. Reshma S. Raut Dessai, constitutes her independent work and the same has not been previously submitted for the award of any other degree, diploma, associateship, fellowship or the other such title.

Goa University
August 2013

Prof. J.A. E. Desa
(Research Guide)
Department of Physics
Goa University
Goa, India.

DECLARATION

I hereby declare that the matter embodied in this thesis entitled, “**Porosity Studies of a Ceramic, a Glass and Clay**” is the result of investigations carried out by me, under the supervision of Prof. J.A.E. Desa and it has not previously formed the basis for the award of any degree, diploma, associateship, fellowship or the other such similar title.

Goa University
August 2013

Ms. Reshma S. Raut Dessai
(Candidate)

ABSTRACT

In a medium, the porosity and distribution of pore sizes affect its important bulk physical properties. This study deals with the characterization of pores in several length domains. Three different porous materials have been studied; a compacted glass; a ceramic; and clays. In each of these, macroscopic, micron and nano-pores have been examined. Various experimental techniques have been utilised; viz. TG/DTA, SEM, X-ray diffraction and SANS. From bulk density measurements, values of porosity were typically in the range of 30 % to 45 %. Thermogravimetric data on the porous glass yielded an estimate of pore connectivity of 45 %. SEM showed that as the sintering temperature increases there is coalescence of larger pores at the expense of smaller sized pores. From SANS measurements on the ceramic, a bimodal distribution of pore sizes was found to be 166 nm and 32 nm. Similar findings in the nano-length scale were also found for the glass and the bentonite clay. SANS was also used to show that the nano pores are connected to the bulk surface of these materials. The method of contrast matching the glassy and ceramic matrices to mixtures of D₂O and H₂O gave isolated pore concentrations to be a factor of 3 to 4 times less than the concentration of connected pores. The average inter-micellar distance of SDS in sodium-bentonite is decreased by 24 % compared to its normal value. Quasielastic Neutron Scattering on water in bentonite clay gave a diffusion constant of $1.8 \times 10^{-5} \text{ cm}^2/\text{sec}$ compared to the bulk water value of $2.5 \times 10^{-5} \text{ cm}^2/\text{sec}$. The results of this thesis are especially relevant to fluid transport in and through porous media. The presence of nano-pores, their links to the surface and quantification of isolated pores constitute the principal new findings of the study.

ACKNOWLEDGEMENT

This Ph.D. thesis is the result not only of my passion for science but also of the valuable support extended to me by my guide Prof. J. A. E. Desa and my Parents.

It is a great privilege to be a student of Prof. Erwin Desa, former Head Department of Physics and former Dean, Faculty of Natural Sciences, Goa University. His knowledge, experience, principles and guidance have helped me to look at the subject in particular and life in general, in a different perspective. It is difficult to express in words my deepest sense of gratitude to my esteemed guide and teacher. I shall always, in my life remain indebted to him for his valuable guidance, immense support and critical evaluation and tireless pursuit for perfection which was an inspiration throughout my Ph.D. course. His logical way of thinking on scientific problems, understanding, encouragement and personal guidance have been of great value for me. I thank my guide for giving me the freedom to investigate the exciting world of porous media. I am also grateful to him for being very patient while reviewing this thesis critically

I am grateful to the Vice Chancellors' nominees Prof. P.R. Sarode and Dr. K.R. Priolkar for their encouraging comments and support throughout my work period.

This thesis would not have come to its completion without the support and funding by UGC-DAE, through a project entitled "Studies of Porous Materials by SANS". My sincere thanks to former and present Mumbai-Centre Directors, Dr. A.V. Pimpale and Dr. V. Siruguri and to Dr. P. Chaddah, Director of UGC-DAE-CSR, who have all facilitated my work. I also express my sincere gratitude to the principal collaborator in this project Dr. Debasis Sen from Solid State Physics Division, BARC for his consistent and generous help, fruitful discussion, expert advice and useful critical analysis in MSANS. I also would

like to thank him for sharing his wide knowledge at various points of discussions. I also would like to thank Dr. S. Muzumder, the principal force behind the MSANS instrument, for his encouragement and cooperation during the course of this work. My sincere thanks to Dr. Vinod Kumar Aswal (SSPD, BARC), for all his generous help with the SANS studies on the samples. My thanks are also due to Dr. R. Mukhopadhyay (presently Head, Solid State Physics Division, BARC) and Dr. S. Mitra (SSPD, BARC), for their active encouragement and generous help with the QENS study on bentonite clay. I am also thankful to Dr. S.L. Chaplot (former Head, SSPD and presently Physics Group Director, BARC) and numerous other members of the Neutron Scattering group of SSPD, BARC for their support, friendliness and advice during the years of this study.

I also would like to thank Dr. Kaushik Daana of CGCRI, Kolkata for his help with the mass loss experiments. I wish to record my gratitude to the former Heads of Glass and Advanced Ceramics Division, BARC, Dr. G.P. Kothiyal and Dr. S. Ramanathan as well as to Dr. Abhijeet Ghosh of the same Division for their help with Mercury Intrusion Porosimetry. My grateful thanks are due to Dr. N. N. Ghosh from BITS Pilani, Goa Campus and Dr. Bhanudas Naik for their help with nitrogen adsorption porosimetry. I would like to acknowledge the help provided with SEM measurements by Dr. Rahul Mohan and the Director of National Centre for Antarctic and Ocean Research, Vasco, Goa as well as the Director of National Institute of Oceanography, Dona Paula, Goa.

I wish to thank the former Deans of the Faculty of Natural Sciences, Goa University and the present Dean Prof. Julio Fernandes. My thanks are also due to the present Head, Physics Department, Prof. R. B. Tangsali and former Head Prof. P. R. Sarode for extending necessary facilities of the department.

My sincere thanks to the other teaching staff of the Physics Department Dr. Uma Subramanian and Dr. R. V. Pai for their support.

I am grateful to all the reviewers of papers and the external examiner of my thesis for their comments and valuable suggestions.

I gratefully acknowledge Goa University for providing me with a Research Studentship for a period of two years.

I am also very grateful to my senior colleague Ms. Shradha Ganorkar and my friend from the Botany Department Ms. Cassie Rodrigues for being supportive at all times and for their stimulating discussions in the course of my research work. I am grateful to all my junior colleagues in the Department: Benedict, Bosco, Elaine, Jason, Kapil, Manoj, Nelson, Nilima, Pranav and Wilson for their kind cooperation and friendship. Assistance rendered by the non-teaching staff of the Department of Physics, Ms. Hermina Araujo, Ms. Eva Baptista, Mr. S. Vaigankar and Mr. S. Salgaokar is also gratefully acknowledged. My sincere thanks are due to the library staff and the administrative staff of Goa University for all the help they provided in bringing this thesis to completion.

In many countless ways, my family has contributed to my efforts. I take this opportunity to thank my parents, sisters, my brother-in law and my little niece Reya, for being supportive and for their encouragement. Without their patience, encouragement and understanding, it would not have been easy.

Above all I thank Almighty God for giving me the courage and confidence to mould this thesis in its present form.

Reshma Raut Dessai

CONTENTS

Abstract.....	i
Acknowledgement.....	ii
Contents.....	v
List of Figures.....	xi
List of Tables.....	xviii
List of Symbols.....	xx
1. Introduction and Objectives.....	1-19
1.1. Introduction of Porous Media.....	1
1.2. Important parameters of porous media.....	5
1.2.1. Porosity.....	5
1.2.2. Tortuosity.....	7
1.2.3. Connectivity.....	8
1.2.4. Permeability.....	8
1.2.5. Flow Rate.....	8
1.2.6. Diffusion.....	8
1.3. The Porous Materials Studied.....	9
1.3.1. Porous Ceramics.....	9
1.3.2. Porous Glass.....	12
1.3.3. Porous Clay.....	15
1.4. Objectives of the Present Study.....	18
1.4.1. Porous ceramic.....	18
1.4.2. Porous Glass.....	18
1.4.3. Porous Clay.....	19
2. Theoretical Considerations.....	20-44

2.1.	Pore structure.....	20
2.2.	Effect of compaction and sintering on pore structure.....	21
2.3.	Theory of flow through porous media.....	22
2.3.1.	Darcy's law.....	22
2.3.2.	Kozeny-Carman equation.....	23
2.4.	Swelling in clay.....	24
2.5.	Capillary rise in hydrology.....	25
2.6.	Models of porous media.....	25
2.7.	Small angle scattering in porous media.....	26
2.7.1.	Salient features of neutrons.....	29
2.7.2.	Scattering length and scattering cross section.....	29
2.7.3.	Form factor of simple geometric objects.....	34
2.7.4.	Contrast Matching.....	34
2.7.5.	Guinier and Porod approximations.....	35
2.8.	Quasi-elastic neutron scattering.....	36
2.9.	Diffusion through a porous medium.....	39
2.10.	Models of Diffusion.....	41
2.10.1.	Jump Diffusion Models.....	41
2.10.2.	Rotational motion.....	43
3.	Experimental methods.....	45-60
3.1.	Introduction.....	45
3.2.	Methods of preparation.....	45
3.2.1.	Sol-Gel Method.....	45
3.2.2.	Compaction and sintering.....	46
3.3.	Porosity and Density by water displacement.....	47

3.4.	Small Angle Neutron Scattering Instrument.....	49
3.5.	Medium Resolution Small Angle Neutron Scattering Instrument.....	49
3.6.	Quasi Elastic Neutron Scattering (QENS).....	50
3.7.	Scanning electron microscopy, X-ray diffraction, thermo-gravimetric analysis and mercury intrusion porosimetry.....	54
3.7.1.	Scanning electron microscopy.....	54
3.7.2.	X-ray diffraction.....	56
3.7.3.	Thermogravimetry and Differential Thermal Analysis (TGA/DTA).....	58
3.7.4.	Mercury Intrusion Porosimetry.....	58
3.7.5.	Infrared spectroscopy.....	59
4.	Nano-Porous Structure of a Porous Ceramic Obtained from Rice Husk.....	61-97
4.1.	Introduction and scientific interest.....	61
4.1.1.	Synthesis of silica from rice husk.....	62
4.1.2.	Comparison of RHS with commercial silica by X-ray diffraction, IR and SEM/EDEX.....	62
4.1.3.	Preparation of ceramic from RHS by the sol-gel method.....	67
4.1.4.	Interpretation of thermogravimetric curves of RHS ceramic.....	68
4.1.5.	Phase change as a function of sintering temperature by X-ray diffraction..	70
4.1.6.	Summary of X-ray and thermal studies of rice husk ceramic.....	70
4.2.	Effect of temperature on pore morphology of RHS ceramic.....	71
4.2.1.	Introduction.....	71
4.2.2.	Density and porosity by water displacement method.....	71
4.2.3.	Nanoporous structure of sintered ceramic by MSANS.....	73
4.2.4.	Nanopore morphology in the sintered ceramic loaded with D ₂ O.....	81
4.2.5.	Estimation of scattering from isolated pores.....	83

4.2.6.	Pore size distribution by Mercury Intrusion Porosimetry.....	87
4.2.7.	Microspore structure by Scanning Electron Microscopy and composition.....	87
4.2.8.	Summary of temperature on porosity of rice husk silica.....	90
4.3.	Effect of compaction pressure on pore morphology.....	90
4.3.1.	Introduction.....	90
4.3.2.	Density and Porosity by water displacement method.....	91
4.3.3.	Effect of pressure on nanoporous structure by MSANS.....	93
4.3.4.	Micro pore structure at different pressures by SEM.....	95
4.3.5.	Summary of effect of pressure on porosity of rice husk silica.....	95
4.4.	Conclusions of Studies on Rice Husk Silica Ceramic.....	97
5.	Porosity Studies of Compacted and Sintered Glass Microspheres.....	98-127
5.1.	Preparation and porosity of a porous glass.....	98
5.1.1.	Introduction.....	98
5.1.2.	Preparation of porous glass from microspheres and their characterizations.....	99
5.2.	Measurements and Discussions.....	100
5.2.1.	Optical microscopy.....	100
5.2.2.	Density and porosity study of compacts.....	102
5.2.3.	Micro-pore morphology of the glass compacts.....	103
5.2.4.	Pore morphology by Mercury Intrusion Porosimetry.....	110
5.2.5.	Neutron scattering study of pores in glass compact.....	113
5.2.6.	Estimation of isolated pores.....	117
5.4.	Thermogravimetry of microsphere compacts.....	121
5.5.	Conclusions of the porous glass study.....	126
6.	Porosity Studies of Bentonite and Kaolinite Clay.....	128-187
6.1.	Introduction Kaolinite and Bentonite.....	128

6.2.	Hydration and pore structure of Kaolin	132
6.2.1.	Experimental.....	132
6.2.2.	Results and discussions.....	132
6.2.3.	Conclusions of studies on kaolinite.....	139
6.3.	Hydration of Bentonite Clay: X-ray, IR-Spectroscopy and SANS study.....	141
6.3.1.	Introduction and Scientific Importance.....	141
6.3.2.	Experimental methods.....	142
6.3.3.	Results and Discussion.....	142
6.3.4.	Summary of hydration of bentonite clay.....	148
6.4.	Effect of pressure and hydration on pore structures of sintered clays.....	150
6.4.1.	Scientific interest.....	150
6.4.2.	Experimental.....	150
6.4.3.	Micro pores in compacts of bentonite and particle shape by SEM.....	151
6.4.4.	Nanoporous Structures of bentonite clay by SANS.....	153
6.4.5.	Results and Discussion.....	153
6.4.6.	Conclusions on effect of compaction pressure on pore structures.....	162
6.5.	Effect of confinement on a micellar solution in a sodium activated bentonite clay	
6.5.1.	Scientific interest.....	163
6.5.2.	Preparation of sodium saturated bentonite.....	164
6.5.3.	Results and Discussions.....	166
6.5.4.	Conclusions of micellar solutions in bentonite clay.....	173
6.6.	Dynamics of Water in Bentonite Clay.....	174
6.6.1.	Scientific and technological importance.....	174
6.6.2.	Experimental Methods.....	176
6.6.3.	Results and Discussion.....	176

6.6.4. Conclusions on diffusion of water in bentonite clay.....	185
6.7. Conclusions on studies of porous clay.....	185
7. Conclusions and Future Studies.....	188-194
7.1. Conclusions.....	188
7.2. Future Studies.....	193
REFERENCES.....	195
LIST OF PUBLICATIONS.....	206

LIST OF FIGURES

Figure #	Title	Page #
1.1	Schematic of the effect of porosity on physical properties.	2
1.2	Tortuous path followed by liquid or contaminant.	7
2.1	Classification of pores in a porous medium.	20
2.2	a) Cubic packing, b) rhombohedral packing, c) cubic packing with two grain sizes d) floral arrangement .	22
2.3	Schematic showing definition of Darcy's law.	23
2.4	Schematic of cylindrical pore connectivity.	26
2.5	Various experimental techniques and their length scales.	28
2.6	Schematic of momentum transfer vector Q .	30
2.7	The sketch of $P(Q)$ and $S(Q)$.	33
3.1	Experimental setup for the water displacement method.	48
3.2	Schematic of SANS at BARC [from Aswal and Goyal 2000].	51
3.3	Schematic of MSANS at BARC [from Mazumder et al., 2001].	52
3.4	Schematic of QENS Instrument at Druva Reactor [from Mukhopadhyay et al., 2001].	53
3.5	Scanning Electron Microscope at NCAOR, Goa.	55
3.6	Instrument used for gold coating on the sample.	55
3.7	Schematic of Bragg's law.	57
3.8	Schematic of X-ray diffractometer.	57
4.1	X-ray diffraction of rice husk silica and that of commercial silica.	63
4.2	FTIR spectra of RHS and its comparison with commercial silica.	63
4.3	SEM micrograph of Rice Husk Silica.	65
4.4	Scheme of preparation of porous glass-ceramic from RHS.	67

4.5	TGA-DTA of RHS ceramic powder fired at 700 °C.	69
4.6	X-ray diffraction of RHS ceramic fired at 700, 800 and 1000 °C for two hours.	69
4.7	Variation of porosity of RHS ceramic with sintering temperature.	72
4.8	Scattering profile of compact unfired and sintered at 800, 1000 °C for 2 hours.	78
4.9	Scattering profile of ceramic sintered at 800 °C for 2 and 4 hours.	78
4.10	Scattering profile of ceramic sintered at 1000 °C at the cooling rate 10 °/C and 30 °/C.	80
4.11	Scattering profile of ceramic sintered at 800 °C and loaded with D ₂ O.	82
4.12	Scattering profile of ceramic sintered at 1000 °C and loaded with D ₂ O.	82
4.13	Scattering profile of ceramic sintered at 800 °C and loaded with a H ₂ O-D ₂ O mixture. Continuous line shows the fitted data.	86
4.14	Scattering profile of ceramic sintered at 1000 °C and loaded with a H ₂ O- D ₂ O mixture. Line shows the fitted data.	86
4.15	Resulting pore size distribution of porous ceramic sintered at 800 °C for 2 hour.	88
4.16	SEM micrographs of ceramic compact sintered at (a) 800 °C for 2 hours (5000X) b) 1000 °C (5000X) for 2 hr.	88
4.17	Variation of porosity of RHS ceramic with compaction pressure.	92
4.18	MSANS data on porous ceramic compacted at different pressures (solid line is the fit of the model to the data).	94
4.19	SEM micrographs of ceramic compact sintered at 800 °C for 2	96

	hours and compacted at (a) 1T, (b) 2T, (c) 4T, (d) 6T (5,000X).	
5.1	Porous glass compacts as prepared.	101
5.2	Optical image of microsphere compact sintered at 640 °C for 6 hours.	101
5.3	Variation of density (by water displacement method) of ceramic sintered at temperature 640 °C with sintering time.	104
5.4	SEM micrograph of (a) 20 μm microsphere sintered at 640 °C for 3 hr (800X), (b) 20 μm microsphere sintered at 640 °C for 6 hr (750 X).	106
5.5	SEM micrograph of 20 μm microsphere sintered at 740 °C for 1 hr (500X).	106
5.6	SEM micrograph at 150X of (a) 100 μm microsphere sintered at 640 °C for 3 hr, (b) 100 μm microsphere sintered at 640 °C for 6 hr, (c) 100 μm microsphere sintered at 640 °C for 24 hr , (d) 100 μm microsphere sintered at 640 °C for 30 hr .	107
5.7	100 μm microsphere sintered at 740 °C for 3 hr (150 X).	108
5.8	Internal structure of 100 μm microsphere sintered at 640 °C for 6 hr (95X).	108
5.9	Neck development when two spheres touch each other.	108
5.10	Schematic of decrease in pore size and the number of pores with increase in sintering time (a) 3 hour, (b) 6 hour and (c) 24 hour.	109
5.11	Pore size distribution of porous glass sintered at 640 °C for 3 hours.	111
5.12	Pore size distribution of porous glass sintered at 640 °C for 24	111

	hours .	
5.13	Pore size distribution as measured by mercury intrusion method; temperature 640 °C for 3hours.	112
5.14	MSANS data of 20 µm sized microsphere compacts fired at 640 °C from 3 to 24 hours.	115
5.15	Pore size distribution of larger pores and smaller pores (insert) for compact of 20 µm microspheres.	115
5.16	USANS data of 100 µm sized microsphere compacts fired at 640 °C from 3 and 24 hours and fired at 740 °C for 3 hours.	116
5.17	USANS data of 100 µm sized microsphere compacts fired at 640 °C for 6 hours and loaded with D ₂ O.	116
5.18	Scattering length density of the H ₂ O-D ₂ O mixture v/s % H ₂ O in the mixture.	120
5.19	USANS data of 100 µm sized microsphere compacts fired at 640°C for 6 hours and loaded with a mixture of H ₂ O- D ₂ O.	120
5.20	Plot of fractional mass loss at temperature (a) 35 °C (b) 50 °C fitted with a 3 rd order polynomial.	122
5.21	Fractional mass loss as a function of time from a compact fired at 640 °C for 3 hours at various temperatures.	124
5.22	Temperature as a function of time for complete dehydration of the 3 hour sintered sample.	124
5.23	Fractional mass loss from a compact fired at 640 °C for 24 hours at various temperatures.	125
5.24	Temperature as a function of time for complete dehydration for the 24 hour sintered sample.	125

6.1	Schematic of the structure of Kaolinite clay [from Grim,1968].	130
6.2	Kaolin clay platelets placed one above the other forming a particle.	130
6.3	Schematic of the structure of Bentonite (Smectite) clay [from Grim, 1968]	131
6.4	Schematic of bentonite particle.	131
6.5	X-ray diffraction study of dry and hydrated kaolin.	133
6.6	TGA-DTA data of Kaolinite powder.	133
6.7	SEM micrographs of (a) kaolin compacted at 1200 °C and (b) kaolin powder.	135
6.8	N ₂ adsorption-desorption isotherm of kaolin.	137
6.9	Pore size distribution of kaolin powder and compact.	137
6.10	USANS data of kaolin compact.	140
6.11	SANS data of kaolin compact and its pore size distribution (insert).	140
6.12	X-ray data of hydrated, fired and dry bentonite.	143
6.13	SANS data on dry and hydrated bentonite clay	146
6.14	Pore size distribution of hydrated bentonite.	146
6.15	Infrared spectra of dry and hydrated bentonite clay.	149
6.16	SEM micrograph of a raw bentonite.	152
6.17	SEM micrograph of compacted bentonite.	152
6.18	Bentonite clay compact dry and sintered at 600 °C.	152
6.19	SANS fitted data on bentonite compact at 1, 2, 5 and 10 T pressures.	156
6.20	Pore size distribution of polydispersed spherical pores in	156

	bentonite.	
6.21	(a) variation of peak of pores size with compaction pressures (b) variation of average pore size with compaction pressures.	157
6.22	Fits to SANS data from dry and D ₂ O loaded bentonite compact .	159
6.23	Fits to SANS data from dry and compact 50%D ₂ O-50%H ₂ O loaded bentonite.	159
6.24	MSANS data fitted for a bentonite fired at 200 °C and 600 °C.	161
6.25	Schematic of adsorption of cationic surfactant on bentonite particles (from Alemdar et al., 2000).	165
6.26	Schematic of adsorption of ionic surfactant on bentonite particles.	165
6.27	X-ray diffraction of bentonite, Na-bentonite and SDS loaded bentonite.	168
6.28	Infrared spectra comparison of bentonite and Na saturated bentonite.	169
6.29	SANS data on micellar (10 % SDS) induced bentonite and Na bentonite clay.	171
6.30	SANS data on micellar (20 % SDS) induced bentonite and Na bentonite clay.	171
6.31	Schematic of micellar charge reduction due to Na ion from clay.	173
6.32	Layout of bentonite clay as barrier.	175
6.33	Thermogravimetric and Differential Thermal Analysis data of bentonite clay.	178
6.34	Fitted QENS spectra from the hydrated and dehydrated bentonite clay at $Q = 1.32 \text{ \AA}$.	182

6.35	Fitted QENS spectra from the hydrated bentonite clay at different Q values.	183
6.36	Variation of HWHM, Γ with Q^2 .	184

LIST OF TABLES

Table #	Title	Page #
4.1	IR modes of rice husk silica and commercial silica.	64
4.2	Elemental composition of RHS.	66
4.3	Density, Porosity and neutron scattering length density of ceramic compacts sintered at different temperatures.	72
4.4	The fitted parameters obtained from SANS analysis for sintered ceramic at different temperature.	79
4.5	Parameters obtained from SANS analysis for ceramic sintered at different times.	79
4.6	Parameters obtained from fitted data for D ₂ O loaded ceramics.	81
4.7	Parameters obtained by SASFIT for ceramic sintered at 800 °C and loaded with a H ₂ O-D ₂ O mixture (DH signifies D ₂ O and H ₂ O).	85
4.8	EDX analysis of ceramic compacts sintered at 800 °C and 1000 °C for 2 hours.	89
4.9	Density, Porosity and neutron scattering length density of ceramic compacts compacted at different pressures	91
4.10	Parameters obtained from SANS analysis for ceramic compacted at 1,4 and 6 T.	93
5.1	Elemental composition of silica microspheres.	99
5.2	Density, Porosity and linear shrinkage of the microsphere (M) samples.	102
5.3	Parameters obtained from fitted data for 20 µm microsphere compact.	114

5.4	Parameters obtained from fitted data for 100 μm microsphere compact.	117
6.1	Surface area, pore volume and pore size of kaolin clay by nitrogen porosimetry.	136
6.2	Parameters obtained from fit to SANS data on hydration of bentonite.	139
6.3	Parameters of scattering centre geometries obtained from SASFIT.	147
6.4	Studies of IR band assignment of bentonite clay by various authors.	147
6.5	Elemental composition of bentonite.	151
6.6	Density, Porosity and neutron scattering length density of bentonite clay compacted from 1 to 10 T pressures and sintered at temperature 600 $^{\circ}\text{C}$.	154
6.7	Parameters obtained from SANS data fit for pores in bentonite clay.	155
6.8	Parameters obtained from SANS data fit for D_2O loaded bentonite compact.	158
6.9	Parameters obtained from MSANS data fit for pores in clay.	162
6.10	Model fit to SANS data for SDS and SDS in bentonite clay.	170
6.11	Micelle separation in bentonite clay.	170
6.12	Comparison of the residence time (τ) and diffusion coefficient (D) obtained for water molecules in different clay systems along with bulk water.	181

Symbols

ϕ	Porosity
V_P	Volume of pore
V	Volume of solid
E	Youngs's Modulus
K_E	Constant in terms of the Poisson's ratio of the material
F	Formation resistivity factor
σ	Electrical conductivity of the porous medium saturated with fluid
σ_f	Conductivity of the conducting fluid
τ	Tortuosity
C_f	Formation compressibility
K	Permeability
μ	Dynamic viscosity
T	Hydraulic tortuosity
S	Specific surface area
C_0	Dimensionless Kozeny constant
r_{eff}	Effective radius of the capillary channel
W_t	Total amount of water present per gm
H	Height of rise of fluid in the capillary tube
σ	Surface tension of fluid against air
α	Angle of contact of water with the tube
G_V	Number of connections of pores per unit volume or connectivity
N_V	Number of nodes
V_V	Volume fraction of pores
Q	Wave vector

ρ	Scattering length density
b_i	Scattering length of a particular atom
V	Volume occupied by n atoms
b	Bound scattering length.
k_0	Incident wave vectors
k	Scattered wave vectors
λ	Incident wavelength of neutrons
$d\sigma/d\Omega$	Differential scattering cross section
$d\Omega$	Solid angle
$I(Q)$	Scattered intensity
ρ_p	Scattering length density of the pore
ρ_m	Scattering length density of the material
R_k	Position vector of the k^{th} pore
$F_k(Q)$	Form factor associated with a pore
$P(Q)$	Single particle structure factor
$S(Q)$	Inter particle structure factor
N_p	Number density of inhomogeneities or pores
$J_1(x)$	Bessel function
ρ_c	Scattering length density of core
ρ_{shell}	Scattering length density of shell
ρ_m	Scattering length densities of solvent
R_g	Radius of gyration
C	Scaling factor
$D(r)$	Pore size distribution of pores
E_i and E_f	Initial and final energies

p_i and p_f	Initial and final momentum
$L(\Gamma, \omega)$	Lorentzian function
Γ	Half width at half maxima (HWHM)
$A(Q)$	Elastic Incoherent Structure Factor (EISF)
$\langle d^2 \rangle$	Mean square of the jump length
$\delta(E)$	Dirac delta function
j_n	Spherical Bessel functions
Qa	Quasi-elastic incoherent structure factors
D_R	Rotational diffusion constant
ρ_a	Apparent density
ρ_g	Geometric density
P	Pressure (capillary)
E	Young's modulus or modulus
E_o	modulus of a material without pores

Chapter 1

Introduction and Objectives

1.1. Introduction of Porous Media

This study is concerned with solids possessing a network of holes which may or may not end on the surface. Such solids are known as porous media. They can be more broadly categorized as solids containing holes or voids, connected or unconnected, and dispersed within it in a regular or random manner [Adler P.M., 1992]. Porous materials are classified by their pore diameter into three types according to the International Union of Pure and Applied Chemistry (IUPAC) [Rouquerol et al., 1994] these are Macropores (pores whose diameters range from a few tens of nanometres to microns), Mesopores (typically pores in the range of 2 nm to 50 nm in diameter) and Micropores (typically pores smaller than 2 nm in diameter). Porous media have a very important role to play in various technological applications such as in hydrology, medicine, engineering industry as well as in environmental studies (natural systems) and basic science. Applications of porous materials include catalyst support [Lee J. et al., 2009], filtration [Sarrade et al., 2003], sensors, thermal insulation [Studart et al., 2010] etc.. Naturally occurring porous media are; soil, rocks, zeolites, bones etc.. Examples of manmade porous media are cement, ceramics, porous glasses etc.. The preparation of any bulk solid in the laboratory or by natural means involves the processes of nucleation and growth of crystals which may be of various sizes and juxtaposed with respect to one another to form the bulk material. As the bulk solid grows, many important physical and chemical properties depend on crystallite sizes, their interfaces and the spaces between them. If the growth conditions are not stable or; if the starting materials are impure; if valency requirements are not met, the gaps or spaces between micro-crystals could be large - with trapped gases and/or pores developing

in the bulk material. The nature of these pores and imperfections can have significant repercussions to mechanical, fluid transport, electrical and optical properties of the bulk.

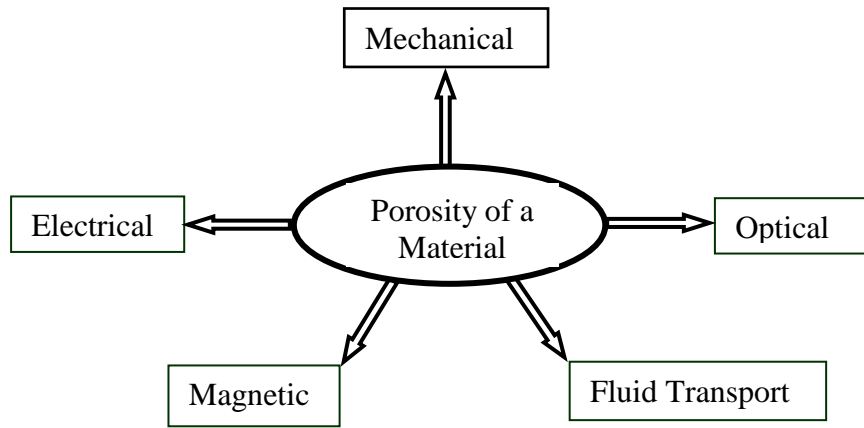


Figure 1.1. Schematic of the effect of porosity on physical properties.

When the material is broken into smaller pieces its properties like magnetic, optical, ferro-electricity in semiconductors change or disappears. The effect on physical properties when the pores of a material are of nano dimensions is particularly marked. Sensors or chemical reactors like glucose sensor used by a diabetic patient could be made long lasting if the pores are used as an enzyme cage for controlling each enzyme reaction [Gabriela P. et al., 2011]. In the chemistry of nanostructured materials as in catalysis, sensing, energy storage and synthesis, the reactions become more effective when the molecular transport path (pores) through which molecules move in and out of nanostructured materials are designed properly [Debra R, 2003].

Catalysis is a surface phenomenon; hence the porous surface is of vital importance as it has more surface area. A one gram grain of iron catalyst has a visible surface area of 1 cm², but when measured with nitrogen adsorption the surface area is found to be 100,000

cm², which arises from the inside surface of pores of the catalyst [Brunauer S., 1976]. Also in mesoporous silica, the surface area is 500-1000 m²/gm which is approximately equal to that of a handball court. In catalysis and separation, porous activated carbon with large surface area and high porosity plays an important role in the effectiveness of such materials [Parminder et al., 2011].

In thin films, voids are formed in large numbers irrespective of the method of preparation (evaporation, electrodeposition, sputtering) during phase transformation from vapour to solid state. It is found that in metals, resistivity increases and corrosion resistance is reduced due to the presence of pores [Nakahara S., 1979]. Porous metals are developed and applied in various fields that include energy absorption, acoustical damping, heat exchange, electrical insulation, electromagnetic wave shields etc.. Porous titanium and its alloys having good mechanical property, corrosion resistance and biocompatibility, has been used in surgical implants [Zhu Ke et al., 2007]. The primary building blocks of the zeolite lattice are silica or alumina tetrahedra. These units link together with their corners forming secondary building block polyhedra which come together to form an array of interconnected channels or cage-like voids. Porous materials also play a key role in fuel cells due to their property of transporting gases. Porous ceramics are used in SOFCs (Solid Oxide Fuel Cells), to provide mechanical support for thin and delicate ceramic oxide electrolytes, and play an important role in current collection on the anode or cathode. Also due to their porosity, they contribute in minimising electrode kinetic losses and mass transport [Brandon and Brett, 2006]. Porous materials are also used in the design of acoustics of an auditorium as part of passive noise control treatment reducing both structure and air-borne sound and vibrations [Olney and Boutin, 2003]. Porous materials can be made of anything and the pores can be filled with different liquids for various applications. Nanometre size silica spheres can be compacted to form a rigid compact after

heating. If the spaces between the spheres are filled with a liquid monomer converting it into a solid polymer and then dissolving the spheres, the product that we get will be a 75% porous material.

The structure of pores in porous media is highly complex [Scheidegger, 1974]. Materials having a complex system of inter-connected pores present a special challenge especially when the pores vary in diameter, length, connectivity and have dimensions from the macroscopic to the mesoscopic. These connected pores allow mass transfer and fluid flow through porous media. Numerical modelling of flow through porous media is generally difficult and plays a fundamental role in petroleum and other industries. This complex interaction of significantly different length scales is not unique to flows in porous media. The difficulty of calculating rates of fluid intake and release by such porous media is such that experimental measurements related to these rates become highly desirable in the modelling of such processes. The understanding of flow of fluid or vapour through porous structure is vital to optimizing different industrial phenomenon such as; oil recovery from a reservoir; the storage of carbon dioxide deep underground in a porous medium (to reduce global warming) etc.. Porous materials like ceramic metal foam or polymeric foam and sintered metal have light weight applications. In filtration, one needs to separate various toxic elements from the filtrate. Flow of water and nutrients in soil for plants takes place through pore (voids) between particles. The movement of water is not straight but follows a tortuous path. The study of flow and diffusion through porous media is vast and has many applications in scientific and engineering applications including filtration, catalysis, petroleum industry, biomedical applications [Bear J., 1972] etc.. A detailed understanding of pore structure and diffusion through pores is important to the study of design and development of these applications.

1.2. Important parameters of porous media

A porous material consists of a matrix, a solid skeleton that surrounds the void or a pore filled with gas or fluid [Adler P.M., 1992]. The important parameters of these materials are porosity, pore size distribution, connectivity, tortuosity, permeability of fluid flow, flow rate, and the change of these parameters over time. These parameters and various other physical and chemical properties depend upon the geometry of the pores. It is also necessary to have a quantitative way of describing the pore density or porosity of the material within the bulk. Most porous materials have small narrow pores having small permeability leading to slow speed of fluid flow through the material. In the design of a porous material it is often required to have both small and large pores as the latter contribute to faster flow in the medium.

1.2.1. Porosity

In studying the pores within the bulk, it is necessary to have a quantitative way of describing the pore density or porosity of the material. Porosity can be thought of as the unfilled volume or percentage volume of a material that is not filled with atoms. It is a measure of the void spaces in a bulk volume of material, expressed as a volume fraction. If the volume of pores is V_p in a solid volume V , then the porous volume fraction is given by $\phi = V_p / V$ and the solid volume fraction is $(1-\phi)$. In addition to this, the extent to which these pores are inter-connected and form channels within the bulk to the surface is an important consideration in the description of fluid flow into and out of a porous material as well as to the strength of the material. The relation between young's modulus E and the porosity ϕ [Ramakrishnan and Arunachalam, 1993; Chawla and Deng, 2005] of a steel is given by expression:

$$E = E_0 \left[\frac{(1 - \phi)^2}{1 + K_E \phi} \right] \quad (1.1)$$

where E_0 is the Young's modulus of the fully dense steel and K_E is a constant in terms of the Poisson's ratio of the material. The relation between elastic modulus of steel and its porosity is [Hardin and Beckermann, 2006] :

$$E(\phi) = E_0 \left(1 - \frac{\phi}{0.5} \right)^{2.5} \quad (1.2)$$

where E is elastic modulus of the material E_0 is the elastic modulus of the sound material and ϕ is the porosity volume fraction. The static properties of these materials depend on porosity, pore size and shape. Porosity also affects the electrical conductivity, the empirical relation between porosity and electrical conductivity is due to Archie (1942) [Lemaitre et al., 1988] and is given by:

$$F = \frac{\sigma_f}{\sigma} = A\phi^{-m} \quad (1.3)$$

The quantity F is the formation resistivity factor, σ is the electrical conductivity of the porous medium saturated with conducting fluid and σ_f is the conductivity of the conducting fluid. The exponent m depends on pore size distribution in a porous medium. The value of m varies from 1 to 4.

1.2.2. Tortuosity

Tortuosity is defined as the property of a curve being twisted. The transport through porous media, the fluid and the contaminant do not flow in straight paths but instead follow a tortuous path around the particle as shown in Figure (1.2), thus having an impact on the

diffusion of a fluid. It is given by the ratio of the actual length of the entire pore channel to the overall length of a sample as given by Equation (1.4):

$$\tau = \left(\frac{L}{L_e}\right)^2 \quad (1.4)$$

Here τ is the tortuosity, L is the length of the channel and L_e is the length of the sample [Bear J., 1972; Maciej et al., 2008]. Higher tortuosity indicates a longer and more complicated path for the flow thus giving a higher resistance to the fluid flow. Tortuosity has an effect on filtration, heat and electrical conductivity and also propagation of sound waves [Rahul et al., 2010].

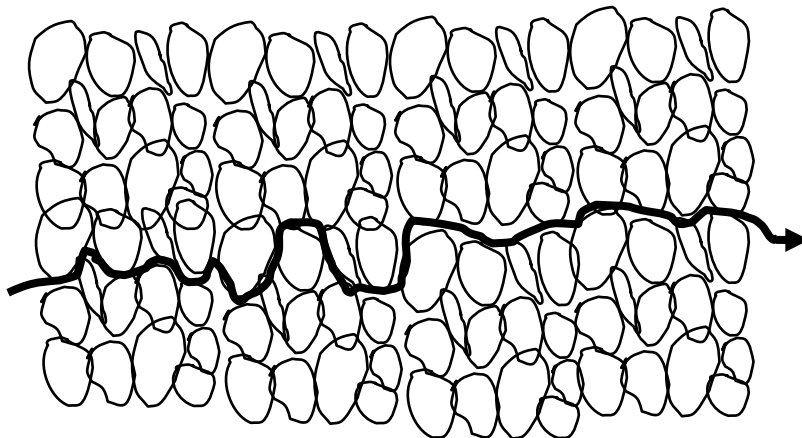


Figure 1.2. Tortuous path followed by liquid or contaminant.

1.2.3. Connectivity

In addition to porosity, the extent to which these pores are inter-connected via channels within the bulk and to the surface is an important consideration in the description of fluid flow into and out of a porous material. Pore interconnectivity is defined as the fraction of open porosity to that of the total porosity [Xigeng and Dan Sun, 2010]. The

pores that are connected are like tunnels and are accessible to liquid, gas or particles. Study of interconnection between pores in a porous structure contributes to the knowledge of permeability and tortuosity which gives a better understanding of flow through porous media. These studies are also important to the study of drug release.

1.2.4. Permeability

Permeability is a measure of the ease with which the fluid flows through a porous medium under applied pressure. Both porosity and permeability are important parameters in removing oil from shales and sandstones.

1.2.5. Flow Rate

In filtration, the time taken by a given volume of the filtrate to pass through the filter is referred as flow rate. The flow rate of a filter is important in determining how rapidly filtration can be completed. Flow rate varies depending upon porosity, thickness and the shapes and sizes of pores. Flow through a porous matrix with low Reynolds number ($Re < 1$) is governed by Darcy's law [Collins R. E., 1976].

1.2.6. Diffusion

Diffusion is a process by which molecules intermingle as a result of their kinetic energy of random motion and transport from higher to lower concentration. Molecular diffusion in porous media occurs when the mean free path is relatively short compared to the mean pore size. Diffusion coefficient is a parameter expressing the transfer rate of a substance by random molecular motion. In porous materials, diffusion is one of the decisive processes, which may control the rate of their practical use.

1.3. The Porous Materials Studied

The porous materials used in the present study are ceramics, glass and a siliceous clay minerals. It is important to discover how the pores within such materials link together to form networks that gave these materials their unique properties. Both macroscopic and microscopic approaches can be used to describe these networks with the former giving porosity values which are related to void fractions while the latter methods lead to estimates of pore size distributions, connectivity's and fractions of blind pores. The optimum usage and development of porous materials will depend on establishing the link between quantitative pore descriptions and bulk physical properties. In this thesis the porosity and pore size distributions in porous samples of a ceramics, a glass and clay have been examined by various methods that are discussed in Chapter 3.

1.3.1. Porous Ceramics

Ceramics are typically inorganic materials moulded from a mass of raw material at room temperature which develop their physical properties through a high-temperature sintering process. Ceramics are considered to be chemically inert materials that are hard and have good thermal and electronic insulating properties [Richard J.D. Tilley, 2004]. In a certain sense they are composites of grains, grain boundaries, and pores. Their functions are essentially governed not only by the characteristics of their constituents but also by their microstructure. Ceramic compacts possessing connected pores have a wide variety of applications such as filtration [Fukasawa et al., 2001], thermal insulation [Ewais et al., 2009], porous burner medium combustion [Mujeebu et al., 2009], water purification, bacteria filtration, hot gas separation and as catalysts [Gough et al., 2004, Studart et al., 2006, Rajamathi et al., 2001]. Pre-existing cracks and flaws lead to a difference between the tensile and compressive performance of a ceramic. These cracks acts as a stress amplifier when the material is placed in tension, leading to a single dominant crack starting

at the tip of a flaw. The dominant crack quickly cuts through the material, ending its life prematurely. In compression, however, stresses around cracks are reduced. Due to this, the ceramics can handle compressive stresses very well [Hardin and Beckermann, 2007]. The presence of cracks and defects in these materials leads to the porosity of the material. Porosity has a major effect on a ceramic's modulus of elasticity and modulus of rupture. Ceramics have a long and useful history in different industries and household applications. Their special usefulness derives from their mechanical strength, thermal and electrical insulating properties which have made them occupy roles as varied as space capsule re-entry insulation tiles [Hilfer G.,2002], special strength air turbine blades, low frictional surfaces, superconducting materials, etc. Thermal conductivity of ceramics is less than that of metals like steel and copper. Various ceramic products are used for thermal insulation due to their low thermal conductivity. The insulating property of ceramics can be enhanced by the introduction of porosity in these materials. Many ceramics have a heterogeneous nature in which several crystalline phases of one constituent coexist with crystallites of other constituents. The juxtaposition of different crystalline grains gives rise to a composite structure in which voids form an integral part of the bulk. The void/pores and their interconnections thus play an important part in the overall average structure of ceramics [Studart et al., 2006]. Some of these ceramics are developed for their porous natures, which are "hydrophilic" and provide capillary wicking and transport of polar substances like water. This unique class of ceramics has become important in finding and measuring the fundamental relationships of liquid/gas/material interactions found in many naturally occurring environments. A porous ceramic is akin to many natural substances like plants, soils, rocks, outcrops, even bone. Such natural materials have crevices and pathways (pores) that allow liquids and gases to mix, migrate and flow. The porosity of ceramics can be varied from 20% to 60% by volume. The porous structures are often

interconnected making liquids and gases flow through the material with low pressure drop. Different pore sizes can accommodate different chemical species and bio-species for various applications. To develop advanced porous ceramic materials for separation of gas and liquid, it is important to understand the transport through the pore space [Kikkinides et al., 2004]. Macro-porous applications pertain to removal of dust particles and bacteria. Meso-porous membranes of these materials are used in separation of large molecules from liquid streams and in water softening. Thin layers of micro-porous ceramics have been used in separating out hydrogen and other gases through pores of diameters less than 2 nm in a process called “molecular filtration” [Verweij H.,1998]. The concept of using nano-diameter pores - in a ceramic membrane - to admit single large molecular units, such as DNA, and thereby electrically detect them as they pass through the pores have been reported as the basis for a highly sensitive biosensor [Anselmetti D.,2012]. Present surgical techniques use glass-ceramics as substitutes for bone [Kumar Singh et al, 2009]. Porous ceramics have also been proposed in bone augmentation and restoration applications in which living bone tissue bonds with the ceramic. Bioactive glass and glass ceramic are known to bond well with bone for silica content between 42 % to 53 %. When such ceramics are implanted near bone tissue, the osteoblast cycle is enhanced and results in bone formation at the interface between ceramic and living bone tissue [Cacciotti et al., 2012]. Due to large surface area (for adsorption) ceramics also have applications as humidity sensors [Kan-Sen Chou et al., 1999]. In the latter, water condensation takes place in pores at a particular temperature and relative humidity [Elizabeth et al., 2002].

1.3.2. Porous glass

Glasses are inorganic materials obtained by fusion and cooled through the glass transition temperature to form a solid without crystallisation [Elliot S. R., 1984]. It is an

amorphous solid that has been around in various forms for thousands of years and has been manufactured for humans use since 12,000 BC. Glasses are produced naturally when a rock containing silica melts at high temperature. Porous glass is an inorganic material that has pores in the nanometer to micrometer range. They have high mechanical strength, thermal stability and chemical resistance to bacteria, wide controlled pore size range and partial transparency. Porous glass obtained by phase separation is well known in various industries such for membrane separation, chromatography, and enzyme carriers and in catalysis, sensors [Reinhardt B., 2012]. Pores in a porous glass are in the range of nm to μm , and can be controlled by heat treatment and sintering. They can be prepared by one of the following methods:

- 1) Metastable phase separation in borosilicate glasses (followed by liquid extraction of one of the formed phases
- 2) Sol-gel process
- 3) Sintering glass powder

Commercially available porous glasses are porous VYCOR glass (PVG) and Controlled Pore Glass (CPG). Porous glass formed has a three-dimensional interconnected porous microstructure containing approximately 96% silica [Kim J. et al.,2007], which is produced by an acidic extraction or a combined acidic and alkaline extraction of phase separated alkali borosilicate glasses [Reinhardt B. et al., 2012]. By regulating the manufacturing parameters, it is possible to produce a porous glass with an average pore size between 0.4 and 1000 nm in a very narrow pore size distribution. One can generate various moulds, for example irregular particles (powder, granulate), spheres, plates, sticks, fibers, ultra thin membranes, tubes, and rings.

Glass microspheres have several commercial applications in pharmaceuticals, filtration, sensors [Nithya shanthi C., 2010], reflective paints, abrasives etc. In filtration use, knowledge of the pore sizes, their inter-connections from surface to bulk and fractions of isolated pores are important. In order to be able to control sizes of pores and their inter-connections, the approach adopted here was to begin from silica micro-spheres and compact these according to a particular heating schedule. Acid leaching of borosilicate glasses was studied by Turner and Winks in the first half of the 20th century. From their investigations it was shown that the chemical stability, density, refractive index, thermal expansion and viscosity are influenced by thermal treatment. Nordberg and Hood in 1934 discovered that alkali borosilicate glasses when thermally treated separate in soluble (sodium borate rich) and insoluble (silica rich) phases. The soluble phase is removed by extraction using mineral acids and a porous silica network remains. After extraction during the sintering process, a silica glass is generated, which has properties approaching those of quartz glass. The manufacturing of such high-silica glasses has been published as the VYCOR-process.

Glass microspheres are small spherical particles with diameters in the micrometer range. These microspheres are available in the size range 20 to 500 μm and can be sieved to obtain a particular desired size. A procedure whereby microspheres of 100 μm diameter ($\pm 10 \mu\text{m}$) can be held together and then fired to form rigid compacts has been reported [Carrasco et al., 2005] together with their bulk properties. The bulk properties depend on the method of compaction and the sintering temperature. A variation in the latter may cause changes in the pore dimensions which can have potential applications in filters, catalysis etc. Due to their porosity such filters will be lightweight and mechanically strong. The fractal-like structures of these porous compacts may be estimated by techniques such as SANS. The high mechanical, thermal, and chemical stability, variable manufacturing of

pore sizes with a small pore size distribution and variety of surface modifications, all contribute to a wide array of applications of a porous glass. The fact that porous glasses can be produced in many different shapes is another advantage for application in industry, medicine, pharmacy research, biotechnology, and sensor technology. The pore size distribution of a porous glass is useful for material separation. These glasses are also used in gas chromatography, thin layer chromatography. An adaptation of stationary phase for a separation problem is possible by a specific modification of the surface of the porous glass.

In biotechnology, porous glasses have uses in DNA related research and the immobilization of enzymes or microorganisms. In addition, porous glasses are used for manufacturing implants, especially dental, for which porous glass powder is processed with plastics to form a composite. The particle size and the pore size influence the elasticity of the composite so as to fit the optical and mechanical properties to surrounding tissue, e.g. the appearance and hardness of dental enamel. Porous glasses in; membrane technology; hyper filtration of sea and brackish water; and ultra filtration in downstream process are other important areas of application. Additionally, they are often appropriate as carriers in catalysts. Porous glasses can be used as membrane reactors as well, on account of their high mechanical, thermal, and chemical stability. Membrane reactors can improve conversion of limited balance reactions, while one reaction product is removed by a selective membrane.

1.3.3. Porous Clay

Clays are porous solids that can absorb ions or molecules having the property of retention and distribution of water or other liquids to the soil. Clays are made up of sheet like (alumina-silicate) structures stacked together having a greater surface area. They can absorb and hold water in these stacked layers. There are three phases in the hydrated clay

matrix: OH radicals bonded to the clay matrix; nano-pores filled with water and; macropores that are not completely filled with water. Wet clays swell and shrink in the dry condition. Their physical and chemical properties can be directly related to their layered, fine-grained (large surface area) structure (Fátima, 2007, Greenwood and Earnshaw, 1984). These properties such as large water retention, low hydraulic conductivity, heat resistance and ion exchange capacities, make clays ideal for many different applications; e.g., production of concrete, brick, paper and ceramics; in catalysis etc.. There are mainly three categories of clay:

1. Kaolinite
2. Smectite
3. Illite

Pores with respect to soil are the spaces between soil particles. In compacted clay the compaction decreases the porosity of the soil increasing its density. Soil particles form aggregates which form larger pores in them which in turn reduces the average pore size under compaction. The porosity of soil may be specified by the number of pores per unit volume. Soil with large and numerous spaces between particles has high porosity, while when there are smaller spaces between particles it has a low porosity. The porosity of soil affects the way water moves through the soil. Soil is composed of solid particles of different sizes (minerals and organic matter) often "glued" together into tiny aggregates by organic matter, mineral oxides and charged clay particles. The gaps between the particles link together forming a complex network of pores and interlinked channels. Through this porous space the soil exchanges water and air with the environment. The movement of air and water also allows heat and nutrients to flow. The number and size of pores determines the rate of absorption and release of fluids / nutrients / pesticides etc. from a given volume

of soil to its immediate surroundings. Physical and chemical conditions that exist on the outside of each clay particle also play a part in the exchange of fluids between the clay particle and its immediate environment.

It is therefore important, on the one hand, to follow all the structural changes that are associated with the adsorption of water molecules in the inter-lamellar spaces (at the scale of the particles) and, on the other hand, to describe the textural modifications induced at larger scales as a result of the swelling of individual particles. The phenomenon of swelling is associated with the hydration of clay. However all clays do not swell on hydration. The Kaolinite group of clays swell little or not at all whereas sodium montmorillonite, on the other hand, characteristically swells in water to many times its dry volume. For naturally occurring porous materials such as oil-bearing rocks or shales, characterization of pores are important for determining those shales which yield higher percentages of oil from extraction processes. Shales have micro to meso pores, which are associated with clay mineral and organic matter. Clay-mineral systems have been shown to exist with a high degree of parallel alignment of the plate-shaped crystals. This results in a high proportion of microporosity and in relatively well defined pore sizes. An Illite is a particular type of clay composed of different siliceous minerals. The hydration of these mineral phases leads to a dramatic change in the bulk properties of the dried clay converting it from a dry powder to a semi-solid homogeneous soft mass. The porosities of the dry and the hydrated clays need to be studied to gain understanding of soft solids and their physical and chemical properties. The movement of air and water in a soft solid such as clay, also control plant nutrient flows. A SANS study [Desa and Ali, 1983] was also performed on Illites and their hydration levels were qualitatively determined by the incoherent levels of scattering from hydrogen at higher momentum transfer values in SANS scattering patterns. The possibility exists - in principle - of using these porous clays

in constructional and agricultural products through their ability to hold pesticides and moisture/water when used in agricultural products or in curing of cement.

Bentonite forms a thixotropic gel when suspended in water due to Van der Waals bonds and electrostatic interaction among the particles. Bentonite has applications in drilling muds, paper coatings, and pharmaceutical products [Paul N. and John R., 2005]. Bentonite is also used in cosmetics, ceramics, polymer nanocomposites and foundry industry [Paluszkiewicz C., 2008]. Compacted bentonite clays have been proposed to be used as barrier materials in hazardous waste containment [Martin B. and Ola K., 2009]. In the context of nuclear waste disposal, compacted clay materials are placed around canisters containing radioactive wastes. Changes in temperature and humidity occur, leading to textural changes. Such changes can be followed by SANS on compacted clay pellets. The extent to which these pores are inter-connected and form channels within the bulk to the surface is an important consideration in the description of fluid flow into and out of a porous material as well as to the strength of the material. Materials having open inter-connected porous structures of either macroscopic or smaller dimensions are well suited to absorbing water within their pores and retaining at least a small fraction of the absorbed H^+ or OH radicals even after a process to drive out the absorbed water.

1.4. Objectives of the Present Study

1.4.1. Porous ceramic

Locally available rice husk can be used to obtain a form of silica which in turn can be transformed into a porous ceramic. The present study aims at studying such a ceramic sintered at different temperatures, for different durations of time. The effect of applying different pressures prior to the sintering stage is also to be investigated for changes in porosity. Both macroscopic and microscopic methods are to be used in assessing pore sizes

and their distributions in the length scale varying from a few microns to nanometers. Assessment of pore connectivity and the extent of unconnected or isolated pores is to be addressed by the use of appropriate microscopic techniques such as SANS and SEM.

These results are of relevance to the applications of this material in filtration, bone replacement therapy etc.

1.4.2. Porous Glass

Commercially available silica microspheres are to be compacted and sintered at different temperatures and for different times in order to obtain porous glass compacts. The porosity of these glasses is to be quantitatively assessed using macroscopic techniques such as bulk density measurements, mercury intrusion porosimetry and TG-DTA. Microscopic methods such as SANS and SEM are to be used for characterisation of nanopores. Both the extent of interconnections of pores and the concentration of isolated pores are to be quantified in these materials.

Optimal use of the silica microsphere compact in its multifarious applications is possible if its porosity is well characterised.

1.2.3. Porous Clay

Commercially available clay such as bentonite and kaolinite are to be heat treated at different temperatures and subsequently hydrated the porosity of the dry clay is to be characterised by usual microscopic methods as well as by SANS and SEM. On account of the special swelling properties of bentonite clay this material is to be loaded with water and examined for determining the special diffusion properties of water within the porous confines of the clay. Similarly the effect of confined spaces within the clay on a micellar solution is to be investigated.

Nuclear waste containment schemes and agricultural applications stand to benefit from a well characterised porous clay.

Chapter 2

Theoretical Considerations

2.1. Pore structure

A porous material has a wide range of pore spaces known as pores and the narrow connecting regions called as throats. The geometry of pores is the most important property of porous media for various applications. The pores in a porous medium are further classified as open pores, closed pores or blind pores. Pores store a liquid or a gas whereas throats usually help in the transport of fluid between pores. A pore network is obtained in a compacted sample. In a network, the pores can be spherical, cylindrical, square, and triangular. Different regions of a porous body are schematically shown in Figure (2.1).

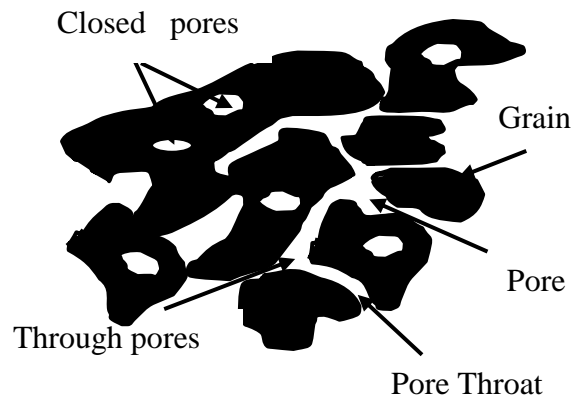


Figure 2.1. Classification of pores in a porous medium.

A porous solid has two phases; a pore phase and a solid phase. The total volume in a porous medium is that due to the total contribution from both the volume of pore (V_{pore}) and volume of solid (V_{solid}) :

$$V_{total} = V_{pore} + V_{solid}$$

Porosity ϕ in terms of volume is given by the ratio of volume of pore to the total bulk volume of the medium. The fractional volume of pores is given by:

$$\phi = \frac{V_{pore}}{V_{total}} \quad (2.1)$$

And $(1-\phi)$ is the fractional solid volume in the sample.

2.2. Effect of compaction and sintering on pore structure

Particle size, shape, packing and sorting affects the porosity of a porous solid. Arrangement of grains in a porous medium is also responsible for variation of porosity. In order to explain the dependence of porosity on the arrangement of grains, consider a grain of spherical shape. For a cubic packing of identical spherical grains, the maximum theoretical porosity is 47.6 % [Collins R.E., 1976] in which cubic spaces can be fitted into the pores. For a rhombohedral packing of spheres the maximum porosity is 26 % in which tetrahedral spaces can be fitted into the pores. Porosity reduces further if smaller spheres are introduced in the structure as shown in Figure (2.2). Compaction decides the packing type and leads to reduction in volume with externally applied pressure. The variation of porosity with change in pressure is given by:

$$\phi_2 = \phi_1 e^{C_f(P_2 - P_1)} \quad (2.2)$$

Where ϕ_1 and ϕ_2 are porosities at pressures P_1 and P_2 , and C_f is the formation compressibility which is a summation of both grain and pore compressibility:

$$C_f = -\frac{1}{V} \frac{dV}{dP}$$

In the case of clay the grains are plate-like and are expected to be susceptible to compaction. Hence the porosity ϕ of clay decreases with increasing depth below the Earth's surface. The variation of porosity in clay with depth is represented by [Athys, 1930].

$$\phi = \phi_0 e^{-\alpha z} \quad (2.3)$$

where z is the depth

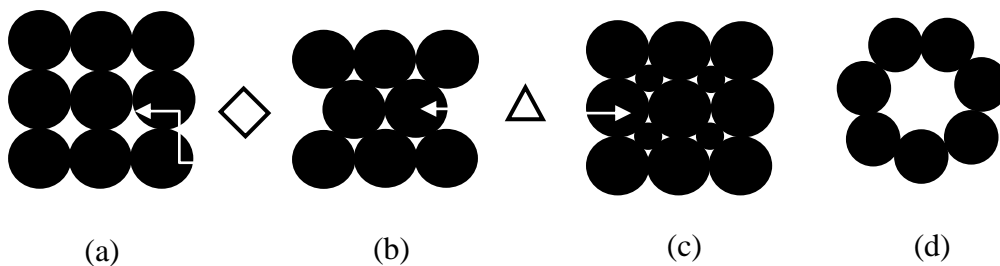


Figure 2.2. a) Cubic packing, b) rhombohedral packing, c) cubic packing with two grain sizes d) floral arrangement.

2.3. Theory of flow through porous media

There are three basic equations for a fluid flow through porous media.

2.3.1. Darcy's law

The permeability κ of a porous material is defined as its fluid conductivity [Collinis R.E., 1976]. Flow through a porous matrix for low Reynolds number ($Re < 1$) is governed by Darcy's law (1956), which states that the fluid flux q (discharge per unit area) is related to the applied pressure gradient ∇p by the linear relation [Bear J.,1972].

$$q = -\frac{\kappa}{\mu} \nabla p \quad (2.4)$$

where κ is the permeability, μ is the dynamic viscosity,

Thus the permeability of a porous material is in units of ‘Darcy’ which is defined as the flow rate of one cubic centimetre per second when a pressure difference of one atmosphere is applied across a cube having unit dimension.

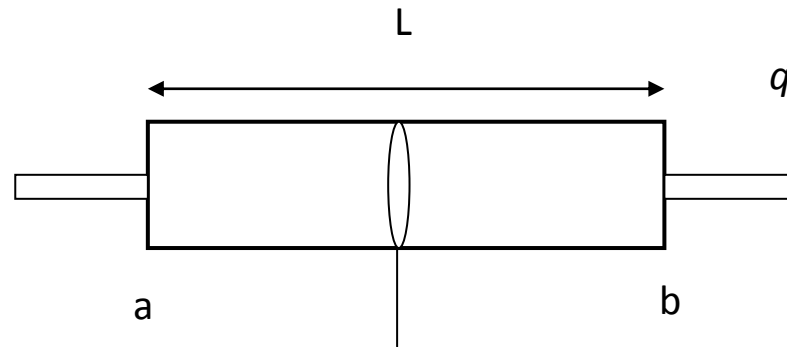


Figure 2.3. Schematic showing definition of Darcy’s law.

2.3.2. Kozeny –Carman equation

The relation between permeability κ and porosity ϕ is given by Kozeny [Kozeny et al., 1998]. For a tortuous flow through a porous medium, the empirical relation between measurable properties of porous media and fluid permeability is provided by Kozeny [Maciejka et al., 2008]

$$k = C_0 \frac{\phi^3}{T^2 S^2} \quad (2.5)$$

T is the hydraulic tortuosity, S is the specific surface area, C_0 is a dimensionless Kozeny constant that depends on the geometry of the capillary channel [Bear J., 1972]. Equation (2.5) as modified by Kozeny-Carman is given by:

$$k = \frac{r_{eff}^2}{8F} \quad (2.6)$$

Where r_{eff} is the effective radius of the capillary channel, F is the formation factor which, in terms of porosity is given by:

$$F = \frac{\tau}{\emptyset}$$

Formation factor is the obstruction offered by a porous a medium to the transport of ions or uncharged molecules and is purely a geometric parameter.

2.4. Swelling in clay

The interlayer swelling for Na-bentonite and Li-smectite is explained by various authors [Sposito and Prost, 1982; Mielenz and King, 1955; Holtz and Bara, 1965; Parcher and Liu, 1965 ; Seed et al., 1962]. The linear equation for swelling is given below [Fink, D. H. and Nakayama, 1972 ; Fink D.H., 1977] .

$$d = \left[9.4 - \frac{\mu a}{S_i} \right] + \left[\frac{\mu(1 - b)}{S_i} \right] W_t \quad (2.7)$$

where the thickness of the individual platelet is 9.4 Å, d is the average spacing of the clay platelets and W_t is the total amount of water present per gm of clay. The plot of d vs W_t is linear. The plot gives intercept of $[9.4 - \mu a/S_i]$ and slope of $[\mu(1 - b)/S_i]$. The shrinkage in dried bentonite is mainly due to structural change in the mineral which in turn causes change in porosity.

2.5. Capillary rise in hydrology

In hydrology capillary action is responsible for moving groundwater from a wet area of soil to a dry area. The difference in soil matrix potential drives capillary action. Capillary action is possible when the adhesive intermolecular forces between the liquid and the substance are stronger than the cohesive intermolecular forces inside the liquid. The same effect is responsible for porous material soaking up liquid. The narrower the tube, the higher the rise in water column. The rise in height can be obtained from the following:

$$h = \frac{2\sigma \cos\alpha}{\rho g r} \quad (2.8)$$

where h is the height of rise of fluid in the capillary tube; σ is surface tension of fluid against air; α is angle of contact of water with the tube; ρ is the density; g is the acceleration due to gravity and r is the equivalent radius of tube.

2.6. Models of porous media

Various mathematical models have been used to understand flow of fluid through porous media. Moisture flow properties of porous media are usually determined based on experiments [Bear J., 1972; Sahima M., 1995; Miguel A., 2000]. The easiest model used to depict the flow through a porous medium assumes the medium to be a bundle of capillary tubes [Scheidegger, 1953]. Several authors have discussed the capillary model and have investigated the correlation of permeability with average pore size or with the pore size distribution curve. A porous material may also be represented by a rectangular network, in which the bonds represent the pores and the nodes the connections between the pores. The connectivity between pores can be found using the equation [Vasconcelos W. L., 1990]:

$$G_V + N_V = B_V + V_V \quad (2.9)$$

Where for porous glass if, G_V is the number of connections of pores per unit volume also referred to as connectivity, N_V denotes number of nodes, B_V is the number of branches and V_V is the volume fraction of pores. For cylindrical pores of equal length L , and individual diameter D , the connectivity may be schematically represented as shown in Figure (2.4).

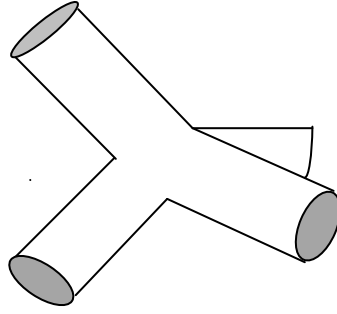


Figure 2.4. Schematic of cylindrical pore connectivity.

From the model proposed by Vasconcelos, pore connectivity can be obtained by:

$$G_V = \frac{S_V^3}{32\pi V_V(1 - V_V)} + 1 \quad (2.10)$$

And permeability K_p can be obtained by relation:

$$K_p = \frac{V_V r_p^2}{16c} \quad (2.11)$$

C is a constant and for cylindrical pore is 8.

2.7. Small angle scattering in porous media

Various techniques can be used to probe the structure of a porous material : Neutron, X-ray and electron diffraction; Small Angle Neutron Scattering (SANS) [Mazumder et al.,2004] and the similar technique using X-rays (SAXS); optical microscopy; Scanning Electron Microscopy (SEM); and Transmission Electron

Microscopy (TEM). The scales that can be probed by small angle scattering as well as various other instruments are shown in Figure (2.5). Small Angle Scattering (SAS) can be used in the characterisation of nanopores in porous media, as this provides information about geometry and morphology of inhomogeneities, typically in the size range 1 nm to 500 nm.

SAS involves the change in momentum of radiation (X-ray, neutron, light etc) due to the interaction of the beam with the molecules of the sample. When there is change in the direction of the beam without exchange of energy with the molecules of the sample, the scattering is called elastic scattering. In case of SANS, neutrons are scattered whereas it is photons that are scattered in the case of SAXS. The scattering originates due to density fluctuations or structural inhomogeneities in the material. Scattering from nanoporous media have sizes of inhomogeneities that fall within the measureable range of SANS making the method useful in the present study. Scattering is based on the principal that a monochromatic plane wave is scattered by the material through an angle 'θ'. The scattered intensity is measured as a function of scattering wave vector, Q, which in elastic scattering has the magnitude :

$$Q = \frac{4\pi}{\lambda} \sin(\theta) \quad (2.12)$$

where λ is the incident wavelength of neutrons and θ is the scattering angle.

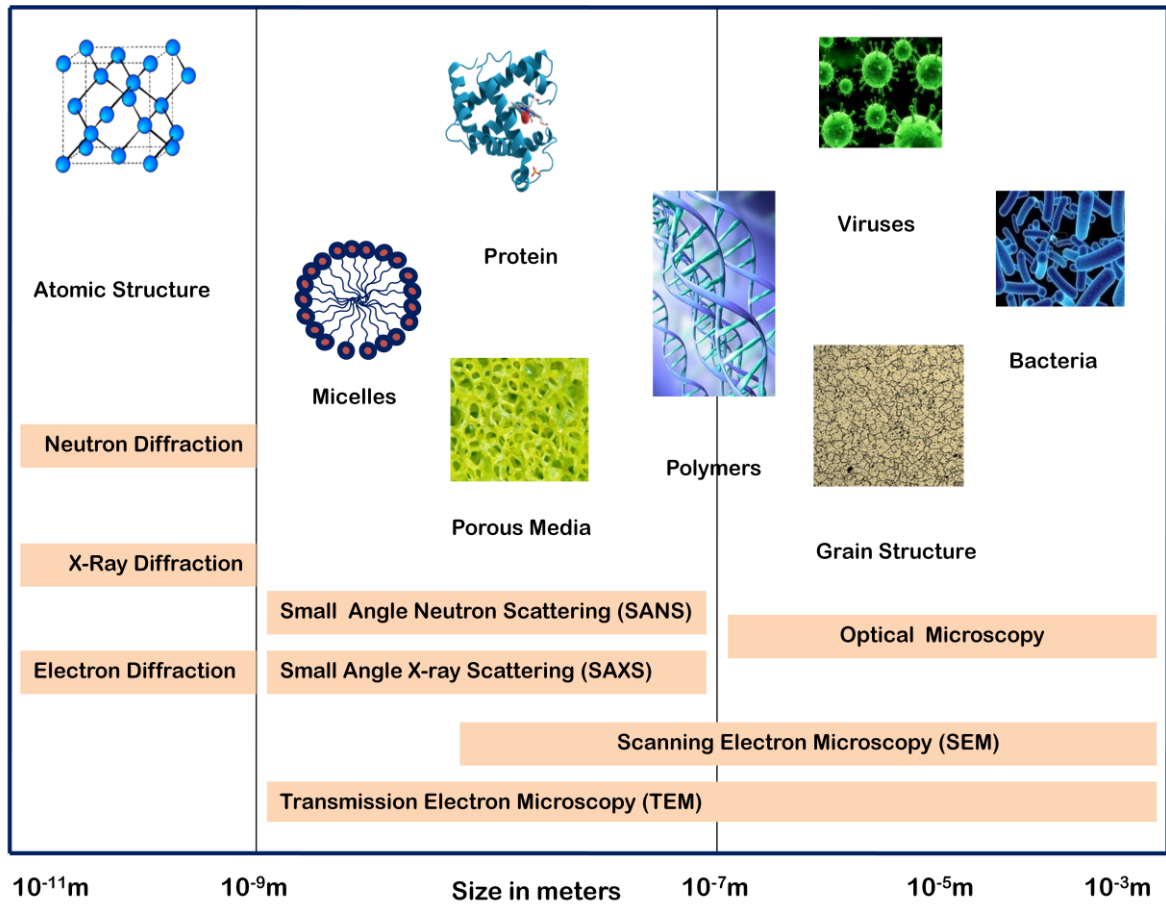


Figure 2.5. Various experimental techniques and their length scales.

2.7.1. Salient features of neutrons

The salient features of neutrons that make them suitable for use in a scattering experiment are given below.

1. The absorption of neutrons by matter is small as they do not have charge. Due to their neutral nature and magnetic dipole moment, neutrons can penetrate matter and interact with the atoms via nuclear and magnetic scattering. Thus, properties of the bulk and magnetic structure can both be measured.
2. The neutron's wavelength is comparable to inter-atomic spacing while its kinetic energy is similar to the energy of excitation in a solid ; hence neutrons can be used in the determination of both position and motion of atoms in condensed matter.
3. In the case of X-ray the scattering length increases with atomic number whereas there is a random variation of neutron scattering length with atomic number. Moreover, isotopes of the same element may show different scattering lengths.
4. The feature of the scattering cross section differing for different isotopes is put to good use in the technique known as contrast matching in SANS.

2.7.2. Scattering length and scattering cross section

The neutron scattering length is related to how strongly a particular nucleus will scatter neutrons. Scattering length per unit volume (scattering length density ' ρ ') for a homogeneous sample consisting of 'n' isotopic species is given by

$$\rho = \frac{\sum_i^n b_i}{V} \quad (2.13)$$

where ρ is the scattering length density, b_i is scattering length of a particular atom and V is volume occupied by n atoms. For a monochromatic incident plane wave $e^{ik_0 \cdot r}$ interacting with the scatterer the scattered wave is represented as $\psi = -\frac{b}{r} e^{ik \cdot r}$ where k_0 and k are incident and scattered wave vectors respectively, b is the bound scattering length. The momentum transfer vector Q for elastic scattering $k = k_0$ is given by Figure (2.6)

$$Q = |k - k_0| = \frac{4\pi \sin\theta}{\lambda} \quad (2.14)$$

Where λ is the incident wavelength of neutrons.

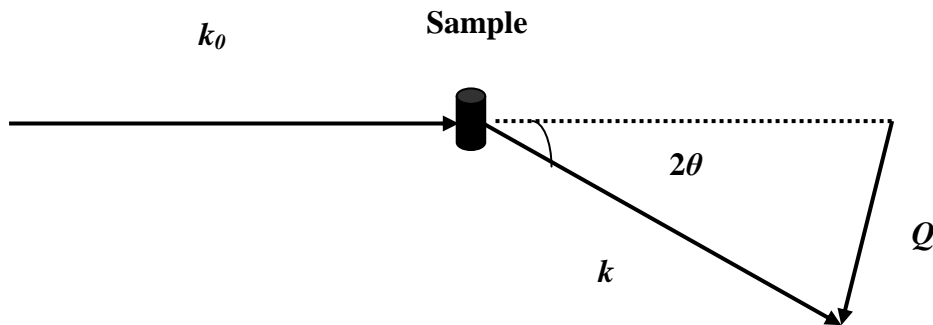


Figure 2.6. Schematic of momentum transfer vector Q .

The scattering cross section is the effective area of collision. The differential scattering cross section $d\sigma/d\Omega$ gives the probability of scattering into the solid angle $d\Omega$.

In a scattering experiment at small momentum transfer values, the measured differential scattering cross-section from a sample of volume V , referred to as the scattered

intensity $I(Q)$ or the macroscopic differential scattering cross-section $d\Sigma/d\Omega$, may be written in terms of the scattering length density difference (per unit volume) between a scattering particle ρ_p and its surrounding matrix ρ_m :

$$I(Q) = \frac{(\rho_p - \rho_m)^2}{V} \left\langle \left| \int_{V_p} \exp(-iQ \cdot r) dr \right|^2 \right\rangle \quad (2.15)$$

In the context of a material having pores whose dimensions are of the order of the incident wavelength, ρ_p refers to the scattering length density of the pore (typically air or vacuum) while ρ_m refers to the scattering length density of the material (sum of scattering length values of each of the constituent atoms of the composition unit multiplied by the number of such units in an unit volume).

If R_k is the position vector of the k^{th} pore and $F_k(Q)$ is the form factor associated with a pore then equation(2.15) can be written as

$$I(Q) = (\rho_p - \rho_m)^2 V_p^2 \left\langle \left| \sum_k F_k(Q) \exp(-iQ \cdot R_k) \right|^2 \right\rangle \quad (2.16)$$

Where $F(Q) = \frac{1}{V} \int_v \exp(-iQ \cdot r) dr$

For monodispersed pores or particles the equation can be expressed as [Glatter and Kratky, 1982]:

$$I(Q) = \frac{N_p (\rho_p - \rho_m)^2 V_p^2}{V_{sample}} \langle |F(Q)|^2 \rangle \cdot \frac{1}{N_p} \left\langle \left| \sum_k \exp(-iQ \cdot R_k) \right|^2 \right\rangle \quad (2.17)$$

The equation can be simplified as

$$I(Q) = \frac{N_p(\rho_p - \rho_m)^2 V_p^2}{V_{sample}} P(Q)S(Q) \quad (2.18)$$

where $P(Q)$ is the single particle structure factor and $S(Q)$ is the inter particle structure factor.

$$P(Q) = \langle |F(Q)|^2 \rangle \quad (2.19)$$

and

$$S(Q) = \frac{1}{N_p} \left\langle \left| \sum_k \exp(iQ \cdot R_k) \right|^2 \right\rangle = \frac{1}{N_p} \left\langle \sum_k \sum_{k'} \exp(iQ \cdot (R_k - R_{k'})) \right\rangle \quad (2.20)$$

$P(Q)$ depends on the shape and size of the inhomogeneities/scattering centres, while the interparticle correlation is determined by $S(Q)$. For a dilute system where the inhomogeneities are spaced far enough apart that the correlation between them is negligible [$S(Q) \approx 1$], if N_p is the number density of inhomogeneities or pores, the above equation can be written as :

$$I(Q) = \frac{N_p(\rho_p - \rho_m)^2 V_p^2}{V_{sample}} P(Q) \quad (2.21)$$

The variations of $P(Q)$ and $S(Q)$ with Q for a hypothetical sample are sketched below Figure (2.7) together with the case when both functions are significant in a given sample.

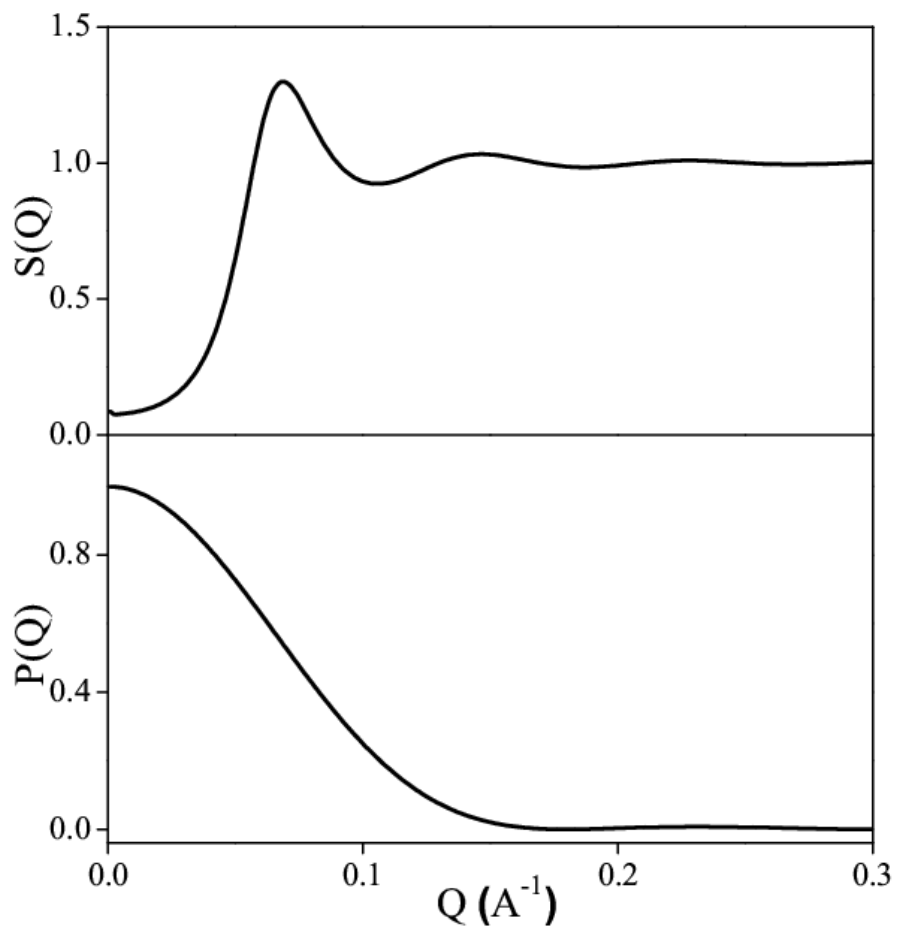


Figure 2.7. The sketch of $P(Q)$ and $S(Q)$.

2.7.3. Form factor of simple geometric objects

The expressions for $P(Q)$ of some standard shapes are listed below [Glatter and Kratky, 1982; Guinier and Fournet, 1955]:

1. Sphere shaped particles of radius R the form factor is given by :

$$P(Q) = \left[\frac{3(\sin QR - QR \cos QR)}{QR^3} \right]^2 \quad (2.2)$$

2. Cylindrical particle with radius R and length $2l$

$$P(Q) = \int_0^{\frac{\pi}{2}} \frac{\sin^2(Ql \cos \beta) 4J_1^2(QR \sin \beta)}{Q^2 l^2 \cos^2 \beta Q^2 R^2 \sin^2 \beta} \sin \beta d\beta \quad (2.23)$$

$J_1(x)$ is a Bessel function and θ is the angle subtended by the principal axis of the cylinder with Q .

3. For an ellipsoidal core-shell model of inner radius R_1 and outer radius R_2

$$P(Q) = \left[(\rho_c - \rho_{shell}) V_1 \frac{3j_1(QR_1)}{QR_1} + (\rho_{shell} - \rho_m) V_2 \frac{3j_1(QR_2)}{QR_2} \right]^2 \quad (2.24)$$

Where ρ_c , ρ_{shell} and ρ_m are the scattering length densities of core, shell and solvent and $J_1(x)$ is a Bessel function.

2.7.4. Contrast Matching

For a system having two phases as in porous media viz. a pore and a matrix having scattering length densities ρ_p and ρ_m , the scattered neutron intensity will be proportional to the contrast factor i.e. $(\rho_p - \rho_m)^2$. The scattering contrast can be varied by using isotopes of

constituent elements of either the matrix or the particle. In the case of pores as the “particles”, an appropriate fluid can be made to fill the pores such that there is a match with the scattering length density of the matrix in which case the scattering profile should either go to zero or to the combined incoherent level of fluid and matrix. For example, as the scattering length densities of hydrogen and deuterium are of opposite sign, ($b_H = - 3.741$ fm and $b_D = 6.664$ fm) there will be a combination of the two in different proportions which would exactly match the scattering length density of the matrix.

2.7.5. Guinier and Porod approximations

Guinier Approximation

At lower Q for a dilute solution of non-interacting monodispersed particles the scattered intensity $I(Q)$ is given by the Guinier approximation which in terms of the radius of gyration is:

$$I(Q) = I_0 \exp\left(-\frac{Q^2 R_g^2}{3}\right) \quad (2.25)$$

where I_0 is the scattering at $Q = 0$.

R_g is obtained from the slope of the plot of $\ln(I(Q))$ vs. Q^2 . The approximation is applicable provided $Q.R_g \leq 1$.

Porod scattering

Information concerning surface and volume irregularities in the medium can also be obtained by SANS. The approximation due to Porod deals with scattering from well defined volumes with clear boundaries. Many materials exhibit scattering at the higher Q range of the measured space. The proportionality of the intensity to Q^{-4} is termed Porod's

law [Porod G., 1951]. This is due to the fact that other structural features do not contribute to scattering in this region of Q . The approximation is valid in the range $lQ \gg 1$

$$\lim_{Q \rightarrow \infty} I(Q) \propto A_s Q^{-4} \quad (2.26)$$

Where l is the reciprocal length.

$$\lim_{Q \rightarrow \infty} I(Q) \propto A_s Q^{-(6-d)} \quad (2.27)$$

In the case of a rough surface having a fractal character (as in clusters and aggregates) the dimension d lies between 2 and 3 and the intensity follows a power law. The power law relation is given by:

$$I(Q) \propto Q^{-D_m} \quad (2.28)$$

This gives a linear plot on a log $I(Q)$ versus Q , D_m is called the mass fractal dimension is obtained in the range $1 < D_m < 3$.

The measured scattered intensity $I(Q)$ of an ensemble of poly-dispersed spherical particles under a local monodisperse approximation can be expressed as [Pedersen J. S., 1994]

$$I(Q) = C \int P(Q, r) r^6 D(r) S(Q, r) dr \quad (2.29)$$

where C is a scaling factor, $D(r)$ is the pore size distribution of pores with radii r .

2.8. Quasi-elastic neutron scattering

In neutron scattering one could measure the change of momentum transfer Q and the energy exchange due to interaction of the neutron beam with the nuclei of the specimen. If E_i and E_f are the initial and final energies and p_i and p_f are similarly the corresponding momentum values, then;

$$\Delta E = E_i - E_f$$

$$\Delta p = p_i - p_f$$

If ω is the angular frequency corresponding to the energy transfer and k_i and k_f are the initial and final wave vectors ;

$$\Delta E = \hbar\omega$$

$$\Delta p = \hbar(k_i - k_f) = \hbar Q$$

Two types of scattering can occur when neutrons scatter from the sample :

1. Elastic scattering - Atoms interact with the neutrons without changing their energy. Here we get information about the position of atoms, $\Delta E = (k_i - k_f) = 0$.
2. Inelastic scattering - there is exchange of neutron energy with the sample. From this type of scattering we can get information about the diffusion of atoms. $\Delta E \neq 0$. When there is a broadening of the elastic peak due to either gain or loss of energy, it is called quasielastic scattering.

In a Quasielastic Neutron Scattering (QENS) experiment, the scattered intensity is analyzed as a function of both energy and momentum transfer. The measured intensity is proportional to the double differential scattering cross section, which is the probability that the neutron is scattered with energy change $dE = \hbar d\omega$, which in turn is proportional to the incoherent scattering law $S(Q, \omega)$ due to the large incoherent scattering cross section of hydrogen.

In general, this scattering law can be written as:

$$\frac{d^2\sigma}{d\Omega d\omega} \propto \frac{|k|}{|k_0|} [\sigma_{coh} S_{coh}(Q, \omega) + \sigma_{inc} S_{inc}(Q, \omega)] \quad (2.30)$$

where σ is the scattering cross-section, $S(Q, \omega)$ is the scattering law and the suffices “*coh*” and “*inc*” are coherent and incoherent components of scattering. For a hydrogenous system $\sigma_{coh} \ll \sigma_{inc}$ (hydrogen), hence the double differential cross section is given by [Bee M., 1988] :

$$\frac{d^2\sigma}{d\Omega d\omega} = \frac{|k|}{|k_0|} [\sigma_{coh} \sigma_{inc} S(Q, \omega)] \quad (2.31)$$

In general the dynamical structure factor $S(Q, \omega)$ can be written as [Pradeep et al., 2004]:

$$S(Q, \omega) = A(Q)\delta(\omega) + [1 - A(Q)]L(\Gamma, \omega) \quad (2.32)$$

where the first term on the right hand side is the elastic part while the second is the quasielastic part. In the second term on the right hand side, $L(\Gamma, \omega)$ is a Lorentzian function with a half width at half maxima (HWHM) Γ . The variation of (HWHM) Γ provides information about the time scale of the motion. Out of the total scattered spectrum the contribution from elastic scattering is called the Elastic Incoherent Structure Factor (EISF) designated as $A(Q)$. EISF is the space Fourier transform of the particle distribution, taken in infinite time and averaged over all the possible initial positions. A negligible contribution of EISF generally corresponds to the presence of pure long-range translational motion. However, for localized motion e.g., rotational motion, this term is expected to have a non-zero value and the variation of EISF with Q is used to determine the information about the geometry of the molecular motion.

2.9. Diffusion through a porous medium

In diffusion, atomic or molecular size particles move randomly from a region of higher to a lower concentration. Fick's law relates the particle mass flux to the concentration gradient. It states that the flux for a steady state system moves from regions of higher to lower concentration with a magnitude proportional to the concentration gradient and is expressed as:

$$F = -D \frac{\partial C}{\partial x} \quad (2.33)$$

Where F is the diffusive flux, that measures the amount of material that will flow, through a small area, for a small time interval. D is the diffusion coefficient that describes the rate at which molecules flow. C is the pore water concentration which depends on time t and distance x .

Fick's second law relates the time rate of concentration changes to the second derivative of the concentration gradient:

$$\frac{\partial C}{\partial t} = D \frac{\partial^2 C}{\partial x^2} \quad (2.34)$$

In porous media diffusion is affected by the length of the diffusion path, tortuosity (τ), the pore geometry, constrictivity (δ). The pore diffusion coefficient D_p is related to diffusion in free (bulk) water D_w by relation

$$D_p = \frac{\delta}{\tau^2} D_w \quad (2.35)$$

Here, tortuosity (τ^2) [Brakel and Heertjes, 1974] is defined as the square of the ratio of the length of actual diffusion paths to the length of their projection on the x -axis, and constrictivity (δ) as a factor accounting for the variable shape and diameter of the pores. In

most of the cases it is not possible to determine (δ). The geometric factor G may be written as

$$\frac{\delta}{\tau^2} = \frac{1}{G} \quad (2.36)$$

Diffusion studies of clay by quasielastic neutron scattering at microscopic scale are least influenced by geometrical particle arrangement. Movement of water in such an environment is different from bulk water motion [Cebula et al.,1981]. In this case the diffusion constant within the pore is given by:

$$D_p = \frac{q}{G} \quad (2.37)$$

where q is the electrostatic constraint and G is geometric factor. At microscopic scale, geometrical restrictions are negligible $G \approx 1$.

Quasi-elastic Neutron Scattering (QENS) is a technique by which the broadening of the elastic diffraction peak due to scattering from a particular molecular species in a fluid is measured and related to the diffusion of such a molecular unit. The method has been successfully applied to the diffusion of propane water in the bulk as well as in enclosed volumes such as pores in zeolites [Mukhopadhyay and Mitra, 2006]. The microscopic diffusion coefficient measured by QENS can be expressed as:

$$D_p (QENS) = D_{clay}(QENS) = D_w \times Q \quad (2.38)$$

The Q and G can be obtained by comparing macroscopic D_p , microscopic D_p (QENS) and D_w . In a porous medium all the volume is not available for diffusion; the flux flow is proportional to porosity ϕ . The effective diffusion coefficient D_e is given by

$$D_e = \phi \quad (2.39)$$

Fick's law is modified [Crank, 1975] as:

$$F = -D_p \epsilon \frac{\partial C_p}{\partial x} \quad (2.40)$$

C_p is the concentration of diffusion species.

2.10. Models of Diffusion

Various models are used in the study of diffusion of molecules in a confined region.

2.10.1. Jump Diffusion Models

Jump diffusion models were developed by [Hall and Ross, 1981; Singwi and Sjölander, 1960] for short distance diffusion. In this model it is assumed that a water molecule oscillates with a certain mean square amplitude $\langle u^2 \rangle$ around an equilibrium position and for an average time (τ_t) before it jumps a distance l to another equilibrium position, where $l^2 \gg \langle u^2 \rangle$. For this type of diffusion, the scattering function is a single Lorentzian [Bée, 1988; Jobic, 2000]. The following models differ in the jump length distribution and also in the broadening $\Gamma_i(Q)$ of the Lorentzian curve [Jobic and Theodorou, 2007].

a) Hall and Ross model (HR) [Hall and Ross, 1981]

In this model the jump length distance follows a Gaussian distribution given by:

$$\rho(r) = \frac{2r^2}{r_0^3 (2\pi)^{1/2}} e^{\left[\frac{-r^2}{2r_0^2} \right]} \quad (2.42)$$

with r_0 and r the initial and final position of the water molecule. The scattering function is given by a Lorentzian whose half-width at half-maximum (HWHM) is :

$$\Gamma(Q) = \frac{\hbar}{\tau_t} \left[1 - \exp\left(-\frac{Q^2 \langle d^2 \rangle}{6}\right) \right] \quad (2.42)$$

Where Q is the momentum transfer vector, $\langle d^2 \rangle$ is the mean square of the jump length and τ is the residence time of a molecule at a quasi equilibrium position with diffusion constant $D = l^2 / 6\tau_t$; before it rapidly jumps to the next quasi equilibrium position.

b) Singwi and Sjölander model (SS) [Singwi and Sjolander, 1960]:

Based on the assumption that a molecule executes an oscillatory motion for a mean time τ_0 and diffuses for mean time τ_1 continuously repeating such a motion. If the time taken to jump in between equilibrium positions is much shorter than the residence time ($\tau_1 \ll \tau_0$), the jump length distribution according to Singwi and Sjölander model is:

$$\rho(r) = \frac{r}{r_0^2} e^{-\left(\frac{r}{r_0}\right)} \quad (2.43)$$

which leads to a broadening defined by:

$$\Gamma_t(Q) = \frac{\hbar \cdot D \cdot Q^2}{1 + D \cdot Q^2 \tau_t} \quad (2.44)$$

and the mean square jump length

$$l^2 = 6r_0^2 \quad (2.45)$$

c) Chudley - Elliot model (CE) [Chudley and Elliott, 1961]

Here the jump distance l is fixed in all the neighbouring sites between which the atoms vibrate.

$$\Gamma_t(Q) = \frac{\hbar}{\tau} \left(1 - \frac{\sin(Q \cdot l)}{Q \cdot l} \right) \quad (2.46)$$

d) Jobic model [Jobic, 2000]

This model is an extension of the Hall and Ross model. The molecule jumps from one site to the other and is delocalised over a length. This model can be used, if the jump length is small compared to the amplitude of the delocalized vibration. The jump length distribution is given by :

$$\rho(r) = \frac{x}{l_0 r_0 (2\pi)^{\frac{1}{2}}} e^{\left(-\frac{(r-l_0)^2}{2r_0^2}\right)} \quad (2.47)$$

Where the distance between two sites is l_0 . The parameter r_0 accounts for the delocalization of the molecule. The mean jump length is then given by

$$l^2 = l_0^2 + 3r_0^2$$

The resultant broadening is given by:

$$\Gamma_t(Q) = \frac{\hbar}{\tau} \left(1 - \frac{\sin(Q \cdot l_0)}{Q \cdot l_0} e^{-\left(\frac{Q^2 r_0^2}{2}\right)} \right) \quad (2.48)$$

All models lead to Fick's law at low Q .

2.10.2. Rotational motion

The model used for the rotational motion of molecules is due to Sears [Sears, 1966]. This model assumes isotropic rotation of hydrogen atoms on a spherical surface, i.e. water molecules rotate around their center of gravity. This model is expressed as:

$$S_{rot}(Q, \omega) = j_0^2(Qa) \cdot \delta(E) + \frac{1}{\pi} \cdot \sum_{n=1}^{\infty} (2n+1) j_n^2(Q, a) \frac{l(l+1)D_R}{\omega^2 + [l(l+1)D_R]^2} \quad (2.49)$$

The term $\delta(E)$ is the Dirac delta function, j_n are the spherical Bessel functions, α is the radius of rotation of the water molecule taken as 0.98 Å (OH distance of the water molecule). $j_0^2(Qa)$ is the elastic incoherent structure factor (EISF) and $(2n + 1)j_n^2(Qa)$ are the quasi-elastic incoherent structure factors corresponding to the spherical Bessel functions $j_l(x)$, and D_R is the rotational diffusion constant. D_R can be obtained by the relation :

$$D_R = \frac{\hbar}{6\tau} \quad (2.50)$$

Chapter 3

Experimental methods

3.1. Introduction

This chapter gives the details of experimental methods employed in the preparation and characterisation of porous media under study. The basic principle of each experimental technique and the instrument used is discussed.

3.2. Methods of preparation

Porous materials are found in nature and have various applications. They can also be synthesised by the following methods:

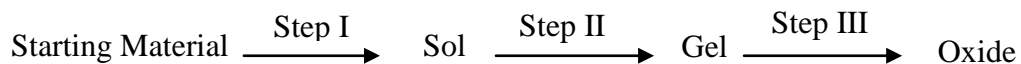
- a. Sol-gel synthesis
- b. Phase separation by acid leaching
- c. Compaction and sintering of the powder.

In the present work, the sol-gel and compaction cum sintering methods were used to prepare the porous ceramic and porous glass samples.

3.2.1. Sol-Gel Method

The sol-gel method is a wet chemical method used in the preparation of glass and ceramics, with the densification occurring at ambient temperatures. A sol is a colloid of a solid dispersed in a liquid. A gel is a three dimensionally interconnected network of a host matrix containing a mobile phase. An often used sol is a metal oxide or a metal chloride in aqueous suspension. If a sol (solution) is taken as a precursor, it gradually forms a diphasic (solid and liquid) gel network. The sol undergoes hydrolysis and polycondensation reaction

[Brinker et al., 1994]. The solid phase structure can range from discrete colloidal particles to a continuous chain-like polymer network [Brinker et al., 1982; Klein and Garvey, 1980]. The liquid phase undergoes a drying process, which results in shrinkage and densification, yielding a microporous glass or ceramic. The steps involved in the sol-gel process are schematically shown :



3.2.2. Compaction and sintering

Sintering is the process whereby heat is supplied to a sample at a temperature below its melting point. Sintering involves short-range diffusion of atoms and relaxation of configurations to lower energy states. Diffusion of atoms across the boundaries of the particles leads to adhesion between particles giving rise to the reduction in surface energy. Change in free energy due to reduction of surface energy is the driving force for densification [Shi J. L., 1999]. The procedure for sintering involves following stages :

1. Mixing a binder with the powder to form a slurry and then drying it.
2. The dried powder is put in the mould and pressed to form a green body (unsintered compact).
3. Low temperature heating of green body typically 340 °C to remove the binder followed by sintering at a higher temperature typically 640 °C to fuse the particles together.

3.3. Porosity and Density by water displacement

Water displacement method was used to obtain bulk porosity of compacts. Density of materials without voids is defined as ratio of mass to volume. For the material with voids the density deviates from the geometrical density since it does not take into account the empty spaces inside the material. For the compact having mass M_s and Volume V_s the geometric density is obtained by Equation (3.1).

$$\rho_g = \frac{M_s}{V_s} \quad (3.1)$$

The porosity of the compact is obtained after the sintering process at different times and temperatures. The weight of the dry compact and its weight in water (immersed in water) was obtained by the arrangement shown in Figure (3.1). Geometric density ρ_g of the compact is calculated by weighing the dry sample and dividing by its volume, calculated from its thickness and diameter. If ρ_w denotes density by water displacement, then the porosity ϕ is obtained from :

$$\phi = 1 - \frac{\rho_g}{\rho_w} \quad (3.2)$$

It is to be noted that the water displacement method is unable to access the isolated or unconnected pores and in all cases where such pores exist, this method leads to errors (underestimation) associated with the existence of these isolated pores. Special methods such as those available to SANS can be successfully applied to the estimation of isolated pores.

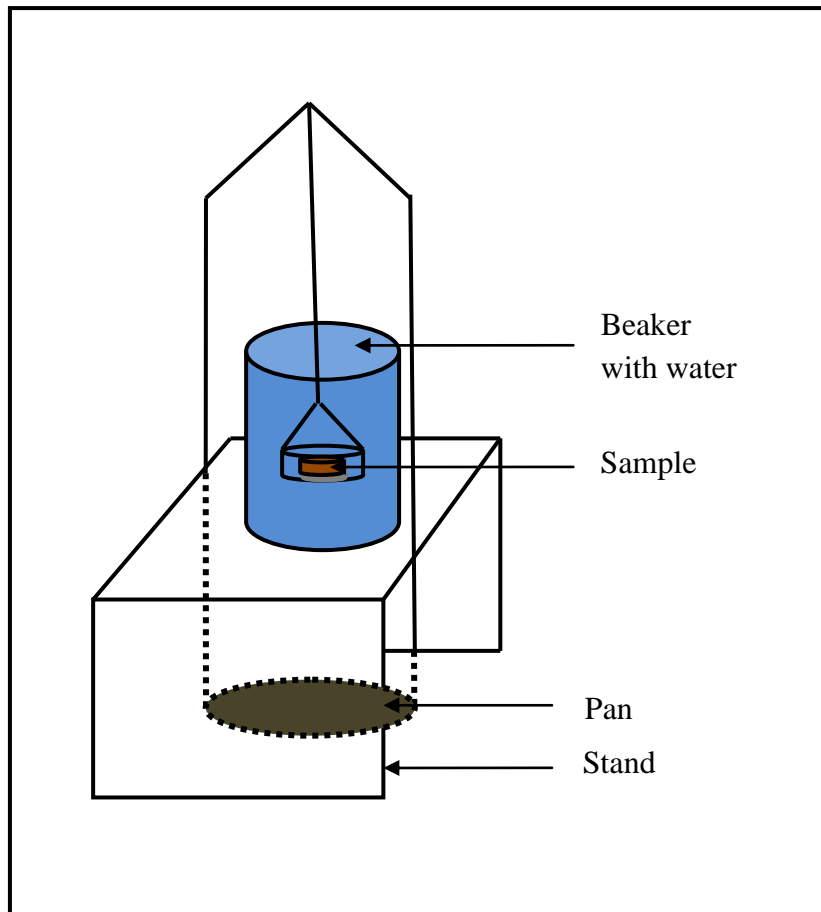


Figure 3.1. Experimental setup for the water displacement method.

3.4. Small Angle Neutron Scattering Instrument (SANS)

Small angle neutron scattering experiments on porous media were performed using the SANS diffractometer in the Guide Tube Laboratory, Dhruva Reactor, Bhabha Atomic Research Centre (BARC), Mumbai. SANS has been used previously in the evaluation of soft matter in various studies [Aswal et al., 2001 ; Aswal et al., 2006 ; Chodankar et al., 2008 ; Kumar and Aswal, 2011]. The schematic of the SANS instrument at Dhruva Reactor, BARC is shown in Figure (3.2). A BeO filter permits neutrons above a wavelength of 5.2 Å to be selected with a resolution ($\Delta\lambda/\lambda$) of 15%. A one meter long He³ positive sensitive detector was used to record the angular distribution of neutrons scattered by the sample. The neutron flux at the center of the Dhruva reactor is $\sim 1.8 \times 10^{14}$ n/cm²/s while the incident neutron flux at the sample position is 2.2×10^5 n/cm²/s. The beam size at the sample position is 1.5 cm x 1.0 cm and the angular divergence of the incident beam is $\pm 0.5^\circ$. The length scale that can be probed through this instrument is 10 - 150 Å. The experiments were performed at room temperature in the Q range 0.015 to 0.35 Å⁻¹. The raw experimental data were corrected for the empty cell scattering and the detector background using standard means [Aswal and Goyal., 2000].

3.5. Medium Resolution Small Angle Neutron Scattering Instrument (MSANS)

The Medium Resolution Double-Crystal based Small Angle Neutron Scattering (MSANS) instrument at Guide Tube Laboratory Dhruva Reactor BARC, Mumbai was used to access larger length scales. This method has been used earlier to study the pore morphology of sintered SiC [Sen et al., 2008], nickel aluminide [Sen et al., 2006], stainless steel [Sen et al., 2004], porous ceria [Patra et al., 2004] etc.. Here the sample is placed between the two silicon crystals cut for (111) reflection [Mazumder et al., 2002]. The incident wavelength is 0.312 nm. The scattering profiles are recorded by rotating the

second or analyser crystal through an angular range while the BF_3 end-on detector is kept fixed. The schematic of the instrument is as shown in Figure (3.3). The experiments were performed at room temperature in the Q range 0.003 to 0.173 nm^{-1} to probe the length scale from 18 to 1000 nm. The samples are placed on a sample holder with a circular slit of 1cm diameter. The measured profiles are corrected for background and instrument resolution [Mazumder et al., 2001].

3.6. Quasi Elastic Neutron Scattering (QENS)

Quasi-elastic neutron scattering measurements were carried out using the QENS spectrometer at Dhruva reactor, Trombay [Mukhopadhyay et al., 2001]. The spectrometer is used in multi-angle reflecting crystal (MARX) mode, which uses a combination of a large analyzer crystal for energy analysis and a position sensitive detector for detecting the scattered neutrons. The schematic of the instrument is as shown in Figure (3.4). The quasielastic data were recorded on all samples in the wave vector transfer (Q) range of $0.67 - 1.8 \text{ \AA}^{-1}$. In QENS the measured data is convoluted with the resolution function of the instrument and then the dynamical parameters involved in the model scattering function by least squares fit to the experimental data is obtained. Dynamics of water in various confined media including clays are suitably studied using quasielastic neutron scattering (QENS) technique [Mitra et al., 2007; Chakrabarty et al., 2006, Chathoth, 2011].

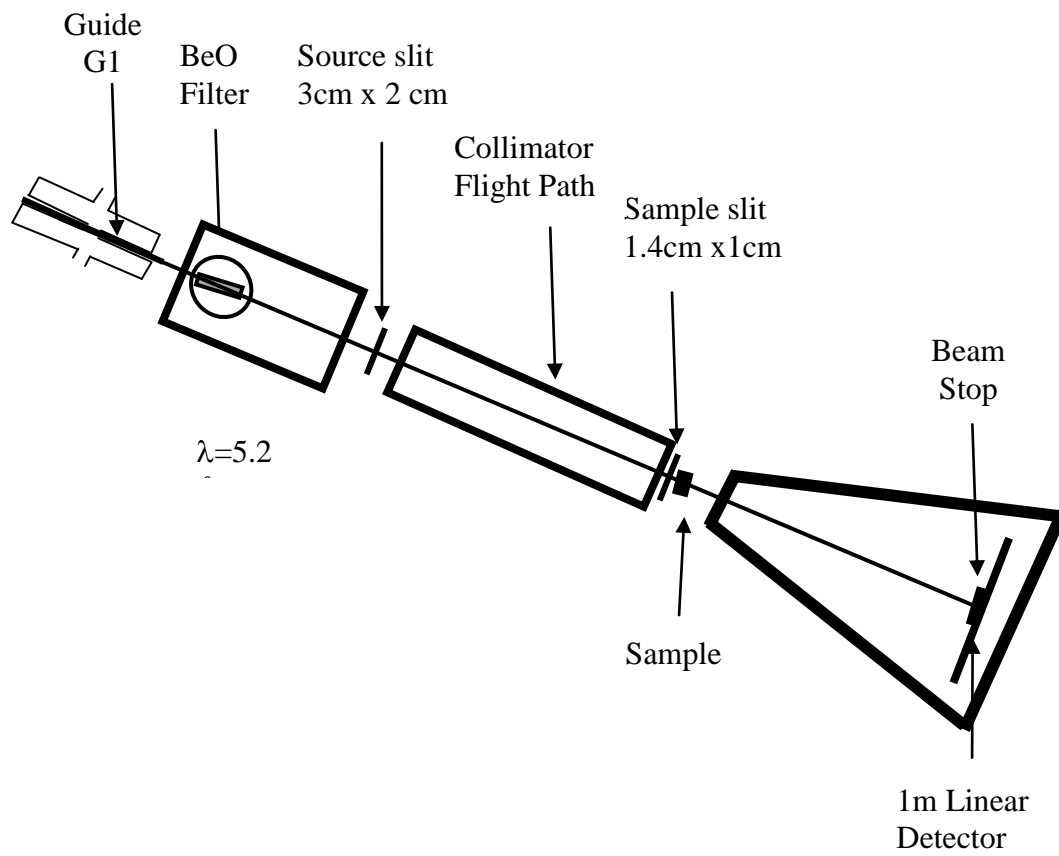


Figure 3.2. Schematic of SANS at BARC [from Aswal and Goyal, 2000].

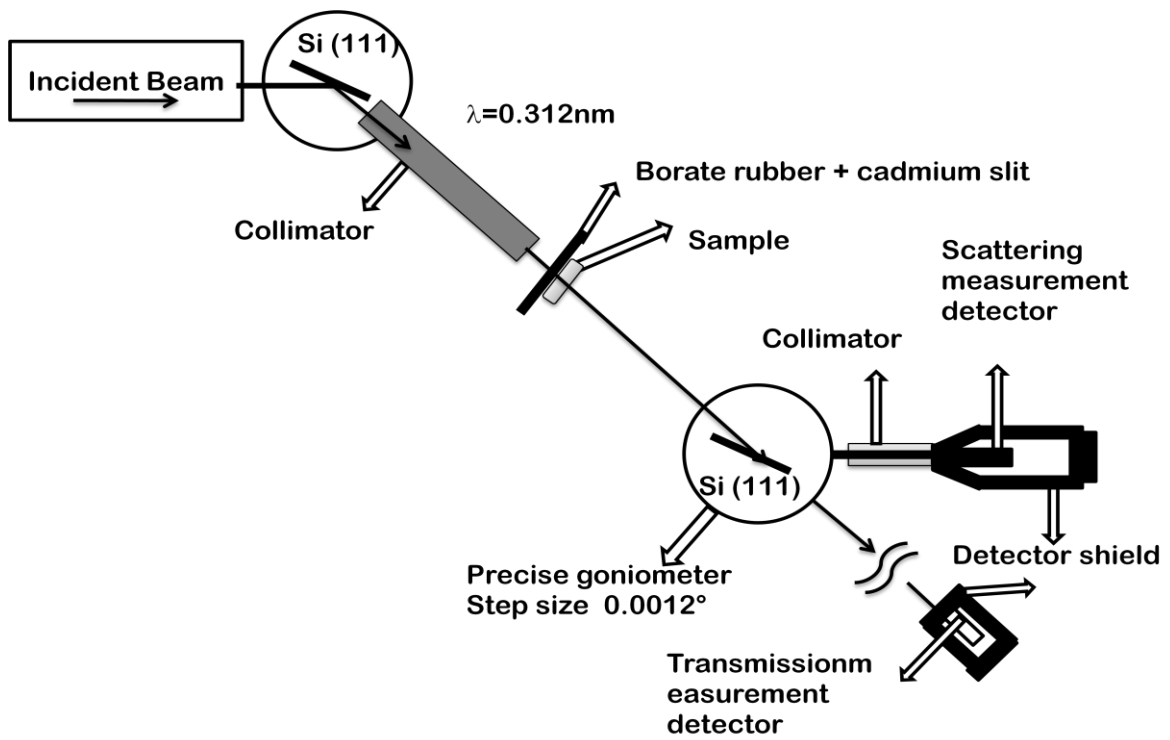


Figure 3.3. Schematic of MSANS at BARC [from Mazumder S. et. al.,2001].

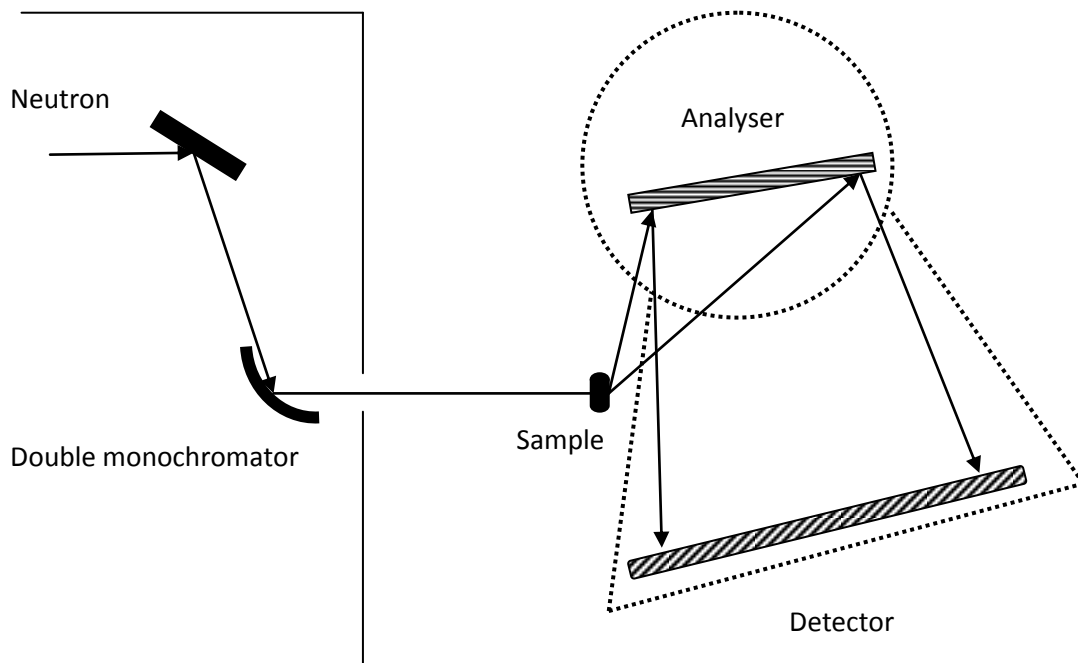


Figure 3.4. Schematic of QENS Instrument at Druva Reactor [from Mukhopadhyay et al., 2001].

3.7. Scanning electron microscopy, X-ray diffraction, thermo-gravimetric analysis and mercury intrusion porosimetry.

This section discusses the various other experimental techniques adopted in characterising the porous media viz. Scanning Electron Microscopy, X-ray Diffraction, Mercury Intrusion Porosity, Thermo-Gravimetric Analysis and Differential Thermal Analysis.

3.7.1. Scanning electron microscopy

The scanning electron microscope uses electrons to view objects. The objects are similar in size to the wavelength of the incident electrons. Since the wavelength of electrons (of keV energies) is of the order of Å, the technique is used for differentiating objects of atomic sizes. The electrons emitted by the electron gun are accelerated through a high voltage and focussed to a coherent beam by condenser lenses. The accelerated electrons then interact with the sample. This interaction between the electron beam and the sample generates secondary electrons, backscattered electrons, photons, visible light and heat. Secondary electrons are used to probe surface morphology and in the present work to obtain micropore geometry. X-rays detected in this technique are used in energy dispersive X-ray (EDX) spectroscopy. EDX was used to identify the elemental composition of the system. A JEOL (15 kV) SEM instrument shown in Figure (3.5) was used to study the surface morphology and composition as well as to obtain the micron-sized variations of porous regions as a function of sintering temperature and compaction pressure. The sintered ceramic pellets and microsphere glass were mounted on double-sided tape on aluminium stubs and sputter coated with gold as shown in Figure (3.6). Micrographs were taken at appropriate magnification for visualisation of pore shape and size variation.



Figure 3.5. Scanning Electron Microscope at NCAOR, Goa.



Figure 3.6. Instrument used for gold coating on the sample.

3.7.2. X-ray diffraction

The X-ray diffraction method was used in this study in order to: Establish the purity of a sample ; Identify existing phases by comparison with appropriate database information ; study hydration in clay (change in d-spacing).

X-rays are scattered (diffracted) by the electrons in the material when X-ray radiation is directed to the sample. In case of crystalline structure where atoms are arranged in regular manner, the scattering results in maxima and minima due to constructive and destructive interference in the diffracted intensity. The maxima follow Braggs law (Figure (3.7)) :

$$n\lambda = 2d\sin\theta \quad (3.3)$$

where n is an integer, λ is the incident wavelength, θ is the diffraction angle and d is the distance between crystal lattice planes. The position and the intensity of maxima are characteristic for the crystallographic structure and the atomic composition of the material. A Rigaku X-ray diffractometer (40 kV and a current of 50 mA) with incident CuK_α ($\lambda = 1.5418 \text{ \AA}$) in the scattering range 3° to 90° was used. An X-ray diffractometer consists of an X-ray generator, a goniometer with sample holder and an X-ray detector as a movable proportional counter. The schematic of X-ray diffractometer is as shown in Figure (3.8). X-rays are generated in the X-ray tube by bombarding a metal target with 10-100 keV electrons.

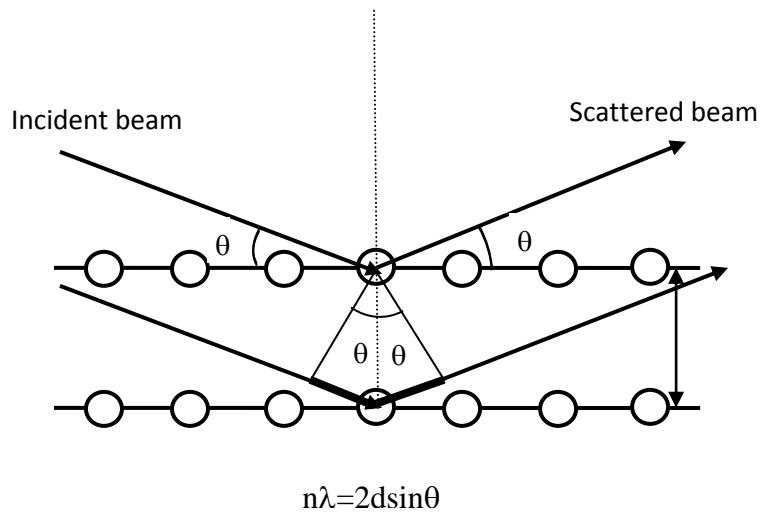


Figure 3.7. Schematic of Bragg's law.

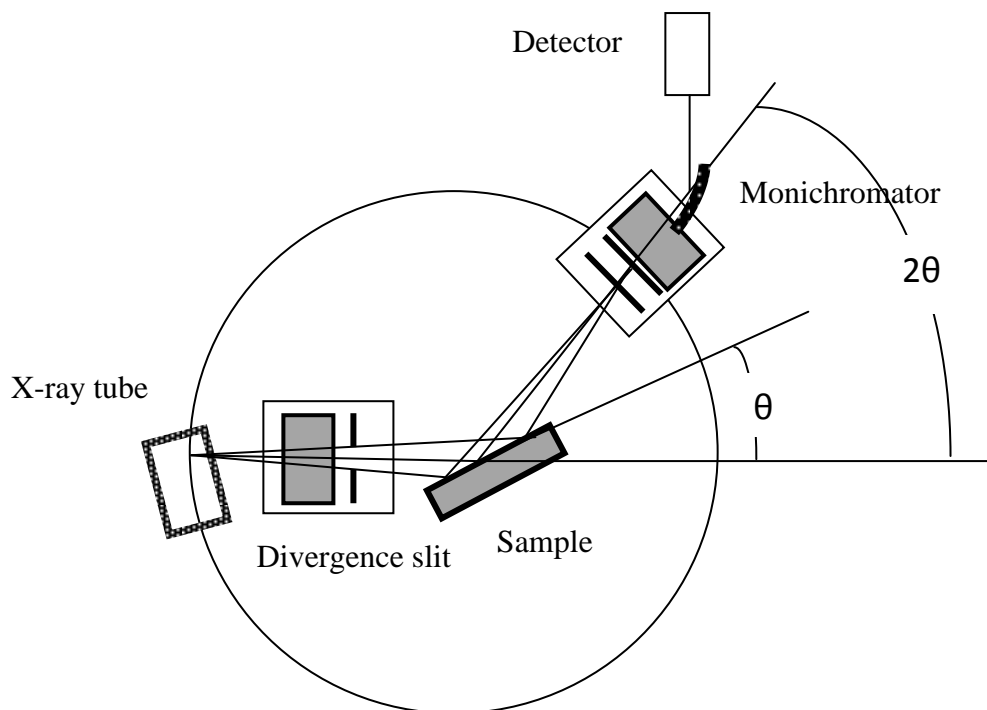


Figure 3.8. Schematic of X-ray diffractometer.

3.7.3. Thermogravimetry and Differential Thermal Analysis (TGA/DTA)

Thermogravimetric analysis (TGA) was used to determine the thermal stability of the material and its combustible component fraction by monitoring the weight change in the material as a function of temperature in air. TGA is used to test the thermal characteristics such as absorbed moisture content. Here the change of sample weight is plotted as a function of temperature or time at a particular heating rate. DTA measures the derivative of TG, showing how fast or slow the weight of sample decreases. A peak in the DTA profile gives information about the type of decomposition species and the temperature at which the decomposition takes place. TG-DTA curves were obtained using a NETZSCH STA 409 PC instrument.

3.7.4. Mercury Intrusion Porosimetry

Mercury Intrusion Porosimetry can investigate pores between 3.5 nm to 500 μm . Mercury is non wetting to most solids because the solid/liquid surface free energy is greater than the solid/gas surface free energy. Mercury cannot flow spontaneously into pores, but under pressure, mercury can be forced into the pores. The total of the pore volumes is the volume of the intruded liquid and pore size is related to pressure by Equation (3.5) [washburn, 1921].:

$$D = -\frac{(4 \gamma \cos\theta)}{p} \quad (3.5)$$

where, D is the pore diameter, p is the intrusion pressure, γ is the surface tension of the intrusion liquid and θ is the contact angle.

The surface tension and contact angles of mercury used in the calculations were 480 dynes/cm and 140° respectively. Measured intrusion volume and pressure were used to

compute pore size, pore volume and pore volume distribution. The following equation defines the pore distribution function:

$$F = -\frac{d \left[100 \times \left(\frac{F_w}{F_d} \right) \right]}{dD} \quad (3.6)$$

where, F_w and F_d are the flow rates through wet and dry samples respectively at the same differential pressure.

3.7.5. Infrared spectroscopy

The energy of the molecule at any given moment consists of rotational, translational, vibrational and electronic component.

$$E_{total} = E_{electronic} + E_{vibrational} + E_{rotational} + E_{translational}$$

FTIR (Fourier Transform Infrared Spectroscopy) is a powerful tool for identifying functional groups by excitation of rotational and vibrational modes to higher energy levels. Vibrational absorption states have corresponding wavelengths of the order of 4000-400 cm^{-1} . The vibration of molecular bonds at various frequencies depends on the element and the type of bond having the specific frequency of vibration. When the bond is excited by absorbing light energy, the frequency of molecular vibration increases. That will give rise to transition between two states and the IR energy will be equal to the difference in the energy between ground state (E_0) and excited state (E_1).

$$E_1 - E_0 = \frac{hc}{\lambda}$$

where h is the planks constant, c is the speedof light, and λ is the wavelength of light. By comparison of the measured infrared spectra to spectra from known compounds and

functional groups the presence or absence of particular compounds and groups were established. The FTIR spectrometer consists of a source of infra red radiation, a grating and a detector. In the Michelson interferometric design, the measured transmitted spectrum is fourier transformed into a frequency spectrum and it is this process that gives instrument its name viz Fourier transform Infra-Red Spectroscopy (FTIR). A SHIMADZU-FTIR 8031 instrument was used in the range from 350-4000 cm^{-1} units.

Chapter 4

Porous Ceramic from Rice Husk

4.1. Introduction and scientific interest

Porous ceramic compacts were prepared by compaction and sintering ceramic powder synthesized from rice husk as a source of silica. Ceramics having SiO_2 are particularly important due to their chemical resistance, modifiable surface and pore size control. Such Porous ceramics have potential applications as in gas/liquid filters, as catalysis, etc. Combustion of rice husk ultimately leads to ash which can be used in the production of natural silica [Kalapathy et al., 2000]. Due to high content of silica, [Kurama et al., 2003; Ikram et al., 1988] rice husk silica has been used in preparation of various silicon based compounds like silicon carbide, solar grade silicon [Kurama et al., 2008], zeolite [Kurama et al., 2008; Sun L., 2001]. The non- carcinogenic and biodegradable nature is responsible for the importance of rice husk silica in ceramic composites [Nayak and Bera, 2009]. X-ray diffraction confirmed the purity of the silica by comparing the diffraction pattern from commercial silica. Filters for fluids, bacteria, etc. have certain requirements of pore sizes, connectivity and permeability. The connectivity across tens of pores is important to the flow and transport of fluid in a porous media. Hence it is necessary for a system to have hierarchical pore structure and connectivity even at the nano-porous scale. This work attempts to find pore size (nano pores) distributions by the SANS technique. The modification of mesoscopic structure under different sintering conditions has been investigated using neutron scattering techniques and scanning electron microscopy. Although pore size can be determined by various methods like mercury intrusion and nitrogen adsorption, SANS has the special advantage of being able to

determine pores of nano meter dimension while being sensitive to the presence of isolated pores.

4.1.1. Synthesis of silica from rice husk

A local variety of rice husk was repeatedly washed with water before being acid leached with HCl (1N) for an hour. The husk was subsequently washed with hot distilled water and dried overnight at 110 °C. Complete combustion in air of the husk was achieved at 700 °C [Kalapathy et al., 2000; Umeda et al., 2007; Shelke et al., 2010] for 6 hours. The product was a whitish ash termed Rice Husk Silica (RHS). The size of silica particles thus obtained was reduced by grinding. The silica obtained was studied for its purity and structural properties by X-ray diffraction, Infrared spectroscopy and SEM.

4.1.2. Comparison of RHS and commercial silica by X-ray diffraction, IR and SEM/EDEX.

Silica obtained from rice husk was compared by X-ray diffraction pattern with that from commercial silica (Thomas Baker, 99%) by Rigaku diffractometer, $\text{CuK}\alpha$, 0.02° step, speed 2°/minute over a scattering angle range from 15 to 120 °C as shown in Figure (4.1). The absence of sharp crystalline reflections and the appearance of broad maxima in the X-ray diffraction patterns of RHS indicate that rice husk ash is in the amorphous state. Comparison with commercially obtained SiO_2 confirms that the RHS is in the amorphous silica state. FTIR-Spectroscopy SHIMADZU-FTIR 8031 have been widely used to obtain chemical structure of RHS collected in the range from 320-4000 cm^{-1} units. Comparison of FTIR spectra of RHS and Commercial silica is shown in Figure (4.2). Vibration modes of both the RHS and silica (commercial) are as given in Table (4.1). Modes due to stretching and bending vibrations of silica are observed at 466, 800 and 1100 cm^{-1} . Rocking motion of oxygen atom bridging silicon atom in siloxane (Si-O-Si) bond is assigned at 464 cm^{-1} .

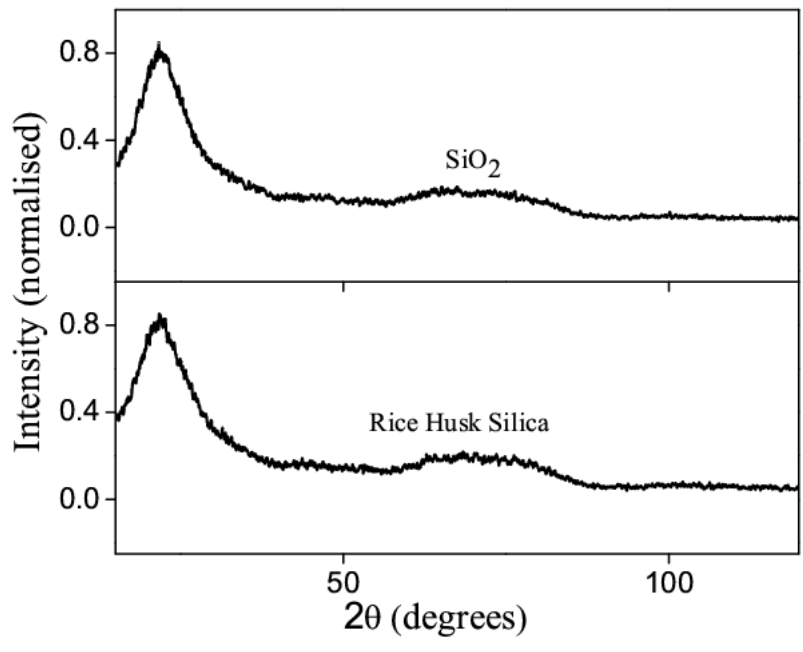


Figure 4.1. X-ray diffraction of rice husk silica and that of commercial silica.

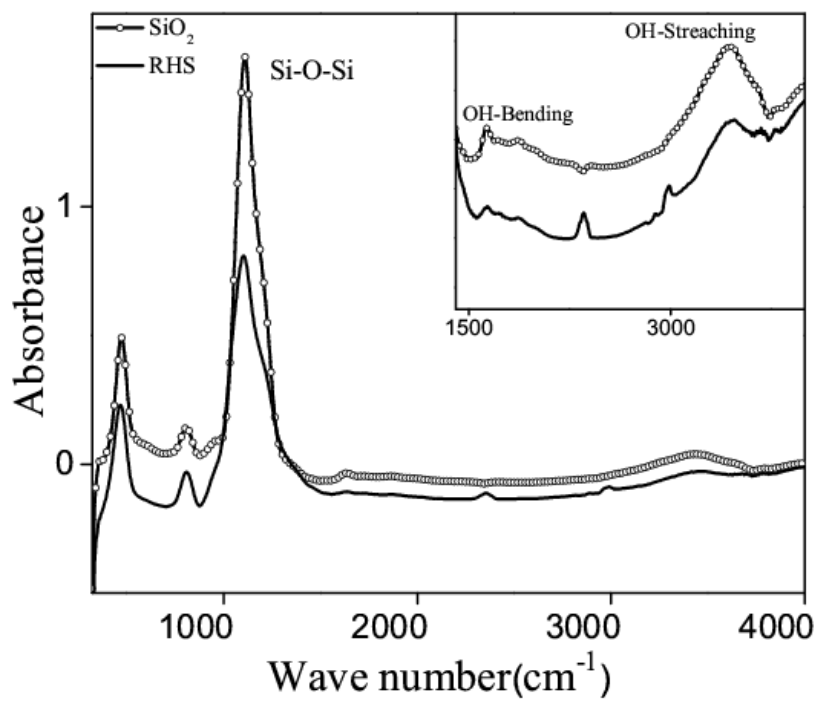


Figure 4.2. FTIR spectra of RHS and its comparison with commercial silica.

Si-O-Si symmetric vibrations of silicon atoms occur at 800 cm^{-1} . Anti-symmetric motion of silicon atoms in siloxane bonds (Si-O-Si) was observed at 1100 cm^{-1} which is the largest peak in the spectrum [Swann and Patwardhan, 2011]. The adsorbed water stretching and bending modes due to H-O-H were observed at 1628 and 3448 cm^{-1} . Thus, FTIR confirmed that the powders consisted of pure silica particles.

Table 4.1. IR modes of rice husk silica and commercial silica.

Obs. No	Modes of RHS	Modes of Silica	
1.	466 cm^{-1}	470 cm^{-1}	Stretching and bending vibrations of silica
2.	800 cm^{-1}	800 cm^{-1}	
3.	1100 cm^{-1}	1109 cm^{-1}	
4.	940 cm^{-1}	940 cm^{-1}	Si-OH stretching
5.	1628 cm^{-1}	1628 cm^{-1}	H-O-H stretching
6.	3436 cm^{-1}	3436 cm^{-1}	H-O-H bending

Surface morphology and composition were obtained by Scanning Electron Microscopy (JEOL, 15 kV) on the RHS and is shown in Figure (4.3). The Micrograph of RHS shows that the particles in the fired samples possess irregular shapes of average lengths of about $600\text{ }\mu\text{m}$ and diameter $100\text{ }\mu\text{m}$. Shape of silica obtained is similar to that of rice husk. The silicon content of RHS was estimated from energy dispersive X-ray (EDX) spectroscopy and is shown in Table (4.2). Carbon is seen to be one of the principal elemental components and is likely to arise from the initial phase of preparation of RHS by combustion. Despite the atomic percentage of carbon being in excess of 12 %, the overall structure of the RHS remains similar to pure silica.

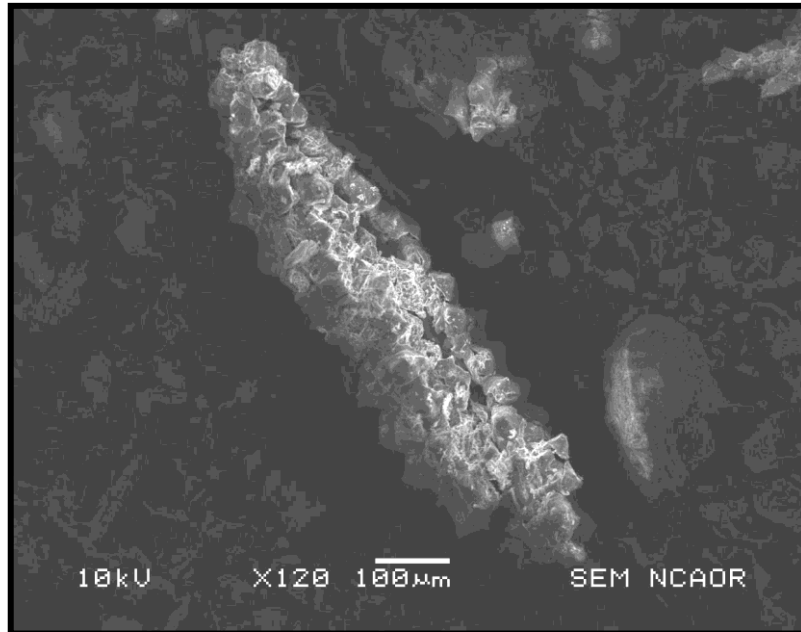


Figure 4.3. SEM micrograph of Rice Husk Silica.

Table 4.2. Elemental composition of RHS.

Obs. No.	Element	Weight%	Atomic%
1.	Carbon	8.26	12.41
2.	Sodium	0.10	0.08
3.	Magnesium	0.05	0.04
4.	Aluminium	0.34	0.23
5.	Silicon	32.05	20.59
6.	Calcium	0.12	0.06
7.	Tin	0.22	0.08
8.	Oxygen	58.86	66.51
9.	Total	100	100

4.1.3. Preparation of Ceramic from RHS by the sol-gel method

The RHS was then used to prepare a porous ceramic by sol-gel process [Nayak and Bera, 2009; Kumar S., 2009] summarized in Figure (4.4). In obtaining uniform nanoparticles used in synthesis of porous ceramic compacts that can be used in separation and filtration, the sol-gel process is the well established method [Kikkinides et al., 2003]. Due to stacking of uniform nanoparticles a narrow pore size distribution can be obtained after compaction and sintering. Sodium calcium silicate sol is prepared from rice husk silica as the starting material at temperature 70 °C. The sol is peptized with HNO₃.

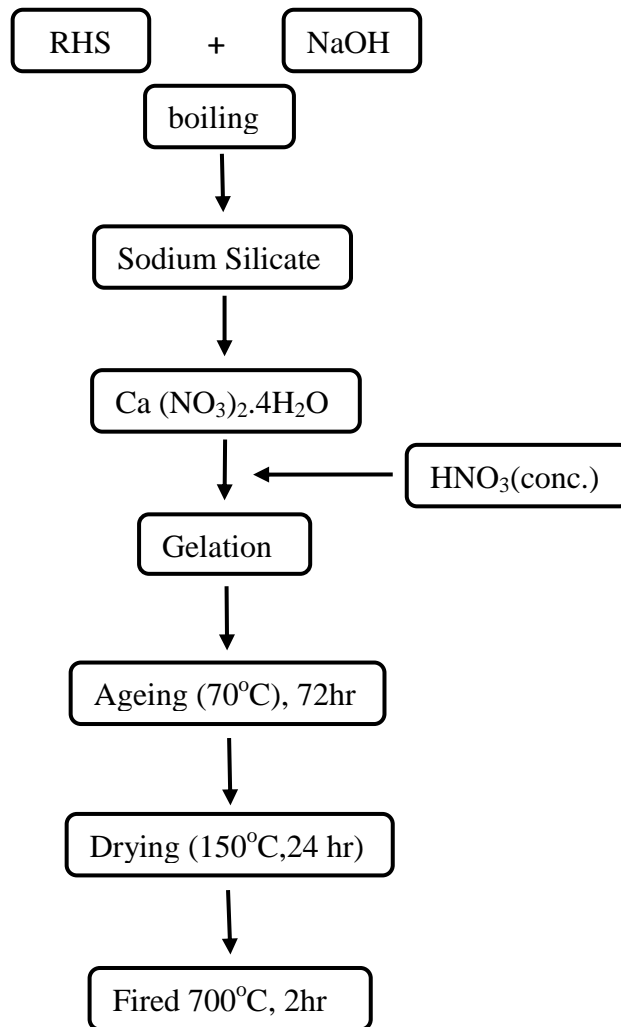


Figure 4.4. Scheme of preparation of porous glass-ceramic from RHS [Kumar S., 2009].

1.6725 gm NaOH pellets were dissolved in 20 ml of double distilled water (i.e. 0.836 gm/c.c. concentration) and warmed. 2.5 gm of RHS obtained by combustion of rice husk was added in boiling condition and the volume increased to 60 ml by adding more water. After one hour the RHS dissolved in water is cooled and filtered. The filtered solution is sodium calcium silicate. 4.9807 gm of $\text{Ca}(\text{NO}_3)_2 \cdot 4\text{H}_2\text{O}$ was dissolved in 30 ml of double distilled water. Concentrated NaNO_3 was added to the above solution while stirring. This was followed by a drop by drop addition of a sodium calcium silicate solution. At regular intervals the concentrated NaNO_3 was added in order to avoid precipitation. Gelation began after 60 minutes of stirring and the solution was left for aging at 70 °C for 3 days. The obtained powder was dried at 150 °C for two days. The powder was then fired at 700 °C for two hours.

4.1.4. Interpretation of Thermogravimetric curves of RHS ceramic

Thermo-gravimetric (TG-DTA) data were obtained with a NETZSCH STA 409 PC instrument (10 °C/min). The objective here was to follow changes of phase brought about by temperature and loss of bound water in the structure. The thermo-gravimetric measurement shows weight loss at about 140 °C and 756 °C corresponding to different endothermic reactions as observed from the differential thermal analysis curve shown in Figure (4.5). The first weight loss of about 10 % at 140 °C is due to loss of gel water which corresponds to a large endothermic peak at 98 °C. The endothermic peak at about 237 °C which is not accompanied with weight loss may be due to structural change. The weight loss of about 21 % may be due to the decomposition of the nitrate compound and residual water. The decomposition of sodium nitrate and calcium nitrate occurs at 750 °C. The peak in the DTA at 237 °C may be due to crystallization of sodium nitrate or/and calcium nitrate. The compacts were sintered above 750 °C for studying its pore structure.

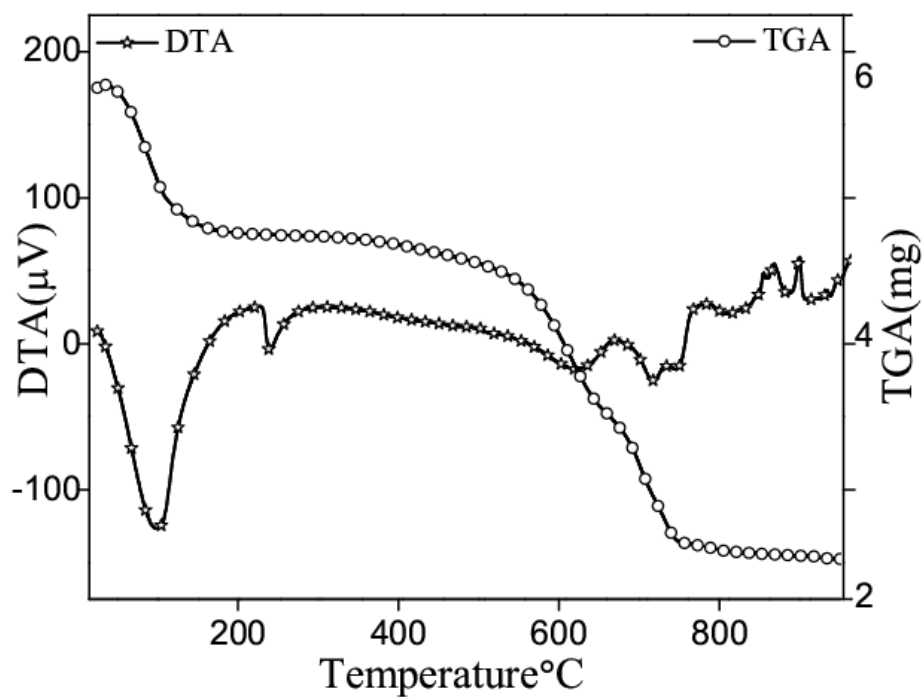


Figure 4.5. TGA-DTA of RHS ceramic powder fired at 700 °C.

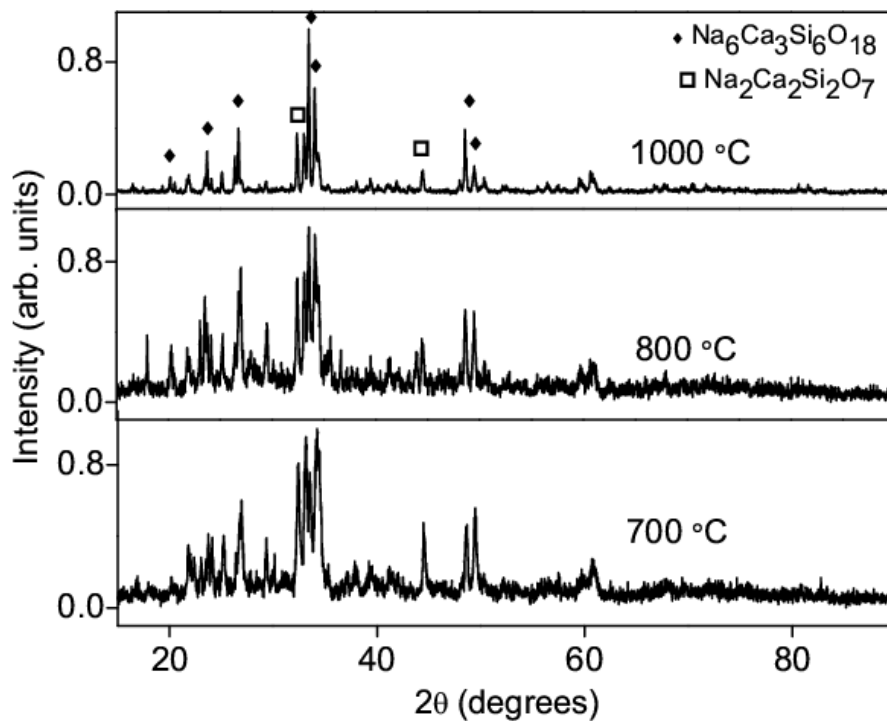


Figure 4.6. X-ray diffraction of RHS ceramic fired at 700, 800 and 1000 °C for two hours.

4.1.5. Phase change as a function of sintering temperature by X-ray diffraction

The ceramic powders were further sintered at 800 and 1000 °C for 2 hr. X-ray diffraction was employed with the intention of confirming the presence of sodium calcium silicate (both crystalline phases) on sintering. The ceramic samples sintered at 700 °C, 800 °C and 1000 °C for 2 hours were examined by X-ray diffraction over the limited scattering angular range of 15 to 90 °C and are shown in Figure (4.6). It is first formed as a glass-ceramic and crystallized partly by heat treatment. The ceramic fired at 700 °C show the presence of sodium calcium silicate with two different crystalline phases $\text{Na}_6\text{Ca}_3\text{Si}_6\text{O}_{18}$ [JCPDS-77-2189] and $\text{Na}_2\text{Ca}_2\text{Si}_2\text{O}_7$ [JCPDS-10-0016]. The powder sintered at 800 °C shows the presence of $\text{Na}_6\text{Ca}_3\text{Si}_6\text{O}_{18}$ and $\text{Na}_2\text{Ca}_3\text{Si}_6\text{O}_{16}$ while that sintered at 1000 °C shows the presence of both $\text{Na}_6\text{Ca}_3\text{Si}_6\text{O}_{18}$ and $\text{Na}_2\text{Ca}_3\text{Si}_6\text{O}_{18}$ phases.

4.1.6. Summary of X-ray and Thermal Studies of Rice Husk Ceramic

Silica has been obtained from rice husk. The purity of RHS sample was confirmed by comparison with commercial silica X-ray diffraction data and with IR spectral data. Silica obtained is amorphous in structure with a broad hump at 22°. Silica content of RHS was obtained from EDX spectroscopy. Shape of silica obtained was similar to that of rice husk. A porous ceramic containing SiO_2 , Na_2O and CaO has been synthesized by sol-gel method from rice husk as the starting material. Thermo-gravimetric data show that a phase transition occurs at 750 °C. The compacts were sintered at 800 and 1000 °C. The X-ray data confirms that sodium calcium silicate forms after the latter transition. X-ray diffraction has shown a glassy-ceramic phase at lower temperatures to give way to a purely crystalline phase at 1000 °C.

4.2. Effect of temperature on pore morphology of RHS ceramic

4.2.1. Introduction

Compacts of the ceramic were formed by applying a pressure of 2T on 500 mg of the powder to yield compacts of diameter 1.3 cm and thickness ~ 2 mm. The compacts were sintered at temperatures 800, 900 and 1000 °C at the rate 10 °/m. The compacts were sintered for 2 hours and 4 hours in air. The bulk density of each compact was obtained by geometric as well as the water displacement method. In this study we have obtained the pore size distribution as a function of temperature. By loading the compact with D₂O and then subjecting to SANS the connectivity between pores was studied. Contrast matching technique, was used to determine number of isolated pores in the sample.

4.2.2. Density and Porosity by water displacement method

Bulk densities for the samples sintered at 800, 900 and 1000 °C, each for two hours, were measured by the water displacement method. For each compact, the density and the bulk porosity was found both by measuring its diameter and thickness to give the “geometric density” as well as by use of the water displacement method. The estimate of the fractional macroscopic porosity as shown in Figure (4.7) was obtained using the formula:

$$\phi = 1 - \frac{\rho_g}{\rho_w} \quad (4.1)$$

where ϕ is the porosity of the compact, ρ_w is the density by the water displacement method and ρ_g is the geometric density of the compact. The porosity values and the scattering length density of the compacts is shown in Table (4.3).

Table 4.3. Density, Porosity and neutron scattering length density of ceramic compacts sintered at different temperatures.

Sample	Geometric Density (g.cm ⁻³) ± 0.005	Density water displacement (g.cm ⁻³) ± 0.0003	Porosity (Fraction of accessible pores) %	Scattering Length Density cm ⁻²
Ceramic-800°C-2hr	1.456	2.5294	42	3.47 x 10 ¹⁰
Ceramic-900°C-2hr	1.464	2.2744	35	3.12 x 10 ¹⁰
Ceramic-1000°C-2hr	1.416	2.0939	32	2.87 x 10 ¹⁰

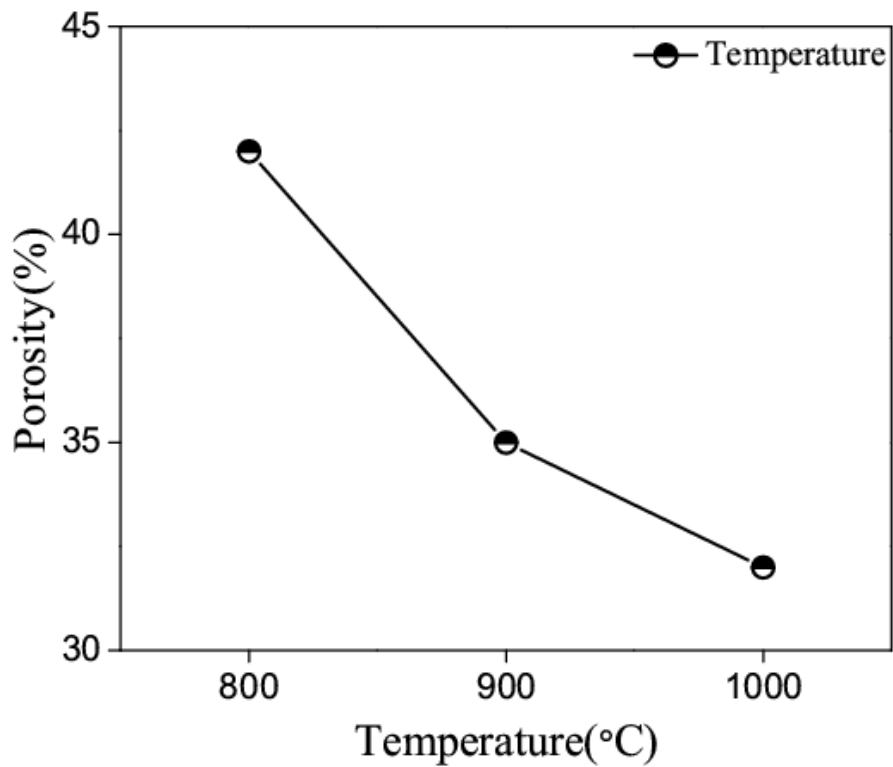


Figure 4.7. Variation of porosity of RHS-ceramic with sintering temperature.

The density of the sample fired at the higher temperature is lower. For a sintering temperature of 800 °C for 2 hours, the geometric density was 1.456 g/cc while the density by the water displacement method was 2.5294 g/cc, leading to a porosity of 42 %. Figure (4.7) show that porosity decreases with increasing sintering temperature. Comparison of the X-ray data (Figure 4.6) shows the “higher temperature” sample to have better signal to noise ratio and better defined crystallinity. From Table (4.3), it is observed that the density (by the water displacement method) and the porosity decrease with temperature. In order to reconcile these apparently conflicting observations, the presence of substantial numbers of blind / unconnected pores is proposed. This argument is based on the idea that water is unable to permeate into the regions occupied by isolated pores and porous channels which get sealed off as the sintering temperature is increased. The parameter ϕ thus refers to the fraction of accessible or connected pores. The fraction of isolated pores together with unconnected pores is given by $(1 - \phi)$. Thus, the fraction of isolated pore decreases as the temperature of sintering increases.

4.2.3. Nanoporous structure of sintered ceramic by MSANS

The porous nature of these ceramics was examined by porosity measurements. Smaller sized pores were examined by medium resolution double crystal based small angle neutron scattering (MSANS). SANS is a non-destructive method which can be applied to ceramics [Sen et al., 2002] for investigating statistically representative microstructures e.g., pore sizes and morphology - in the mesoscopic length scale - of samples which would otherwise be difficult to quantify especially when there are closed or blind pores. This technique has also been used to investigate pore structure in rocks [Sen et al., 2002] and coal [Sen et al., 2001]. Scattering arises due to fluctuation in scattering length density contrast of the compacts. In the present case the contrast is between the difference in

scattering length density of pores and the matrix. The profile of SANS, maps the shape and size of the scattering density inhomogeneity in the material (pores in porous compacts). A 1 cm diameter circular slit was used at the sample stage. The scattered intensity is measured as a function of wave vector transfer Q . The measured data were corrected for background, transmission and resolution broadening. Scattering data for the unfired compact and compacts fired at 800 °C and 1000 °C for 2 hours are shown in Figure (4.8). The measured scattered intensity $I(Q)$ (where Q is the momentum vector transfer) of an ensemble of poly-dispersed spherical particles under local monodisperse approximation can be expressed as [Pedersen J. S., 1994; Sen et al., 2003]:

$$I(Q) = C \int P(Q, r) r^6 D(r) S(Q, r) dr \quad (4.2)$$

where C is a scaling factor, $D(r)$ is the pore size distribution of pores with radii r and the probability of finding pores within radius r and $r + dr$ is represented as $D(r) dr$. In the present case $D(r)$ is assumed to be lognormal distribution,

$$D(r) = \frac{1}{\sqrt{2\pi\sigma^2 r^2}} \exp \left[-\frac{\left[\ln \left(\frac{r}{r_0} \right) \right]^2}{2\sigma^2} \right] \quad (4.3)$$

where r_0 is the median radius and σ represents polydispersity of the distribution. Assuming that the pores are sphere shaped, $P(Q, r)$ is the form factor of a sphere with radius r and is given by the following expression [Pedersen J. S., 1994].

$$P(Q, r) = 9 \frac{[(\sin(Qr) - Qr \cos(Qr))]^2}{(Qr)^6} \quad (4.4)$$

The structure factor, $S(Q)$, for the fractal aggregates is given by [Teixeira J., 1988] as:

$$S(Q) = 1 + \frac{1}{(Qr_0)^d} \frac{d \Gamma(d-1)}{\left[1 + \frac{1}{Q^2 \xi^2}\right]^{(d-1)/2}} \times \sin[(d-1)\tan^{-1}(Q\xi)] \quad (4.5)$$

Here, ξ is the upper cut-off of the fractal size, r_0 is a radius pertaining to the lower limit of the associated fractal (size of particles that aggregate to give fractal structure) and d is the fractal dimension which depends on aggregation. The basic relation from fractal theory for mass fractals is $M \propto r^{-d}$, M represents the mass and r the size. The term fractal was specifically introduced for temporal and spatial phenomena that exhibit partial correlations over many length scales. It also represents complexity of geometry of porous volumes.

As seen from the plots, the broad profiles in MSANS data with two distinct zones in scattering data as shown in Figure (4.8) indicate that the scattering originated from pores with two widely separated length scale within the compacts as seen by the neutrons. The larger length is due to larger pores and the presence of smaller pores is indicated in the smaller length scale, both of which are slightly modified in the process of sintering. Scattering arises from both isolated as well as connected pores. The SANS data have been fitted to a model assuming spherical shapes of scattering centres. To estimate pore size distribution Equation (4.2), has been fitted with a non-linear least squares technique. Two distributions are used to fit the profile in the entire Q range. To incorporate the effect of two size distribution the intensity of scattering can be expressed as a function of number of spherical scattering centres, the single scattering pore form factor and a structure factor. The number of larger and smaller scattering centres per unit volume pertaining to the lower and higher Q regions of $I(Q)$ respectively were obtained by fitting the scattered intensity function to the calculated intensity Equation (4.6):

$$I(Q, a_1, b_1, a_2, b_2, x_2, d_2) = n_1 P(Q, a_1, b_1) + n_2 P(Q, a_2, b_2) S(Q, a_2, x_2, d_2) \quad (4.6)$$

where Q = wave vector transfer

a_1, b_1 = pore size and variance, respectively for larger pores.

a_2, b_2 = pore size and variance, respectively for smaller pores.

x_2 = fractal aggregate size.

d_2 = fractal dimension.

n_1 & n_2 are the number of scattering centres in lower and higher regions of Q .

To estimate n_1 and n_2 i:e the density of scattering centres, the scattering data is represented in absolute scale. The scattering profile was converted to absolute scale using Equation (4.7) [Mazumder et al., 2001]:

$$\frac{d\Sigma}{d\Omega}(Q) = \frac{I(Q)}{I_m(0)\Delta\theta_h\Delta\theta_v t} \quad (4.7)$$

where $I(Q)$ is the transmission and background corrected intensity; t is the thickness; $I_m(0)$ intensity for blank measurement at $Q = 0$ (estimated by extrapolation); $\Delta\theta_h$ is the FWHM of the Bragg reflected intensity of the incident beam after the second crystal reflection in this double crystal instrument; and $\Delta\theta_v$ is measured by the ratio of detection aperture to sample detection distance. In this case $\Delta\theta_h = 1.5 \times 10^{-4}$ and $\Delta\theta_v = 0.012$.

In the model that has been fitted to the SANS data, domains of average sizes of 164 nm and 32 nm with fractal dimension of 2.88, with aggregate size of 125 nm for sintered compacts, whereas the pore sizes obtained from unfired compact are 190 nm and 29 nm. The parameters obtained from fitted data are shown in Table (4.4). No significant change

in small pore structure as a result of the heating schedule was indicated. Scattering plots are nearly identical (on a log-log scale) for the two different sintering temperatures indicating that the density of scattering centres in the nano-metric size regime is unchanged for these conditions. The ratio (n_1/n_2) for the ceramic sintered at 800 °C is ~ 0.135 and for the compact sintered at 1000 °C it is ~ 0.161 . From this ratio it can be concluded that there is a small increase in the numbers of larger pores with increase in temperature. The large decrease in intensity from unfired to sintered compacts indicates loss of water - both adsorbed and bound water - due to sintering at 800 and 1000 °C. For a sintering temperature of 800 °C and for two sintering times - 2 hours and 4 hours - it was observed that the SANS scattering patterns are almost identical. This is to be expected and is confirmed from the fits (using SASFIT) to the data sets shown in the Table (4.5). The effect of different heating and cooling rates up to a temperature of 1000 °C and a dwell time of 2 hours does have an appreciable effect on the scattering profiles as shown in Figure (4.10). Not only is the strength of SANS scattering intensity affected, but also the shape of the profile. In addition, the samples were heated and cooled in two different furnaces which have had different rates of cooling. Although quantitative conclusions may not be drawn from these, it is clear that both rates of heating and cooling are indeed important to the nano-sized porous structures of these ceramics as shown in Figure (4.10).

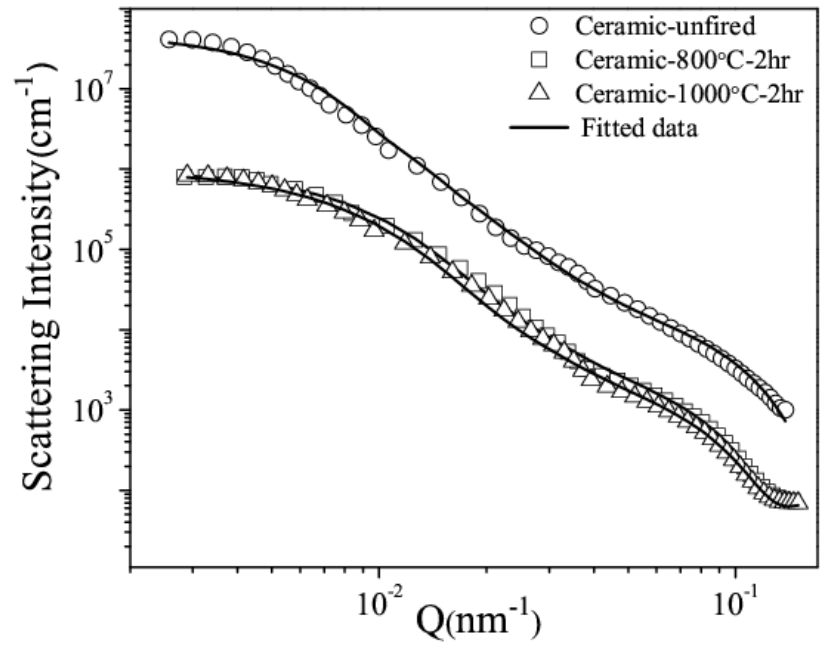


Figure 4.8. Scattering profile of compact unfired and sintered at 800, 1000 °C for 2 hour.

(Errors are within the size range of symbol)

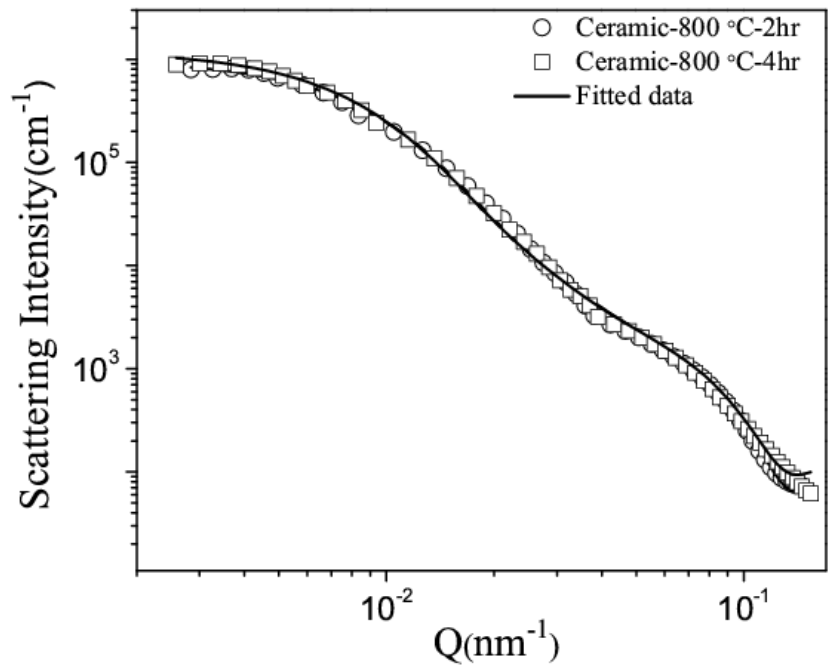


Figure 4.9. Scattering profile of ceramic sintered at 800 °C for 2 and 4 hour.

Table 4.4. The fitted parameters obtained from SANS analysis for sintered ceramic at different temperatures.

Sample Ceramic	Pore radius (nm)		No. of scattering centres		Fractal dimension 'd'
	Lower Q 0.0028-0.037 nm ⁻¹	Higher Q 0.042-0.15 nm ⁻¹	n ₁ (per cc) lower Q	n ₂ (per cc) higher Q	
Unfired	190 ± 19	29 ± 1	1.27 x 10 ¹¹	9.95 x 10 ¹¹	2.84
800 °C- 2hr	164 ± 8	32 ± 1	6.14 x 10 ¹⁰	4.54 x 10 ¹¹	2.88
1000 °C- 2hr	166 ± 9	32 ± 2	6.59 x 10 ¹⁰	4.09 x 10 ¹¹	2.85

Table 4.5. Parameters obtained from SANS analysis for ceramic sintered at different times.

Sample Ceramic	Pore radius (nm)		No. of scattering centres		Fractal dimension 'd'
	Lower Q 0.0028- 0.037 nm ⁻¹	Higher Q 0.042- 0.15 nm ⁻¹	n ₁ (per cc) lower Q	n ₂ (per cc) higher Q	
800°C-2hr	162 ± 8	32 ± 1	6.14 x 10 ¹⁰	4.54 x 10 ¹¹	2.88
800°C-4hr	163 ± 7	32 ± 1	7.21 x 10 ¹⁰	5.59 x 10 ¹¹	2.87

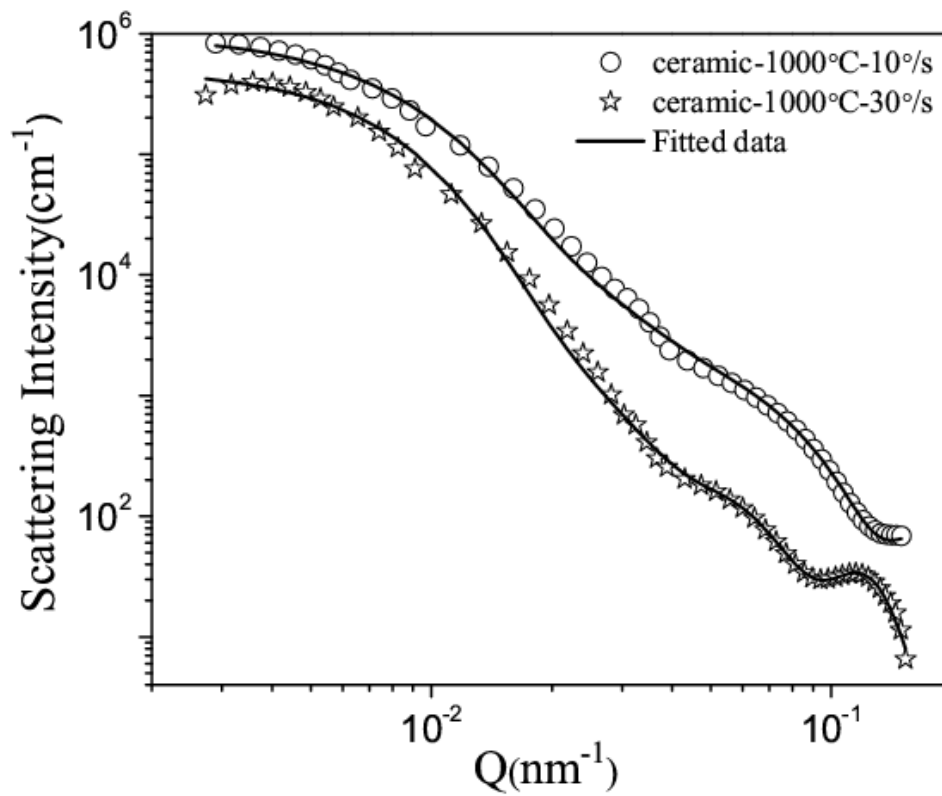


Figure 4.10. Scattering profile of ceramic sintered at 1000°C at the cooling rate 10°C and 30°C . (Errors are within the size range of symbol)

4.2.4. Nanopore morphology in the sintered ceramic loaded with D₂O

Connectivity between the pores was ascertained from scattering experiments on the ceramic compact impregnated with heavy water. Scattering data for dry and D₂O loaded compacts are shown in Figures (4.11) and (4.12). However, inclusion of D₂O in the compact causes a decrease in the intensity due to a lower contrast factor between the ceramic and the pores now occupied by D₂O. Since the nano pores get filled with D₂O, this size domain is therefore linked to the surface via connections to other pores of similar and larger dimensions. The fluid permeability and the pore size suggest that this material may be a promising candidate for application as a filter or as a catalytic surface.

Table 4.6. Parameters obtained from fitted data for D₂O loaded ceramics.

Sample Ceramic	Pore radius (nm)		No. of scattering centres		Fractal dimension 'd'
	Lower Q 0.0028-0.037 nm ⁻¹ ± 5%	Higher Q 0.042-0.15 nm ⁻¹ ± 5%	n ₁ (per cc) lower Q	n ₂ (per cc) higher Q	
800 °C-4hr	163 ± 15	29 ± 1	7.24 x 10 ¹⁰	4.89 x 10 ¹¹	2.80
800 °C- 4hr+ D ₂ O	164 ± 14	29 ± 3	4.44 x 10 ¹⁰	3.34 x 10 ¹¹	2.77
1000 °C-2hr	164 ± 16	27 ± 3	6.17 x 10 ¹⁰	1.81 x 10 ¹¹	2.95
1000 °C+D ₂ O	166 ± 16	29 ± 4	2.80 x 10 ¹⁰	4.87 x 10 ¹⁰	2.76

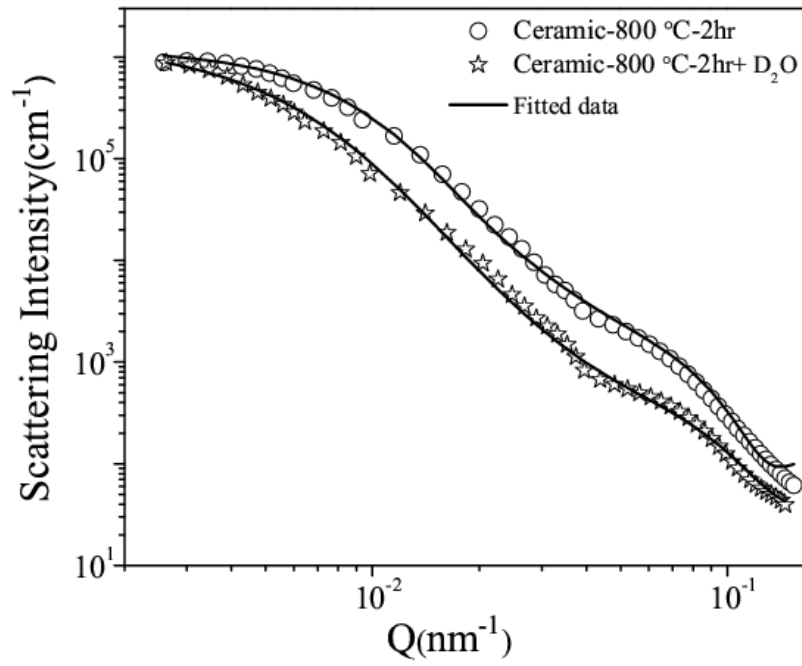


Figure 4.11. Scattering profile of ceramic sintered at 800 °C and loaded with D₂O.

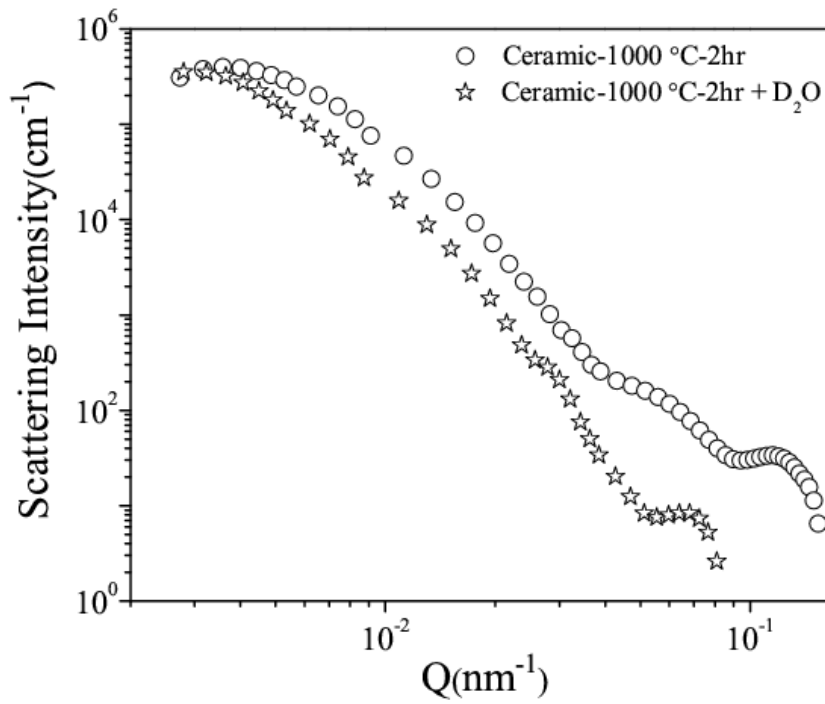


Figure 4.12. Scattering profile of ceramic sintered at 1000 °C and loaded with D₂O.

4.2.5. Estimation of Scattering from Isolated Pores

In the scattering from a ceramic compact, the scattering arises due to the contrast between the matrix and the pores. In a porous compact there are both connected and isolated pores, hence the total intensity scattering contribution is from both connected as well as the isolated pores. When the compact is loaded with a fluid like water the connected pores get filled with water whereas the isolated pores remain empty. The scattering length density of the matrix can be matched to that of the liquid in the pores by varying the composition and density of the fluid until it matches the scattering length density of the matrix. The scattering intensity in this case will be due to only isolated pores. In the experiments here, the relative concentration of H₂O and D₂O was chosen to nearly match the scattering from the matrix. In this case the scattering contrast between the matrix and the pores filled with the mixture will be null. Hence an estimate of the isolated pores can be obtained - in principle - by this contrast match experiment. This has achieved by the following procedure. The scattering intensity for any sample is given by Equation (4.8)

$$I(Q) = N(\rho_p - \rho_m)^2 V^2 P(Q) S(Q) \quad (4.8)$$

Where, ρ_p = Scattering length density of pore, ρ_m = Scattering length density of the matrix, and N = Number density.

If $\rho_p \sim 0$ as when the pores are air filled;

$$I(Q) = N(\rho_m)^2 V^2 P(Q) S(Q) \quad (4.9)$$

Thus, the total scattering intensity from a dry porous compact is given as:

$$I_{meas} = I_{conn.pore} + I_{isola.pore} \quad (4.10)$$

Using Equation (4.6)

$$I(Q)_{meas.dry} = [(\rho_m)^2 V^2 n_1 P(Q) + n_2 P(Q) S(Q)]_{conne.} + [(\rho_m)^2 V^2 n_1 P(Q) + n_2 P(Q) S(Q)]_{iso.} \quad (4.11)$$

For the sample loaded with a fluid like D₂O, the intensity is given by:

$$I(Q)_{D_2O} = [(\rho_{D_2O} - \rho_m)^2 V^2 n_1 P(Q) + n_2 P(Q) S(Q)]_{conne.} + [(\rho_m)^2 V^2 n_1 P(Q) + n_2 P(Q) S(Q)]_{iso.} \quad (4.12)$$

When the scattering length density of the fluid loaded in a compact is matched with that of the scattering length density of the matrix by using a combination of D₂O and H₂O or any other liquid, then the contrast in the first term of equation (4.12) tends to zero. Hence the contribution to the scattered intensity will now be from only due to isolated pores.

$$I(Q)_{D_2O+H_2O} = [(\rho_m)^2 V^2 n_1 P(Q) + n_2 P(Q) S(Q)]_{iso.} \quad (4.13)$$

Such a contrast matching experiment was performed using a mixture of H₂O and D₂O in the right proportion to match the scattering length density of the matrix. Scattering length density of a compact sintered at 800 °C and 1000 °C were 3.16 x 10¹⁰ cm⁻² and 3.67 x 10¹⁰ cm⁻² respectively. To match this scattering length density of the matrix, the compacts were loaded with a combination of H₂O and D₂O in the proportion of 46 % for H₂O and 54 % of D₂O in ceramic sintered at 800 °C and 39 % for H₂O and 61 % for D₂O in ceramic sintered at 1000 °C. The samples were soaked in this mixture for 24 hours. The MSANS measurement profiles on these samples are as shown in Figure (4.13) and (4.14). Most of the scattering in this data set is from isolated pores. The data were fitted using Equation (4.2) for both the dry compact to a model with spherically-shaped pores having mass

fractal arrangement. The same model fit used for the contrast matched compact, a small departures from the actual data profile, hence the isolated pores obtained from this fit are taken as first approximation fits. This difference in the fit could have been due to the contribution of various factors; difficulties with measurement of transmission factor for the loaded sample; effect of multiple scattering and the use of a simplistic model for the geometry of these isolated pores. Nevertheless, the estimate of the density of isolated pores shows that these are a factor of three lower than the other pores. From Table (4.7) it is seen that in sample (1) the number of larger and smaller pores are respectively $7.64 \times 10^{10}/\text{cc}$ and $4.31 \times 10^{11}/\text{cc}$. From the contrast matched data the connected pores were found to be $2.84 \times 10^{10}/\text{cc}$ and $1.18 \times 10^{11}/\text{cc}$ respectively. Similarly for sample (2) the density of larger and smaller pores were found to be $9.85 \times 10^{10}/\text{cc}$ and $3.31 \times 10^{11}/\text{cc}$ respectively while the connected pore concentrations were $6.21 \times 10^{10}/\text{cc}$ and $1.11 \times 10^{11}/\text{cc}$. It has thus been shown that the percentage of isolated pores decreases as the sintering temperature increases from 800°C to 1000°C .

Table 4.7. Parameters obtained by SASFIT of ceramic sintered at 800°C and loaded with a $\text{H}_2\text{O}-\text{D}_2\text{O}$ mixture (DH signifies D_2O and H_2O).

Ceramic sintered	Pore radius (nm)		No. of scattering centres		Fractal dimension 'd'
	Lower Q 0.0028-0.037 nm^{-1}	Higher Q 0.042-0.15 nm^{-1}	n_1 (per cc) lower Q	n_2 (per cc) higher Q	
1- 800°C -2hr	168 ± 15	33 ± 2	7.64×10^{10}	4.31×10^{11}	2.88
1- 800°C - 2hr+DH	166 ± 14	34 ± 3	4.80×10^{10}	3.13×10^{11}	2.96
2- 1000°C -2hr	166 ± 16	33 ± 3	9.85×10^{10}	3.31×10^{11}	2.90
2- 1000°C - 2hr+DH	166 ± 12	35 ± 3	3.64×10^{10}	2.20×10^{11}	2.53

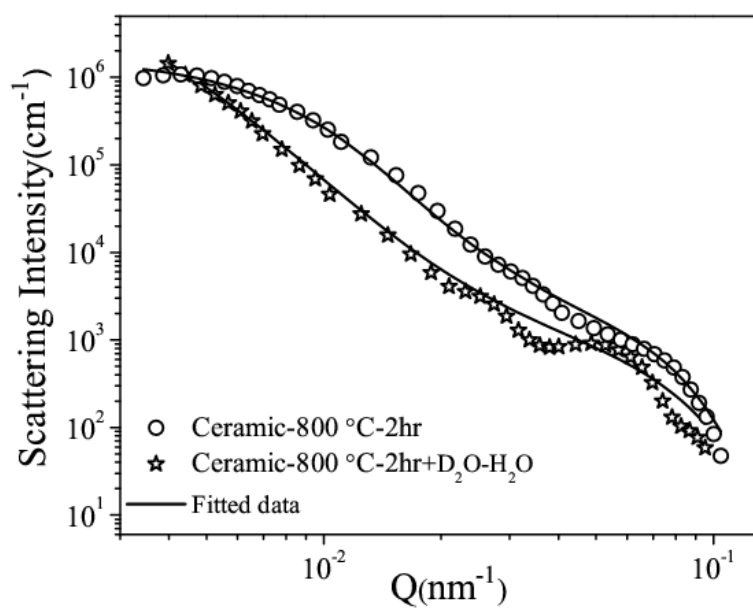


Figure 4.13. Scattering profile of ceramic sintered at 800 °C and loaded with a H₂O-D₂O mixture. Continuous line shows the fitted data. (Errors are within the size range of symbol)

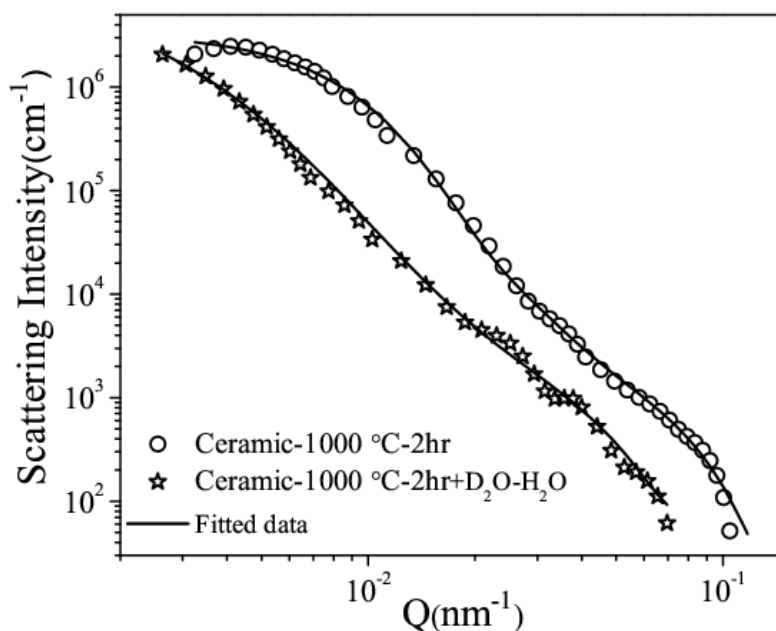


Figure 4.14. Scattering profile of ceramic sintered at 1000 °C and loaded with a H₂O- D₂O mixture. Line shows the fitted data.

4.2.6. Pore size distribution by Mercury Intrusion Porosimetry

Pore size distribution of the ceramic compacts sintered at 800 °C and 1000 °C were obtained by A PASCAL 440 Series of Thermo Scientific, Mercury Intrusion Porosimeter at Glass and Advanced Ceramic Division at BARC, Mumbai.

Mercury Porosimetry is based on the law of capillary action that governs / controls the penetration of liquids in small pores. The physical parameter measured in mercury porosimetry is the volume penetrated by mercury at a given pressure. The angle of contact for mercury with glass is 141.3 °. The diameter of cylindrical pores was calculated from Equation (3.5). Average pore diameter obtained at lower sintering temperature is 228 nm and at higher sintering temperature was 124 nm. The pore size distribution obtained is as shown in Figure (4.15).

4.2.7. Micro-pore structure by Scanning Electron Microscopy

Scanning electron microscopy shows the microstructure to undergo appreciable coalescence of micrometric ceramic particles for sintering temperature and pressure changes. Morphological characterization of the compacts regarding the surface modifications that occurred during sintering of compacts at 800 °C and 1000 °C for 2 hours was observed by SEM micrographs and is shown in Figure (4.16). It is seen that the ceramic compact fired at 800 °C is highly porous. As the sintering temperature is increased to 1000 °C, it is observed that the ceramic structure coalesces while reducing its porosity. EDX data shows that as the sintering temperature changes from 800 °C to 1000 °C there is almost no change in weight percentage of constituents. Pore sizes obtained were in the range 0.4 μm to 2.3 μm.

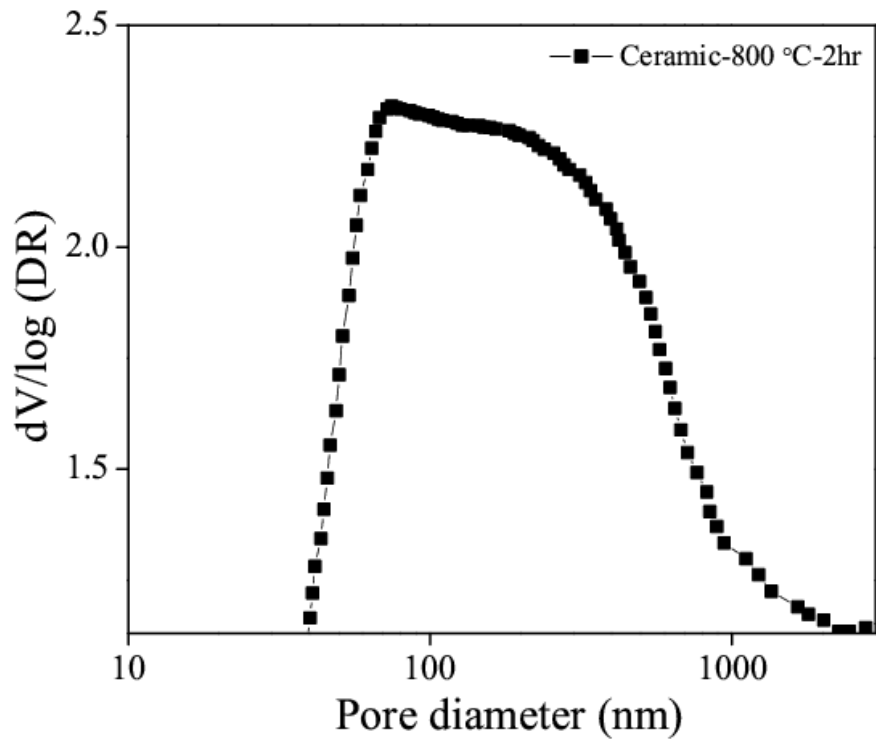


Figure 4.15. Resulting pore size distribution of porous ceramic sintered at 800 °C for 2 hour.

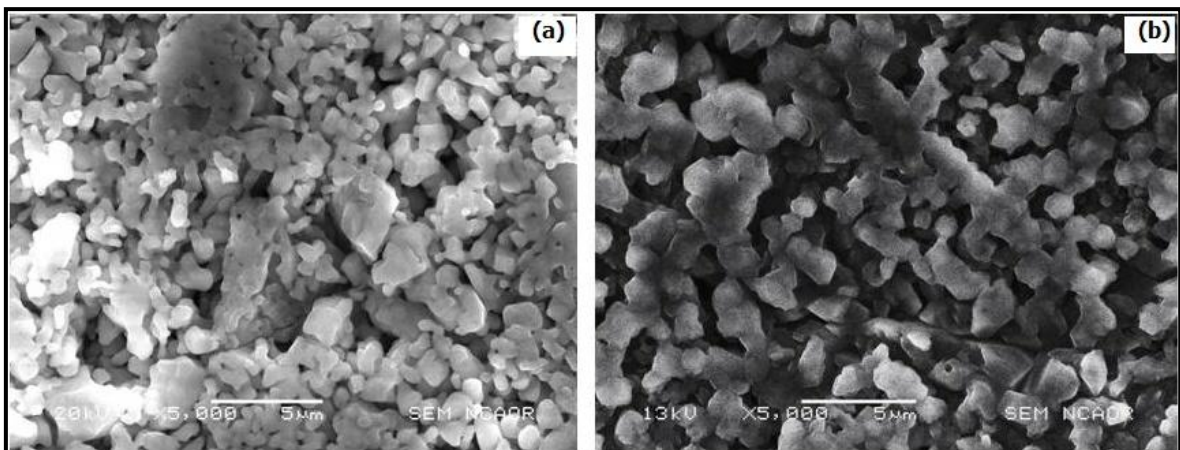


Figure 4.16. SEM micrographs of ceramic compact sintered at (a) 800 °C for 2 hours (5000X) b) 1000 °C (5000X) for 2 hr.

Table 4.8. EDX analysis of ceramic compacts sintered at 800 °C and 1000 °C for 2 hours.

Element	Weight% (800 °C)	Weight% (1000 °C)	Occuring in
Carbon	10.06	10.72	CO ₂
Sodium	16.90	16.56	Na ₂ O
Magnesium	0.01	0.01	MgO
Aluminium	0.10	0.07	Al ₂ O ₃
Silicon	13.94	13.94	SiO ₂
Calcium	7.31	6.27	CaO
Zinc	0.08	0.02	ZnO
Oxygen	51.06	52.41	All compounds
Total	100	100	

4.2.8. Summary of temperature on porosity of rice husk silica

The ceramic has been found to have a hierarchical range of pore sizes spanning over from micrometric to nano-metric dimension. From bulk density measurements, porosities (due mainly to accessible or connected macroscopic pores) of the compacted and sintered ceramics (at 800 °C and 1000 °C) vary between 42 % and 32 %. Scanning electron microscopy has shown pores of micron sizes ranging from ~ 0.4 to 2.3 μm. The particles have also been seen to coalesce at higher temperatures giving rise to reduction of pore concentration especially the larger ones and a decrease in numbers of isolated pores. Small angle neutron scattering measurements data showed a good intensity of scattering indicating the presence of nano-sized scattering centres. Further, fits to the SANS data to spherical scattering centres give 166 nm and 32 nm as the individual size with 130 nm as the aggregate size having a fractal dimension of 2.87. The high fractal dimensions of these materials in the nano-metric range coupled with the fact that these pores admit water indicates that there are relatively small numbers of such pores with good connectivity to each other. Isolated pores were estimated - to a first approximation - by loading the compacts with an adequate combination of H₂O and D₂O to obtain the contrast match. The number of isolated pores, of larger and smaller sizes for sintered compacts at 800 °C and 1000 °C were estimated to be ~ 4.80 x 10¹⁰ and 3.13 x 10¹¹; 3.64 x 10¹⁰ and 2.20 x 10¹¹ respectively. Thus, the percentage of isolated pores was found to decrease with sintering temperature.

4.3. Effect of compaction pressure on pore morphology

4.3.1. Introduction

In order to probe the evolution of its hierarchical mesoscopic and microscopic porous structure and tailor the pore size distribution the ceramic powder was also

compacted at different pressures (2T, 4T and 6T) and sintered at 800 °C for 4 hr. The porosity variations were studied by density measurement. Pore structure was obtained by SEM and SANS technique.

4.3.2. Density and Porosity by water displacement method

Samples were compacted at different pressures ranging from 1 to 6T and sintered at temperatures of 800 °C for 2 hours. The difference between geometric density and density by water displacement method gave fractional macroscopic porosities in the range of 47 % to 37 %. The variation of porosity with pressure is shown in Figure (4.17). It is clear that porosity due to accessible pores decreases with increasing compaction pressure though at different rates. This finding is in line with the results of the sintering temperature measurements. As expected, densification of the porous ceramic increases with pressure. The porosity obtained is shown in Table (4.9).

Table 4.9. Density, Porosity and neutron scattering length density of ceramic compacts compacted at different pressures.

Sample specification	Geometric Density (g.cm ⁻³) ± 0.005	Density water displacement (g.cm ⁻³) ± 0.0003	Porosity (Fraction of accessible pores) %	Scattering length density cm ⁻²
Ceramic-800 °C-1T	1.252	2.3821	47	3.275 x 10 ¹⁰
Ceramic-800 °C-2T	1.349	2.3093	41	3.175 x 10 ¹⁰
Ceramic-800 °C-4T	1.388	2.3278	40	3.200 x 10 ¹⁰
Ceramic-800 °C-6T	1.433	2.3104	37	3.176 x 10 ¹⁰

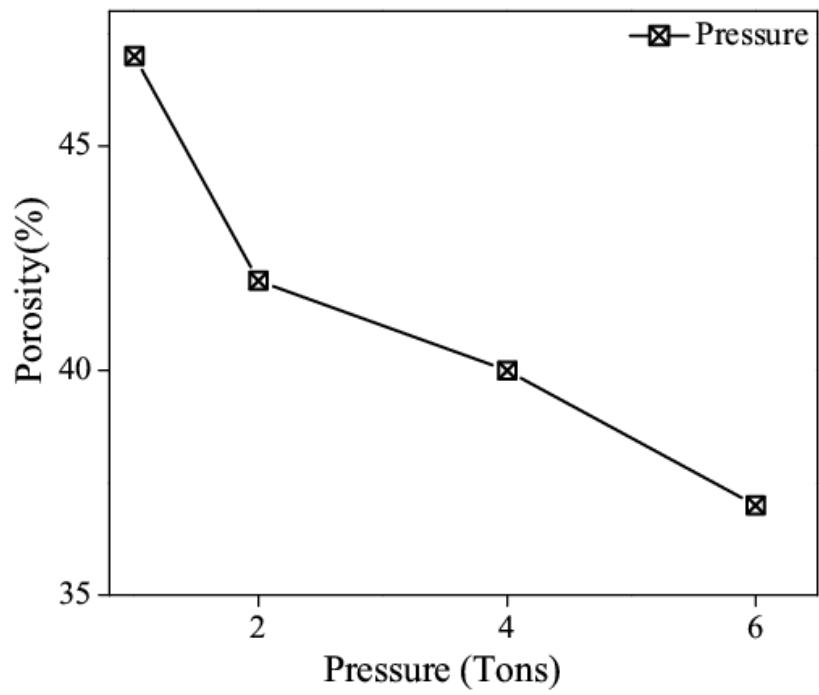


Figure 4.17. Variation of porosity of RHS ceramic with compaction pressure.

4.3.3. Effect of pressure on nanoporous structure by MSANS

The samples listed in Table (4.9) which were prepared under different compaction pressures were examined for their nanoporous structures by MSANS. The data are shown in Figure (4.18). A spherical pore model using the SASFIT programme applied to these data yielded a bimodal distribution with parameters shown in Table (4.10).

It is noted that while there were no significant effects of temperature on pore structure, the same is not true for the effect of pressure on these structures. It is seen that as the compaction pressure increases from 1T to 6T, the size of pores both at the lower and higher Q regions of the SANS data decrease by approximately 10 % of their values at the lower pressure - as qualitatively expected.

Table 4.10. Parameters' obtained from analysis for ceramic compacted at 1,4 and 6 T

Sample specification	Pore radius (nm)		No. of scattering centres		Fractal dimension 'd'
	Lower Q 0.0028-0.037 nm ⁻¹	Higher Q 0.042-0.15 nm ⁻¹	n ₁ (per cc) lower Q	n ₂ (per cc) higher Q	
Ceramic-800°C-1T	170 ± 14	30 ± 3	5.42 x 10 ¹⁰	4.45x 10 ¹¹	2.92
Ceramic-800°C-4T	164 ± 13	26 ± 2	6.89x10 ¹⁰	5.51x10 ¹¹	2.95
Ceramic-800°C-6T	156 ± 10	24 ± 2	8.54x10 ¹⁰	4.33x10 ¹¹	2.97

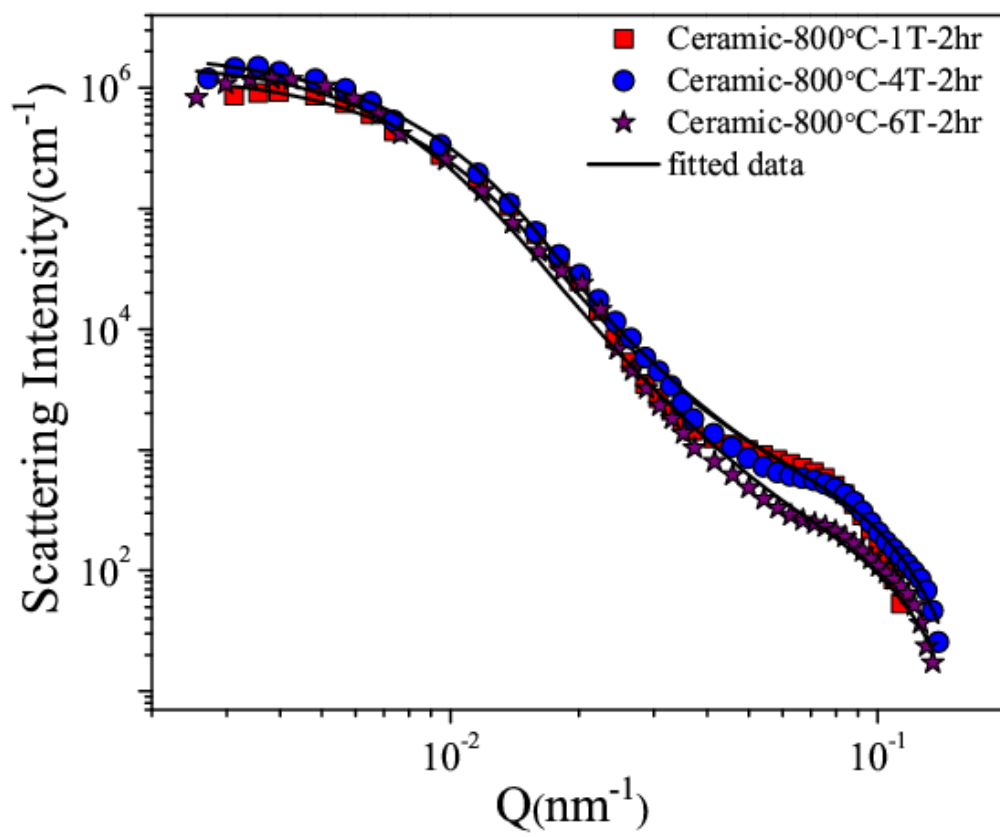


Figure 4.18. MSANS data on porous ceramic compacted at different pressures (solid line is the fit of the model to the data).

4.3.4. Micro-pore structure at different pressures by SEM

Scanning electron micrographs were obtained on the compacts sintered at different pressures and temperatures 800 °C to check their effect on micro porosity. Figure (4.16) shows Scanning Electron Micrographs of ceramic compacts fired at 800°C and 1000°C for 2 hours. In the resolution of these micrographs, the average pore size is found to be less than 0.5 µm. For a given sintering temperature, increase in the sintering time causes the particles to progressively coalesce, with average pore size increasing from 0.7 µm to 1.5 µm. On the other hand, as the compaction pressure increases - for a sintering temperature of 800 °C - from 1T to 6T the SEM shows that particles coalesce forming larger pores. The reduction of accessible pores means that the re-organization of particles due to pressure and temperature conditions causes larger macroscopic pores to form while causing many porous channels to be sealed off or become isolated (Figure 4.19).

4.3.5. Summary of effect of pressure on porosity of rice husk silica

Accessible porosity of ceramic compacted at different pressures and then sintered is decreased with compaction pressure. The decrease in porosity is due to densification and sintering. Although there is not much change in pore size at larger length scale, there is an appreciable decrease in pore size in the smaller or nano-metric length scale. The particle coalescence is confirmed by Scanning Electron Microscopy.

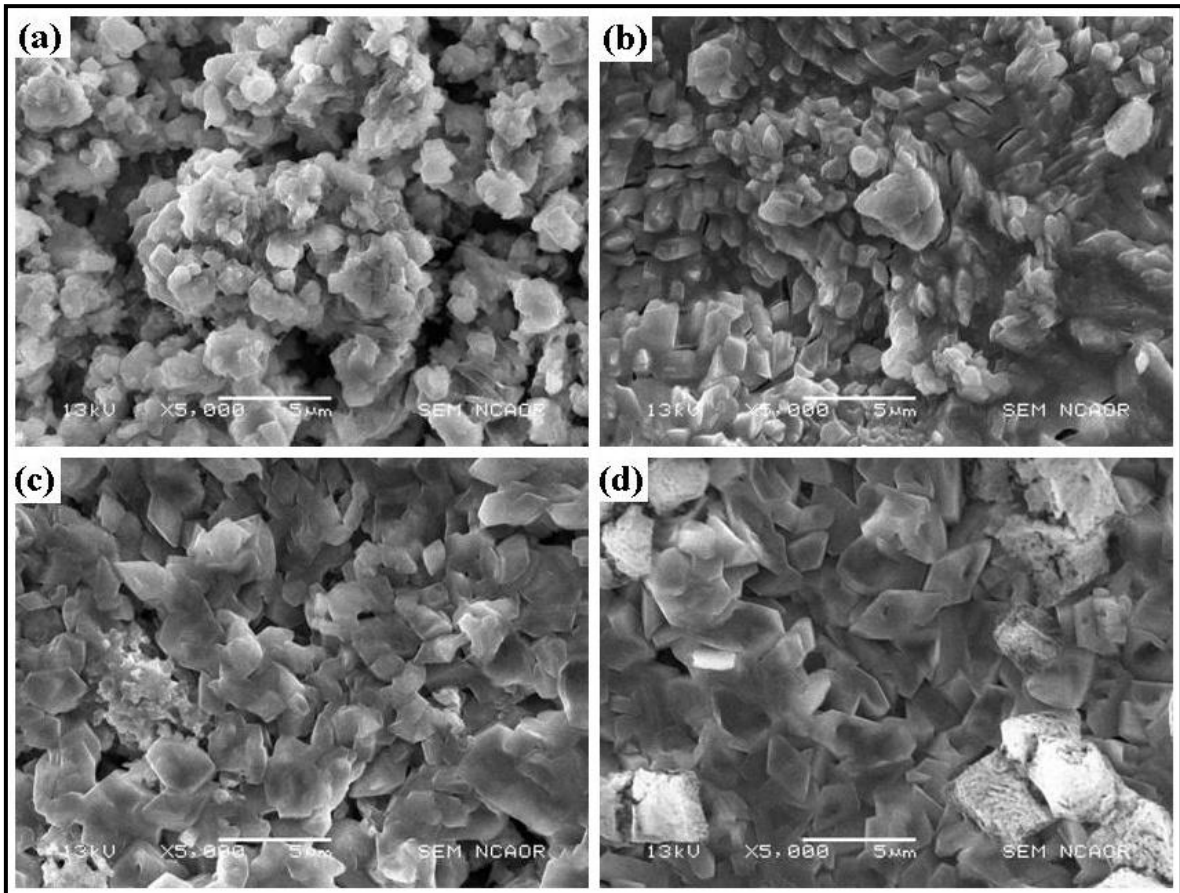


Figure 4.19. SEM micrographs of ceramic compact sintered at (a) 800 °C for 2 hours and compacted at (a) 1T, (b) 2T, (c) 4T, (d) 6T (5,000X).

4.4. Conclusions of Studies on Rice Husk Silica Ceramic

A porous ceramic has been synthesized from rice husk as the starting material. X-ray diffraction has shown a glassy-ceramic phase at lower temperatures to give way to a purely crystalline phase at 1000 °C. The ceramic has been found to have a hierarchical range of pore sizes - from macroscopic to nanometric dimension. From bulk density measurements, porosities (due mainly to macroscopic pores) of the compacted and sintered ceramics (at 800 and 1000 °C) vary from 32 % to 47 %. Existence of micrometric (~ 0.5 μm to 2.5 μm) pores is evident from SEM which shows that in this range, pore size increases with sintering temperature. These pores coalesce under sintering at the higher compaction pressure causing the number of bigger pores to diminish.

USANS on all the dry ceramics has shown the presence of two pore size domains of ~ 166 nm and 32 nm where smaller pores are arranged in mass fractal morphology having a fractal dimension between 2.80 to 2.97. For different sintering temperatures, the pore densities of the larger and smaller sized pores were found to be 1.3 to $1.9 \times 10^{10}/\text{cc}$ and 1.5 to $10 \times 10^{11}/\text{cc}$ respectively. For different compaction pressures the variation of pore sizes was 5.4 to $8.5 \times 10^{10}/\text{cc}$ for the larger pores and 4.3 to $5.5 \times 10^{11}/\text{cc}$ for the smaller pores. Heavy water absorbed by the ceramic is found to percolate evenly into the nano-sized pores without appreciably changing their morphology. The high fractal dimensions of these materials in the nano-metric range coupled with the fact that these pores admit water indicates that there is good connectivity to each other.

The method of contrast matching has yielded estimates of bimodal distributions of isolated pores which decreased in number as the sintering temperature increased from 800 to 1000 °C. For the 800 °C sintered sample the decrease was 2.8×10^{10} while for the 1000 °C sintered sample the number decreased by a factor of 3.

Chapter 5

Porosity Studies of Sintered Glass Microspheres

5.1. Preparation and porosity of a porous glass

5.1.1. Introduction

Porous glasses are important materials in a wide variety of different applications such as filters for fluids, building materials, insulation in electrical equipment, containers, etc. Due to their controlled porosity and insulating property they are also used in applications such as thermal insulators, substrates for catalysts [Matamoros et. al., 2002]. Microporous materials with nanometer size pore diameter are of interest, because of their material characteristics such as large internal surface area, unique pore structure, adsorption capacity and catalytic activity. Macroporous materials with pore diameter more than 30 nm have been reported using polystyrene latex spheres in colloidal solution. Formation of porosity on two or three different length scales in an ordered fashion with interconnectivity between the pores and with hierarchical structure would be advantageous for a variety of applications. In the present study the sintering process is used to prepare porous glass from microspheres of silica [Carrasco M.F., 2005]. In such a process there is softening of the glass, relative re-arrangement of the microspheres to obtain complex geometrical pore shapes and a denser sintered product. The complexity of these porous structures is such that only average bulk parameters relating to the pores may be reliably obtained. The resultant porosity has been studied here by several techniques including bulk density, Mercury Intrusion Porosimetry, Scanning Electron Microscopy and Small Angle Neutron Scattering. The compacts of silica microspheres were formed using polyethylene glycol as the initial compacting agent. Silica microspheres of two sizes; 100 and 20 μm

were used in the study. Bulk properties depend on the method of compaction and the sintering temperature and time [Savitha C., 1995]. Thermogravimetric method was used to study fractional mass loss through these compacts at constant temperature.

5.1.2. Preparation of porous glass from microspheres and their characterizations

Silica microsphere manufactured by Potters- Ballotini S.A were sieved in the size range 90-106 μm and 10-20 μm . The elemental composition of the microspheres was determined by Energy dispersive spectroscopy and is given in Table (5.1).

Table 5.1. Elemental composition of silica microspheres.

Element	Composition in Weight %
Carbon	8.90
Sodium	5.86
Magnesium	1.72
Aluminium	0.93
Silicon	23.42
Potassium	0.12
Calcium	3.19
Iron	0.12
Oxygen	55.74
Total	100

Porous glass compacts were prepared according to the following schedule [Carrasco M.F., 2005].:

1. Coating of microsphere with a binder to achieve compaction. The compacts were made using 85 wt % of microspheres mixed with 15 wt % polyethylene glycol (PEG)

as a binder. The mixture was diluted with 10 ml absolute alcohol and dried in the oven at temperature 60 °C for 24 hours.

2. In the second step the dried mixture was weighed out as ~550 mg placed inside mould of 13 mm diameter and pressed under a pressure of 2T for approximately 2 min. The pellets were placed on an alumina plate with Al₂O₃ powder loosely spread on the surface.
3. In the third step the compacts were subjected to thermal treatment. The binder is removed by placing compacts at 340 °C for 30 minutes. To give mechanical strength to the compact the temperature was raised to 640°C and compacts were sintered at this temperature for various sintering times; 3, 6, and 24 hours. The temperature of one compact was raised to 740 °C for 3 hours. The compacts were cooled slowly within the furnace to room temperature to avoid stress in the glass. Finally the porous compacts were washed with deionised water and dried at 50 °C. The sintered compacts are as shown in Figure (5.1).

5.2. Measurements and Discussion

5.2.1. Optical microscopy

When these compacts were observed in reflection with an optical microscope (LYNX at 40X) it was observed that the size of pore decreased with increasing sintering time. For lower sintering times, the pore connectivity was well defined two dimensionally. However, in the case of compacts treated at a temperatures of 740 °C it was observed that the spheres were fused with the pores not being clearly visible. The compact appeared to fuse into a bulk glass. The optical picture of a compact sintered at 640 °C fired for 6 hours is shown in Figure (5.2).



Figure 5.1. Porous glass compacts as prepared.

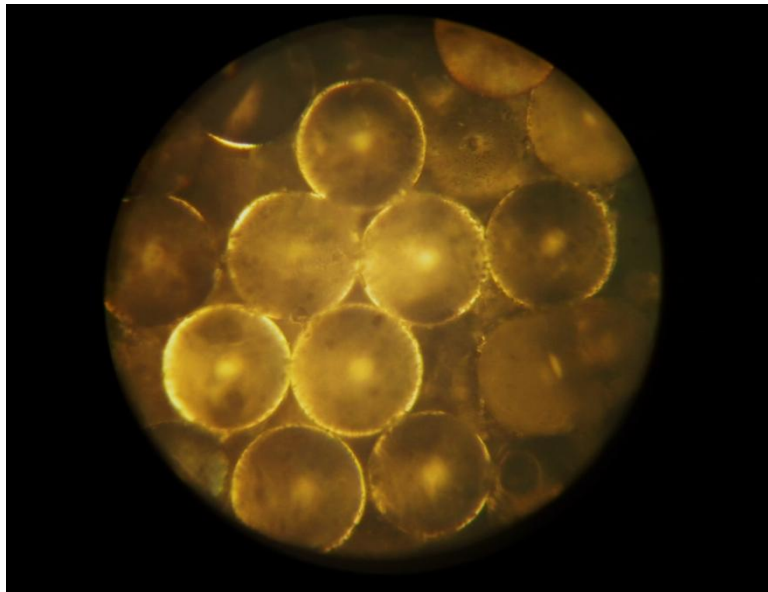


Figure 5.2. Optical image of microsphere compact sintered at 640 °C for 6 hours.

5.2.2. Density and porosity study of compacts

The important structural parameter in a porous media is its porosity (ϕ). The porosity of all the compacts was obtained by measuring the density of compact by its geometric and by water displacement method. The difference between these two values gave an estimate of the porosity. It is seen that there is a variation of porosity and density with sintering time. The linear shrinkage of the compact diameter was estimated after sintering as shown in Table (5.2).

Table 5.2. Density, Porosity and linear shrinkage of the microsphere (M) samples.

Sr. No	Sample details	Geometric density g/cc ± 0.005	Density by water displacement g/cc ± 0.0003	Porosity (%)	Linear Shrinkage (%)
1	M-20 μ m-640 °C-3hr	1.683	2.4791	32	4
2	M-20 μ m-640 °C-6hr	1.722	2.3340	26	7
3	M-20 μ m-640 °C-24hr	2.002	2.4531	18	14
4	M-100 μ m-640 °C-3hr	1.446	2.4636	41	1.4
5	M-100 μ m-640 °C-6hr	1.644	2.5007	34	3.5
6	M-100 μ m-640 °C-24hr	1.628	2.3488	30	4.1
7	M-100 μ m-740 °C-3hr	1.833	2.1954	16	6.3
8	M-100 μ m-640 °C-30hr	2.226	2.4050	7	11.5

An examination of Table (5.2) shows that there is a variation of density values obtained by both the methods that were employed. This indicates that there is a large number of open porosity which leads to flow of fluid through these compacts. It is observed that there is increase in geometric density with sintering temperature; this trend is not observed in density by water displacement method as shown in Figure (5.3). As the sintering time was increased from 3 hours to 24 hours, the density (by the water displacement method) decreases and subsequently increases. The increase in density for the 24 hours sintered compact is attributed to the fact that there may be smaller number of isolated or blind pores in this sample. The percentage linear shrinkage of diameter increases with sintering time for 20 μm and 100 μm . These observations taken together indicate that as the length of sintering time at a given temperature (640 °C) increases, the microspheres begin to move closer together in their bid to achieve lower energy configurations. This trend may be explained if microspheres move together as a function of sintering time. This is also supported by the SEM micrographs Figure (5.4) and (5.6). It is possible that the surfaces of the microspheres become slightly mobile at 640 °C and permit surface tension forces to cause relative movement over a period of several hours. It is also seen that the bulk porosity of compact decreases with sintering time and temperature.

5.2.3. Micro-pore morphology of the glass compacts

A JEOL Scanning Electron Microscope was used to compare the pore structures and the average number of immediate neighbours around each microsphere for the three different sintering times. The SEM micrographs for the compacts sintered at 640 °C for various sintering times and 740 °C for 3 hours are shown in Figures (5.4) to (5.8). It may be observed that as the sintering time increases, there is a tendency for the microspheres to

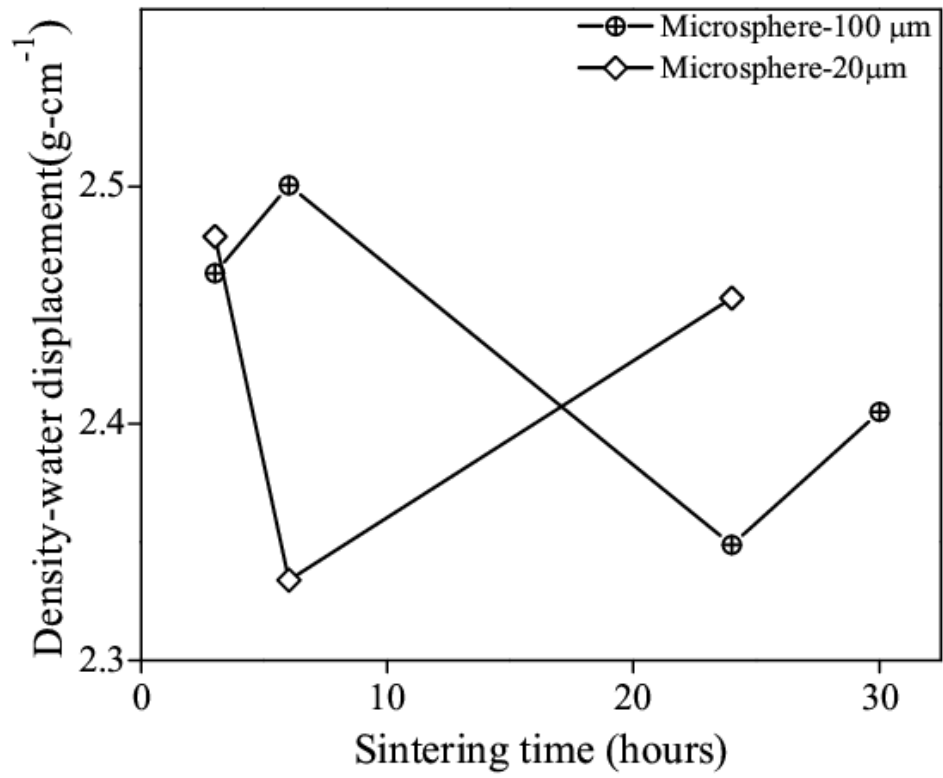


Figure 5.3. Variation of density (by water displacement method) of ceramic sintered at temperature 640 °C with sintering time.

agglomerate with their immediate neighbours and permit some pore sizes to increase while others to decrease. The process by which this happens has been outlined by [Shaw N. J., 1989] who considered the process of densification of ceramics during sintering. Thus for low sintering time the spheres just touch each other forming pores in the range 0.5 to 20 μm for the 20 μm size spheres and 20 to 100 μm for 100 μm size spheres compacted and sintered for 3 hours. The porous volumes that connect the larger pores have been assumed - for the sake of the model - to have cylindrical geometry while the larger pores were approximated as spheres. Although this amounts to simplification of the geometry of these porous spaces, the model serves as a first iteration. For the sample sintered for 30 hours, there appears to be melting of the microsphere surface and a consequent fusion of spheres as shown in Figure 5.6 (d). It is also noted that at shorter sintering times the spherical shape of microspheres is preserved, whereas at higher sintering time and temperature hexagonal close packing of the spheres affects their morphology. The morphology of the surface is similar to that of the interior of each compact as shown in Figure (5.8). A detailed view of microspheres in contact with each other forming a neck between them is given in Figure (5.9).

A simple 2-D scheme to represent the morphology of these compacts with changes in sintering time is shown in Figure (5.10). In this attempt, the larger porous volumes are represented as circles connected to neighboring pores with narrow passages (cylinders in three dimensions). Although this representation is limited to few micrographs, it may be noted that at the higher sintering times there are fewer number of spherical pore volumes but a larger number of interconnecting passages. This is in agreement with the above observation that at higher sintering times the microspheres tend to agglomerate and coalesce causing fewer but interconnected pore volumes.

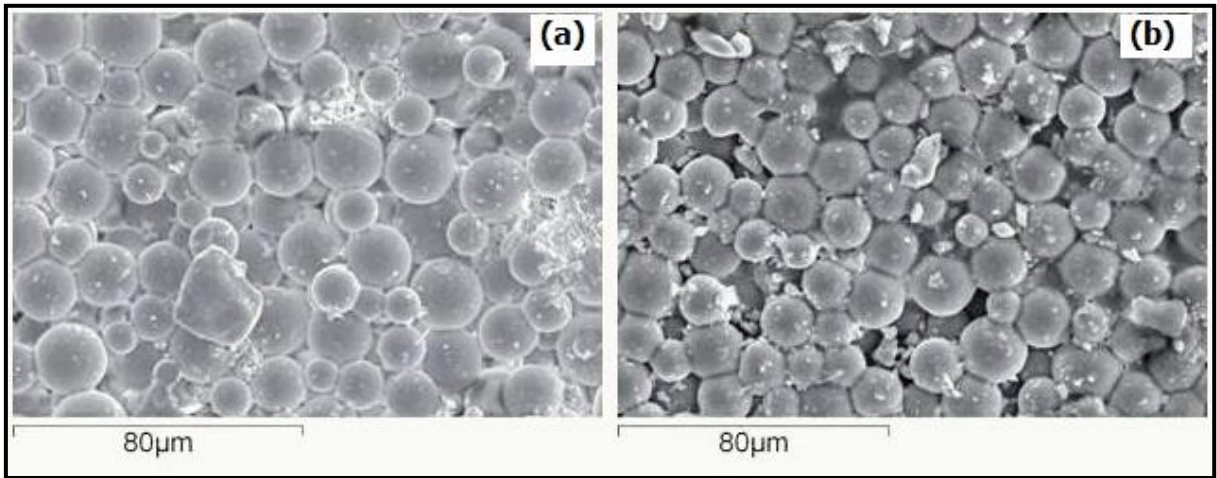


Figure 5.4. SEM micrograph of (a) 20 μm microsphere sintered at 640 $^{\circ}\text{C}$ for 3 hr (800X),
(b) 20 μm microsphere sintered at 640 $^{\circ}\text{C}$ for 6 hr (750 X).

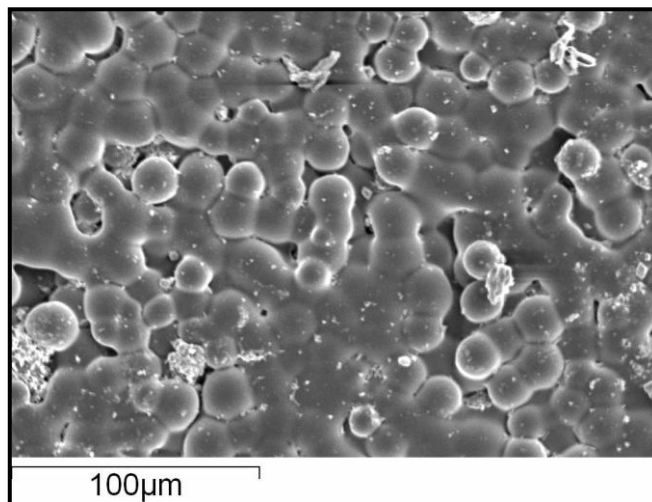


Figure 5.5. SEM micrograph of 20 μm microsphere sintered at 740 $^{\circ}\text{C}$ for 1 hr (500X).

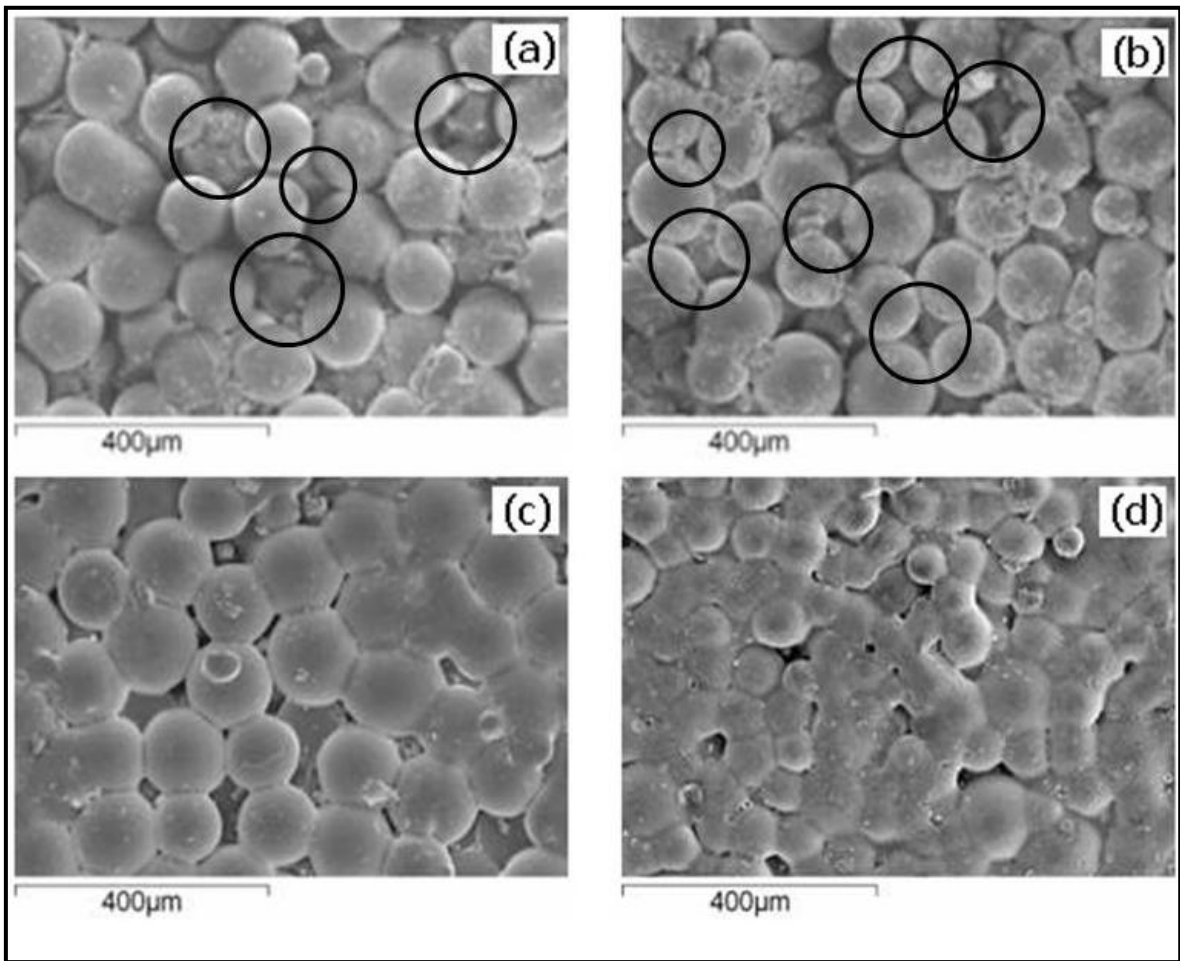


Figure 5.6. SEM micrograph at 150X of (a) 100 μm microsphere sintered at 640 $^{\circ}\text{C}$ for 3 hr, (b) 100 μm microsphere sintered at 640 $^{\circ}\text{C}$ for 6 hr, (c) 100 μm microsphere sintered at 640 $^{\circ}\text{C}$ for 24 hr , (d) 100 μm microsphere sintered at 640 $^{\circ}\text{C}$ for 30 hr .

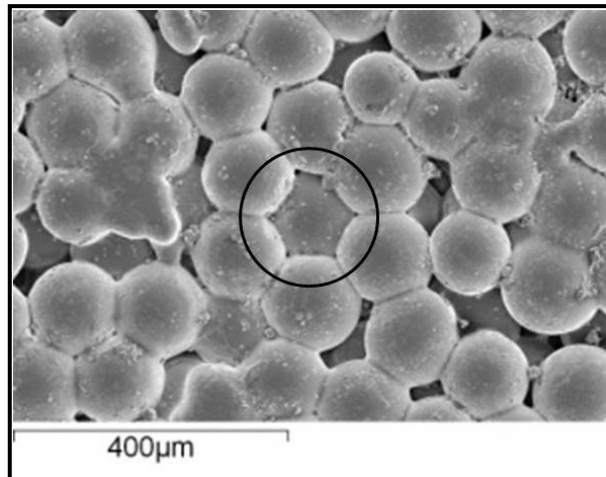


Figure 5.7. 100 μm microsphere sintered at 740 °C for 3 hr (150 X).

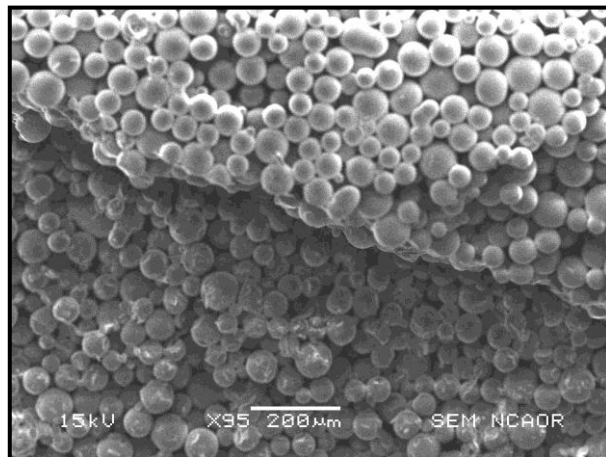


Figure 5.8. Internal structure of 100 μm microsphere sintered at 640 °C for 6 hr (95X).

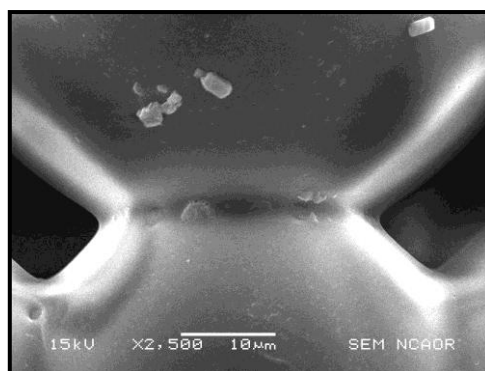


Figure 5.9. Neck development when two spheres touch each other.

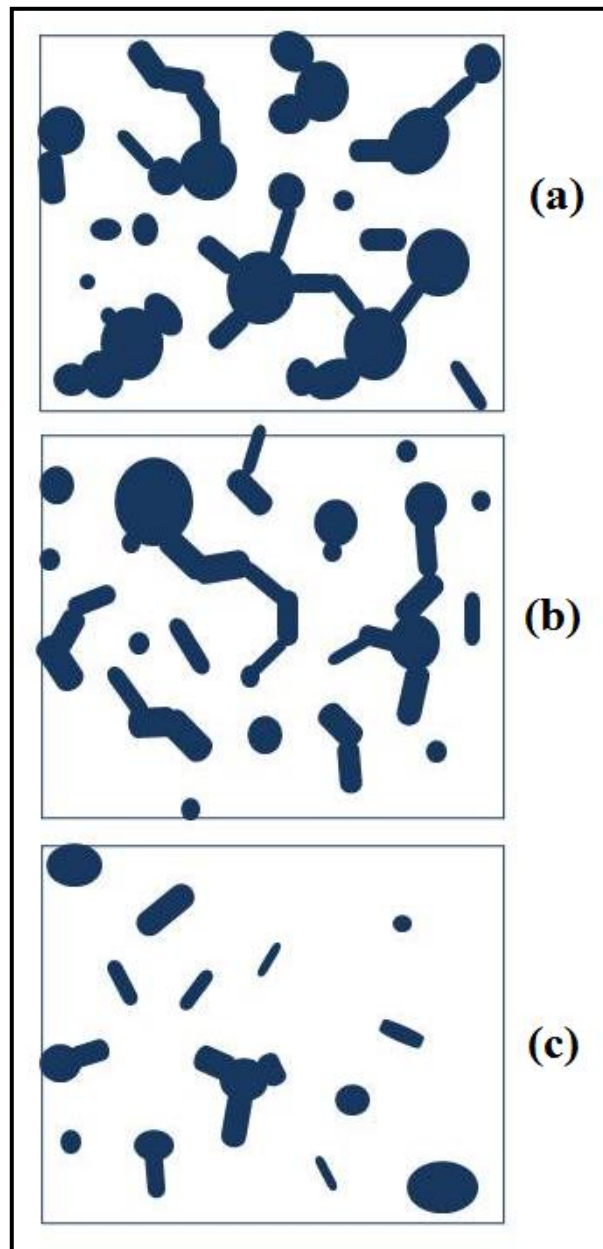


Figure 5.10. Schematic of decrease in pore size and the number of pores with increase in sintering time (a) 3 hour, (b) 6 hour and (c) 24 hour.

5.2.4. Pore morphology by Mercury Intrusion Porosimetry

The most common methods of obtaining pore size distribution are Nitrogen Adsorption and Mercury Intrusion Porosimetry. Only the later method was used for these microsphere compacts. A PASCAL 440 Series of Thermo Scientific was used for nano pore size distribution in the porous glass compact sintered at 640 °C for 3 hours and 24 hours and Quantachrome Pore Master Model was used to obtaining micro pore size distribution of the compact fired at 640 °C for 3 hours. The results obtained by this method are sometimes not in agreement with the data from SANS as porosimetry considers all volumes from macro to micro to confirm to a particular model of pore shape. SANS data on the other deals exclusively with the nanoporous regime and is confined to models of pore shape and size only of nano dimensions.

The pore size distributions obtained for the compacts sintered at 640 °C for 3 hours and 24 hours are shown in Figures (5.11) and (5.12). The distribution function in the figure is defined as $[-(dV/d \log D)]$, where V is the specific pore volume i:e volume of a unit mass of the compact. The area under the curve in a pore size range is related to the volume of pores in that range. A bimodal distribution of pore sizes was obtained for both sizes. The smaller- sized distribution of pores have a maximum of 40 nm for the sample sintered for 3 hours while for the sample sintered for 24 hours the maximum occurs at 19 nm. The larger sized distribution peaks at approximately 70 nm for both samples.

Similarly the average pore size for compact - fired at 640 °C for 3hr in the micrometer range gives a monomodal distribution having an average pore size of 29 μm as shown in Figure (5.13). Although the mercury intrusion method gives the diameters of equivalent cylindrical pores, SEM reveals that the pores likely are a composite of fractal-like volumes.

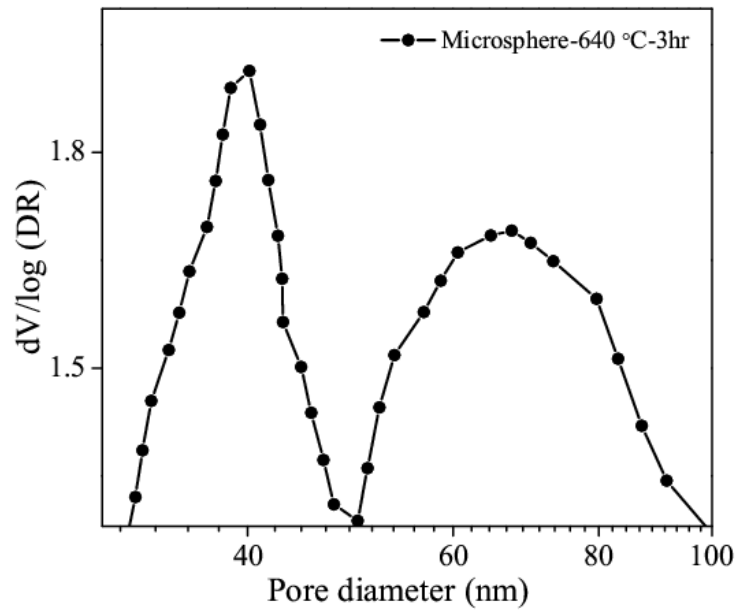


Figure 5.11. Pore size distribution of porous glass sintered at 640 °C for 3 hours.

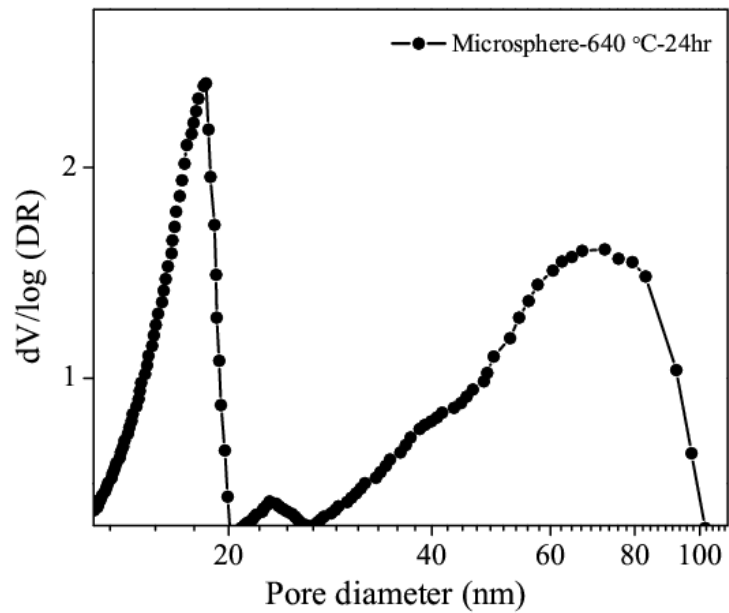


Figure 5.12. Pore size distribution of porous glass sintered at 640 °C for 24 hours.

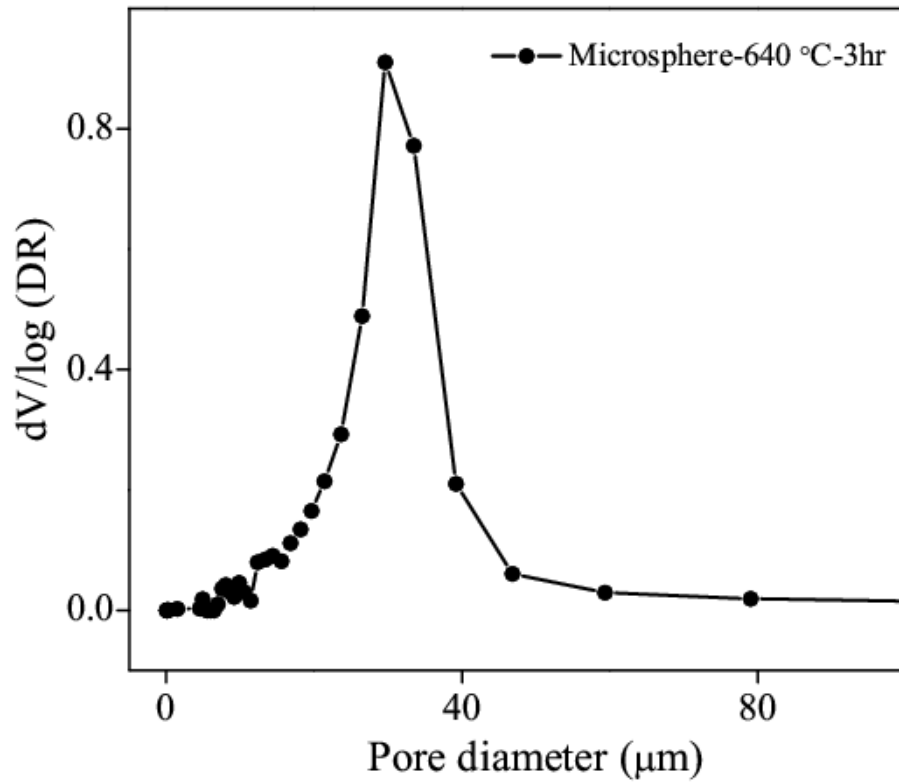


Figure 5.13. Pore size distribution as measured by mercury intrusion method; temperature 640 °C for 3hours.

5.2.5. Neutron scattering study of pores in glass compact

Small Angle Neutron Scattering measurements were performed on samples with a medium resolution instrument which has a double-crystal arrangement. The accessible Q (wave vector transfer) range was 0.003 nm^{-1} to 0.173 nm^{-1} with an incident wavelength of 0.312 nm . The porous compacts of thickness 2 mm and diameter 13 mm were used in the study. The measured data were corrected for background, transmission and resolution broadening.

The scattered beam in a SANS measurement arises on account of scattering length density contrast between pores and microspheres in a given compact. Thus the scattering centers are effectively porous volumes in a sample whose sizes and shapes are indirectly obtained through model fitting of the scattered intensity data. The form and the magnitude of scattered intensity $I(Q)$ is a function of porosity, pore size, matrix density and elemental composition. The slopes of I versus Q on a log plot varied from -3.0 to -3.4 (Figure 5.14) indicating complexity in the shapes of scattering centers or fractal-like scattering regions. The parameters obtained from USANS are due to the nanoporous volumes rather than the pores between the spheres which are of micron dimensions. The nano-sized scattering centers may be surface imperfections of the microspheres themselves and/or be the result of the process of compaction and sintering of the compacts. The process leading to the generation of these pores is at present not known. Decrease in overall intensity was observed in going from 3 to 24 hours sintering time. The fits to the SANS data were performed assuming only spherical geometry of pores and the parameters obtained are shown in Table (5.3) for $20 \text{ }\mu\text{m}$ diameter of microspheres and Table (5.4) for $100 \text{ }\mu\text{m}$ diameter of microspheres. From these data there appears to be a bimodal distribution of pore sizes. For $100 \text{ }\mu\text{m}$ diameter microspheres the distribution is in qualitative agreement

with the earlier mentioned mercury intrusion data. The maxima of these distributions, however, do not match but are nevertheless of comparable orders of magnitude. For the 20 μm microsphere compact data, a small interference maximum is observed at about 0.09 nm^{-1} (6 hours sintering) which shifts to a slightly lower Q value (0.0881 nm^{-1}) for a sintering time of 24 hours. This shift corresponds to inter-pore separations increasing from 66 nm to 71 nm as the sintering time increases from 6 to 24 hours. For the 100 μm microsphere compact sintered at $640 \text{ }^\circ\text{C}$ for 24 hours a small interference peak at $\sim 0.11 \text{ nm}^{-1}$ shifts to a lower value of 0.07 nm^{-1} for a compact sintered at higher temperature of $740 \text{ }^\circ\text{C}$ for 3 hours. This corresponds to an inter-pore separation increasing from 57 to 87 nm. Considering both these trends from Figures (5.14) and (5.15), it appears that as the microspheres move towards each other with increase in time or temperature, isolated pores have larger separations as compared to inter pore separations prior to isolated pores being formed.

A compact (100 μm sized microsphere) sintered for 6 hours was loaded with D_2O and subjected to SANS Figure (5.16). The decrease in intensity is due to the lower scattering length density contrast term caused by D_2O filling the pores. This indicates that the D_2O not only fills the micron sized pores but also occupies the pores of nano dimension.

Table 5.3. Parameters obtained from fitted data for 20 μm microsphere compact.

Sample Specification	Pore size nm	Polydispersity	Pore size nm	Polydispersity
Micro-20-640C-3hr	173	0.30	51	0.35
Micro-20-640C-6hr	180	0.36	52	0.35
Micro-20-640C-24hr	164	0.49	63	0.48

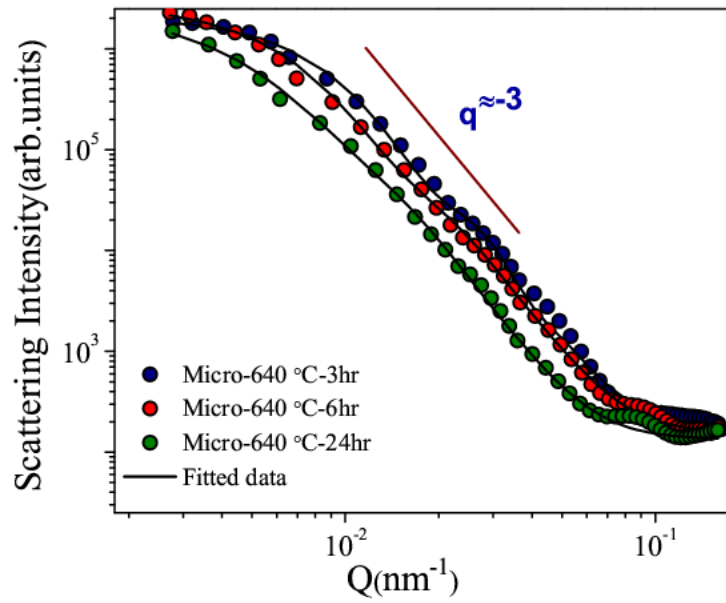


Figure 5.14. MSANS data of 20 μm sized microsphere compacts fired at 640°C from 3 to 24 hours (Errors are within the size range of symbol).

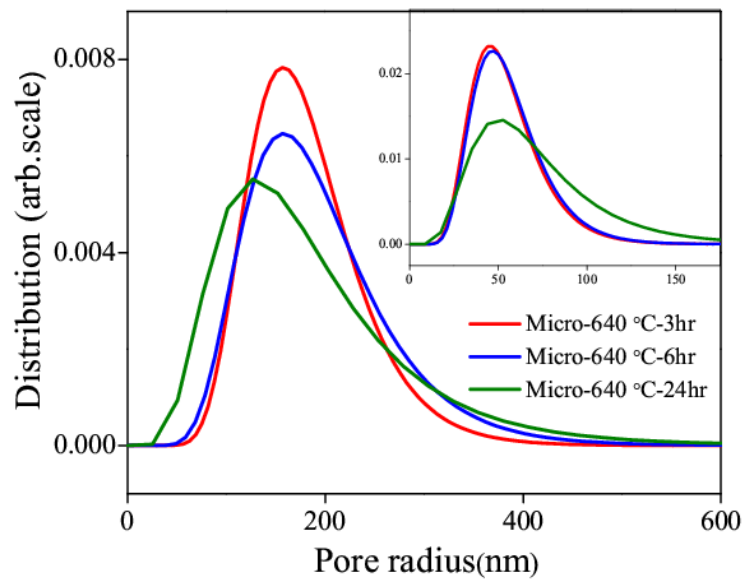


Figure 5.15. Pore size distribution of larger pores and smaller pores (insert) for compact of 20 μm microspheres.

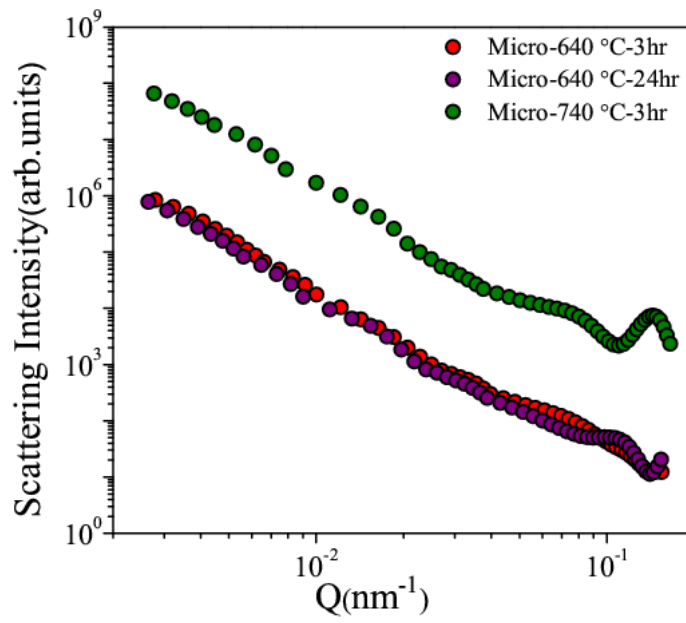


Figure 5.16. USANS data of 100 μm sized microsphere compacts fired at 640 $^{\circ}\text{C}$ from 3 and 24 hours and fired at 740 $^{\circ}\text{C}$ for 3 hours.

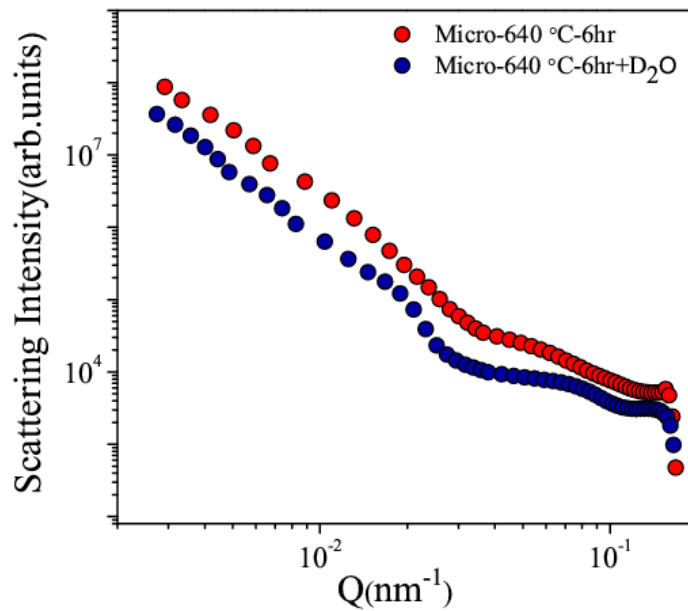


Figure 5.17. USANS data of 100 μm sized microsphere compacts fired at 640 $^{\circ}\text{C}$ for 6 hours and loaded with D_2O .

Table 5.4. Parameters obtained from fitted data for 100 μm microsphere compact.

Sample specification	Pore size nm	Poly dispersity	Pore size nm	Poly dispersity	Pore size nm	Poly dispersity
Micro-100-640 °C- 3hr	222	0.52	113	0.37	27	0.35
Micro-100-640 °C- 24hr	187	0.59	136	0.37	48	0.31

5.2.6. Estimation of isolated pores

Scattering in a compact is due to contrast between the pore and the matrix. The contribution to the scattering intensity from the dry porous compact is due to both connected as well as isolated pores. In order to obtain isolated pores [shown in section 4.2.5] the compact was loaded with the combination mixture of H_2O and D_2O . The scattering length density of the matrix was matched by loading the pores in the compact with a proper combination of H_2O and D_2O . In the experiments here, the relative concentration of H_2O and D_2O was chosen to nearly match the scattering from the matrix. Hence an estimate of the isolated pores was obtained - in principle - by contrast match experiment.

The scattering intensity for any a porous compact is given by:

$$I(Q) = K N(\rho_p - \rho_m)^2 V^2 P(Q) \quad (5.1)$$

Where, ρ_p = Scattering length density of pore.

ρ_m = Scattering length density of the matrix.

N = number density ; K = a constant

If $\rho_p \sim 0$ as when the pores are air filled:

$$I(Q) = K N(\rho_m)^2 V^2 P(Q) S(Q) \quad (5.2)$$

Thus, the total scattering intensity from a dry porous compact is given as

$$I_{meas} = I_{conn.pore} + I_{isola.pore} \quad (5.3)$$

$$I(Q)_{dry} = K [N(\rho_m)^2 V^2 P_1(Q) S_1(Q)]_{conne.} + K [N(\rho_m)^2 V^2 P_2(Q) S_2(Q)]_{iso.} \quad (5.4)$$

For the sample loaded with a fluid like D₂O, the intensity is given by:

$$I(Q)_{D_2O} = [N(\rho_{D_2O} - \rho_m)^2 V^2 P_1(Q) S_1(Q)]_{conne.} + [N(\rho_m)^2 V^2 P_2(Q) S_2(Q)]_{iso.} \quad (5.5)$$

When the scattering length density of the fluid loaded in a compact is matched with that of the scattering length density of the matrix by using a combination of D₂O and H₂O or any other liquid, then the contrast in the first term of Equation (5.5) tends to zero. Hence the contribution to the scattered intensity will now be from only the isolated pores.

$$I(Q)_{D_2O+H_2O} = [N(\rho_m)^2 V^2 P_2(Q) S_2(Q)]_{iso.} \quad (5.6)$$

Such a contrast matching experiment was performed using a mixture of H₂O and D₂O in a proportion to match the scattering length density of the matrix ($3.349 \times 10^{10} \text{ m}^{-2}$).

Figure 5.18 displays the scattering length density of the H₂O-D₂O mixture as a function of H₂O percentage in the mixture. For a value of scattering length density approximately equal to that of the matrix ($3.349 \times 10^{10} \text{ m}^{-2}$) the percentages of H₂O and D₂O were respectively 43.89 % and 56.11 %. For the experiment, the sample was first soaked in the mixture for 24 hours. The USANS measurement was made following this and the data are shown in Figure (5.19). Most of the scattering in this data set is from

isolated pores. In the dry compact, interference peaks are observed at 0.057 nm^{-1} and 0.095 nm^{-1} corresponding to separations between pores of 110 nm and 66 nm respectively. The SANS data with the included water mixture show these peaks to shift to values of $Q = 0.027 \text{ nm}^{-1}$ and 0.0714 nm^{-1} thereby increasing the distance of separation to 87 nm. Fitting the data from the dry compact to a model with hard sphere structure factor it was observed that the compacted glass has larger pores of radius $248 \pm 13 \text{ nm}$ with concentration of 3.096×10^{10} pores per unit volume. The model yielded smaller size pores of radius $49 \pm 3 \text{ nm}$ with a hard sphere volume fraction of 0.28 and 1.798×10^{11} pores per unit volume. Using the same model to fit the data from the compact loaded with the optimum water mixture yielded the larger pore density of 1.238×10^{10} and smaller size pore concentration of 5.58×10^{10} pores per unit volume. It may be noted that the numbers obtained in the latter fit to the scattering supposedly from isolated pores are only to be taken as first approximation fits. Difficulties with measurement of transmission factor for the loaded sample, effect of multiple scattering and the use of a simplistic model for the geometry of these isolated pores may all have contributed to the deviation of the fit from the measured data in the region 8×10^{-1} to $2 \times 10^{-2} \text{ \AA}^{-1}$. Nevertheless, the estimate of the density of isolated pores shows that these are ten times lower than the other pores.

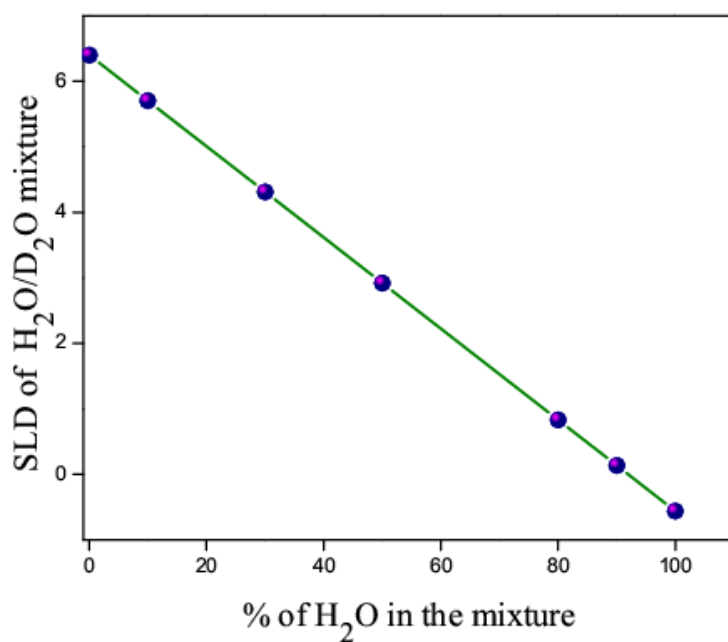


Figure 5.18. Scattering length density of the H₂O-D₂O mixture v/s % H₂O in the mixture.

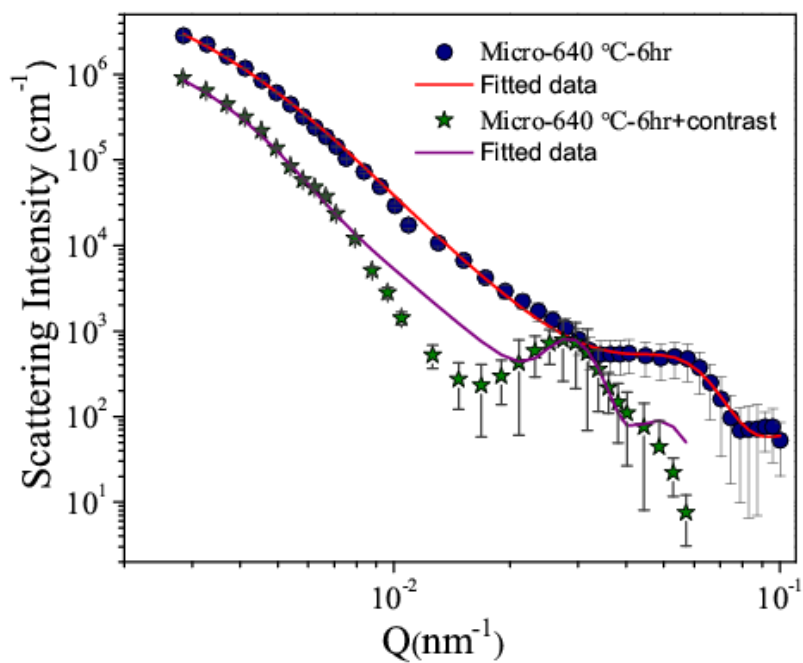


Figure 5.19. USANS data of 100 μm sized microsphere compacts fired at 640°C for 6 hours and loaded with a mixture of H₂O-D₂O.

5.3. Thermogravimetry of Microsphere Compacts

In order to better understand the interconnections of pores in these compacts, and to obtain an empirical model of fluid loss, the rate of evaporation of water from a known mass of sample was studied by thermogravimetry. The study of evaporation from nanopores is very important in the field of catalysis, oil extraction, mixture separation and pollution control [Lorenzo et al., 2010]. The gravimetric technique was used to obtain the rate of evaporation from microsphere compacts at temperatures 50 °C and 35 °C. These measurements (at CGCRI, Kolkata) were performed on microsphere compacts fired at 640 °C for 3 hours and 24 hours. Empirical fits to the mass loss data are relevant to applications of fluid retention and loss in these compacts. The rates of mass loss at two different constant temperatures; 35 °C and 50 °C for a compact sintered at 640 °C for 3 hours and loaded with H₂O were measured. From a 3rd order polynomial fit to the data, as shown in Figure (5.20), the rate of mass loss was 3.33282×10^{-4} and 6.13906×10^{-4} for 35 °C and 50 °C respectively. The rate of mass loss at 50 °C is almost double that at 35 °C indicating that there is faster evaporation from the pores as the temperature rises.

Fractional mass loss at various temperatures from this compact is shown in Figure (5.21). It can be seen that at lower temperatures the rate of loss is initially slower and reaches the expected asymptotic value as the complete mass loss takes place from the pores through their interconnections. At higher temperatures the saturation is attained rapidly. An exponential was fitted to the dehydration points (times at which the asymptotic values are first reached) at different temperatures Figure (5.22). The equation fitted to this data was:

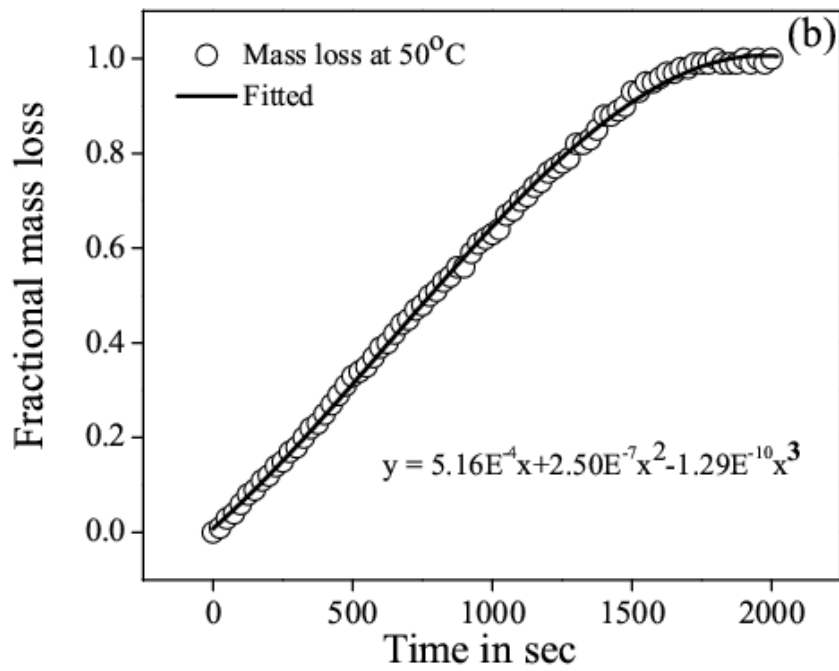
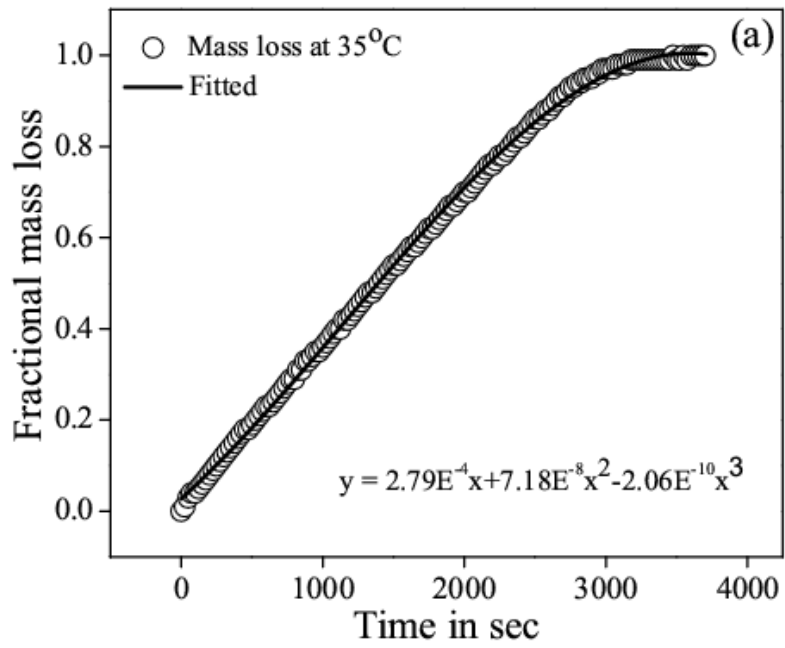


Figure 5.20. Plot of fractional mass loss at temperature (a) 35 °C (b) 50 °C fitted with a 3rd order polynomial.

$$Y = 33.5 + 126e^{-0.0016x} \quad (5.7)$$

Where Y represents the mass loss and X the time variable as the loss begins from the saturation value.

A similar fit to the data from the sample sintered at 24 hours gave:

$$Y = 42 + 136e^{-0.0006x} \quad (5.8)$$

The ratios of Equation (5.7) to (5.8) at the temperatures 75, 85, 95 and 105 °C yielded an average value of 0.45 ± 0.01 . The interpretation of this ratio is that the sample sintered for 3 hours losses all its absorbed water in a time that is 45% shorter than the time taken for the 24 hour sintered sample to dehydrate. Thus, it may be surmised that the sample that was sintered for a longer time had 45 % fewer interconnections to the surface. It is likely that this percentage of fewer connections also occurs in the bulk of the compact. Although the loss of interconnections was expected from a qualitative assessment, the quoted percentage loss is considerably higher than expected.

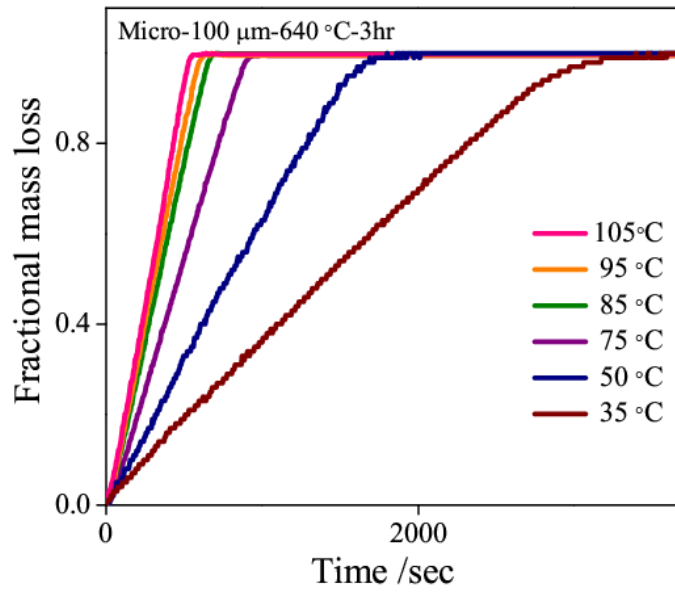


Figure 5.21. Fractional mass loss as a function of time from a compact fired at 640 °C for 3 hours at various temperatures.

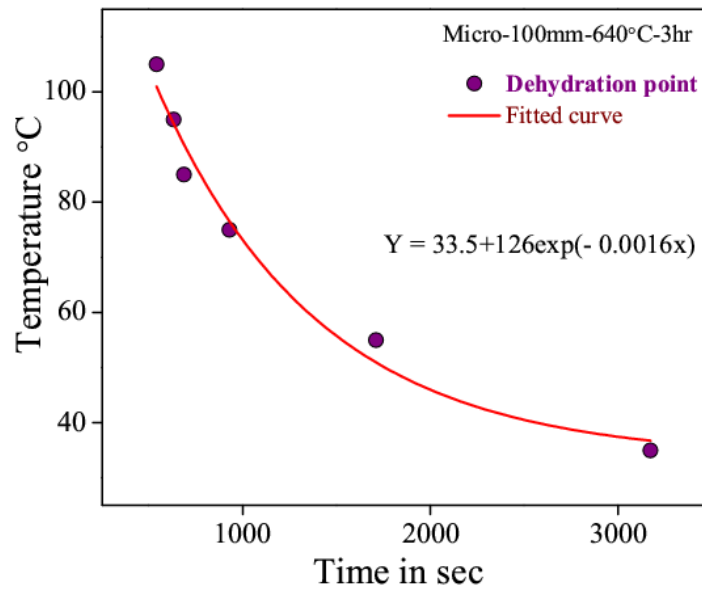


Figure 5.22. Temperature as a function of time for complete dehydration of the 3 hour sintered sample.

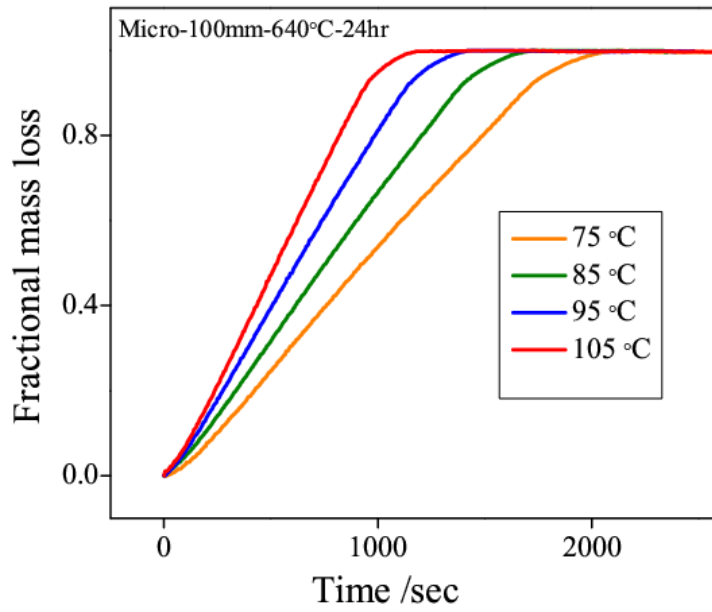


Figure 5.23. Fractional mass loss from a compact fired at 640 °C for 24 hours at various temperatures.

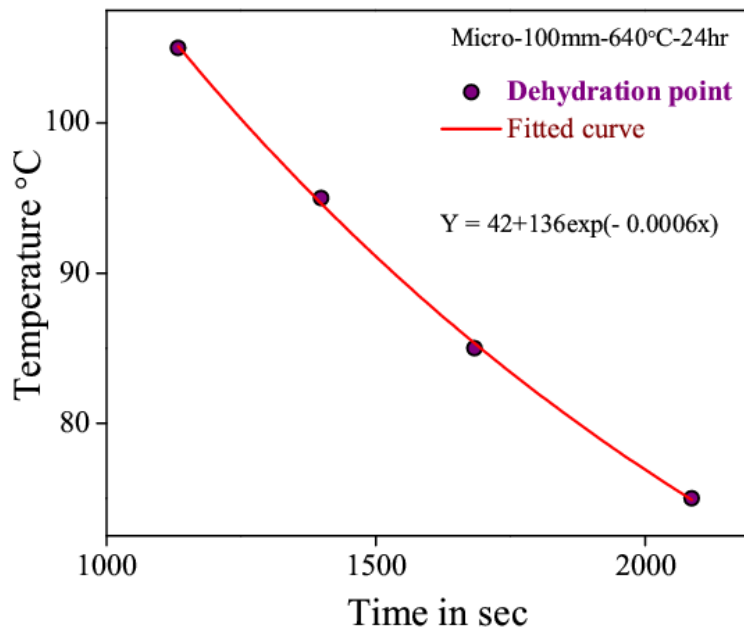


Figure 5.24. Temperature as a function of time for complete dehydration for the 24 hour sintered sample.

5.4. Conclusions of the porous glass study

Silica microspheres having diameters in the range of $5\mu - 20\mu$ and $106\mu - 110\mu$ have been compacted and sintered at $640\text{ }^{\circ}\text{C}$ for 6 to 24 hours to form porous yet rigid compacts. Density measurements of the compacts show a trend with sintering time which may be related to the process of densification of the compacts in which the microspheres move relative to each other. This gradual process leads to agglomeration of nearest-neighbour microspheres, causing the existing pores to become larger and possibly more interconnected. The latter is supported by SEM micrographs of the compacts sintered for 3, 6 and 24 hours. The porosities of these compacts varies from 32 % to 45 % of free volume. The compaction process leads to an arrangement of spheres which is modified during the sintering process in which the spheres come closer together forming a rigid body. The SEM micrographs show a variation of pore sizes of widths $2\mu - 20\mu$ and lengths of $2\mu - 60\mu$. As the sintering time is increased, the sphericity of microspheres is slightly altered from a sphere to a polyhedron depending on the number of neighboring spheres. The number of pores is also seen to reduce with sintering time as the spheres coalesce with each other. A bimodal distribution of pore size distribution was also obtained from MIP.

MSANS data indicate a fractal-like agglomerate structure within this compact from the power law behaviour of the scattered intensity over a wide wave vector transfer range. The connectivity of pores was studied by loading the compact with heavy water and studying its intensity pattern. Pores in the compact are interconnected with channels. The decrease in intensity due to the lower scattering length density contrast (caused by D_2O filling the pores) indicated that the D_2O not only fills the micron-sized pores but also occupies the pores of nano dimensions. These findings are of relevance in the separation and filtration applications. One of the unique features of SANS viz contrast matching

method has been effectively employed in estimating the number of isolated pores in the sample sintered at 640 °C for 6 hours. The isolated pore density was estimated to be 1.23×10^{10} pores per unit volume for larger pores and 5.58×10^{10} pores per unit volume for smaller sized pores.

From thermogravimetric measurements the rate of weight loss at 50 °C was found to be almost double that at 35 °C indicating that there is faster evaporation from the pores as the temperature rises. At higher temperatures the asymptotic weight loss was attained rapidly. It was found that the sample sintered for 3 hours lost all its absorbed water in a time that was 45% shorter than for the 24 hour sintered sample. This finding is linked to the assertion that there are 45 % fewer interconnections to the surface for the longer sintering time.

Chapter 6

Porosity Studies of Kaolinite and Bentonite Clay

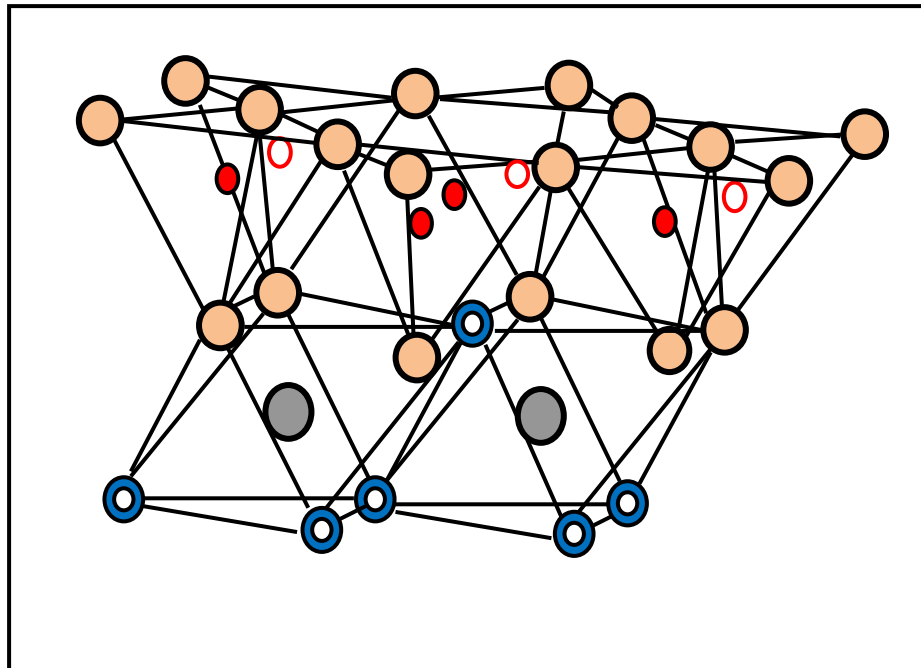
6.1. Introduction Kaolinite and Bentonite

Kaolin is a hydrated alumina silicate having chemical formula $(Al_2Si_2O_5(OH)_4)$. It was first discovered in the mountainous province of Kiangsi, China in A.D. 500 and first used to make high quality porcelain. Kaolin has applications in medicine, ceramics, paper industry, refractories etc.. It is mainly composed of fine grained plate-like particles. Components of kaolin are kaolinite, quartz, mica, feldspar and illite. It is formed by rock weathering of anhydrous aluminium silicate found in granite. The process that converts the hard granite into kaolin is known as “Kaolinisation”. Kaolin’s structure is of 1:1 type consisting of an SiO_4 tetrahedral (T) sheet joined to an AlO_6 octahedral (O) sheet by sharing a plane of oxygen [Grim, 1968]. Inter-layer distances are typically 7.2 Å. Particles are hexagonally shaped with diameter of 1 µm and thickness of 0.1 µm [Mitchell J. K., 1976]. Kaolin layers are uncharged, making it a non-swelling clay with the water residing between clay particles. It is shown by experiment and calculations that the two sides (T or O) interact very differently with water i.e the tetrahedral side is hydrophobic (weak hydrogen bond), whereas the octahedral side is hydrophilic (strong hydrogen bond) [Tunega et al ., 2002]. The schematic structure of kaolinite and a clay platelet are shown in Figure (6.1) and Figure (6.2). Hydration and pore size distribution studies of this clay are presented here.

Bentonite is a smectite type swelling clay mineral having the chemical formula $Al_2O_3 \cdot 4SiO_2 \cdot H_2O$. It is a naturally occurring hydrated aluminium silicate clay mineral (affinity to water) composed mostly of montmorillonite and beidellite, saponite, nontronite,

and hectorite minerals [Onal and Sarikaya, 2006]. Bentonite clay structure is 2:1 type, with octahedral coordinated aluminium sandwiched between two tetrahedral sheets (TOT) of silicon oxide (TOT) as shown in Figure (6.3). Both the sheets are linked through shared oxygen that makes up a single unit (Platelet). Clay platelets are layered one above the other forming a crystal, with each platelet having a thickness of 1 nm, and a diameter of a few microns [Paul et al., 2005]. Aluminium atoms are replaced by magnesium or iron atoms (Isomorphous substitution) leading to charge deficiency in the unit structure [Gulten and Kadir, 1999]. Clay platelets are repelled by the negative sodium (or calcium) cation on the surface and have positive charge on the edges (Figure 6.4) which would be balanced by the exchanging cations [Bhattacharyya and Gupta, 2008]. The addition of water causes the sodium ion to hydrate, generating a negative charge on the clay plate. Due to electrostatic repulsion these platelets move apart causing swelling in the clay leading to increase in its overall volume. The water is adsorbed on the basal surface of the clay and is called its bound water. The distance between the individual layers increases with the uptake of water, with a number of water molecules intercalated between individual layers [Newman and Brown, 1987]. Calcium bentonite swells to a very small extent whereas sodium bentonite swells 5-15 times its volume. Bentonites clay occur in three types: Natural calcium bentonite or calcium montmorillonite; Natural sodium bentonite or sodium montmorillonite; and sodium activated bentonites or sodium activated montmorillonites.

Clay is initially partially saturated with structurally bound water and the externally added water gets adsorbed, that resides in interlayer's and between the particle voids pushing the platelets to move apart leading to swelling of clay. Various aspects of clay water interaction in bentonite clay are discussed here that includes hydration, effect of compaction pressure, micelle interaction and diffusion of water molecules.



7.2 Å
 Hydroxyl
 Aluminium
 Silicon

Figure 6.1. Schematic of the structure of Kaolinite clay [from Grim, 1968]

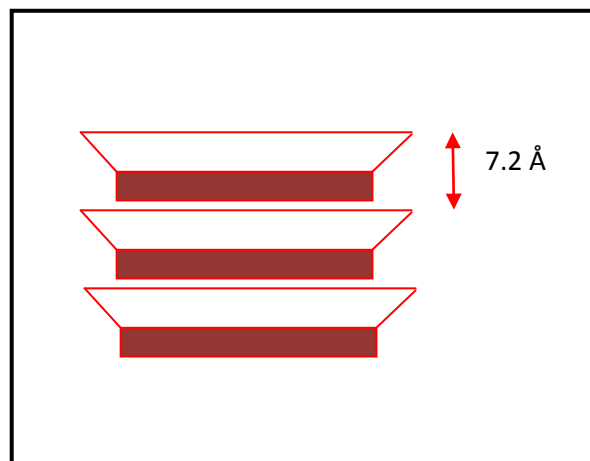


Figure 6.2. Kaolin clay platelets placed one above the other forming a particle.

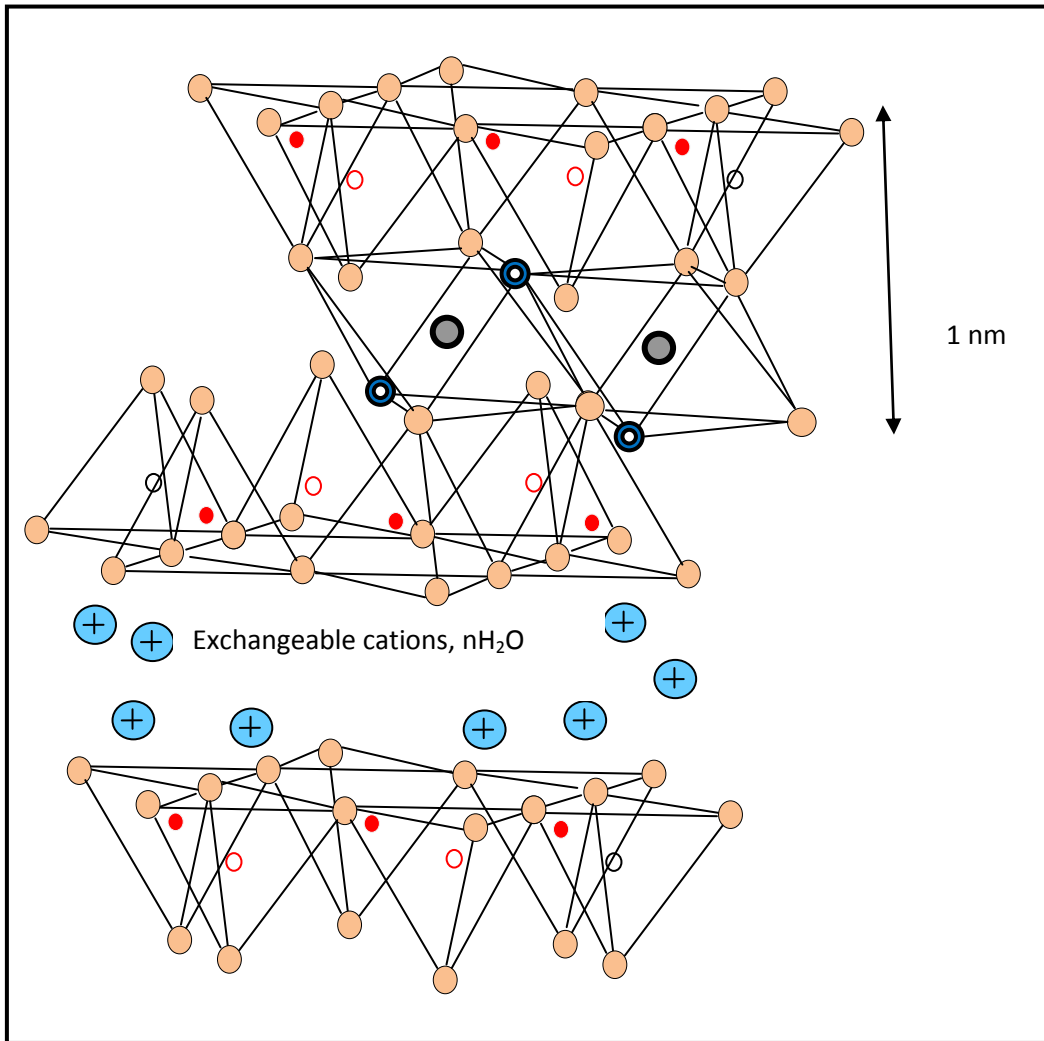


Figure 6.3. Schematic of the structure of Bentonite (Smectite) clay [from Grim,1968]

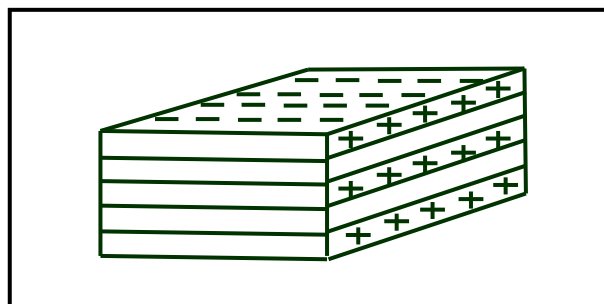


Figure 6.4. Schematic of bentonite particle.

6.2. Hydration and pore structure of Kaolin

6.2.1. Experimental

In the present study Kaolin was obtained from Thomas Baker (extra pure). The clay was hydrated by adding 10 parts of water for 1 part of clay over a week's period. Clay hydration was studied by X-ray diffraction. The dehydration was studied using a NETZSCH STA 409 PC TG-DTA instrument. The micrographs were obtained with a JEOL Scanning Electron Microscope (at National Centre for Antarctic and Ocean Research, Vasco, Goa). For obtaining pore size distribution, the gas adsorption technique was applied using a Micromeritics TriStar/3000 nitrogen adsorption desorption surface area and porosimetry analyser. The compacted clay was also studied for its pore size distribution by SANS.

6.2.2. Results and discussions

Both dry and hydrated kaolin were studied by X-ray diffraction and the data are shown in Figure (6.5). It is observed that the two patterns are almost identical in peak positions and intensities. Thus, for the hydration schedule adopted here, it may be said that there is little or no absorption of water by the dry kaolin powder with no changes in the inter-layer structure of the clay. Clay dehydration was studied by thermo-gravimetric measurements in which the clay was heated at a constant rate while recording its change in mass. It is observed from the TGA curve that the clay begins to decompose at a temperature of about 27 °C and the decomposition takes place in three steps. There is an overall weight loss of approximately 12 mg from room temperature to 1000 °C as shown in Figure (6.6). The slight increase of the TGA curve after each decrease may be due to instrumental error and may be ignored. From the DTA curve an exothermic peak is observed at 135 °C and an endothermic peak at 478 °C. The endothermic peak indicates

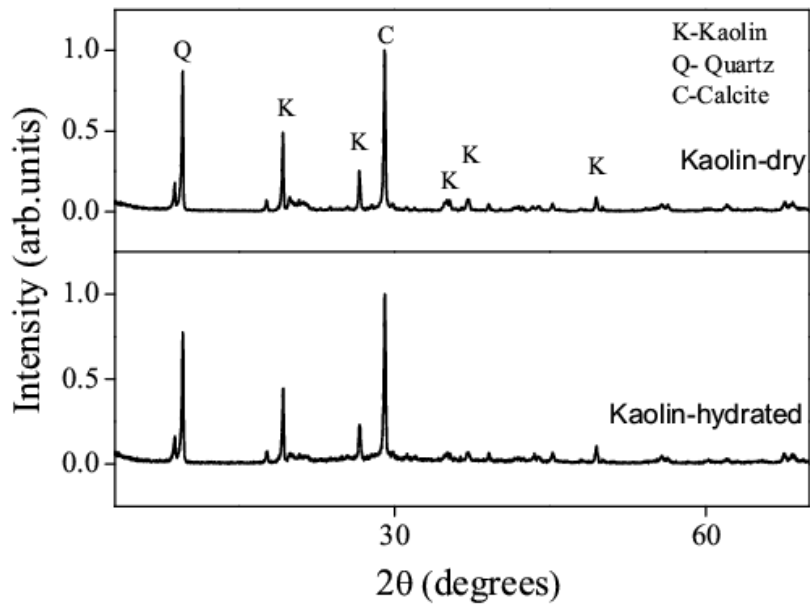


Figure 6.5. X-ray diffraction study of dry and hydrated kaolin.

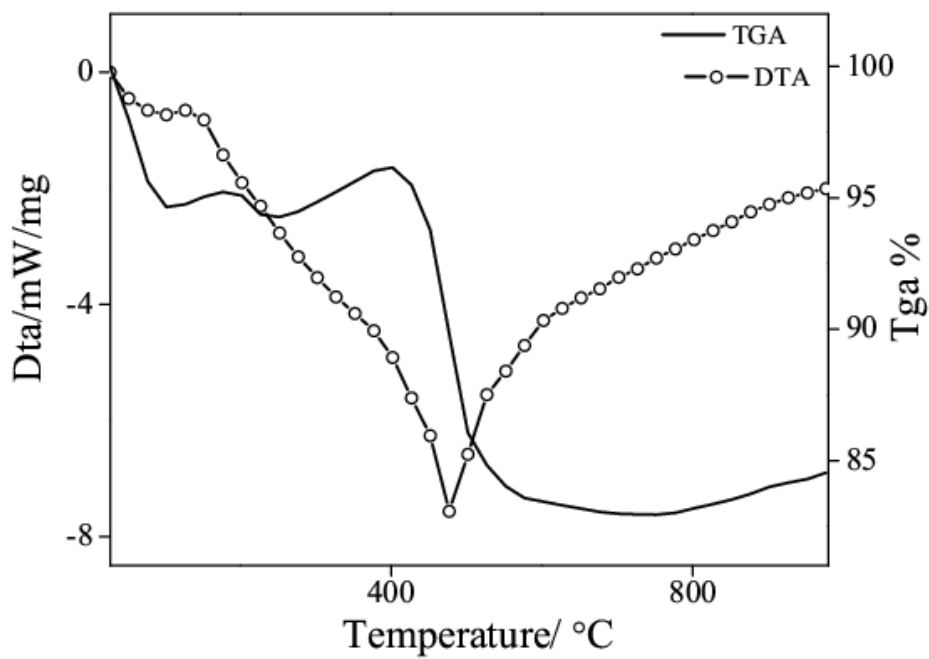


Figure 6.6. TGA-DTA data of Kaolinite powder.

that a structural change takes place which is associated with the loss of hydroxyls groups. There is realignment of the octahedral and tetrahedral silica sheets after hydroxyls are removed. Upon heating, kaolinite starts to lose water at approximately 400 °C, and the dehydration becomes almost complete at approximately 525 °C (Grim, 1968). SEM micrographs on the Kaolin powder and its compacted and sintered state (at 1200 °C) are shown in Figure (6.7). The presence of large grains with pores between them are clearly visible in the compacted and sintered sample. The total surface area of the material were estimated by using the Brunauer, Emmett and Teller (BET) equation [Brunauer et al. 1938]:

$$\frac{p}{w(p_0 - p)} = \frac{1}{w_m c} \frac{c - 1}{w_m c} \frac{p}{p_0} \quad (6.1)$$

where : W is the weight of gas adsorbed; p is the pressure of nitrogen in the pores ; p_0 is the equilibrium pressure; p/p_0 is the relative pressure; w_m is the weight of adsorbate on monolayer; and c is the BET dimensionless constant. Pore size distributions were obtained by Barrett, Joyner, and Halenda (BJH) equation (Barrett et al. 1951). BJH model is a modified Kelvin model (filling and evacuation of pores through capillaries) in which the desorption data is used. It applies only to the mesopore and small macropore size range. The volume pore size distribution according to the BJH model is obtained by the following equation:

$$\ln \frac{p}{p_0} = - \frac{2\gamma V_L}{DRT} \cos\theta \quad (6.2)$$

Where: γ is the surface tension of nitrogen; V_L is the molar volume of liquid nitrogen; D is the pore diameter; T is boiling point of nitrogen; θ is the angle of contact; and R is the Universal gas constant.

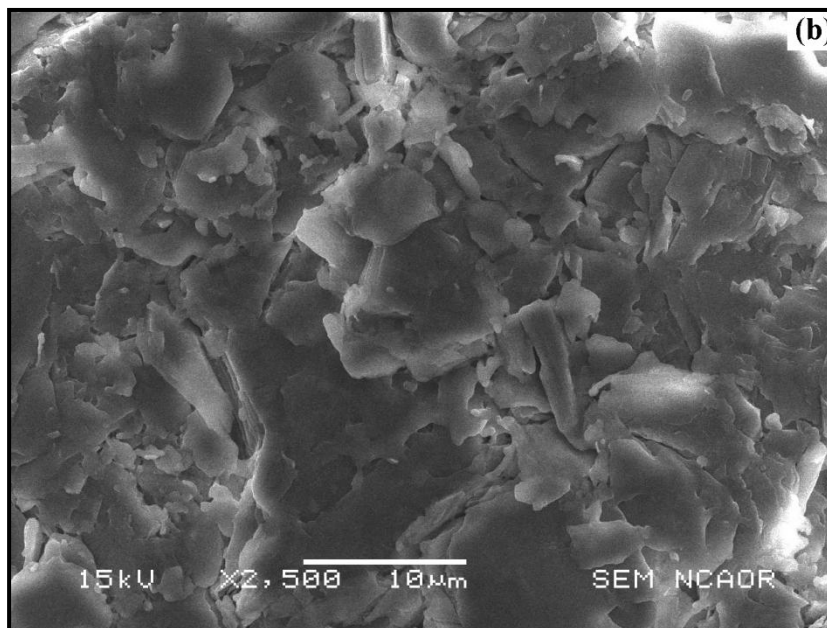
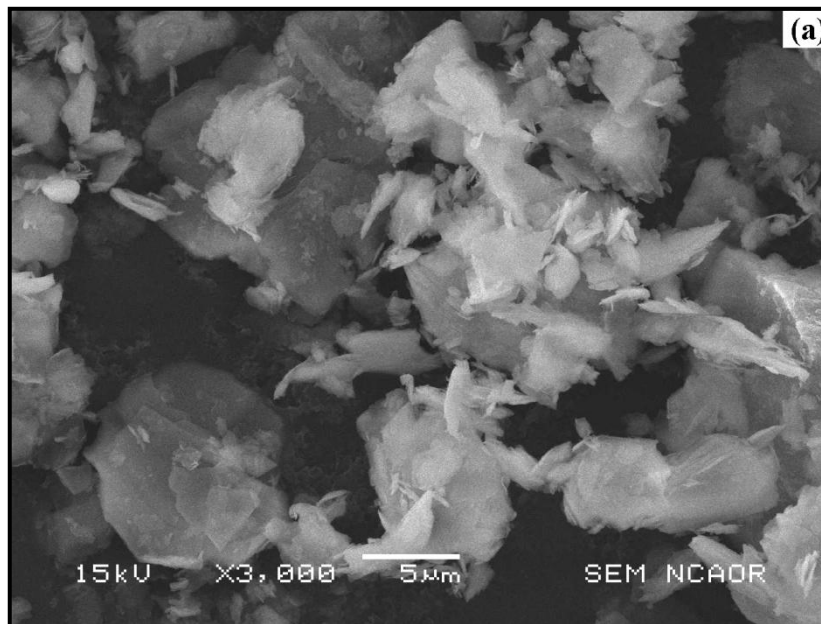


Figure 6.7. SEM micrographs of (a) kaolin compacted at 1200 °C and (b) kaolin powder.

The t-plot statistical thickness method is sometimes used to describe the statistical thickness of the film of adsorbed gas on the porous surface [De Boer et al., 1966; Meyers J.J. et al., 2001]. The analysis of pore size distribution is summarized in Table (6.1).

Table 6.1. Surface area, pore volume and pore size of kaolin clay by nitrogen porosimetry

Obs. No.	Measurement	Kaolin powder	Kaolin compact sintered
1.	BET Surface Area	6.09 m ² /g	9.66 m ² /g
2.	Pore volume by BJH Desorption	0.039 cm ³ /g	0.035 cm ³ /g
3.	BJH Desorption average pore diameter	21.3 nm	12.6 ±1.0 nm
4.	t-plot external surface area	3.64 m ² /g	10.8 m ² /g

Figure (6.8) shows the adsorption-desorption isotherm on kaolin powder and compact. The isotherm is of type II and hysteresis of H3 type indicating that the material is mesoporous. The type II isotherm represents unrestricted monolayer-multilayer adsorption and H3 type hysteresis indicate that the particles are plate-like giving rise to slit shaped pores having average diameters of 21 nm and 13 nm for the powder and the compacted clay respectively. Although the nitrogen adsorption data indicate nano-metre dimensions of pores in this powder sample, it is clear that these “pores” merely represent the spaces between particle grains and Figure (6.9) is a representation of the size distribution of these spaces. It is also to be noted that the X-ray diffraction data presented above relate to the structures of the grains themselves which do not admit water into the layered structure constituting each grain and does not therefore lead to swelling of the bulk clay.

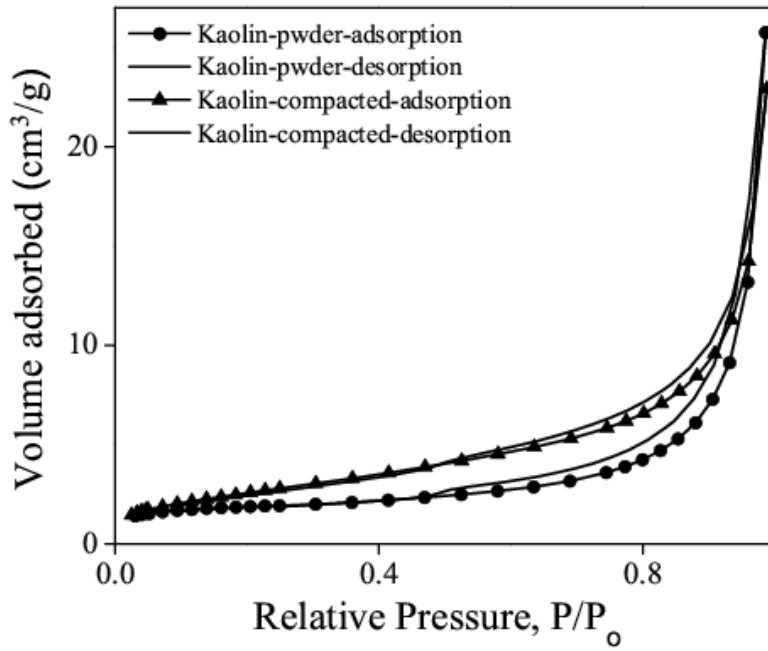


Figure 6.8. N₂ adsorption-desorption isotherm of kaolin.

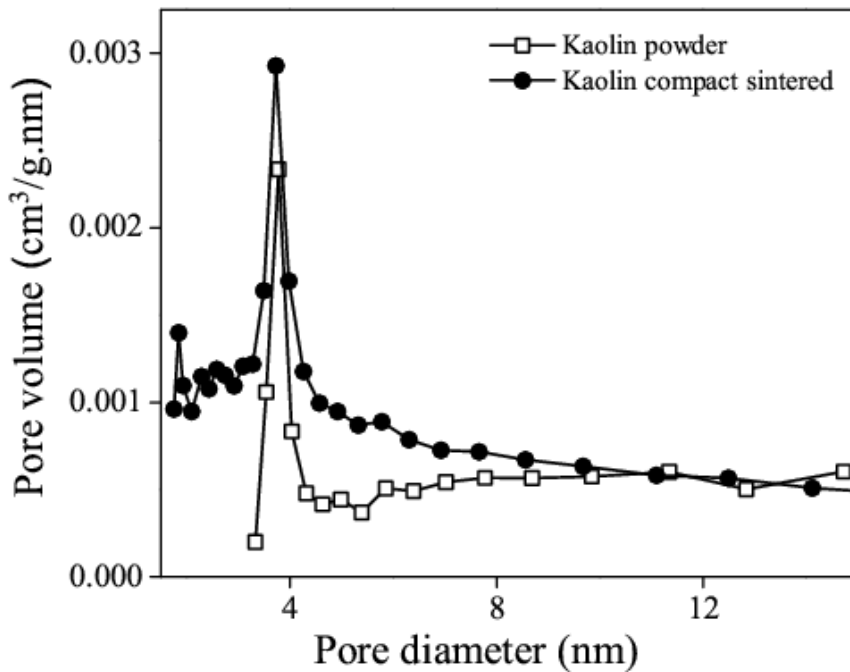


Figure 6.9. Pore size distribution of kaolin powder and compact.

Gas adsorption desorption studies are insensitive to the presence of isolated pores are therefore unable to estimate their concentration. Special methods such SANS utilizing contrast matching are employed for estimation of blind pores. However this method was not employed for the studies on clays reported here.

Small Angle Neutron Scattering measurements were performed on kaolin clay fired at 400 °C and 1200 °C with a medium resolution instrument which has a double-crystal arrangement. The accessible Q (wave vector transfer) range was 0.003 nm^{-1} to 0.173 nm^{-1} . The measured data were corrected for background, transmission and resolution broadening and are shown in Figure (6.10). The scattering from the clay fired at two different temperatures is seen to be closely similar. This is reflected in the radii of gyration (from Guinier plots) which were found to be 32 nm for clay fired at 400 °C and 33 nm at 1200 °C. A fractal dimension of 2.7 was found from the higher Q range data of the MSANS pattern .

SANS data (using a different instrument whose Q range of measurement was 0.017 \AA^{-1} to 0.35 \AA^{-1} on un-sintered kaolin and sintered at 600 °C with and without D_2O are shown in Figure (6.11). For both samples, it may be noted that D_2O decreases the intensity – as expected – by the same amount. It is estimated that for correlations above a correlations distance of 60 \AA , the heavy water enters the nano-porous volumes from the surface of the samples. The D_2O loaded sample intensities are seen to be higher than those for the dry samples above 0.1 \AA on account of incoherent scattering level from the heavy water itself being higher than scattering from smaller sized pores whose correlation distance is less than 60 \AA . Pore radii and other parameters (obtained from SASFIT) are shown in Table (6.2). Smaller values of the pores at these dimensions are found for the

sintered sample. Qualitatively, this is to be expected as the grains have a tendency to compact together as the sintering temperature increases.

Table 6.2. Parameters obtained from fit to SANS data on hydration of bentonite.

Sample	Sphere		
	Radius (Å)	Fractal dimension	Polydispersity
Kaolin-dry	18.2 ± 0.1	2.83	0.36
Kaolin-D ₂ O	16.4 ± 0.1	2.78	0.08
Kaolin-600 °C	12.3 ± 0.1	2.84	0.34
Kaolin-600°C - D ₂ O	12.9 ± 0.1	2.80	0.18

6.2. 3. Conclusions on studies on kaolinite

As the hydrated kaolin clay did not show any shift in d-spacing, it indicates that water does not penetrate the clay interlayer. The clay is dehydrated above temperature 525 °C and due to removal of hydroxyl groups there is realignment of the octahedral and tetrahedral silica sheets. Compacted and sintered clay shows micropores in the range 0.5 to 4 μm. The pore size distribution was obtained by nitrogen adsorption desorption porosimetry. The particles are disc shaped having slit shaped pores of average diameter 21 nm and 13 nm for powder and compacted kaolin clay respectively. From SANS, the pore sizes obtained were 18 Å for dry clay and 12 Å for sintered clay compact. Thus, the SANS technique is particularly well suited to the smallest range of nano-pores which show a decrease in size when the clay is sintered.

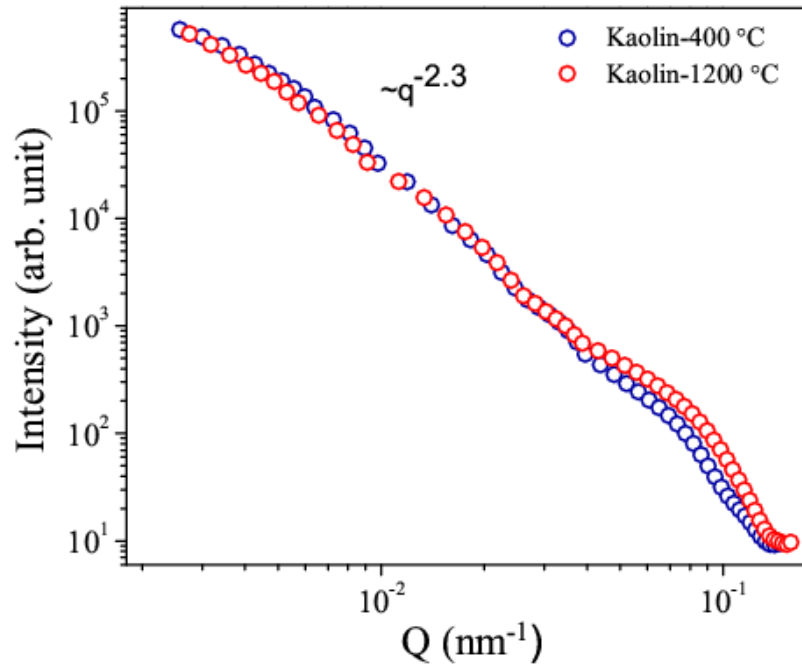


Figure 6.10. USANS data of kaolin compact.

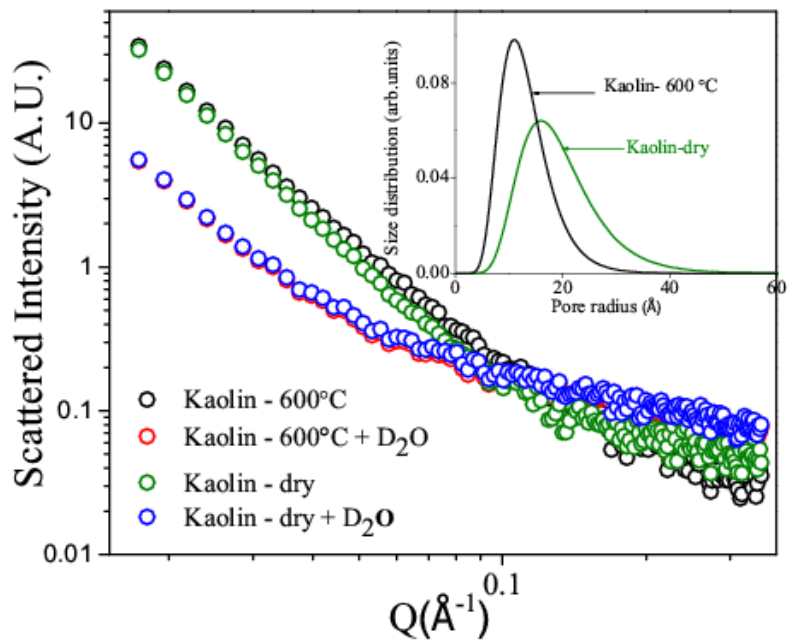


Figure 6.11. SANS data of kaolin compact and its pore size distribution (insert).

6.3. Hydration of Bentonite Clay: X-ray, IR-Spectroscopy and SANS study

6.3.1. Introduction and Scientific Importance

Clay hydration is directly influenced by relative humidity, temperature and pressure. Water molecules interact with the charged or uncharged surfaces of clay minerals. Hydration of clay is a result of short range attractive forces on negatively charged clay particles and the interlayer surface due to hydrogen bonding or charged surface dipole attraction or both [Mitchell J. K., 1976]. In surface hydration H₂O molecule may form hydrogen bond with exposed oxygen or hydroxyl on the tetrahedral layer surface. Cation hydration leads to increase in ionic radii of cation resulting in increase in interlayer pores space. Cation hydration dominates particle surface hydration. In swelling the expandable 2:1 type clay intercalates to one, two, three or four layers of water molecules in the interlayer [William J. and Ning Lu., 2006]. The nature and the strength of forces that a water molecule experiences depend on its position within the pore space, that is, the distance to the clay surfaces. The hydration of clay not only affects the permeability and migration of fluid, but also has influence on chemical, transport, pore pressure, material strength and diagenetic mineral reactions both within the backfill and the adjacent wall rock of underground repositories [Montes et al., 2003; Melkior et al., 2004; Warr et al., 2007]. Clay hydration, swelling and large surface area gives rise to adsorption property which has application in catalysis [Breen et al., 1997], as a barrier in nuclear waste and in nanocomposite materials [Dentel et al., 1995]. The hydration of a bentonite clay was studied by X-ray diffraction, Small Angle Neutron Scattering (SANS) and by Fourier Transform Infrared Spectroscopy (FTIR). Some structural implications of these results are discussed. Such studies may be of use in understanding fluid retention and release in clay.

Hydration is known to occur through the inclusion of the hydroxyl radical within the layered structure of the clay.

6.3.2. Experimental methods

The clay was hydrated by the addition of de-ionised water while permitting adequate time (typically 30 minutes) for the water to be fully adsorbed. This was continued until saturation was achieved (i.e. no further absorption) at a 10:1 weight ratio of water to clay. The changes associated with the first reflection peak (d-spacing) of bentonite clay as a function of hydration was studied on hydrated and dry samples using a Rigaku X-ray diffractometer with incident CuK_α operating at 40kV and 50 mA in the scattering angular range 3° to 70° . The structural changes in the interlayer (e.g. pore size, shape etc.) has been studied by using SANS diffractometer at B.A.R.C. of wavelength 5.2 \AA was used in the Q range (wave vector transfer) of 0.017 \AA^{-1} to 0.35 \AA^{-1} . The SANS profile is corrected for background and instrument resolution. An FTIR-8900 SHIMADZU spectrophotometer was used in the vibrational spectroscopic investigation about hydration and moisture content in clays in the wave number range of 350 to 4000 cm^{-1} .

6.3.3. Results and Discussion

The ordered clay platelets gives rise to the known reflections in bentonite. The d spacing (interlayer distance) for the (001) plane was obtained for dry, fired and hydrated bentonite. The X-ray diffraction patterns of raw bentonite in Figure (6.5-b) show that the major reflection peaks in this clay are those due to montmorillonite which is responsible for the swelling of clay. The other minor phases present in the clay are those due to the presence of kaolin, quartz and illite (JCPDS for montmorillonite 13-0135, quartz 89-8936, calcite 83-0578). The d-spacing for the (001) plane was calculated from Equation (3.3),

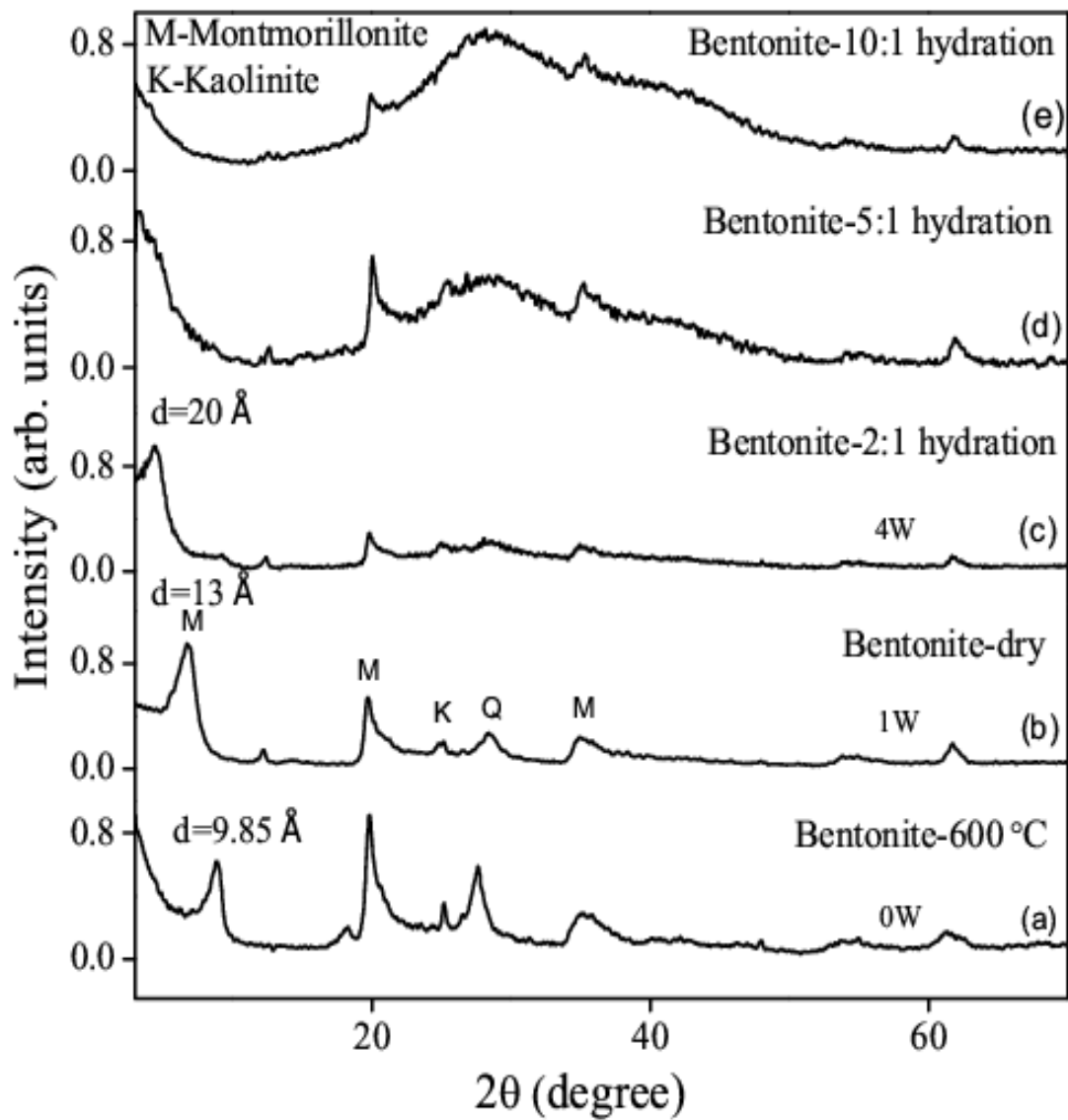


Figure 6.12. X-ray data of hydrated, fired and dry bentonite.

and was found to be 13 Å which is the basal reflection from montmorillonite having one layer of water molecules [David A., 2006]. For the clay heated at 600 °C for 4 hours the X-ray pattern shows (Figure (6.5-a)) that the (001) plane is shifted to a higher angle, thus decreasing the d-spacing to 9.8 Å. Reduction of d-spacing is due to the removal of bound water at 600 °C. After hydration of water to clay in 2:1 ratio, the d-spacing expanded to 20 Å leading to four layers of water in the interlayer of clay Figure (6.5-c). The number of intercalated water layers represent the hydration state of the clay. The presence of water causes swelling within the layers and the resultant structural changes. The partially hydrated bentonite (5:1 ratio) shows crystalline as well as amorphous phases. In the 10:1 water to clay ratio, the clay partially transforms to an amorphous phase as shown in Figure (6.5-e). The only peaks present after hydration are those due to montmorillonite while the peaks of kaolinite, calcite and quartz are replaced by an amorphous phase. This reflects that there is percolation of water molecules through the pores causing a transformation from the crystalline to amorphous phase. This indicates reduction of order in the clay layers leading to exfoliation of clay structure. As the hydration proceeds, the clay becomes a thixotropic gel forming a network of pores that restricts the flow of ions or molecules through it. This network subsequently breaks when the clay is dried.

The SANS data were taken on dry bentonite, fully hydrated and at half the hydration maximum. Small Angle Neutron Scattering data were corrected and normalised as shown in Figure (6.13). SANS data shows monotonous decrease in intensity for increasing scattering vector Q . The hydrogen atom of the water molecules majorly contribute to the constant incoherent background therefore, by observing the level of incoherent scattering at the higher values of Q , an estimate of the extent of hydration can be obtained. Thus, the partially hydrated sample has the expected level of scattering. This may be interpreted as additional evidence for the uniform absorption of water and its

inclusion within the layered structure in these particular samples. The scattering length density contrast increases when water occupies the pores in the clay and the measured intensities of both partial and fully hydrated clays are thus expected to be higher than that for the dry clay. Thus, the semi-hydrated sample has an intensity that is about half of the fully hydrated sample with the scattering at the higher values of Q being dominated by incoherent scattering. The water content doubled in fully hydrated clay. A $\ln(I)$ versus $\ln(Q)$ plot of the data from the dry sample gives a slope of 2.71 which is indicative of complex fractal-like scattering centres. For a hydrated sample from power law distribution it is observed that the fractal dimension decreased to 2.06 indicating that due filling of (Interlayer spaces) pores the clay platelets were pushed apart increasing the pore size. Hydration in clay may be considered to occur by a process in which there is subdivision of pores. There is range of pore sizes in dry clay which get filled with the hydration product during the process of hydration. The water is adsorbed by the capillary forces in the open channel when the clay is placed in contact of water. The water percolates through the voids into the elementary sheets thereby swelling the clay.

By assuming that the scattered intensity is obtained from a network of spherical pores (voids) between the individual platelets, the data was fitted by the SASFIT programme. The results of the fits are summarized in Table (6.3) and the pore size distribution is shown in Figure (6.14). Interlayer space increases resulting in larger particle size causing changes in the porosity of the clay. The hydration kinetics is controlled by these pores in clay. Only the connected pores are important in permeability. Hydration of clay was also studied by FTIR-spectroscopy. FTIR spectra obtained in the range 350 cm^{-1} to 4000 cm^{-1} show vibrational modes of bentonite clay (figure (6.15)). Studies of band assignment of bentonite clay by various authors are shown in Table (6.4).

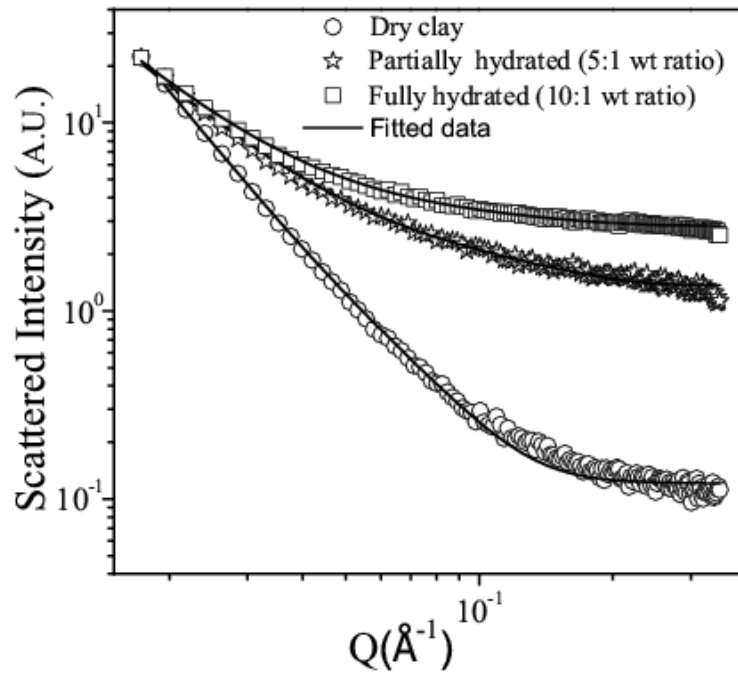


Figure 6.13. SANS data on dry and hydrated bentonite clay.

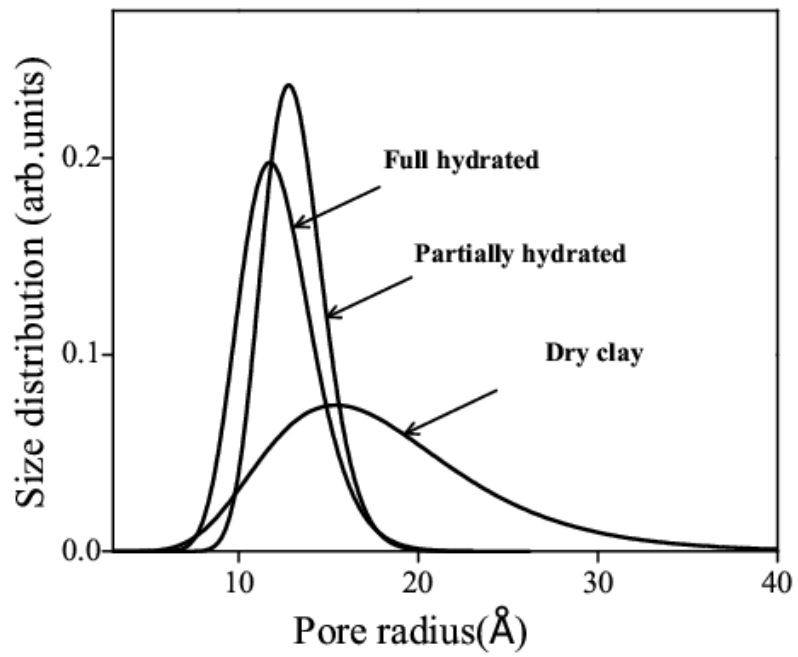


Figure 6.14. Pore size distribution of hydrated bentonite.

Table 6.3. Parameters of scattering centre geometries obtained from SASFIT.

Sample	Sphere		
	Radius (Å)	Fractal dimension	Polydispersity
Bent-dry	12 ± 0.1	2.71	0.30
Bent-5%-hydration	13 ± 0.1	2.06	0.13
Bent-10%-hydration	14 ± 0.3	2.14	0.11

Table 6.4. Studies of IR band assignment of bentonite clay by various authors.

Band	Ayari et al., 2005	Isci et al., 2006	Huaming et al., 2010	Present work
Si-O-Fe	420	—	—	422
Si-O	470	467	469	468
Si-O-Al	520	521	520	525
Al-Al-OH	915	915	916	914
Si-O(str)	1030	1036	1040	1034
Si-O(str)	1100	1100	—	1110
OH-(ben)	1635	1642	1636	1640
OH-(str)	3430	3426	3457	3438
Al-Al-OH	3620	3628	3618	3623

Hydration features of bentonite clay are attributed to structural OH, in the octahedral surface layer and the interlayer of the clay. The behavior of interlayer water molecules depends on the moisture level of interlayer cations. It is seen that the water peak broadens as the hydration proceeds. A significant difference is observed in the Si-O stretching region ($1150 - 950 \text{ cm}^{-1}$) between the spectra of raw bentonite and the hydrated bentonite. It is observed that Si-O stretching modes are present; that vibrational band frequencies do not change; and that intensities at 466 and 1024 cm^{-1} are greatly reduced in the hydrated sample. The peaks at 3628 , 3450 , and 1632 cm^{-1} are respectively due to asymmetric, symmetric stretching modes of hydroxyl in bonded water and H-O-H bending modes. The strong band at 1111 cm^{-1} is due to Si-O bending vibrations while the bands at 1034 and 464 cm^{-1} are due to Si-O-Si stretching modes.

6.3.4. Summary of hydration of bentonite clay

The hydration of a bentonite clay has been studied by several methods. XRD patterns of the dry, partially hydrated and fully hydrated clays have shown the presence of kaolinite, calcite and quartz together with montmorillonite in the dry sample. The interlayer spacing increases from 9.8 \AA to 20 \AA as the hydration progresses. As the hydration proceeds to the fully hydrated state, the first three phases get progressively replaced by an amorphous phase while montmorillonite is retained. Thus, included water is likely to cause the phases other than montmorillonite to become amorphous. This leads to exfoliation of the clay layers. In addition, the presence of OH groups may be causing existing pores to lengthen. SANS data confirm that the level of hydration of the layered crystalline structure is as expected and is likely to be due to hydroxyl ions within the crystalline layers of montmorillonite. A significant broadening of the water peak is observed as the hydration proceeds.

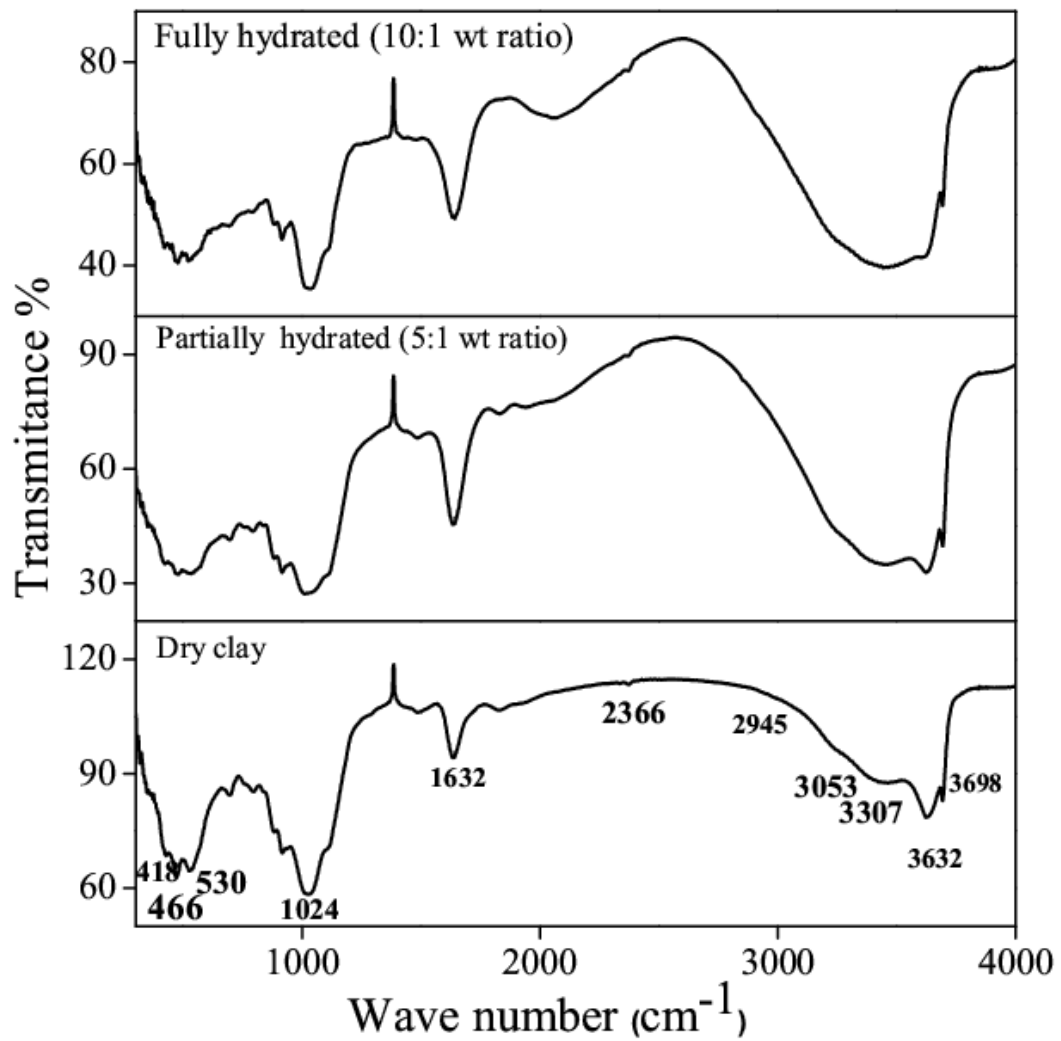


Figure 6.15. Infrared spectra of dry and hydrated bentonite clay.

6.4. Effect of pressure and hydration on pore structures of sintered clays

6.4.1. Scientific interest

Compacted bentonite is considered as a possible buffer material for a high level radioactive waste disposal due to its macroscopic properties such as low porosity and low water permeability [Miller et al., 2002; JNC, 2000]. Such properties make them useful as engineered barriers to prevent migration of pollutants [Xie M, 2004]. When water is added to clay in addition to the hydration of the layered structure the particles of clay form clusters with water occupying the volume between the clusters. Thus in a potential application of porous clay pellets in the hydration and release of pesticides into soil, the geometry and interconnection of pores would be of much relevance. Compaction affects the water adsorption by capillarity which depends on the geometry of interparticle pore spaces. Pores and their interconnections in the micron size domain are best studied by SEM. Small Angle Neutron Scattering was also employed here as it is sensitive to pores in the length scale of the interlayer spaces (typically a few nm) to large pores sizes (several hundred nanometers).

6.4.2. Experimental

Commercial bentonite clay powder was compacted at different pressures and pellets of 13 mm diameter and thickness 2mm were prepared. The compacted clay were studied by SEM, SANS in the Q range 0.017 to 0.35 \AA^{-1} and MSANS in the range 0.0003 to 0.017 \AA^{-1} instrument at Dhruva Reactor BARC, Mumbai and by water displacement method. Amounts of 500 mg of clay powder are weighed and compacted at 1, 2, 5 and 10 T pressures and sintered at 600 °C for 4 hours in a furnace. Compacts were also studied by loading a D₂O and a combination of D₂O and H₂O. They were dipped in liquid for one hours time.

6.4.3. Micro pores in compacts of bentonite and particle shape by SEM

The micrograph of the bentonite clay obtained by JEOL Scanning Electron Microscopy in Figure (6.16) shows an aggregate of bentonite platelets formed by a stack of elementary layers. The aggregated particles are of various shapes and sizes having crystalline features. From these SEM images it is observed that particle dimensions are typically ranging from 1 to 6 μm . Micrograph of a bentonite compacted at 2 T pressure indicate that the inter aggregated pores are made up of aggregated particles of clays and are shown in Figure (6.17). Inter aggregate pores are seen to be formed of diameter 0.1 to 2 μm . When the clay compact is placed in contact with water these micropores absorb the liquid immediately with subsequent movement of the water through nanopores (formed during compaction) and interlayer pores, leading to swelling of the clay. The surface elemental composition of bentonite by EDEX is given below:

Table 6.5. Elemental composition of bentonite.

Element	Composition in Wt %
Silicon	30.59
Magnesium	0.38
Aluminium	9.32
Iron	2.62
Calcium	0.63
Potassium	0.42
Sodium	1.5
Oxygen	54.54
Total	100

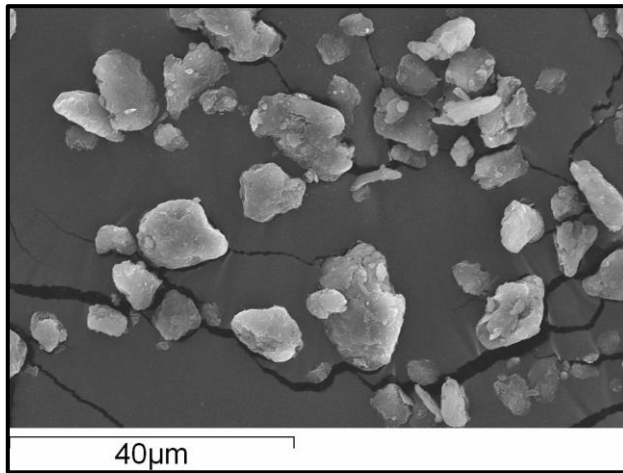


Figure 6.16. SEM micrograph of a raw bentonite.

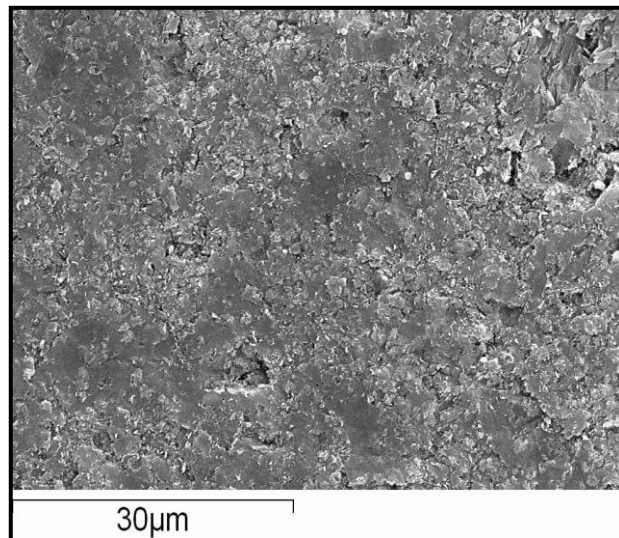


Figure 6.17. SEM micrograph of compacted bentonite.



Figure 6.18. Bentonite clay compact dry and sintered at 600 °C.

6.4.4. Nanoporous Structures of Bentonite Clay by SANS

Dense compacted clays can be easily examined by neutron scattering as neutrons interact only weakly with most matter and are therefore good probes for bulk average structural assessments. The scattered intensity depends on neutron scattering length density contrast between the medium and the aggregated pores. Bentonite clay is known to exhibit a diversity of pore sizes: primarily bimodal pore size distribution of intra and inter-particle modes on a log scale [Push et al., 1990; Eduardo and Rafaela, 2010]. The scattering length densities of loose bentonite compact, D₂O and H₂O are respectively 3.67×10^{10} , 6.38×10^{10} , and $-0.56 \times 10^{10} / \text{cm}^2$. The scattering length density contrast for bentonite hydrated with H₂O is $(3.67 - (-0.56))^2 \times 10^{20} = 17.9 \times 10^{20} / \text{cm}^2$ while for bentonite deuterated with D₂O is $(3.67 - 6.38)^2 \times 10^{20} = 7.34 \times 10^{20} / \text{cm}^2$. Contrast of bentonite with H₂O is 2.4 times more than that of bentonite with D₂O. When a mixture of light and heavy water is used in 50% - 50% relative proportions, the scattering length density contrast of the mixture is $2.90 \times 10^{10} / \text{cm}^2$.

6.4.5. Results and Discussion

For each compact, the density and the bulk porosity was found both by measuring its diameter and thickness to give the “geometric density” as well as by use of the water displacement method as discussed in Section (3.3). Results are shown in Table (6.6). The fractional macroscopic porosities were obtained in the range 35 – 39 %. From the variation of porosity with pressure, it is clear that porosity decreases with increasing compaction pressure though at different rates. As expected, densification of the porous compacted clay increases with pressure. Compared to loose clay the scattering length density decreases with compaction pressure. Decrease in density and scattering length density is attributed to the fact that the porous volume decreases as the compaction pressure increases. The usual

experimental corrections were applied to the SANS data which were then normalized to absolute scale. Figure (6.19) shows the intensity profile for the compacted clay. For intensities below about 0.1 \AA^{-1} (corresponding to a correlation length of about 60 \AA), the increase in compaction pressure produces larger numbers of scattering centres with correlation lengths more than 60 \AA . Simultaneously, the number of smaller pores beyond 0.2 \AA^{-1} decreases as the pressure increases to 5 T. It is to be noted that the number of larger pores almost reaches an asymptotic value for pressures of 2 T and beyond. For the 10 T data, there is an appreciable increase in the number of smaller pores beyond about 0.1 \AA^{-1} . An empirical model is thus envisaged in which smaller pores coalesce into larger ones for applied pressures between 2 T and 10 T. For the highest pressure of 10 T, it is likely that in addition to the process of coalescence of smaller to larger pores, the clay platelets are forced together in a way that creates appreciable numbers of smaller pores.

Table 6.6. Density, Porosity and neutron scattering length density of bentonite clay compacted from 1 to 10 T pressures and sintered at temperature $600 \text{ }^\circ\text{C}$.

Compact fired at $600 \text{ }^\circ\text{C}$ for 4 hours	Geometric Density in g/cm^3 (± 0.005)	Density water displacement g/cm^3 (± 0.0005)	Porosity %	S.L.D (cm^{-2})
Bentonite-1 T	1.490	2.4680	39	3.548×10^{10}
Bentonite -2 T	1.512	2.4558	38	3.529×10^{10}
Bentonite -5 T	1.514	2.4115	37	3.466×10^{10}
Bentonite -10 T	1.532	2.3830	35	3.433×10^{10}

By assuming that the scattered intensity is obtained from a network of spherical pores (voids) between the individual platelets, the data was fitted by the SASFIT programme. The lower Q region was first fitted to an empirical model of scattering from spherical pores and later extended to the rest of the full region of measured Q. The results

of these fits are summarized in Table (6.7). The functional forms of the scattered intensity for such a system of scattering centres is as given earlier (Section 4.2.3.). The number of scattering centres per unit volume, n_1 , were obtained by fitting the measured to the calculated intensity function as per Equation (6.3):

$$I(Q, a_1, b_1, x_1, d_1) = n_1 P(Q, a_1, b_1) S(Q, a_1, x_1, d_1) \quad (6.3)$$

The pores size distribution for each compaction pressure is as shown in Figure (6.19). There is a clear trend towards smaller average pore size as the compaction pressure increases. The average pore size in each distribution is listed in Table (6.7) together with fractal dimension and polydispersity (related to the FWHM). The variation of average pore size with compaction pressure is shown in Figures (6.21 (a) and (b)). This particular variation may be taken to represent the quantification of the response of pore size to application of pressure to the clay. The average pore size does not decrease appreciably beyond a compaction pressure of 5 T.

Table 6.7. Parameter obtained from SANS data fit for pores in bentonite clay.

Compaction Pressure	Mean of the pore size distribution (Å)	Peak position of the distribution (Å)	Fractal dimension	Polydispersity	No. of scattering Centers per cc
1 T	19.15 ± 0.13	16.81	2.63	0.356	4.94 x 10 ¹⁷
2 T	14.92 ± 0.19	13.52	2.61	0.346	8.49 x 10 ¹⁷
5 T	13.91 ± 0.42	11.91	2.60	0.303	1.15 x 10 ¹⁸
10 T	12.02 ± 0.26	10.06	2.63	0.326	1.51 x 10 ¹⁸

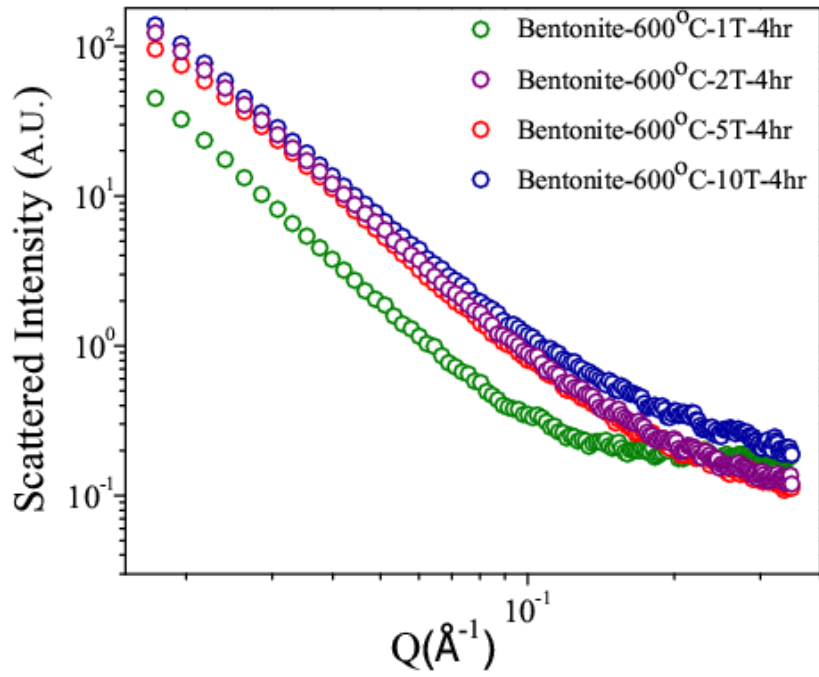


Figure.6.19. SANS fitted data on bentonite compact at 1, 2, 5 and 10 T Pressures.

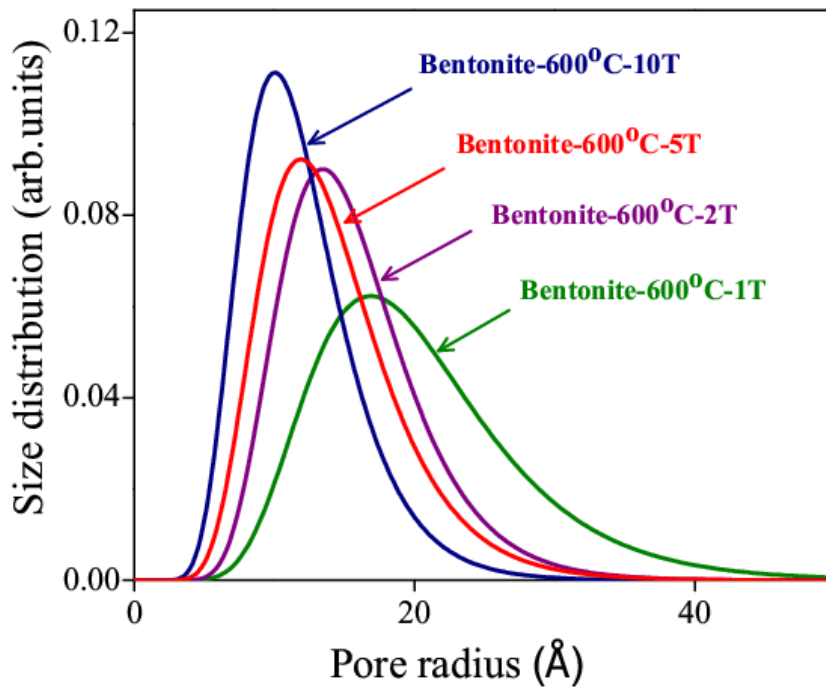


Figure 6.20. Pore size distribution of polydispersed spherical pores in bentonite.

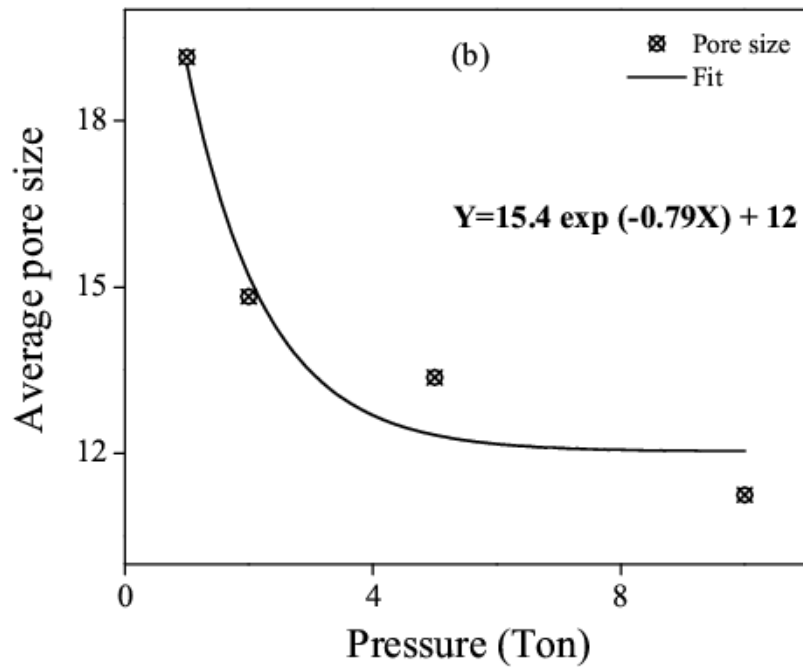
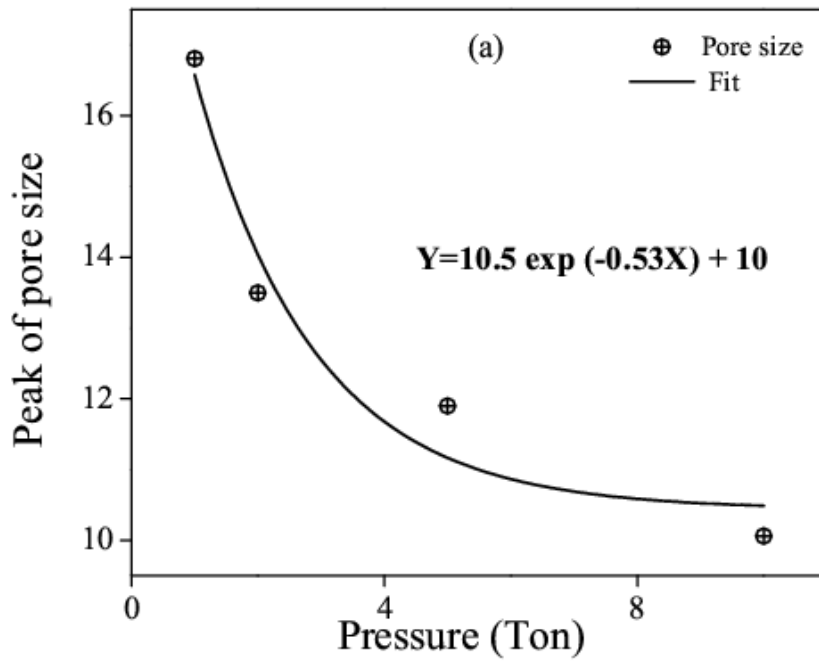


Figure 6.21. (a) variation of peak of pores size with compaction pressures (b) variation of average pore size with compaction pressures.

The results of the bentonite compact that was pressurized under 2 T was loaded with D₂O [Figure (6.22)], and a combination of 50 : 50 % of D₂O and H₂O [Figure (6.23)] are discussed below. The compact loaded with D₂O shows decrease in intensity due to the lower contrast factor and an approximately horizontal level due to the small incoherent contribution from D₂O. Similarly for the mixed D₂O and H₂O loading, it may be noted that this intensity runs parallel but lower to the dry bentonite indicating that the mixture fills the pores from the microscopic (few μ s) to nano dimensioned pores in a uniform fashion. In this combination of light and heavy water loading, the incoherent level beyond about 0.1 \AA^{-1} is due to the hydrogen of the water. From fits to the data (SASFIT), as shown in Table (6.8), the average assumed spherical pore centre of scattering is about 16 \AA . From this it may be said that, the shape of the scattering curve stays the same while pores of all dimensions are filled with D₂O.

Table 6.8. Parameter obtained from SANS data fit for D₂O loaded compact.

Sample	Sphere		Polydispersity
	Radius (\AA)	Fractal dimension	
Bentonite-dry	13.76 ± 0.37	2.63	0.313
Bentonite+ D ₂ O	15.67 ± 0.15	2.58	0.263
Bentonite+D ₂ O+H ₂ O 50 : 50 %	16.60 ± 0.06	2.66	0.313

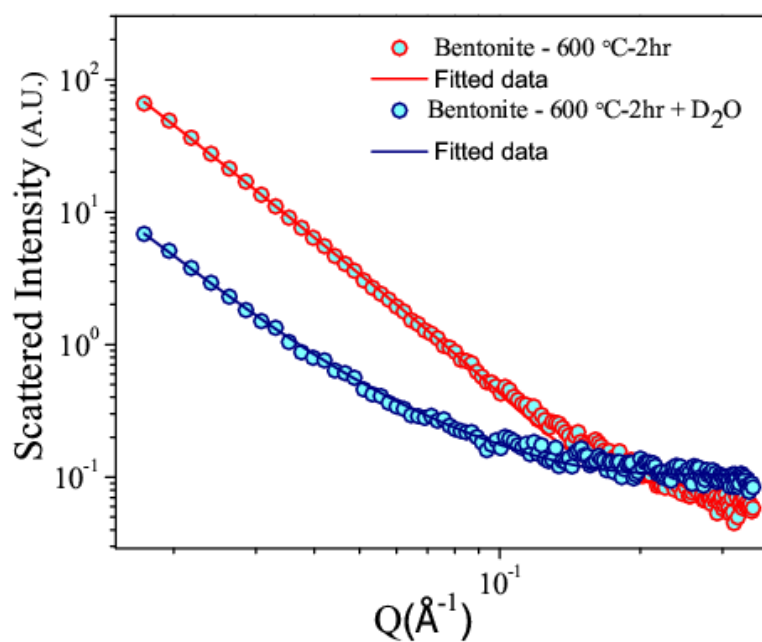


Figure.6.22. Fits to SANS data from dry and D₂O loaded bentonite compact .

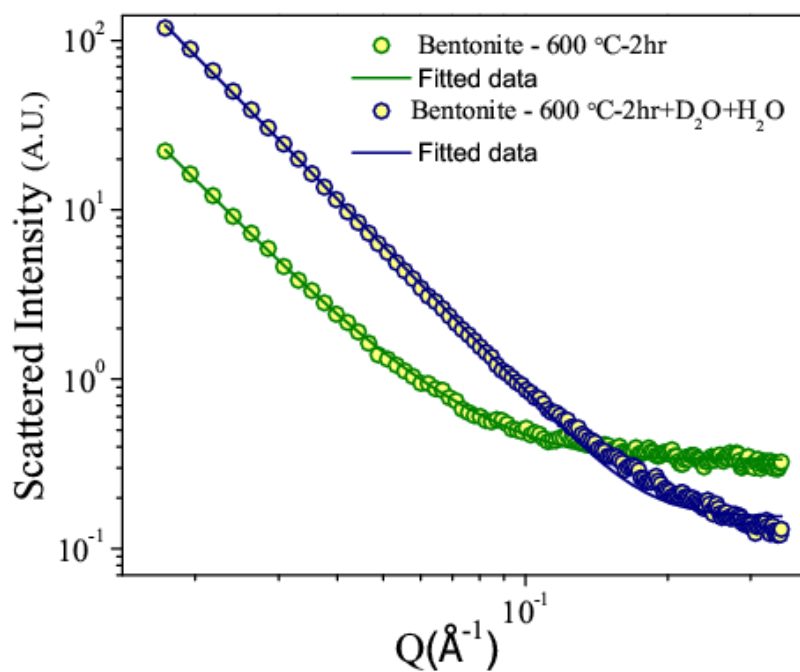


Figure.6.23. Fits to SANS data from dry and compact 50%D₂O-50%H₂O loaded bentonite

(Errors are within the range of symbol).

Medium resolution Small Angle Neutron Scattering experiments (USANS at B.A.R.C.) were also performed on dry and fired bentonite compact and the results are discussed here. In this case we have two different models fitted to the data viz: polydispersed spherical pores and polydispersed cylindrical pores. The intensity equation for polydispersed sphere and the form factor is given by equation (section 4.2.3). SANS intensity is given by:

$$I(Q) = C \int P(Q, r) r^6 D(r) S(Q, r) dr$$

The form factor for cylinder of diameter $2R$ and the height $2H$ is given by:

$$P(Q) = \int_0^{2\pi} \frac{\sin^2(QH \cos\beta) 4J_1^2(QR \sin\beta)}{Q^2 H^2 \cos^2\beta Q^2 R^2 \sin^2\beta} \sin\beta d\beta \quad (6.4)$$

Where β is the angle between Q and the cylinder axis, J_1 is the first order basal function. Intensity is as shown in Figure (6.24). For the clay fired at 600°C , the intensity was found to be lower over most of the measured Q region. Heating at this temperature is likely to remove the OH radicals (i.e. “crystalline water”) causing the scattering length of the “dry” matrix to be higher and resulting in an increased scattering length density contrast with the air-filled pores. The data were fitted to scattering functions due to spheres and cylinders and the results are as shown in Table (6.9). The cylindrical pores act like connecting channels for spherical pores through which the transport of water/fluids can take place. This model thus includes inter-pore connectivity which is necessary if water is to fill pores of these nano-metric dimensions.

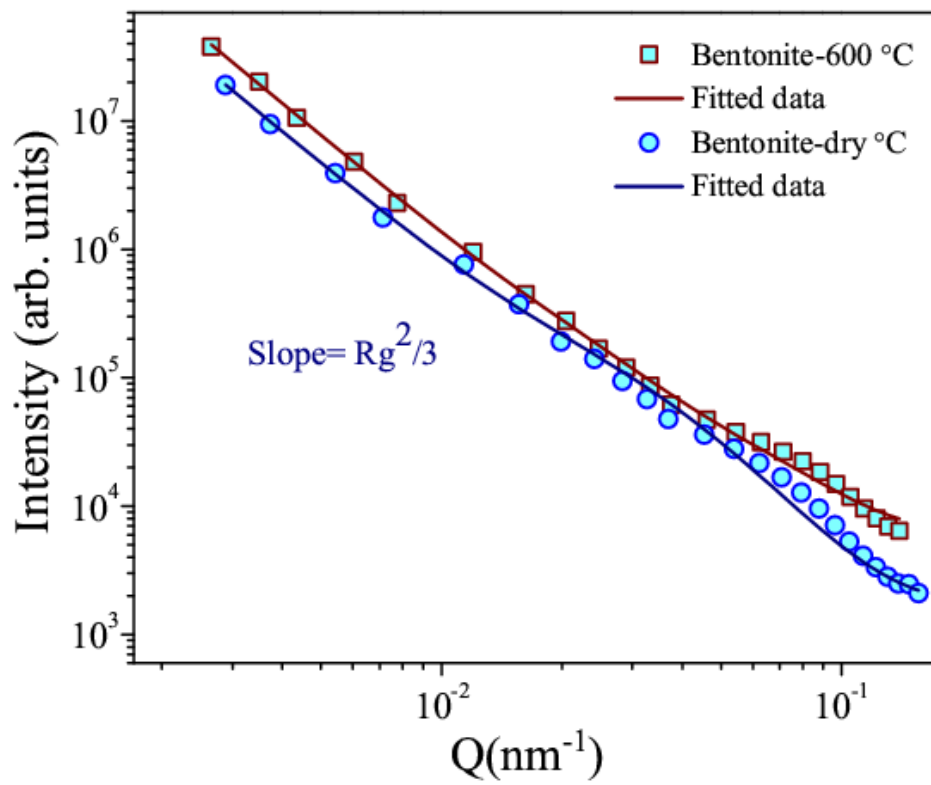


Figure 6.24. MSANS data fitted for a bentonite fired at 200 °C and 600 °C.

Table 6.9. Parameter obtained from MSANS data fit for pores in clay.

Sample	Sphere		Cylinder	
	Radius nm	Fractal dimension	Radius nm	Length nm
Bentonite-dry	36	2.43	13	259
Bentonite-600°C	41	2.47	16	210

6.4.6. Conclusions on Effect of Compaction Pressure on Pore Structures

The bentonite compacted at various pressures were studied for their nano pore size variation by SANS. It has been noted that there is a decrease in porosity and pore sizes as the compaction pressure is increased and the number of larger pores almost reaches an asymptotic value for pressures of 5T and beyond. It is likely that at 10T compaction pressure the clay platelets are forced together such that it creates smaller pores apart from bigger pore formation due to coalescence. The intensity pattern of compacts loaded with D₂O and the combination of H₂O plus D₂O runs parallel to the dry compact indicating that the mixture fills the nano pores in a uniform fashion showing connectivity in between pores. The fired clay compact can be used to store plant nutrients, water, pesticides etc which can be released slowly to the surrounding environment depending on the gradients between the compact and surroundings such as temperature, humidity, pressure, chemical potential etc. Since the matrix to store the water /nutrients would be clay, no harm to the soil or environment would be caused by the clay which could be chosen to be of the same material as the soil or fully compatible with it.

6.5. Effect of Confinement on a Micellar Solution in a Sodium Activated Bentonite

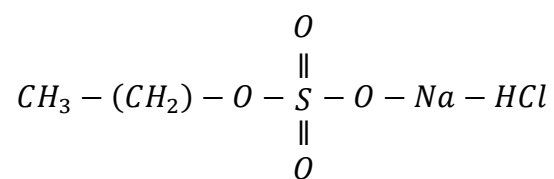
6.5.1. Scientific interest

Organo clays have various applications as in paint, cosmetics [Lucilene et al.,2008], electric materials [Jae and Young, 2011], adsorbant, and geochemical barrier in waste landfill [Frost et al., 2006]. Surfactants are amphiphilic molecules consisting of hydrophilic polar head and hydrophobic non polar tail [Aswal et al., 2006]. When a surfactant is added to water and loaded into the clay compact it interacts with the clay in a way that depends on whether the surfactant is ionic or anionic [Güngör et al.,2001]. Interaction of the particles (micellar agglomerates) will be different according to the interaction behaviour of surfactant with clay mineral. Cationic (non ionic) surfactant gets adsorbed on the negative surface of the clay platelet as shown in Figure (6.25) [Alemdar et al., 2000]. For an anionic surfactant like SDS the heads of the molecules anchor to the positive edge of the clay particles Figure (6.26) leading to redistribution of charge on the edge. Surfactants hold on to the clay surface with weak Van der Waals bonds. This affects the flow behavior of the system. By the addition of proper concentration of the surfactant, the structural properties of the clay-water system can be controlled [Alemdar et al., 2000]. The surfactant affects the rheological behavior of clay which is important in various technological applications [Gungor et al., 2001]. Excess of salt allows the control of the aggregation number and structure in the case of ionic surfactants. Ionic strength can be effectively tailor [Mohanty et al., 2007, Renoncourt et al., 2007] the properties of aggregates which has applications in drug delivery nanocarriers [Peer et al., 2007] due to which this study is of importance. Swelling nature of bentonite increases with higher content of sodium in clay [Clark and Moyer, 1974]. The structure of surfactant layer is studied by SANS [Goyal and Aswal, 2001]. In petroleum recovery and environmental soil

remediation process, surfactant adsorption from solution to the solid surface mostly occurs on the walls of pores in porous media. This adsorption constitutes a loss of valuable surfactant and dictates the economics of an oil recovery or remediation process. Here we report the structural arrangement of micelles in the pores of compacted bentonite. Also studied was the effect on micellar charge of cationic content. The structural properties of confined solution can be obtained using coherent scattering technique (SANS). The compacted clay was loaded with the SDS micellar solution and studied by SANS. Detailed modeling of the in-situ SANS experiments revealed information of the size and shape of the micelles at a different concentration. The aim of this investigation was to follow the changes induced by the addition of different concentrations of micelles on the bentonite clay interlayer.

6.5.2. Preparation of sodium saturated bentonite

Alluminosilicate layered bentonite clay was used for the study. The surfactant used in this study was Sodium Dodecyl Sulphate (SDS) which is an anionic surfactant having the formula $\text{CH}_3(\text{CH}_2)_{11}\text{SO}_4\text{Na}$. SDS is an anionic surfactant which is soluble in water having molecular weight 288.3 g/mol with the following chemical formula:



The bentonite clay used here (Thomas Baker) was a swelling smectite type of clay. The swelling bentonite was saturated with sodium by using NaOH. 500 ml of NaCl solution (1 M concentration) was prepared and added to 20 gm of dry bentonite clay [Nuntiya et al., 2008]. The clay was saturated with NaCl solution and the process repeated 5 times. The solution in the beaker was continuously stirred for 1 hr at room temperature.

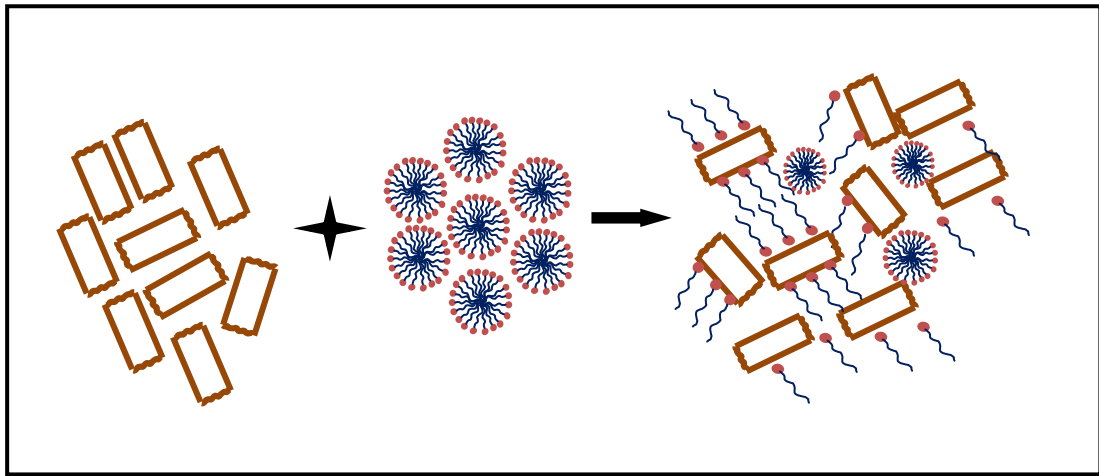


Figure 6.25. Schematic of adsorption of cationic surfactant on bentonite particles.

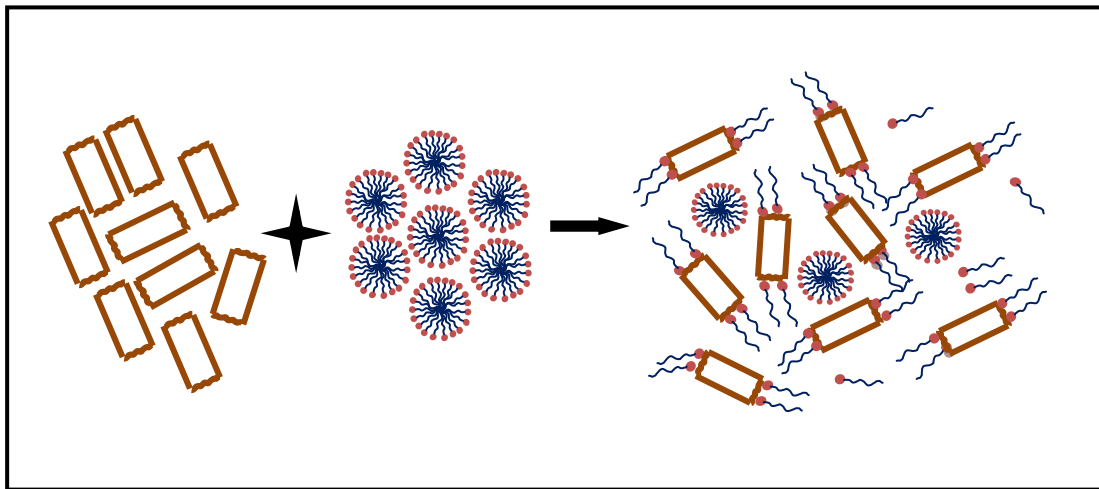


Figure 6.26. Schematic of adsorption of ionic surfactant on bentonite particles.

The clay was then allowed to settle for 24 hrs and the supernatant solution was decanted the next day. The centrifuge was stirred again with 1 M Na Cl solution with decanting of the supernatant solution the next day. The step was repeated consecutively for three days. The product was washed with distilled water and separated in a centrifuge until the solution was free of chlorides. The Na-bentonite obtained was dried in an oven at 100 °C. The dry bentonite and Na-bentonite clay powder was then compacted under pressure of 2 T for 2 minutes. The compacts of sodium clay were loaded with micellar solution (10 % , 20 %) of SDS. The structural modification of clay after Na saturation was studied by X-ray diffraction and Infrared spectroscopy. The effect on micellar formation in the confined pores of bentonite and Na- bentonite was studied by SANS.

6.5.3. Results and Discussions

The X-ray diffraction patterns of the dry clay, sodium saturated clay and SDS loaded clay are shown in Figure (6.27). The principal reflection from bentonite clay is the (001) plane whose d-spacing is 12 Å. The reflection peak of the SDS loaded clay shows that there is an increase in d-spacing from 12 to 19 Å due to surfactant adsorption in the inter-layers. A 15 Å spacing due to a minor peak is also seen. In the Na-bentonite pattern it is observed that the peaks at 12 °, 25 ° and 26 ° get enhanced. The enhanced reflections of quartz are likely to be due to those planes that contain sodium.

The Infrared spectra of sodium saturated and untreated bentonite in the range 350 to 2000 cm⁻¹ is shown in Figure (6.21). The untreated bentonite clay shows absorption bands at 1632 cm⁻¹ due to symmetric stretching modes of hydroxyl in bonded water and H-O-H bending modes. The bending vibrations at 1032 and 524 cm⁻¹ are due to Si-O-Si stretching modes. Peaks at 914 and 787 cm⁻¹ are due to Al-OH and Al (Mg)-Al-OH bonds respectively. The sodium saturated bentonite shows an increase in the wave number for

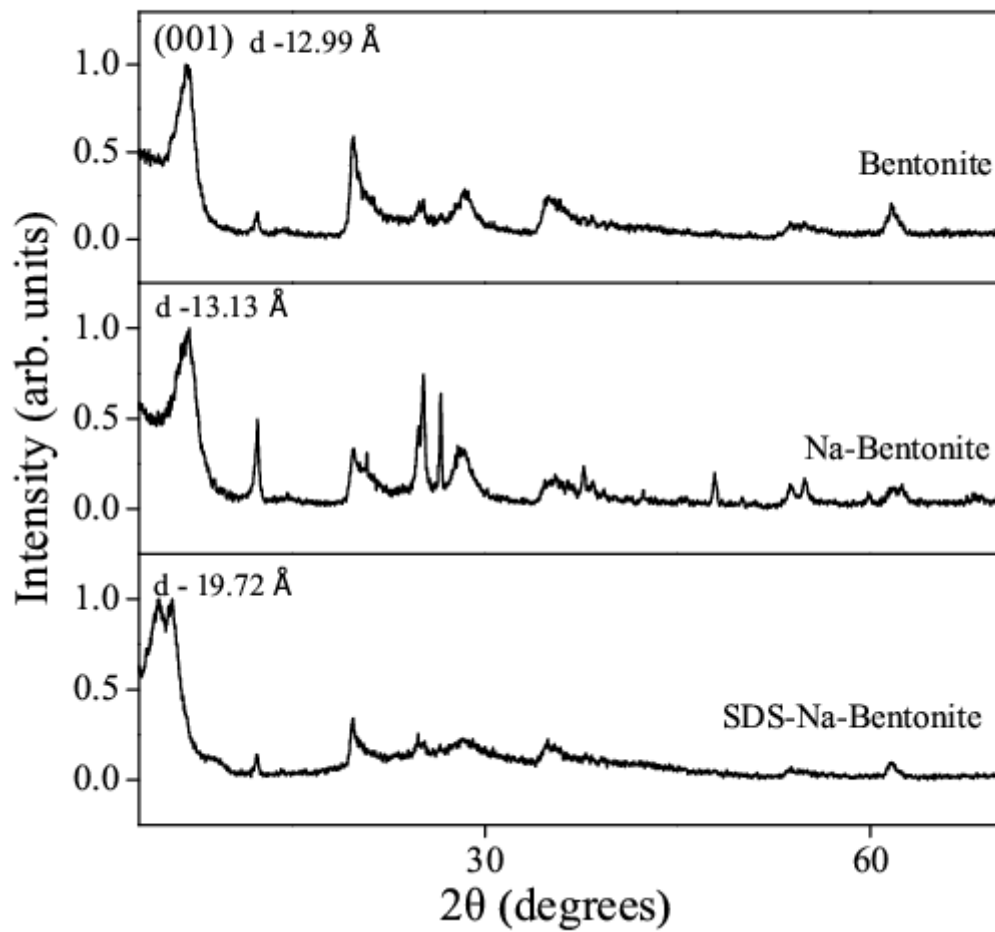


Figure 6.27. X-ray diffraction of bentonite, Na-bentonite and sds loaded bentonite.

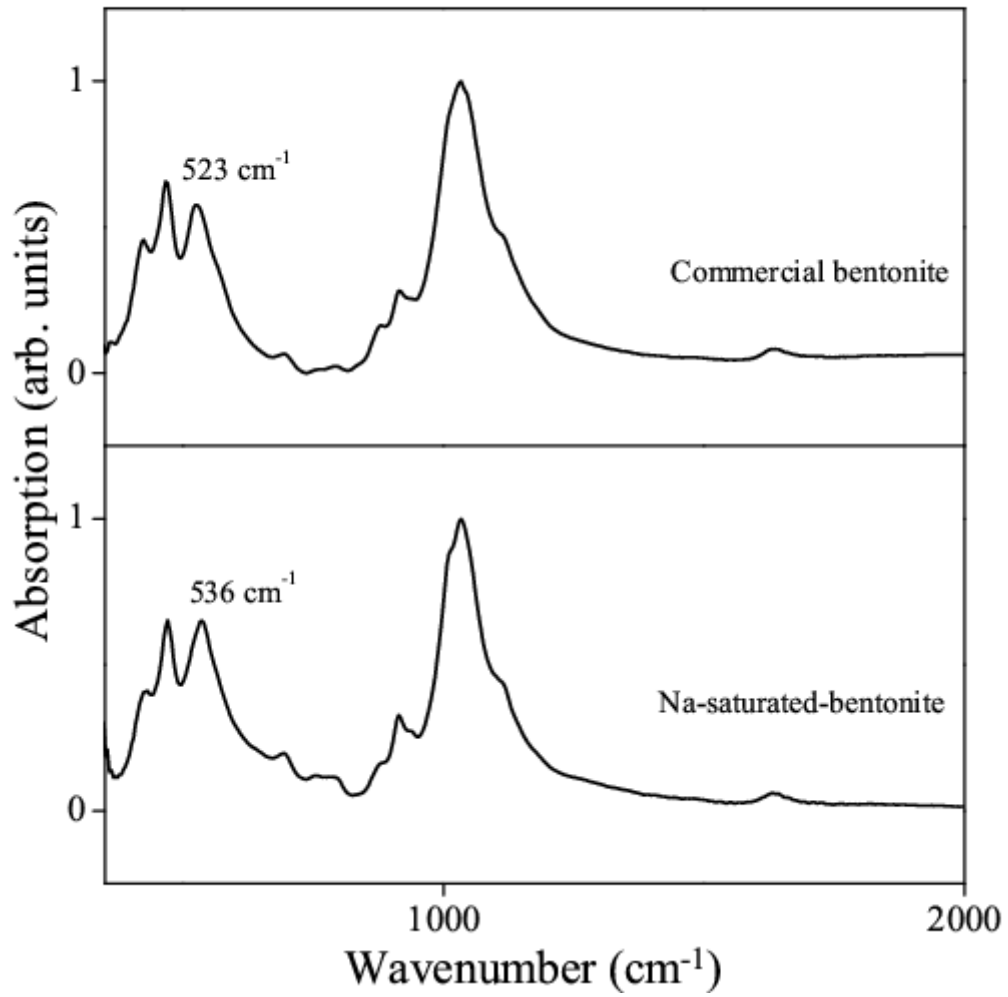


Figure 6.28. Infrared spectra comparison of bentonite and Na saturated bentonite.

Si-O-Al from 523 to 536 cm^{-1} . This indicates that there are changes due to sodium saturation in the crystal structure.

The compacts were examined by SANS on a dry clay - with and without inclusion of the SDS micellar solution. From data fitting to the model of spherically shaped pores (Using SASFIT), it is found that the pores formed in compacted Na bentonite have an average radius of 16 Å with a fractal dimension of 2.7. When the clay compact is loaded with a micellar solution, the contrast between clay and pore is reduced because D_2O fills these pores giving a lower contrast factor and hence a lower $I(Q)$. The volume of surfactant monomer 'V' was obtained by Tanford's formula. The Tanford's formula is given as:

$$V = [27.4 + (26.9 \times N)] + V_g \quad (6.5)$$

where N is the number of carbon atoms in the chain, V_g is the volume of head group for SDS the values are: $N = 12$, $V_g = 350 \text{ Å}^3$. Hence the volume of surfactant monomer was obtained as 700.2 Å^3 . Semi major 'a', minor axis 'b' and fractional charge ' α ' of micelle have been determined from analysis. The micellar aggregation number was calculated by formula:

$$\text{Aggr. no.} = \frac{4\pi ab^2}{3V} \quad (6.6)$$

When Na-bentonite is loaded with SDS, the aggregation number of the micelle is reduced. The effective charge reduces, resulting in a decrease of the average separation and the interference peak shifting to higher Q. Thus, Na has an important role to play in the reduction of effective charge causing micellar interaction to be reduced from 69 to 53 Å. SANS data for micellar solution were collected for 10 wt.% and 20% SDS and fitted with the form factor of an ellipsoidal core shell and a structure factor from a Hayter-Penfold analysis. The parameters obtained from fit are shown in Table (6.10).

Table 6.10. Model fit to SANS data for SDS and SDS in bentonite clay.

Sample	Semimajor axis a (Å)	Semiminar axis b (Å)	Aggregation No.	Volume fraction	Effective charge 'e.u.'	Fractional charge
SDS (10%)	65 ± 9	14.0 ± 0.7	75	0.18	39	0.52 ± 0.01
SDS (20%)	72 ± 10	14.0 ± 0.7	84	0.27	35	0.41 ± 0.01
SDS bentonite	54 ± 2	14.0 ± 0.1	63	0.11	32	0.49 ± 0.02
10% SDS-Na bentonite	53 ± 2	14.0 ± 0.1	62	0.20	27	0.43 ± 0.01
20% SDS Na bentonite	44 ± 5	14.0 ± 0.1	52	0.23	10	0.19 ± 0.01

Table 6.11. Micelle separation in bentonite clay.

Sample	Micelle separation
SDS (10%)	69
SDS (20%)	60
SDS bentonite	67
SDS-Na bentonite	52
Nabe-20% Sds	53

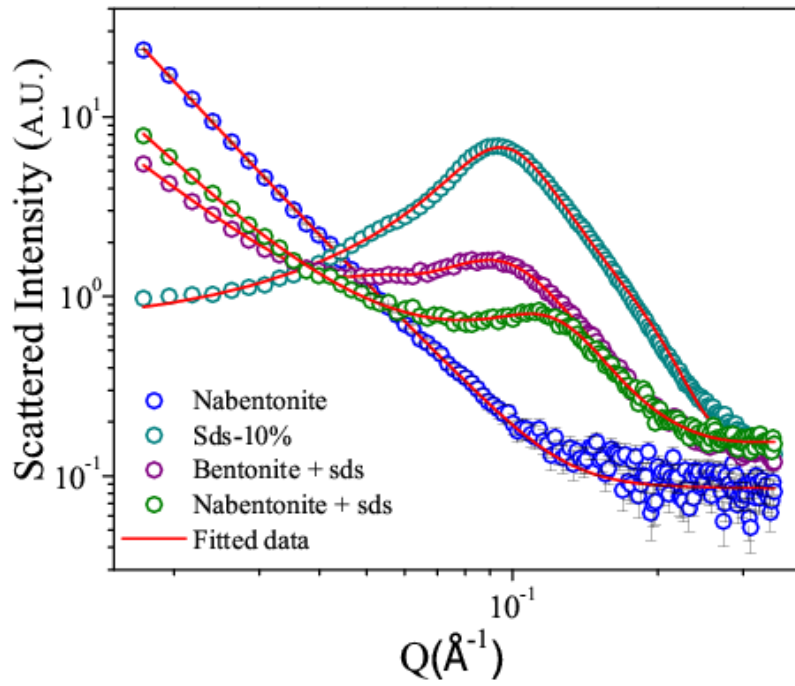


Figure.6.29. SANS data on micellar (10 % SDS) induced bentonite and Na bentonite clay.

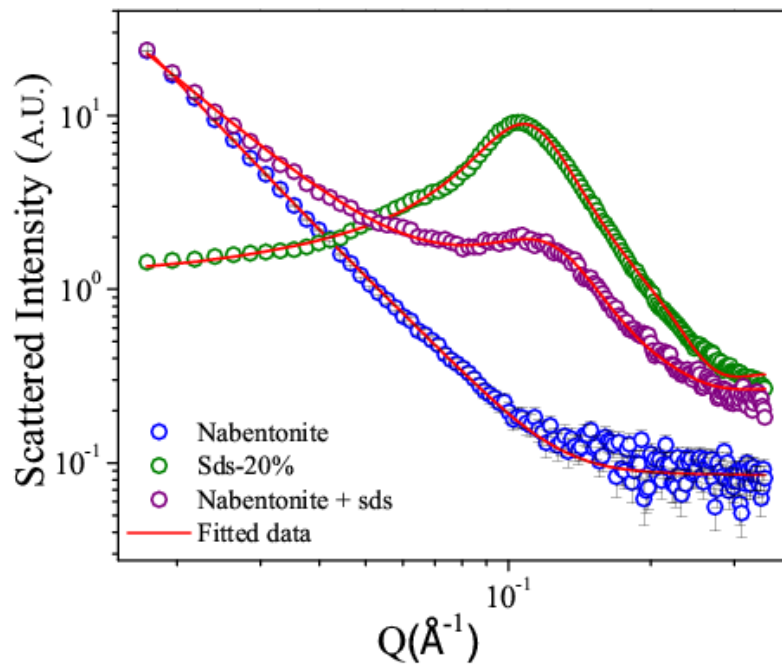


Figure.6.30. SANS data on micellar (20 % SDS) induced bentonite and Na bentonite clay.

The data profile is shown in Figure (6.29) and (6.30). The micelles are found to be prolate ellipsoidal with semi-major and minor axes of 65 Å and 14 Å respectively for 10 % sds solution with an effective charge of 39 e.u. and the aggregation number of 75. The semimajor axis for 20 % SDS solution is 72 Å. With effective charge of 35 e.u. and the aggregation number of 84 and micelle micelle interaction obtained from the peak for 10 % SDS is 69 Å and 60 Å for 20 % SDS and is reduced to 52 Å for a Na bentonite compact loaded with 10 % SDS solution. It is noted that the effective charge on each micelle is the product of the fractional charge on each SDS molecule and the aggregation number or number of molecules constituting a micelle. When the SDS concentration increases from 10% to 20%, the size of each micellar aggregate increases.

However, on account of the reduction of the fractional charge, the effective charge on each micelle decreases. When SDS is loaded in bentonite or sodium bentonite, there is a reduction in fractional charge caused by the positive ions present on the surface of the clay pores e.g. Na^+ which would be attracted to the negative surface of each micelle thereby reducing its net charge as shown schematically in Figure (6.31). Sodium is present in normal bentonite but is enhanced in concentration in the case of sodium-bentonite. The sodium ions affect the fractional charge of each SDS molecule and hence the volume, aggregation number and the effective charge on each of these confined micelles. It is to be noted that the extent of change of fractional charge is not linearly dependent on SDS concentration as borne out by the associated numbers in the case of 20 % SDS compared with 10 % SDS (Table 6.10). The effect of such changes in the fractional charge and aggregation numbers of SDS micelles would be expected to be important when considering the intake and outflow of micellar solutions from clays. The rates of absorption and loss of

the SDS solution from bentonite would thus no longer be merely dependent on gradients of concentration, temperature, pressure etc but also on electrostatic forces present within the nano-pores of the clay.

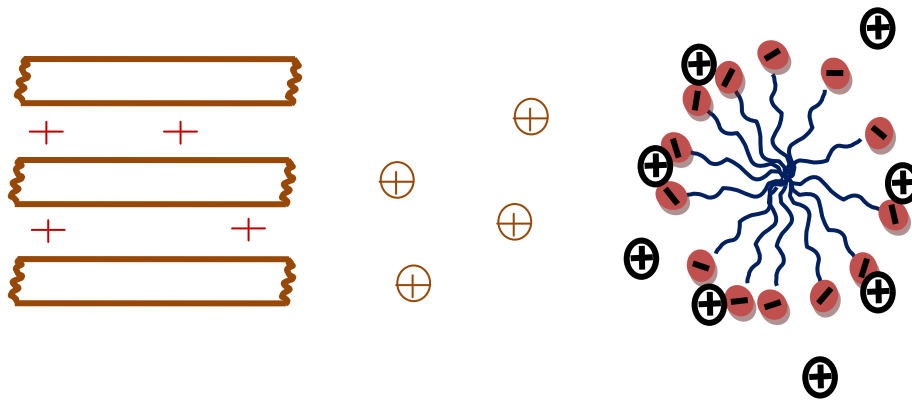


Figure 6.31. Schematic of micellar charge reduction due to Na ion from clay.

6.5.4. Conclusion on micellar solutions in bentonite clay

X-ray diffraction data has shown that the interlayer spacing of clay increases from 12 Å to 19 Å for SDS loaded clay. SANS data has shown that SDS loaded clay shows a decrease in average micelle-micelle separation. From model fits to the SANS data, it is seen that the sodium ion is important in causing the micellar charge to decrease from 39 to 27 e.u for 10 % SDS loaded in clay and in reducing the effective charge from 35 to 10 e.u. for 20 % SDS solution loaded into sodium bentonite. The SANS data shows the broad interference peak to move to a higher Q value implying that mutual micellar repulsion decreases when SDS is confined in sodium bentonite. The interpretation of these data is that there are changes in micellar aggregation, size and effective charge on the micelles when SDS is loaded in sodium bentonite.

6.6. Dynamics of Water in Bentonite Clay

6.6.1. Scientific and Technological Importance

Water diffusion in clay depends on geometry of pores, porosity, tortuosity, constrictivity and by the interaction between water and clay. Behaviour of water in clay is different from that of bulk water and has been studied by various authors [Cebula et al., 1981, Malikova et al., 2006, Skipper et al., 2006]. Diffusion of water in bentonite clay is of fundamental interest to the technology for nuclear waste repositories [Sánchez et al., 2008] as well as in agriculture. Two types of water are found between clay particles; inter-particle water that is important in its effectiveness as a barrier; and interlayer water [Swenson et al., 2002]. The dynamics of water confined in clay minerals is important for the understanding of the properties of water within and the transport mechanisms of dissolved components. This has an important bearing on the containment and disposal of radioactive waste. The study of diffusion and dynamics of water in this clay by quasi-elastic neutron scattering can be used in improving the hydro-chemical behavior of the clay. As compacted bentonite may be used in high level radioactive waste as an additional barrier material for the containment canister. Transport of chemicals by diffusion is important in understanding the geological processes and the diffusion coefficients can be used in the design and evaluation of waste containment barriers [Shackelford, 1991]. Therefore, it is important to determine and understand the diffusion and transport of water in compacted bentonite. The radioactive waste burial site is at several hundred meters below the water table in a drilled tunnel surrounded by rocks. The 50% saturated bentonite is placed around the canister containing waste material. Due to saturation of bentonite very large capillary and electrochemical forces are developed which compresses the clay platelets leading to large swelling pressure of magnitude greater than hydrostatic pressure.

This pressure forces the clay to migrate to the fractures of the surrounding rocks that reduces swelling and removes the material from the protective shield of the clay around the waste canister and stops the migration of radionuclide [Wersin et al., 2007]. The aluminosilicate layer of clay has water retention and ion exchange properties. Interlayer pores of clays provide an ideal environment for the study of confined fluids, and are of relevance to many research subjects, such as cement chemistry, biological interactions, hydro-geological and petrological processes. Bentonite can intercalate water into its layered surface structure. The physical and chemical properties of clay can be related to their layered structures. Radioactive materials can be dissolved in the water and removed by diffusion through interlayer spacing of clay [Marry et.al, 2008]. The schematic of bentonite clay as barrier is as shown in Figure (6.32).

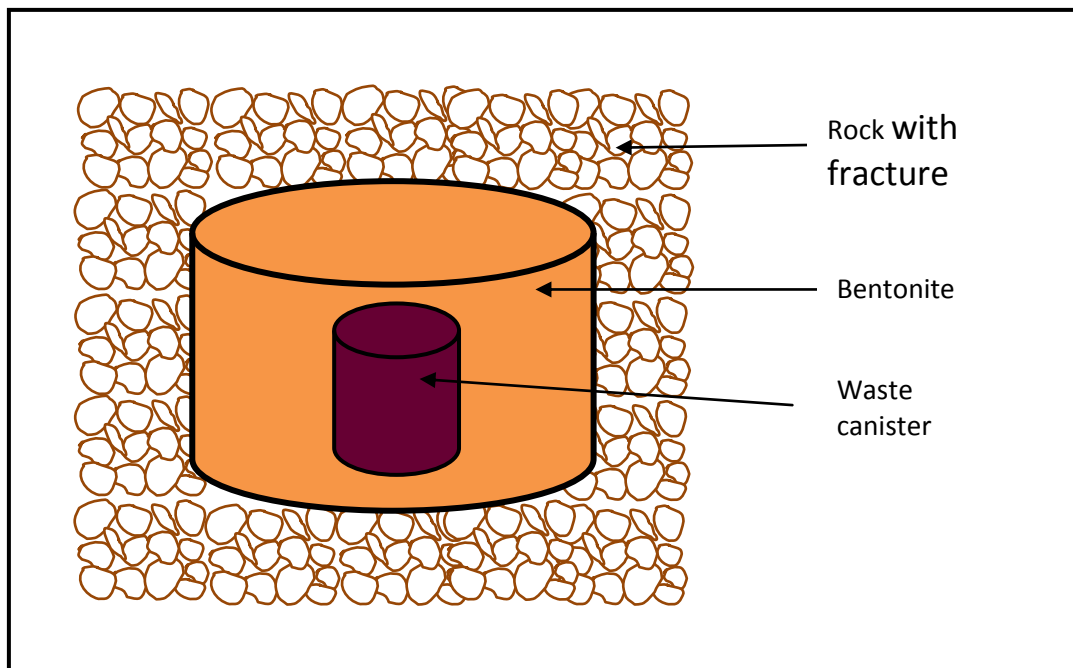


Figure 6.32. Layout of bentonite clay as barrier.

Diffusion of water confined in bentonite clays was studied using the Quasi-Elastic Neutron Scattering (QENS) technique. The crystalline phases of the clay and changes

brought about by hydration were studied by X-ray diffraction. Phase changes as a function of temperature were also followed by Thermogravimetry and Differential Thermal Analysis (TG-DTA). The latter are of use in understanding fluid retention and release in clays.

6.6.2. Experimental Methods:

Dehydration of clay was studied by Thermo-Gravimetric Analysis with Differential Thermal Analysis (TG-DTA) with a NETZSCH STA 409 PC instrument (10 °C/min). The objective here was to follow changes of phase brought about by temperature and loss of bound water in the structure.

Quasi-elastic neutron scattering spectrometer at Dhruva reactor, Trombay [Mukhopadhyay et al., 2001] was used to obtain the diffusion coefficient of water in bentonite clay. In the present configuration this instrument has an energy resolution of 200 μeV with incident neutron energy of 5 meV as obtained from a standard vanadium sample. QENS measurements were recorded on both hydrated as well as dehydrated bentonite clay in the wave vector transfer (Q) range of 0.67 \AA^{-1} to 1.8 \AA^{-1} at 300 K. Data from the dehydrated sample were used to estimate the contribution of the sample other than water. For dehydration, the sample was heated at 420 K under vacuum (15 mb) for a period of about 15 hours. The weight of the sample was recorded before and after the dehydration process. About 12 % sample weight loss was observed after dehydration, which was independently confirmed by TGA.

6.6.3. Results and Discussion.

Phase changes as a function of temperature were followed by TGA-DTA, the data is shown in Figure (6.33). The two-step weight loss observed in the TGA data show that

water which is adsorbed and weakly bound to the surface and inter-lamellar spaces is released at 116 °C. In the second step there is gradual removal of structural OH of clay interlayers and weight loss due to lattice water at about 420 °C (dehydroxilation). A total of 12 % weight loss was observed in the temperature range 100 °C to 420 °C. In the DTA plot, an endothermic peak at 142 °C is attributed to removal of adsorbed and interlayer water of clay. A characteristic endothermic peak of montmorillonite appears at 749°C followed by a small exotherm at about 920°C are present here, which are characteristic of both montmorillonite and illite. This information of hydration and dehydration were useful in obtaining the temperature range which was taken into account for the experimental setting.

This range was taken into account for QENS experimental settings. In a neutron scattering experiment with a hydrogenous sample, the measured intensity is proportional to the incoherent scattering law $S(Q, \omega)$ given by equation (6.7).

$$S(Q, \omega) = A(Q)\delta(\omega) + [1 - A(Q)]L(\Gamma, \omega) \quad (6.7)$$

Here Q is the wave vector transfer and ω is the angular frequency, $A(Q)$ is the amplitude of the elastic peak, $L(\Gamma, \omega)$ is a Lorentzian function with a half width at half maxima (HWHM) Γ . It is convenient to analyse the data in terms of elastic incoherent structure factor (EISF), which is the fraction of the elastic intensity present in the total $S(Q, \omega)$. Therefore, $A(Q)$ in Equation (6.7) is the EISF. Information about the geometry of the molecular motion can be directly obtained by analysing the behaviour of EISF.

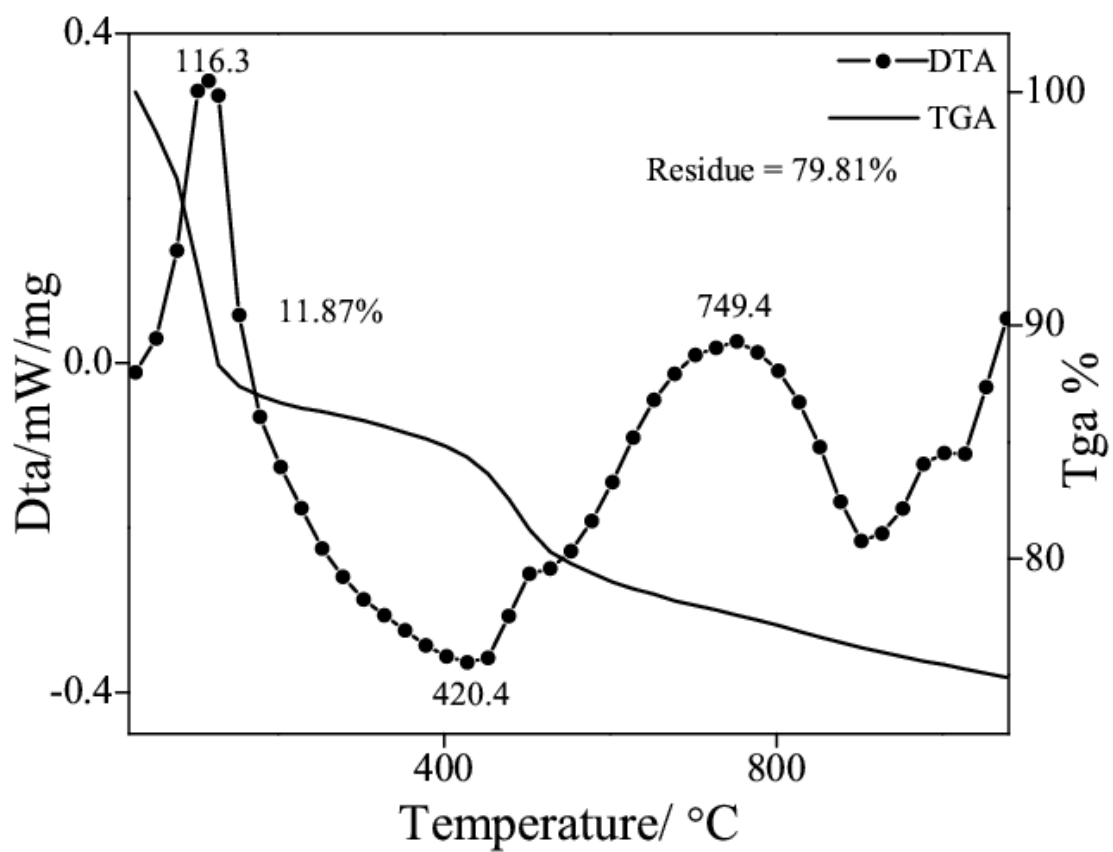


Figure 6.33. Thermogravimetric and Differential Thermal Analysis data of bentonite clay.

The QENS spectra were recorded for both water hydrated and dehydrated bentonite clay. Significant quasi elastic broadening was observed in case of hydrated clay whereas dehydrated clay did not show any broadening over the instrument resolution (Figure 6.34). Thus, the broadening observed in case of water sorbed (hydrated) clay is related to the dynamical motion of water molecules. The dehydrated clay data were used to estimate the elastic contribution from the clay alone. The Elastic and quasielastic contribution from the QENS data were separated by fitting experimental data with the scattering law in Equation (6.7). The parameters, $A(Q)$ and $\Gamma(Q)$ were obtained by least squares fit. The resulting fits for all the measured samples at typical Q values are shown in Figure (6.35). The elastic component other than that from the dehydrated sample was found to be negligible and a single Lorentzian function was good enough to describe the quasielastic part, indicating that the observed dynamics correspond to the translational diffusion of the water molecules. The simplest model of translational motion is Brownian diffusion, and is described by Fick's law ($\Gamma(Q) = DQ^2$), where D is the self-diffusion coefficient of water. Fick's law is not applicable at large wave vector transfer since diffusion process at atomic scale becomes important. This behaviour is described by jump diffusion models where the particle spends considerable time at a site called the residence time (τ), before instantly jump to another site. The distance covered by the particle in a jump is called the jump length. This model of jump diffusion can then be classified depending upon the degree of order in the environment, which in turn determines the distribution of jump lengths. In case of a more disordered environment, the distribution of jump lengths could be random or Gaussian. The corresponding jump diffusions are known as Singwi-Sjölander (SS) [Singwi S., 1960] and Hall and Ross (HR) [Hall and Ross, 1981] jump diffusions respectively. It may be noted that in these two jump diffusion models, the difference is that of a microscopic detail. In case the system is studied at a larger length scales or equivalently at smaller Q values,

the information about finer details is lost and the mechanism of the diffusion resembles to that of Brownian motion. The variation of $\Gamma(Q)$ with Q^2 is therefore linear at low Q values and the diffusion coefficient can be obtained simply from the slope of this curve in the region of small Q values. However, at higher Q values, as finer details of the jump diffusion start to emerge, the variation of $\Gamma(Q)$ with Q^2 remains no more linear and saturates to a value, which is indicative of the residence times involved in the jump process. Both the jump diffusion models have been used earlier to describe water dynamics in clay minerals [Sánchez et al., 2008; Swenson et al., 2002]. In the present case, we have employed both jump diffusion models to describe the variation of experimental obtained $\Gamma(Q)$ with Q^2 . The SS model, which employs a random distribution of jump lengths, variation of $\Gamma(Q)$ with Q^2 is given by [Singwi S., 1960]. The HR model assumes a Gaussian distribution of jump length, which results the variation of $\Gamma(Q)$ [Hall and Ross, 1981].

The variation of I , as obtained from QENS data, with Q^2 is shown in Figure (6.36). The solid and dashed lines in Figure (6.36) correspond to the least squares fit with (SS model) Equation (2.44) and 3 (HR model) Equation (2.42) respectively.

Table 6.12. Comparison of the residence time (τ) and diffusion coefficient (D) obtained for water molecules in different clay systems along with bulk water.

System	Interlayer spacing (\AA)	SS model		HR model	
		D_{SS} ($\times 10^{-5} \text{cm}^2/\text{sec}$)	τ_{SS} (ps)	D_{HR} ($\times 10^{-5} \text{cm}^2/\text{sec}$)	τ_{HR} (ps)
Sodium Bentonite [Present work]	13	1.8 ± 0.3	3.6 ± 0.4	1.7 ± 0.2	5.0 ± 0.5
Native saponite [Chakrabarty et al.,2006]	14	1.3 ± 0.3	4.5 ± 1.0	1.2 ± 0.3	6.2 ± 1.0
Intercalated saponite [Chakrabarty et al.,2006]	18	1.8 ± 0.4	3.6 ± 1.0	1.5 ± 0.3	5.0 ± 1.0
Na-Montmorillonite [Sánchez et al.,2008]	14.8	1.21 ± 0.12	11.9 ± 1.0	0.98 ± 0.05	13.8 ± 0.6
Na-Montmorillonite					
Kaolinite [Sánchez et al.,2008]	7.16	2.81 ± 0.19	2.1 ± 0.1	2.50 ± 0.12	2.8 ± 0.1
Bulk water [Sánchez et al.,2008]	-	2.37 ± 0.08	1.0 ± 0.06	2.30 ± 0.10	1.6 ± 0.1

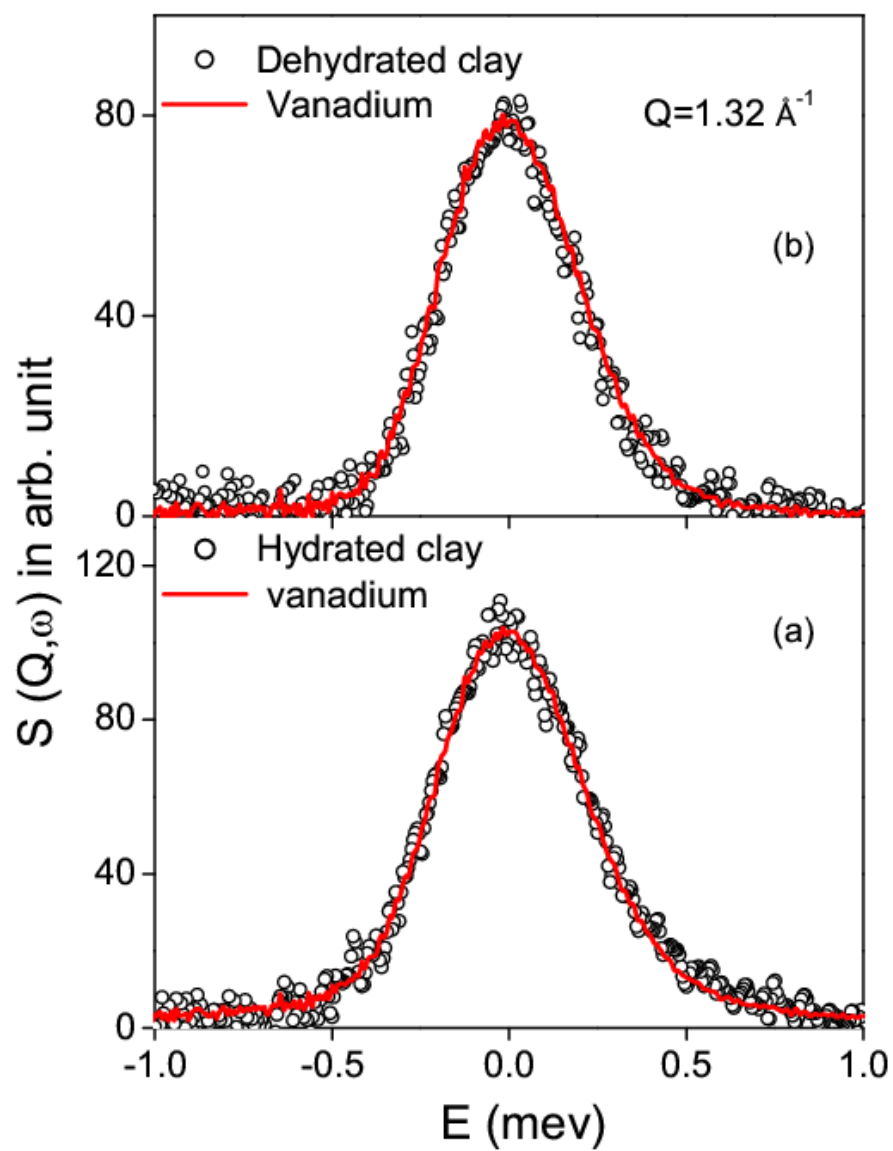


Figure 6.34. Fitted QENS spectra from the hydrated and dehydrated bentonite clay at $Q = 1.32 \text{ \AA}^{-1}$.

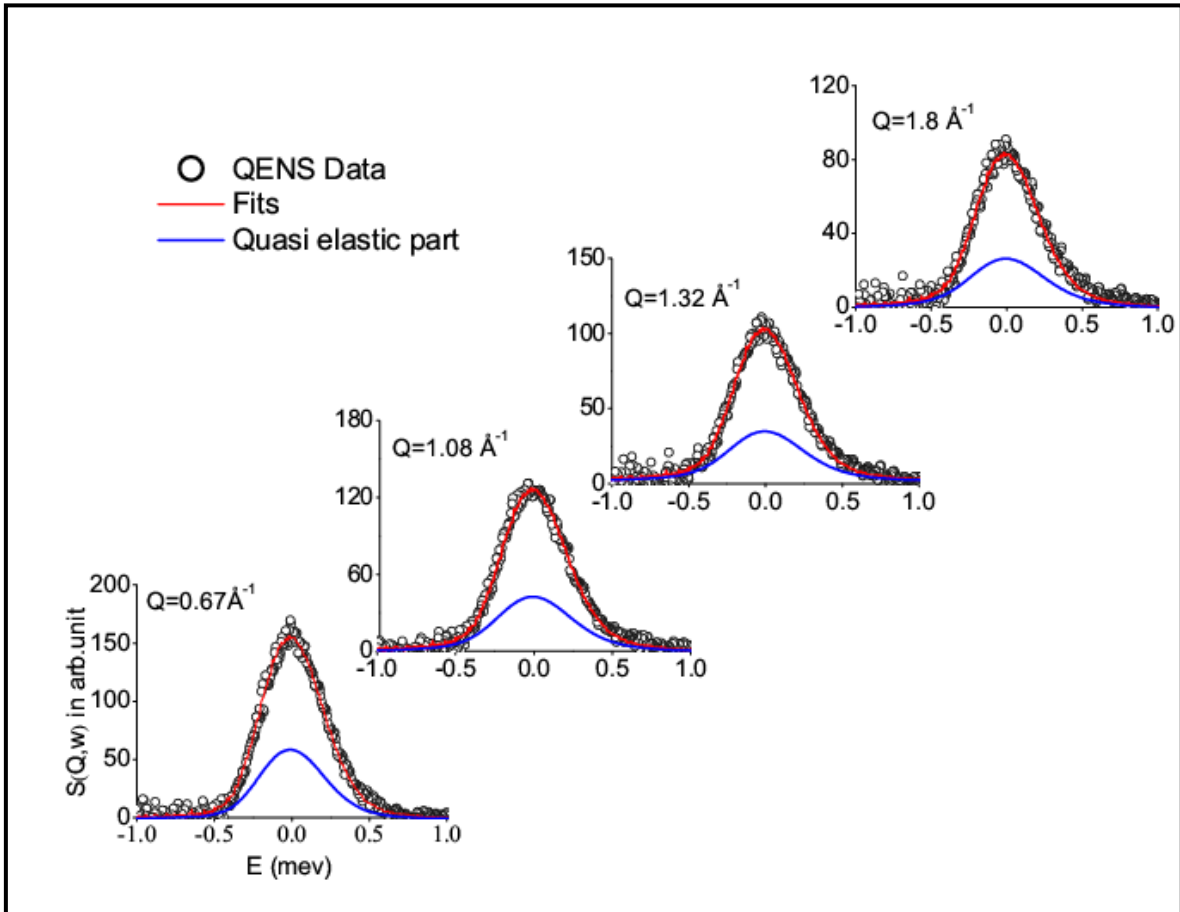


Figure 6.35. Fitted QENS spectra from the hydrated bentonite clay at different Q values.

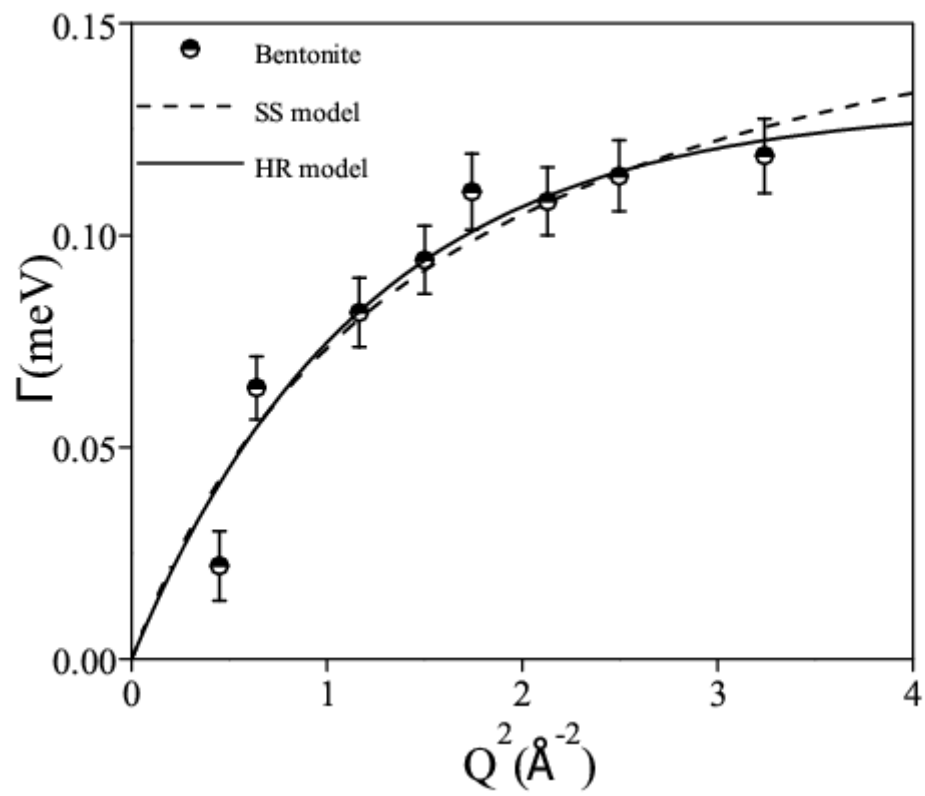


Figure 6.36. Variation of HWHM, Γ with Q^2 .

6.6.4. Conclusions on diffusion of water in bentonite clay

The QENS experiment has been carried out on hydrated as well as dehydrated clay using the QENS spectrometer at Dhruva reactor, Trombay at 300 K. Significant quasi-elastic broadening was observed in case of hydrated bentonite clay whereas dehydrated clay did not show any broadening over the instrument resolution. Analysis of QENS data reveals that diffusion of water occurs through jump diffusion characterized by random distribution of jump lengths. Translational diffusion coefficient of water in bentonite clay is found to be smaller than that of bulk water at room temperature and a higher residence time of.

We have studied dynamics of water in natural bentonite clay using neutron scattering technique. It is found that the motion of the water can be described by random jump diffusion model. Values of residence-time, jump length and diffusion coefficient of confined water have been obtained and compared with bulk water. The dynamics of water in clays is found to be hindered in comparison to the bulk phase. This can be explained in terms of the effect of the confinement and attractive interaction with the clay.

6.7. Conclusions on studies of porous clay

Kaolinite is a non swelling clay. Thus when hydrated there is no change in d-spacing. There was a loss of weight of 12 mg when the clay was completely dehydrated at approximately 525 °C. Micron-sized pores were found to decrease in size when the clay was compacted and sintered. The surface area of the clay was obtained by nitrogen adsorption porosimetry and was found to be equal to 6.0918 m²/g. The isotherm is of type II while the hysteresis was of H3 type indicating that the material was macroporous. The type II isotherm represents unrestricted monolayer-multilayer adsorption and H3 type hysteresis indicates that the particles are plate-like. The average pore size of loose clay was

21 nm and when compacted it was decreased to 13 nm. From the Guinier plot of the MSANS data, the radius of gyration was found to 32 nm, while from SANS the pore size was 13 Å. The connectivity between pores of all sizes was verified from the fact that the intensity was found to decrease when D₂O was loaded in the clay compact. This happens when the fluid that is loaded into the clay causes a lowering of the contrast factor between the clay matrix and the nano-pores filled with this fluid.

The swelling clay Bentonite was studied in detail on account of its various applications. The hydration of a bentonite clay was studied by XRD and SANS on the dry, partially hydrated and fully hydrated clays. The major phase in bentonite was found to be that of montmorillonite with some presence of kaolinite, calcite and quartz as minor phases. Due to hydration the interlayer spacing was found to increase from 9.8 Å to 20 Å. When fully hydrated, the clay partially transforms to an amorphous phase. The peaks of kaolinite, calcite and quartz are replaced by an amorphous phase. The only peaks present are those due to montmorillonite. The presence of water causes swelling within the layers with the observed structural changes. The partially hydrated bentonite (5:1 ratio) shows crystalline as well as amorphous phases. This leads to exfoliation of the clay layers. In addition, the presence of OH groups may be causing existing pores to lengthen. SANS data confirm that the level of hydration of the layered crystalline structure is as expected and is likely to be due to hydroxyl ions within the crystalline layers of montmorillonite.

From SANS the pore size in clay is found to decrease with compaction pressure. It is likely that at 10 T compaction pressure the clay platelets are forced together with the creation of a new and smaller pores in addition to bigger pore formation due to coalescence. The fired compacts loaded with D₂O and the combination of H₂O plus D₂O show that the intensity runs parallel to the dry compact. This indicates that the mixture fills

the nano pores in a uniform fashion on account of connectivity between pores. From this finding, a possible application for the fired clay compact would be to store plant nutrients, water, pesticides etc which can be later released slowly to the surrounding environment depending upon the changes in temperature, humidity, pressure, chemical potential etc. This will not cause harm to the soil or environment as the clay would become part of the soil with time. Interlayer spacing in clay is increased from 12 Å to 19 Å for SDS loaded clay. SANS data has shown that SDS loaded clay shows a decrease in average micelle-micelle separation. From model fits to the SANS data, it is seen that the sodium ion is important in causing the micellar charge to decrease from 39 to 27 e.u for 10% SDS loaded in clay and in reducing the effective charge from 35 to 10 e.u. for 20% SDS solution loaded into sodium bentonite clay. Thus, the mutual micellar repulsion decreases when SDS is confined in sodium bentonite. This indicates that there are changes in micellar aggregation, size and effective charge on the micelles when SDS is loaded in sodium bentonite.

Diffusion of water in bentonite clay was studied by Quasi-elastic Neutron Scattering (QENS) on hydrated and dry clay. The diffusion of water occurs through jump diffusion characterized by a random distribution of jump lengths. Translational diffusion coefficient of water in bentonite clay was found to be $1.8 \times 10^{-5} \text{ cm}^2/\text{s}$, which is smaller than that of bulk water ($2.5 \times 10^{-5} \text{ cm}^2/\text{s}$) at room temperature and a residence time of 3.6 ps. The dynamics of water in clays was found to be hindered in comparison to the bulk phase. This can be explained in terms of the effect of the confinement and the attractive interaction with the clay.

Chapter 7

Conclusions and Future Studies

7.1. Conclusions

Three different types of porous materials have been studied in this work. These have different potential applications owing to their compositions and bulk physical and chemical properties. The porous materials were, a ceramic, a compacted porous glass and kaolinite and bentonite clay.

The first material was a ceramic powder prepared by the sol-gel method from silica which was derived from rice husk as its source. The powder was compacted and sintered at different temperatures and times. In the rice husk silica ceramic the glassy phase was converted to a purely crystalline phase at 1000 °C. The ceramic compacts were found to have a hierarchical range of pore sizes – from macroscopic to nanometric dimension. Bulk porosity was found to vary from 32 to 47 %. Micrometric (~ 0.5 to 2.5 μ m) pore sizes were evident from SEM micrographs which shows that in this range, pore size increases with sintering temperature. The pores were found to coalesce under higher sintering temperature and compaction pressure causing the number of bigger pores to diminish. Two distinct zones in the scattering profile indicated scattering from two different length scales. The pores were modelled assuming polydispersed spherical geometry for the scattering centres. The fits show good agreement with measured data at all Q values and with a small Chi Square value. MSANS on all the dry ceramics has shown the presence of two pore size domains of ~ 166 nm and 32 nm where smaller pores are arranged in mass fractal morphology having a fractal dimension between 2.80 to 2.97. The bigger pores are inter particle voids and smaller sizes are intra particle pores. The pore densities of the larger and

smaller sized pores were found to be respectively 1.3 to 7.2×10^{10} /cc and 1.5 to 10×10^{11} /cc respectively. The pore size gets significantly modified with sintering temperature and compaction pressure, but almost no significant change in pore radius is observed when sintered at different times. Interconnectivity between the pores was ascertained from compact loading with heavy water and subjecting it to MSANS. The decrease in intensity profile indicates that the heavy water absorbed by the ceramic is found to percolate evenly into the nano-sized pores without appreciably changing their morphology. The high fractal dimensions of these materials in the nano-metric range coupled with the fact that these pores admit water indicates that there are relatively small numbers of such pores (eg. 10^{11} /cc) with good connectivity to each other. The fluid permeability and the pore size suggest that this material may be a promising candidate for applications as a filter or as a catalytic surface. Using a contrast matching technique, an attempt was made to estimate the density of isolated pores in the compact. Such a contrast matching experiment was performed using a mixture of H_2O and D_2O in the right proportion to match the scattering length density of the matrix. The number of Isolated pores were obtained to a first approximation and were found to decrease with sintering temperature.

The second material was a porous glass composed of compacted silica microspheres. Silica microspheres of diameter 100 and $20 \mu m$ were first compacted and then sintered to form a rigid compact that can have applications in filtration of gases and liquids. Porosity of these compacts was found to vary with sintering time and temperature in range 45% to 32% . The pore shape depends on the number of neighbouring spheres. As the spheres coalesce with each other with increase in sintering time, the number of pores reduces. Microstructural change and micropores were observed by SEM. The densification process with sintering time leads to agglomeration of nearest-neighbour microspheres, causing some of the smaller pores to disappear while other existing pores to become larger

and possibly more interconnected. SANS data indicate a fractal-like agglomerate structure within this compact from the power law behaviour of scattered intensity over a wide wave vector transfer range. The pore sizes obtained from these data had radii ~173 nm and 51 nm for a compact sintered at 640 °C for 3 hours. This was found to be modified at higher sintering times. An interference peak obtained at higher Q corresponds to interpore separation and was found to be shifted at higher Q for increase in sintering time. The connectivity of pores was studied by loading the compact with heavy water and studying its intensity pattern. Pores in the compact are interconnected with channels. The decrease in intensity due to the lower scattering length density contrast caused by D₂O filling the pores indicated that the D₂O not only fills the micron sized pores but also occupies the pores of nano dimension. These findings are of relevance in separation and filtration applications. One can fill these open channels with absorbents as well as other materials, thus providing a confined environment for the solvent and a new type of glass-absorbent composite. By a SANS contrast matching experiment an estimate of the density of isolated pores is found to be three times lower than other pores. The rate of mass loss from a compact loaded with water was studied at different temperatures using thermogravimetry. For a compact sintered at 640 °C for 3 hours and loaded with H₂O, a 3rd order polynomial fit to the data, gave the rate of mass loss of 3.33282×10^{-4} mg/sec and 6.13906×10^{-4} mg/sec for compacts sintered at 35 °C and 50 °C respectively. The rate of weight loss at 50 °C is almost double that at 35 °C indicating that there is faster evaporation from the pores as the temperature rises. At higher temperatures the asymptotic weight loss was attained rapidly. An exponential was fitted to the dehydration points (times at which the asymptotic values are within a few percent of being reached) at different temperatures and found that the sample sintered for 3 hours losses all its absorbed water in a time that is 45% shorter than the time taken for the 24 hour sintered sample to dehydrate. Thus, it may be surmised

that the sample that was sintered for a longer time had 45 % fewer interconnections to the surface. It is likely that this percentage of fewer connections also occurs in the bulk of the compact. Although the loss of interconnections was expected from a qualitative assessment, the quoted percentage loss is considerably higher than expected. A bimodal distribution of pore size distribution was also obtained from MIP.

The third material was clay, a swelling (bentonite) and non swelling (kaolinite). Clays are complex hierarchical and deformable porous media whose structures and organizations vary at different spatial scales and on external conditions, particularly water environment. The clay porosity was studied as a function of its hydration. The variation of porosity with compaction pressure was also studied. The effect on a micellar solution within clay was studied by loading a compact with SDS solution as well as the diffusion coefficient of water in bentonite clay. The clays that were studied were bentonite (swelling clay) and kaolinite (non swelling clay). The hydration of a bentonite clay has been studied by XRD and SANS studies on the dry, partially hydrated and fully hydrated clays. The major phase in bentonite was found to be that of montmorillonite with some presence of kaolinite, calcite and quartz as minor phases. The interlayer spacing increases from 9.8 Å to 16 Å as the hydration progresses. As the hydration proceeds to the fully hydrated state, the first three phases get progressively replaced by an amorphous phase while montmorillonite is retained. Thus, included water is likely to cause the phases other than montmorillonite to become amorphous. This leads to exfoliation of the clay layers. In addition, the presence of OH groups may be causing existing pores to lengthen. SANS data confirm that the level of hydration of the layered crystalline structure is as expected and is likely to be due to hydroxyl ions within the crystalline layers of montmorillonite.

Nano pore size variation in bentonite compacted at different pressures were studied by SANS. Pore size is found to decrease with compaction pressure. It is likely that at 10 T compaction pressure the clay platelets are forced together with the creation of smaller pores apart from bigger pore formation due to coalescence. The intensity pattern of compacts loaded with D₂O and the combination of H₂O plus D₂O runs parallel to the dry compact indicating that the mixture fills the nano pores in a uniform fashion showing connectivity in between pores. The fired clay compact can be used to store plant nutrients, water, pesticides etc which can be released slowly to the surrounding environment depending on the gradients between the compact and surroundings such as temperature, humidity, pressure, chemical potential etc. Since the matrix to store the water / nutrients would be clay, no harm to the soil or environment would be caused by the clay which could be chosen to be of the same material as the soil or fully compatible with it. Interlayer spacing in clay is increased from 12Å to 19Å for SDS loaded clay. SANS data has shown that SDS loaded clay shows a decrease in average micelle-micelle separation. From model fits to the SANS data, it is seen that the sodium ion is important in causing the micellar charge to decrease from 38 to 27 e.u for 10% SDS loaded in clay and in reducing the effective charge from 35 to 14 e.u. for 20% SDS solution loaded into sodium bentonite clay. Thus, the mutual micellar repulsion decreases when SDS is confined in sodium bentonite. This indicates that there are changes in micellar aggregation, size and effective charge on the micelles when SDS is loaded in sodium bentonite.

Diffusion of water in bentonite clay was studied by Quasi-elastic Neutron Scattering (QENS) experiment on hydrated and dry clay. The diffusion of water occurs through jump diffusion characterized by random distribution of jump lengths. Translational diffusion coefficient of water in bentonite clay is found to be $1.8 \times 10^{-5} \text{ cm}^2/\text{s}$, which is smaller than that of bulk water ($2.5 \times 10^{-5} \text{ cm}^2/\text{s}$) at room temperature. It is found that the

motion of the water molecule can be described by the random jump diffusion model. The values of residence-time and diffusion coefficient of confined water were found to be 3.6 ± 0.4 ps, and $1.8 \pm 0.3 \times 10^{-5}$ cm²/sec respectively and were shown to be smaller than such values in bulk water. The dynamics of water in clays was found to be hindered in comparison to the bulk phase. This can be explained in terms of the effect of the confinement and attractive interaction with the clay.

7.2. Future Studies

The results obtained from the SEM and the SANS investigations can provide useful input information for preparing and tailoring various materials with specific properties. The important properties of these systems like dielectric measurements and mechanical strength could be studied for various applications such as insulators and higher strength materials. The estimate of isolated pores by the SANS technique represent a unique method of estimating these concentrations which are important in certain bulk properties such as tensile strength, insulating character etc. Attention to proper corrections in these estimation needs to be carefully considered. The ceramic could be tested with Simulated Body Fluid solution as part of bone regenerative studies. In the diffusion studies of water in bentonite, different hydration states could be examined for variations in diffusion constant, residence time, diffusion length in order to better understand the process of diffusion in this material. Diffusion studies can also be done on rock samples to obtain information about the amount of water or oil that can be contained in a given volume of rock sediment. The experience gathered from these works will enable us in future to correlate the different physical properties of a material with its mesoscopic structures obtained from SAS, e.g., behaviour of the dielectric properties and/or the fracture

toughness of a ceramic with its pore structure and porosity, the variation of the strength of cement or concrete with modification of pore structure during the hydration reaction etc.

REFERENCES

- Adler P.M., Porous Media, Geometry and Transports. Butterworth-Heinemann, Woburn: Mass, (1992).
- Alemdar A., Atıcı O. and Güngör N., Materials Letters, 43 (2000) 57 - 61.
- Anselmetti D., Nat. Nanotech., 7 (2012) 81 - 82.
- Aswal V. K., Goyal P. S. and Kohlbrecher J., Chem. Phys. Lett., 349 (2001) 458 - 462.
- Aswal V. K. and Kohlbrecher J., Chem. Phys. Lett., 425 (2006) 118 - 122.
- Aswal V. K. and Goyal P. S., Curr. Sci. India, 79 (7) (2000) 947 - 953.
- Aswal V. K., Kohlbrecher J., Goyal P. S., Amenitsch H. and Bernstorff S., J. Phys.: Condens. Matter, 18 (2006) 11399 - 11410.
- Athy L.F., Bull. Amer. Assoc. Petrol. Geol., 14 (1930) 1 - 24.
- Ayari F., Srasra E. and Trabelsi-Ayadi M., Desalination, 185 (2005) 391 - 397.
- Barrett E.P., Joyner L.G. and Halenda P.P., J. Amer. Chem. Soc., 73 (1951) 373 - 380.
- Bear J., Dynamics of fluids in porous media, Elsevier: New York, (1972).
- B'ee M., Quasielastic Neutron Scattering: Principles and Applications in Solid State Chemistry, Biology and Materials Science, Adam Hilger: Bristol, (1988).
- Bhattacharyya K. G. and Sen Gupta S., Chem. Eng. Journal., 136(1) (2008) - 13.
- Brakel J. V. and Heertjes P. M., Int. J. Heat Mass Transfer, 17 (1974) 1093 - 1103.
- Brandon N. P. and Brett D. J. Phil. Trans. R. Soc. A., 364 (2006) 147 - 159.
- Breen C., Watson R., Madejovà J., Komadel P. and Klapyta Z., Langmuir, 13(1997) 6473 - 6479.
- Brinker C. J., Sehgal R., Hietala S.L., Deshpande R., Smith D. M., Lop D. and Ashley C. S., J. Membr. Sci., 94 (1994) 85 - 102.
- Brinker C.J., Keefer K.D., Schaefer D. W. and Ashley C. S., J. Non-Crystalline Solids, 48 (1982) 47 - 64.

- Brunauer S., Pure & Appl. Chem., 48 (1976) 401 - 405.
- Brunauer S., Emmett P.H. and Teller E., J. Amer. Chem. Soc., 60 (1938) 309 - 319.
- Cacciotti I., Lombardi M., Bianco A., Ravaglioli A. and Montanara L., J. Mater Sci. Mater Med., 23 (2012) 1849 - 1866.
- Carrasco M.F., Mendiratta S.K. and Ferreira J.M., Eur. Phys. J. Appl. Phys. 30 (2005) 91 - 99.
- Cebula D.J., Thomas R.K. and White J.W., Clay and Clay minerals, 29 (1981)241-248.
- Chakrabarty D., Gautam S., Mitra S., Gil A., Vicente M. A. and Mukhopadhyay R., Chem. Phys. Lett., 426 (2006) 296.
- Chathoth S. M., Mamontov E., Kolesnikov A. I., Gogotsi Y. and Wesolowski D. J., EPL, 95 (2011) 56001.
- Chawla N. and Deng X., Materials Science and Engineering A., 390 (2005) 98 - 112.
- Chodankar S., Aswal V. K., Kohlbrecher J., Vavrin R., and Wagh A. G., Phys. Rev. E, 77 (2008) 031901.
- Chudley C.T. and Elliott R.J., Proceedings of the Physical Society of London, 77 (1961) 353.
- Clark D. A. and Moyer J. E., An evaluation of tailings ponds sealants, Environmental Protection Agency: report, (1974).
- Collins R. E., Flow of fluid through porous materials: Penn well publishing company, (1976).
- Crank J., The Mathematics of Diffusion, Pergamon Press: Oxford, (1975).
- David A. L., App. clay sci., 34 (2006) 74 - 87.
- De Boer J. H., Lippens B.C, Linsen B.G., Broeckhoff J.C.P., Van den Heuvel A., and Onsinga T.V., J. Colloid Interface Sci., 21 (1966) 405.
- Debra R. R., Catal. Rev., 299 (2003) 1698 - 1701.

- Dentel S.K., Bottero J.Y., Khatib K., Demougeot H., Duguet J.P. and Anselme C. *Water Res.*, 29 (1995) 1273 - 1280.
- Desa J.A.E., Ali K.S., Pavlovic A.S., Crystallinity and hydrogen content of illites, *Am. Crystal. Asso., Meeting Columbia, Missouri*, (1983).
- Eduardo E. A. and Rafaela C., *Front. Archit. Civ. Eng. China*, (2010).
- Elizabeth C. D., Oomman K. V. Keat G. O., Dawei G., Maggie P. and Craig A.G., *Sensors*, 2 (2002) 91 - 110.
- Elliot S. R., *Physics of Amorphous Materials*, Longman group Ltd., (1984).
- Ewais E. M. M., Ahmed Y.M.Z. and Ameen A.M.M., *J. Ceram. Process. Res.*, 10 (2009) 721 - 728.
- Fátima G. S., *Water diffusion through compacted clays analyzed by neutron scattering and tracer experiments*, Thesis (2007).
- Fink D. H. and Nakayama F. S., *Soil Sci.*, 114 (1972) 355 - 358.
- Fink D. H., *Clays and Clay Minerals*, 25 (1977) 196 - 200.
- Frost R. and Hongping H., Yang D., Yuan P. and Shen W. J. *Colloid Interface Sci.* 297 (2006) 235 - 243.
- Fukasawa T., Deng Z.Y. and Ando M., *J. Mater. Sci.*, 36 (2001) 2523 - 2527.
- Gabriela P., Otilia S. B. and Vlad-Oros B., *Biosensors for Health, Environment and Biosecurity*: publisher Intech, (2011).
- Glatter O. and Kratky O., *Small-Angle X-ray Scattering*, Academic press: London, (1982).
- Gough J. E., Clupper D.C. and Hench L.L., *J. Bio. Mater. Res.*, 69 A (2004) 621 - 628.
- Goyal P. S. and Aswal V. K., *Curr. Sci.*, 80(8) 2001.
- Greenwood N.N. and Earnshaw, A., *Chemistry of the Elements*, Pergamon Press: Oxford, (1984).

- Grim R. E., Clay Mineralogy, McGraw-Hill: New York, (1968).
- Guinier A. and Fournet G., Small-Angle Scattering of X-rays, Wiley: New York, (1955).
- Gülten A. and Kadir M. Y., Turk J. Chem., 23 (1999) 105 - 113.
- Güngör N., Alemdar A., Atici O. and Ece I.O., Materials Letters, 51 (2001) 250 – 254.
- Hall P. L. and Ross D.K., Mol. Phys., 42 (1981) 673.
- Hardin H.A. and Beckermann C., Proceedings of the 60th SFSA technical and operating conference, Paper No.4.3, steel founders, society of America, Chicago, IL (2006).
- Hardin R. A. and Beckermann C., Proceedings of the 61th SFSA technical and operating conference, Paper No.5.8, steel founders, society of America, Chicago, IL, (2007).
- Hilfer G., IAF abstracts, 34th COSPAR Scientific Assembly, The Second World Space Congress, Houston: TX, USA, (2002).
- Holtz W.G. and Bara J.P., International Research and Engineering Conference on Expansive Clay Soils, Texas A & M Press: California, (1965) 120 - 151.
- Huaming Y., Yuehua D., Chunfang D. and Shengming J., App. Clay Sci. 47 (2010) 351 - 355.
- İkrâm N. and Akhter M., J. Mater. Stieme., 23 (1988) 2379 - 81.
- İsci S., Unlu H. C., Atici O. and Gungor N., Bull. Mater. Sci., 29(5) (2006) 449 - 456.
- Jae-Jun P. and Young-Bum P., Trans. Elec. Electro. Mater. 12 (3) (2011) 93 - 97.
- JNC, Safety assessment of the geological disposal system. Supporting report 3. In H12 Project to establish technical basis for HLW disposal in Japan. JNC Tech. Rep., JNC TN1410 2000-004.

- Jobic H., Recent Advances in Gas Separation by Microporous Ceramic Membranes In: Kanellopoulos, N.K. (Ed.): Elsevier, (2000) 109 - 137.
- Jobic H. and Theodorou D.N., Micropo. Mesopo. Mate., 102 (2007) 21 - 50.
- Kalapathy U., Proctor A. and Shultz J., Bioreso. Tech., 73 (2000) 257 - 264
- Kan-Sen C., Tzy-Kuang L. and Feng-Jiin Li., Sensors and Actuators B 56 (1999) 106 - 111.
- Kikkinides E. S., Stoitsas K. A. and Zaspalis V. T., J. Colloid Interface Sci., 259 (2003) 322 – 330.
- Kikkinides E.S., Stoitsas K.A., Zaspalis V.T. and Burganos V.N., J. Membr, Scie., 243 (2004) 133 - 141.
- Kim J., Sunhwa L. and Dongwook S., J. Ceram. Proce. Res., 8 (3) (2007) 208 - 212.
- Klein L.C. and Garvey G.J., J. of Non-Crystalline Solids, 38 (1980) 45.
- Koponen A., Kataja M. and Timonen J., Int. J. of Mod. Phy., 9(8) (1998) 1505 - 1521.
- Kumar Singh R., Srinivasan E.A. and Kothiyal G.P., J Mater Sci. Mater Med., 20 (2009) S147 - S151.
- Kumar S. and Aswal V. K., J. Phys.: Condens. Matter, 23 (2011) 035101.
- Kumar S., B. Sol-gel synthesis and in vitro characterization of bioactive glass ceramics using rice husk ash waste material Department of Ceramic Engineering, Tech thesis, NIT Rourkela, (2009).
- Kurama H. and Kurama S. K., 18 International Mining Congress and Exhibition of Turkey IMCET, 3 (2003) 431 - 435.
- Kurama S. and Kurama H., Ceramics International, 34 (2008) 269 - 272.
- Lee J., Han S. and Hyeon T., J. Mater. Chem. 14 (2004) 478 - 486.
- Lemaitre J., Troadec J. P., Bideau D., Gervoist A. and Bougaul E., J. Phys. D: Appl. Phys., 21 (1988) 1589 - 3592.

- Lorenzo B., Giampaolo M., Lifeng L., Woo L., Ulrich G., and Benoit C., *Langmuir*, 26(14) (2010) 11894 - 11898.
- Lucilene B. P., Ana Rita Morales A. R., Díaz F. R.V., *App. Clay Sci.* 42 (2008) 8 - 24.
- Maciej M., Arzhang K. and Zbigniew K., *Phys. Rev. E*, 78 (2008) 026306.
- Malikova N., Cadene A., Marry V., Dubois E. and Turq, P., *Phys. Chem. B* 110 (2006) 3206 - 3214.
- Marry V., Malikova N., Cadene A., Dubois, E., Durand-Vidal S., Turq P., Breu J., Longeville S. and Zanotti J. M., *J.Phys. Condens., Matter*, 20, (2008) 104205.14.
- Martin B. and Ola K., *Geochimica et Cosmochimica Acta*, 73 (2009) 1908 - 1923.
- Matamoros-veloza Z., Yanagisawa K., Rendon-angeles J.C. and Yamasaki N., *J. Mat. Sci. Let.*, 21 (2002) 1855 - 1858.
- Mazumder S., Sen D. Saravanan T. and Vijayaraghavan P.R., *Curr. Sci.*, 81 (2001) 257 - 262.
- Mazumder S., Sen D., Saravanan T. and Vijayaraghavan P.R., *J. Neutron Res.*, 9 (2001) 39-57.
- Mazumder S., Sen D., Saravanan T. and Vijayaraghavan P.R., *Applied Physics A Mat. Sci. & Proc.*, 74 (2002) S183 – S185.
- Mazumder S., Sen D. and Patra A. K., *J. Phys.*, 63(1) (2004) 165 - 173.
- Melkior T., Mourzagh D., Yahiaoui S., Thoby D., Alberto J.C., Brouard C. and Michau N., *Appl. Clay Sci.*, 26 (2004) 99 - 107.
- Meyers J., Nahar S., Ludlow D.K. and Liapis A.I., *J. Chroma A*, 907 (2001) 57 - 71.
- Mielenz R.C. and King M.E., *National Conference on Clays and Clay Technology*, 1st, Berkeley: California, 169 (1955) 196 - 254.
- Miguel A. F., *Contribution to flow characterization through porous media. Int. J. Heat Mass Transf.*, 43 (2000) 2267 - 2272

- Miller C.J., ASCE M., Yesiller N., ASCE A.M., Yaldo K. and Merayyan S., *Journal of Geochemical and Geotechnical Engineering*, 128 (9) (2002) 733 - 742.
- Mitchell J.K., *Fundamentals of Soil Behavior*, John Wiley & sons, Inc.: New York (1976).
- Mitra S., Pramanik A., Chakrabarty D., Jurányi F., Gautam S. and Mukhopadhyay R., *J. Phy.: Conf. Ser.*, 92 (2007) 012167
- Mohanty A. Patra T and Dey J. J. *Phys. Chem. B*, 111 (2007) 7155 - 7159.
- Montes H.G., Duplay J., Martinez L. and Mendoza C., *Appl. Clay Sci.*, 22 (2003) 279 - 293.
- Mujeebu M. A., Abdullah M. Z., Abu Baker M. Z., Mohamad A. A., Muhad R. M. N. and Abdullah M. K., *J. Env. Manage.*, 90 (2009) 2287 - 2312.
- Mukhopadhyay R., Mitra S., Paranjpe S.K. and Dasan- nacharya B.A. (2001) *Nuclear Instrumentation Method A*, 474 (2001) 55 - 66.
- Mukhopadhyay R. and Mitra S., *Indian J. Pur. & Appl. Phy.*, 44 (2006) 732 - 740.
- Nakahara S., *Thin Solid Films*, 64 (1979) 149 - 161.
- Nayak J.P. and Bera J., *Phase Transitions.*, 82 (2009) 879 - 888.
- Newman A.C.D. and Brown G., *The chemical constitution of clays, Chemistry of Clays and Clay Minerals*, Mineralogical Society Monograph, 6. Longman Technical and Scientific, Harlow, Essex, UK. (1987) 1–128.
- Nithya S. C., Rakesh G., Mahato A. K., *Int. J. Pharm. Tech Res.*, 2(1) (2010) 675 - 681.
- Nuntiya A., Sompech S., Aukkaravittayapun S. and Pumchusak J., *Chiang Mai J. Sci.*; 35 (1) (2008) 199 - 20.
- Olny X. and Boutin C., *J. Acoust., Soc. Am.*, 114 (2003) 73 - 89.
- Onal M. and Sarikaya Y., *Powder Technol.*, 172 (2007) 14 - 18.

- Paluszkiwicz C., Holtzer M. and Bobrowski A., *J. of Molecular Structure*, 880 (2008) 109 - 114.
- Parcher J.V. and Liu PCh., *J. Soil Mech., Foundations Division* 91(SM3) (1965) 1 - 17.
- Parminder K., Joseph T. H. and Nguyen S. T., *ACS Catal.*, 1 (2011) 819 - 835.
- Patra A. K., Ramanathan S., Sen D. and Mazumder S., *Pramana J. Phy.*, 63 (2004) 327 - 331.
- Paul C. N. and John R. B., *J. Non-Newtonian Fluid Mech.*, 131 (2005) 44 - 52.
- Pedersen J. S., *J. Appl. Crystallogr.*, 27 (1994) 595 - 608.
- Peer D., Karp J. M., Hong S., Farokhzad O. C., Margalit R., Langer R., *Nanotech.* 2 (2007) 751 - 760.
- Porod G., *Z- Kolloid*, 124 (1951) 83.
- Pradeep T., Mitra S., Sreekumaran A. N., and Mukhopadhyay R., *J. Phys. Chem. B*, 108 (2004) 7012-7020
- Pusch R., Karnland O. and Hokmark H. *GMM - A general microstructural model for qualitative and quantitative studies of smectite clays. Report SK. B - 90-43.* 94
- Rahul V., Banks-Lee P. and Abdel-Fattah S., *J. of Eng. Fibers and Fabrics*, 5(3) (2010) 7 - 15.
- Rajamathi M., Thimmaiah S., Morgan P.E.D. and Seshadri R., *J. Mater. Chem.*, 11 (2001) 2489 - 2492.
- Ramakrishnan N. and Arunachalam V.S., *J. Am. Ceram. Soc.* 76 (1993) 2745 - 52.
- Reinhardt B., Enke D. and Syrowatka F., *J. Am. Ceram. Soc.*, 95 (2) (2012) 461 - 465.
- Renoncourt A., Vlachy N., Bauduin P., Drechsler M., Touraud D., Verbavatz J. M., Dubois M., Kunz W. and Ninham B. W., *Langmuir*, 23 (2007) 2376 - 2381.
- Richard J. D. T., *Understanding solids - The science of materials*, John Wiley & Sons, (2004).

- Rouquerol J., Avnir D., Fairbridge C.W., Everett D. H., Haynes J.H., Pernicone N., Ramsay J.D.F., Sing K. S. W. and Unger K.K. *Pure Appl. Chem.*, 66 (8) (1994) 1739-1758.
- Sahimi M., *Flow and Transport in Porous Media*. VCH, Weinheim, (1995).
- Sánchez F. G., Jurányi F., Gimmi T., Loon L. V., Unruh T., and Diamond, J. *Chem. Phys.* 129 (2008) 174706.
- Sarrade S., Guizard C. and Rios G.M. *Sep. Purif. Technol.* 32 (2003) 57 - 63.
- Savitha C. N., and David J. G., *J. Eur. Cera. Soc.*, 15 (1995) 655 - 660.
- Scheidegger A.E., *Examination of the physics of theories of orogenesis*, *Bull. Geol. Soc. Am.*, 64 (2) (1953) 127 - 150
- Scheidegger A. E., *The physics of flow through porous media*, University of Toronto Press, (1974).
- Sears, V.F., *Theory of Cold Neutron Scattering by Homonuclear Diatomic Liquids. 2. Hindered Rotation*. *Can. J. of Phy.*, 44 (1966) 1299
- Seed H.B., Woodward R.J. and Lundgren R. A., *J. of Soil Mech. and Found. Div.*, 88 (SM3) (1962) 53–87.
- Sen D., Bahadur J., Mazumder S., Mahata T., Syambabu M. and Sinha P.K., *Pramana J. Phy.* 71 (2008) 979 - 984.
- Sen D., Patra A.K., Mazumder S. and Roy S. K., *Physica B*, 385–386 (2006) 607 - 610.
- Sen D., Patra A. K., Mazumder S., Mitra J., Dey G. K. and De P. K., *Pramana J. Phy.* 63 (2004) 321 - 326.
- Sen D., Mazumder S. and Tarafdar S., *J. Mater. Sci.*, 37 (2002) 941.
- Sen D., Patra A.K., Mazumder S. and Ramanathan S., *J. Alloys Comp.*, 340 (2002) 236 - 241

- Sen D., Mazumder S., Chitra R. and Chandrasekaran K.S., *J. Mater. Sci.* 36 (2001) 909 - 912.
- Sen D., Patra A.K., Mazumder S. and Ramanathan S., *Journal of Alloys and Compounds*, 361 (2003) 270 - 275.
- Shackelford Ch.D., *J. Cont. Hydro.*, 7 (1991) 177 - 217.
- Shaw N. J., *Powder Metallurgy International*, 21(3) (1989) 16 - 21.
- Shelke V. R., Bhagade S. S. and Mandavgane S.A., *Bull. Chem. React. Eng. Catal.*, 5 (2) (2010) 63 - 67.
- Shi J.L., *J. Mater. Res.*, 14(4) (1999) 1378 - 1388.
- Singwi K. S. and Sjolander A., *Phys. Rev.*, 119 (1960) 863 - 871.
- Skipper N.T., Lock P.A., Titiloye J.O., Swenson J., Mirza Z.A., Howells W.S. and Fernandez-Alonso F., *Chemical Geology*, 230 (2006) 182 - 196.
- Sposito G. and Prost R., *Chem. Rev.*, 82 (1982) 553 - 573.
- Studart A. R., Gonzenbach U. T., Tervoort E. and Gauckler L. J., *J. Am. Ceram. Soc.*, 89 (2006) 1771 - 89.
- Studart A. R., Studer J., Lei X., Kisun Y., Shum H. C. and Weitz D. A, *Langmuir*, 27(3) (2010) 955 - 964.
- Sun L., *Ind. Eng. Chem. Res.* 40 (2001) 5861 - 5877.
- Swann G. E. A. and Patwardhan S. V., *Clim. Past*, 7 (2011) 65 - 74.
- Swenson J., Bergman R., Bowron D. T. and Longeville S., *Philos. Mag. B*, 82 (2002) 497.
- Teixeira J., *J. Appl. Crystallogr.*, 21(1988) 781 - 785.
- Tunega D. , Benco L., Haberhauer G., Martin H. G. and Hans L., *J. Phys. Chem. B*, 106 (2002) 11515 - 11525.
- Umeda J., Kondoh K. and Michiura Y., *Materials Trans.*, 48 (2007) 3095 - 3100.

- Vasconcelos W. L., DeHoff R. T. and Hench L. L. J. Non-Cryst. Solids. 121 (1990) 124.
- Verweij H., Adv. Mater., 10(17) (1998) 1483 - 1486.
- Warr L. and Berger J., Physics and Chemistry of the Earth, 32 (2007) 247 – 258.
- Washburn E.W., Proc. of the National Acad. of Sci., 7 (1921) 115.
- Wersin P., Johnson L.H. and McKinley I.G. Physics and Chemistry of the Earth, 32 (2007) 780
- William J. L. and Ning L., Clays and Clay Minerals, 54 (4) (2006) 516 - 529.
- Xie M., Agus S. S., Schanz T. and Kolditz O., Int. J. Numer. Anal. Meth. Geomech., 28 (2004) 1479 - 1502.
- Xigeng M. and Dan S., Materials, 3 (2010) 1 - 12.
- Zhu K.L.I., Feng C., Zhu Z.G., Chin. Phy. Lett., 24 (2007) 187 - 190.

LIST OF PUBLICATIONS

Journal Publications:

1. Effects of pressure and temperature on pore structure of ceramic synthesized from rice husk: A small angle neutron scattering investigation, R. Raut Dessai, J.A.E. Desa, D. Sen, S. Mazumder, *J. of Alloys & Compounds*, 564 (2013) 125-129.
2. Nano-Porous Structure of a Porous Ceramics from Rice Husk, Reshma Raut Dessai, J. A. E. Desa, D. Sen, S. Mazumder, *Trans. Ind. Ceram. Soc.*, 71(4) (2012) 198-203.
3. Diffusion of Water in Bentonite Clay. *Journal of Physical society of Japan*, Reshma R. Dessai, V.K. Sharma, S.A. Prabhudesai, S. Mitra, J.A.E. Desa and R. Mukhopadhyay,

AIP Journal Publications:

1. Pore Structures of Compacted Glass Microspheres, Reshma Raut Desai, J.A.E. Desai, D. Sen and S. Mazumdar, *AIP Conf. Proc.*1313 (2010) 313-315.
2. Ultra small angle neutron scattering study of porous glass, Reshma R. Desai, J. A. Erwin Desai, D. Sen and S. Mazumder, *AIP Conf. Proc.*1349 (2011) 527-528.
3. Hydration of Bentonite clay by X-ray and Neutron scattering, Reshma R. Desai, J. A. Erwin Desai, V.K.Aswal, *AIP Conf. Proc.* 1447 (2012) 197-198.
4. Diffusion of water in Bentonite clay by X-ray and Neutron scattering, V. K. Sharma, S. A. Prabhudesai, R. Raut Dessai, J. A. Erwin Desai, S. Mitra, *AIP Conf. Proc.* 1512 (2013) 918-919.

Conferences and Symposia

1. Attended National Symposium on Science & Technology of Glass and Glass-Ceramics from Oct. 13-17, 2008, at Bhabha Atomic Research Centre, Mumbai.
2. Attended School on Neutrons as Probes of Condensed Matter from Oct. 5-10, 2009 at Bhabha Atomic Research Centre, Mumbai.

3. Attended Conference on Neutron Scattering and Mesoscopic systems from Oct. 12-14, 2009 organised by BARC, Mumbai in collaboration with Goa University, Goa.
4. Poster entitled “Structural and Porosity studies on Compacted Glasses” was presented at the International Congress in Glass from Sep.21-25, 2010, at Brazil.
5. Poster entitled “Pore Structures of Compacted Glass Microspheres” was presented at International Conference on Physics of Emerging Functional Materials from Sep.22-24, 2010, at Bhabha Atomic Research Centre, Mumbai.
6. Poster entitled “Ultra small angle neutron scattering study of porous glass” was presented at DAE-SSPS symposium held from Dec. 26-30, 2010, at Manipal.
7. Poster entitled “Structure and optical studies of Erbium and Holmium doped Borate glass” was presented at the National Conference on Science, Technology and Applications of Rare Earths, from Aug.19-20, 2011, at Munnar Kerala. (Received best poster presentation award).
8. Poster entitled “Hydration studies of Bentonite clay” was presented at DAE-SSPS symposium from Dec. 19-23, 2011, held at SRM University, Chennai.
9. Attended Workshop on “Scientific/Research Paper Writing” Organised by National academy of sciences India, from 8 -10 June 2012 at C.I.F.E. Mumbai.
10. Poster entitled “Nano-porous structure of a porous ceramic from rice husk” was presented at National Symposium on Materials and Processing from Oct. 10-12, 2012, at Bhabha Atomic Research Centre, Mumbai.
11. Oral Presentation on “SANS Study of a Micellar Solution Confined in a Bentonite Clay” was presented at International symposium on Neutron scattering from January 14-17, 2013, at Bhabha Atomic Research Centre, Mumbai.